
Carbon emissions from tropical wetlands

Dissertation zur Erlangung des akademischen Grades
Doktor der Naturwissenschaften (Dr. rer. nat.)

am Fachbereich für Physik und Elektrotechnik
der Universität Bremen

Vorgelegt von
Alexandra Klemme

- 06.08.2021 -



Universität
Bremen

Gutachter:

PD Dr. Thorsten Warneke
Prof. Dr. Mihalis Vrekoussis

Weitere Mitglieder der Prüfungskommission:

Prof. Dr. Annette Ladstätter-Weißmayer
Prof. Dr. Stefan Bornholdt
Dr. Matthias Buschmann
Thomas Visarius

Datum des Kolloquiums:

01.10.2021

Abstract

Carbon dioxide (CO₂) and methane (CH₄) are the two most important anthropogenic greenhouse gases. Due to human influences, their concentrations in the atmosphere have increased over the past 150 years, causing increased warming of the Earth's surface. For the global budgets of CO₂ and CH₄ it is not only important to assess anthropogenic emissions of CO₂ and CH₄ but also to understand the response of their natural fluxes to a changing climate.

Wetlands are one of the world's largest carbon pools. While natural wetlands represent a CH₄ source to the atmosphere, slow decomposition processes due to anaerobic conditions in their waterlogged soils lead to net carbon accumulation in wetlands. Especially peat soils, which consist of dead and decaying plant material, sequester large amounts of carbon from the atmosphere and, in their natural state, represent an atmospheric carbon sink. Among these peat soils are tropical peatlands which represent a globally significant carbon store. More than half of the known tropical peatlands are located in Southeast Asia. In recent years, the Southeast Asian peat carbon store has been destabilized due to deforestation and the transformation into plantations, causing high CO₂ emissions from peat soils and increased leaching rates of peat carbon into rivers.

High carbon leaching rates from Southeast Asian peat soils indicate that the carbon content in and the CO₂ emissions from peat-draining rivers in this region are high. Estimates based on field data suggest only moderate CO₂ emissions. The first part of this study aims to explain this phenomenon. It is found that carbon decomposition in peat-draining rivers is hampered by low *pH*. This limits CO₂ production in and emissions from peat-draining rivers. Data collected for this study yield an exponential *pH* limitation that shows a good agreement with laboratory measurements from high latitude peat soils. Additionally, the results suggest that enhanced input of carbonate minerals increase CO₂ emissions from peat-draining rivers by counteracting the *pH* limitation. This points out an important feedback mechanism of human activities that cause such inputs of carbonate minerals, like the deforestation of river catchments, liming in plantations and enhanced weathering projects.

Enhanced weathering is a CO₂ removal strategy that accelerates the CO₂ uptake by weathering via the distribution of rock-powder over land. During weathering, atmospheric CO₂ is converted into bicarbonate, which precipitates in soils and is washed out and transferred via rivers into the ocean. Weathering is favoured by warm and humid conditions and therefore target areas for enhanced weathering include the tropics. Among the suggested target areas

are tropical peatlands. The second part of this study investigates the impact of enhanced weathering on CO₂ emissions from tropical peat regions. Results indicate that enhanced weathering would destabilize the peat carbon store, which could offset the CO₂ uptake by enhanced weathering. Based on a case study for Sumatra, the *pH* dependence of peat decomposition is incorporated in enhanced weathering scenarios. The resulting emission estimates suggest that the enhanced weathering induced *pH* increase causes enhanced CO₂ emissions from peat soils, peat-draining river and coastal areas that amount to at least 50 % and potentially more than 150 % of the estimated CO₂ uptake by enhanced weathering.

The third research topic in this study aims to evaluate wetland CH₄ emissions by use of satellite data and a global transport model. Model runs show that the impact of CH₄ emissions from individual wetlands on regional atmospheric XCH₄ can be observed via satellite. Wetland CH₄ emission datasets vary strongly in regional CH₄ emission flux rates and flux seasonality. Model runs using these differing datasets were able to reproduce the atmospheric CH₄ concentrations and variations observed by satellites. The JSBACH emission dataset shows the best correlation to satellite data. However, the good agreement observed for all datasets indicates that the cause for the good representation of atmospheric CH₄ are modelled nudging fluxes rather than correct wetland emission fluxes. Further evaluation of these fluxes reveal a missing CH₄ source of approximately 120 TgCH₄ yr⁻¹ in the model. Comparison with published CH₄ budgets suggests that the reason for this CH₄ emission deficit could be missing inland water emissions. Model budgets considering these additional fluxes suggest higher inland water CH₄ emissions and atmospheric CH₄ sinks than stated in recent top-down estimates by the Global Carbon Project.

Contents

1. Objective and outline	1
2. Wetlands in the global carbon cycle	3
2.1. The global carbon cycle	3
2.1.1. Atmospheric carbon dioxide (CO ₂)	4
2.1.2. Atmospheric methane (CH ₄)	5
2.1.3. Climate change mitigation	7
2.2. Carbon dynamics in wetlands and other aquatic systems	7
2.2.1. Organic carbon species in aquatic systems	10
2.2.2. Inorganic carbon species in aquatic systems	11
2.2.3. Aerobic decomposition	12
2.2.4. Anaerobic decomposition	13
2.2.5. Atmospheric gas exchange with surface waters	14
3. Methods	15
3.1. River campaigns and measurements	15
3.1.1. Dissolved CO ₂ measurements	16
3.1.2. Water-atmosphere flux measurements	17
3.1.3. DOC measurements	18
3.1.4. Particulate carbon measurements	19
3.1.5. pH and dissolved O ₂ measurements	19
3.2. Catchment properties and additional parameters	20
3.2.1. Determination of catchment properties	20
3.2.2. Atmospheric gas exchange coefficients	21
3.2.3. River carbon yields	21
3.3. Global atmospheric chemistry and transport model	22
3.3.1. TM5-MP chemistry and transport model	22
3.3.2. CH ₄ emission datasets	23
3.4. Satellite CH ₄ data	24
3.4.1. SCIAMACHY satellite	25
3.4.2. GOSAT satellite	25

4. Limitation of CO₂ production in peat-draining rivers	27
4.1. Background and objective	27
4.2. Study area	28
4.3. Interdependence of river carbon parameters	29
4.3.1. Correlation of river DOC, pH, CO ₂ and O ₂ with peat coverage	29
4.3.2. Correlation of river CO ₂ and O ₂ with DOC and pH	31
4.4. Natural limitation in river CO ₂ due to inhibition of decomposition	33
4.4.1. Quantification of the pH and O ₂ impact on decomposition rates	33
4.4.2. Evaluation of linear and exponential pH limitation of decomposition	36
4.5. Suspension of maximum CO ₂ concentration in the Simunjan river	39
4.6. Conclusion	41
5. Response of tropical peat areas to enhanced weathering	43
5.1. Background and objective	43
5.2. Study area	44
5.3. Enhanced weathering estimates	45
5.4. Response of soil carbon mobilisation to enhanced weathering	46
5.4.1. Dependency of CO ₂ and DOC mobilisation from peat soils on pH	46
5.4.2. Response of CO ₂ emissions from soils to enhanced weathering	48
5.4.3. Response of DOC leaching from soils to enhanced weathering	49
5.4.4. Response of DIC leaching from soils to enhanced weathering	50
5.5. Response of river carbon export to enhanced weathering	51
5.5.1. Description of river box-model	51
5.5.2. Response of river CO ₂ emissions to enhanced weathering	52
5.5.3. Response of river DOC and DIC discharge to enhanced weathering	56
5.6. Response of coastal carbon emissions to enhanced weathering	58
5.6.1. Description of coastal water mixing calculations	58
5.6.2. Response of coastal CO ₂ emissions to enhanced weathering	59
5.7. Sumatra's carbon emission response to enhanced weathering	62
5.8. Conclusion	63
6. Towards validation of wetland CH₄ emissions	65
6.1. Background and objective	65
6.2. Study Area	66

6.3.	Impact of individual wetlands on regional atmospheric XCH ₄	67
6.4.	Differences between the wetland emissions datasets	69
6.4.1.	Diagnostic wetland CH ₄ emission datasets	69
6.4.2.	Prognostic wetland CH ₄ emission datasets	72
6.5.	Modelled CH ₄ concentrations and nudging fluxes	74
6.5.1.	Modelled nudging emissions	74
6.5.2.	Correlation of modelled XCH ₄ with satellite data	75
6.5.3.	Correlation of de-trended annual XCH ₄ variations to satellite data	77
6.5.4.	Impact of wetlands on modelled XCH ₄ for model runs including nudging	79
6.6.	Deficit in the modelled XCH ₄	81
6.6.1.	Deficit in the model CH ₄ budget	81
6.6.2.	Evaluation of CH ₄ sources and sinks	82
6.7.	Conclusion	84
7.	Overall Conclusions	87
8.	Outlook	89
A.	Appendix	91
A.1.	Abbreviations	91
A.1.1.	Acronyms	91
A.1.2.	Chemical formulas	91
A.2.	Appendix to chapter 4	92
A.2.1.	Additional figures and tables	92
A.2.2.	Discussion of individual river campaigns	96
A.2.3.	CO ₂ emission estimates for Southeast Asian peat-draining rivers	97
A.3.	Appendix to chapter 5	99
A.3.1.	Additional figures and tables	100
A.4.	Appendix to chapter 6	101
A.4.1.	Additional figures and tables	101
A.4.2.	Seasonality of wetland CH ₄ emissions	104
A.4.3.	Correlation of modelled XCH ₄ to satellite data for additional regions	111
	References	119
	Acknowledgements	135

List of Figures

1.1.	Time series of global surface temperature anomaly	1
2.1.	Illustration of global carbon cycle	4
2.2.	Time series of global atmospheric CO ₂ concentrations	5
2.3.	Time series of global atmospheric CH ₄ concentrations	6
2.4.	Global map of peatland coverage	9
2.5.	Schematic of carbon dynamics in tropical wetland regions	10
2.6.	Bjerrum plot of inorganic carbon species as function of pH	12
3.1.	Picture of equipment used for measurements at Southeast Asian rivers	16
3.2.	Headspace setup for dissolved CO ₂ measurements	17
4.1.	Map of Southeast Asian study area and rivers	28
4.2.	Pictures of Southeast Asian peat-draining rivers	29
4.3.	Dependency of measured river parameters on peat coverage	30
4.4.	Dependency of river CO ₂ and O ₂ on DOC and pH	32
4.5.	Correlation between river depths and gas exchange coefficients	35
4.6.	Correlation plots of CO ₂ and O ₂ for linear decomposition approach	36
4.7.	Correlation plots of CO ₂ and O ₂ for exponential decomposition approach	37
4.8.	Data dependence on peat coverage including abnormal Simunjan campaigns	41
5.1.	Map of Sumatran study area	44
5.2.	Dependency of CO ₂ and DOC mobilisation from peat soils on pH	47
5.3.	Dependency of carbon mobilisation from peat soils on pH increase	48
5.4.	Carbonate induced change in river pH and CO ₂ versus original river pH	53
5.5.	Carbonate induced change in river O ₂ and DOC versus original river pH	54
5.6.	River emission response to enhanced DIC and DOC leaching	55
5.7.	River emission response to DOC leaching for different DIC leaching rates	56
5.8.	Response of carbon export from rivers to enhanced DIC and DOC leaching	57
5.9.	Coastal emission response to enhanced DOC and DIC leaching	60
5.10.	Coastal emission response to DOC leaching for different DIC leaching rates	61
5.11.	Overview of Sumatra's carbon emission response to enhanced weathering	62
6.1.	Map of selected tropical wetland regions	66
6.2.	Impact of emissions from individual wetlands on local atmospheric XCH ₄	68
6.3.	Global map of wetland CH ₄ emissions	69
6.4.	Latitudinal distribution of wetland CH ₄ emissions	70
6.5.	Regional wetland CH ₄ fluxes from diagnostic datasets	71

6.6.	Exemplary seasonality of wetland CH ₄ emissions for the Amazon region . . .	72
6.7.	Global map of wetland CH ₄ emissions from prognostic datasets	73
6.8.	Regional wetland CH ₄ fluxes from prognostic datasets	73
6.9.	Global distribution of nudging fluxes	75
6.10.	Time series of modelled and measured XCH ₄ in the Amazon region	76
6.11.	Time series of modelled and measured XCH ₄ seasonality in the Amazon region	78
6.12.	Impact of wetland emissions on XCH ₄ in selected wetland regions	80
6.13.	XCH ₄ deficit for model runs without nudging	81
6.14.	Model CH ₄ budget compared to budgets stated by the GCP	83
A.1.	Correlation between river discharge and river water volume	93
A.2.	Dependency of river CO ₂ and O ₂ on DOC for individual river campaigns . . .	96
A.3.	Dependency of river CO ₂ and DOC on local precipitation	97
A.4.	Correlation between river carbon yields and peat coverage	98
A.5.	Time series of parameters derived via the river box-model	100
A.6.	Correlation between modelled and measured river parameters	100
A.7.	Global wetland CH ₄ emission maps for diagnostic GCP datasets	101
A.8.	Global wetland CH ₄ emission maps for prognostic GCP datasets	102
A.9.	Detailed model CH ₄ budget compared to budgets by the GCP	103
A.10.	Seasonality of wetland CH ₄ emissions from the Congo region	104
A.11.	Seasonality of wetland CH ₄ emissions from the Ganges region	105
A.12.	Seasonality of wetland CH ₄ emissions from the Southeast Asian region . . .	106
A.13.	Seasonality of wetland CH ₄ emissions from the Pantanal region	107
A.14.	Seasonality of prognostic wetland CH ₄ emissions from the Amazon region .	108
A.15.	Seasonality of prognostic wetland CH ₄ emissions from the Congo region . .	108
A.16.	Seasonality of prognostic wetland CH ₄ emissions from the Ganges region . .	109
A.17.	Seasonality of prognostic wetland CH ₄ emissions from the SE Asian region .	109
A.18.	Seasonality of prognostic wetland CH ₄ emissions from the Pantanal region .	110
A.19.	Time series of modelled and measured XCH ₄ in the Congo region	111
A.20.	Time series of modelled and measured XCH ₄ in the Southeast Asian region .	112
A.21.	Time series of modelled and measured XCH ₄ in the Ganges region	113
A.22.	Time series of modelled and measured XCH ₄ in the Pantanal region	114
A.23.	Time series of modelled and measured CH ₄ seasonality in the Congo region .	115
A.24.	Time series of modelled and measured CH ₄ seasonality in the SE Asian region	116
A.25.	Time series of modelled and measured CH ₄ seasonality in the Ganges region .	117
A.26.	Time series of modelled and measured CH ₄ seasonality in the Pantanal region	118

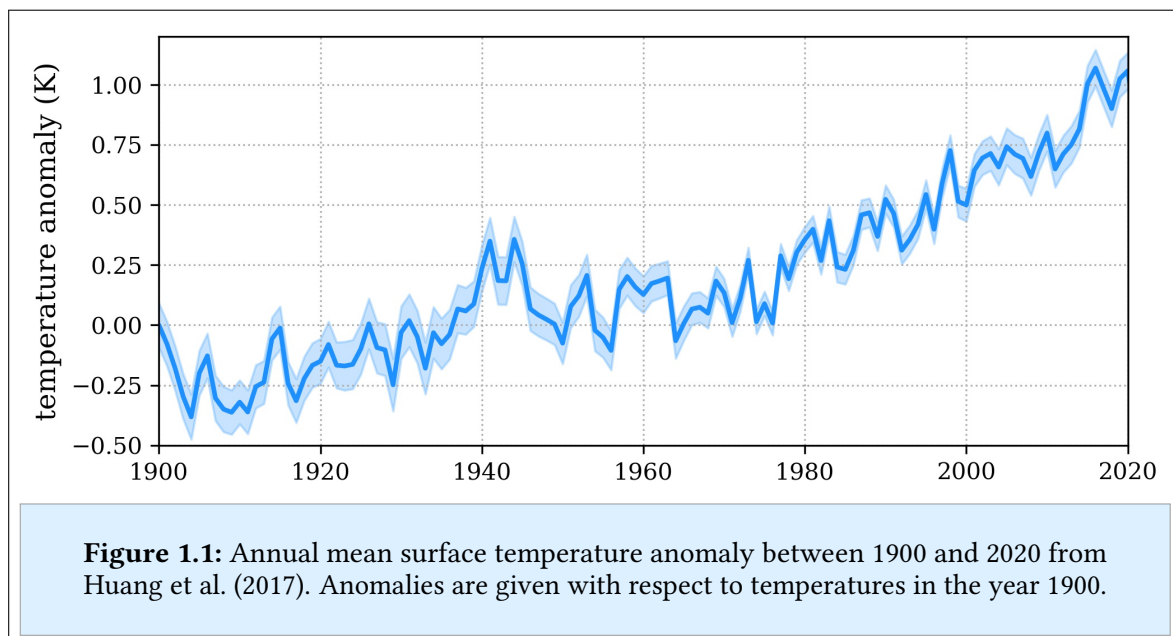
List of Tables

2.1. Description of wetland types	8
3.1. CH ₄ emission sectors and global emissions	23
3.2. List of models that computed wetland CH ₄ emission datasets	24
4.1. Decomposition parameters from linear <i>pH</i> approach	37
4.2. Decomposition parameters from exponential <i>pH</i> approach	38
4.3. Limitation of in-river decomposition caused by low <i>pH</i> and O ₂	39
4.4. Measured data for the four Simunjan campaigns	40
5.1. Previous enhanced weathering estimates	45
5.2. Soil feedback on enhanced weathering application on Sumatra	49
5.3. River feedback on enhanced weathering application on Sumatra	58
5.4. Coastal response to enhanced weathering application on Sumatra	61
6.1. CH ₄ emission estimates from the GCP	66
6.2. Description and location of selected wetland regions	67
6.3. Average CH ₄ emissions from selected wetland regions	70
6.4. Correlation of modelled XCH ₄ in the Amazon region to satellite data	77
6.5. Correlation of modelled XCH ₄ variations in the Amazon region to satellite data	79
6.6. Nudging fluxes from model runs based on diagnostic emission datasets	82
6.7. Atmospheric CH ₄ burden derived from model budgets compared to literature	84
A.1. Derived river catchment properties	92
A.2. Measured river water properties	93
A.3. Conducted river campaigns in Southeast Asia	94
A.4. Limitation of in-river decomposition based on the linear <i>pH</i> approach	94
A.5. Equations to be optimized for exponential decomposition limitation by <i>pH</i>	95
A.6. Equations to be optimized for linear decomposition limitation by <i>pH</i>	95
A.7. River carbon yields and outgassing fractions	99
A.8. Comparison of regional river CO ₂ emissions to literature	99
A.9. Emissions from selected wetland regions as stated in diagnostic datasets	102
A.10. Emissions from selected wetland regions as stated in prognostic datasets	103
A.11. Correlation of modelled XCH ₄ in the Congo region to satellite data	111
A.12. Correlation of modelled XCH ₄ in the SE Asian region to satellite data	112
A.13. Correlation of modelled XCH ₄ in the Ganges region to satellite data	113
A.14. Correlation of modelled XCH ₄ in the Pantanal region to satellite data	114

- A.15. Correlation of modelled XCH₄ variations in the Congo region to satellite data 115
- A.16. Correlation of modelled XCH₄ variations in the SE Asian region to satellite data 116
- A.17. Correlation of modelled XCH₄ variations in the Ganges region to satellite data 117
- A.18. Correlation of modelled XCH₄ variations in the Pantanal region to satellite data 118

1. Objective and outline

Climate and climate change mitigation studies have become highly relevant in the recent decades due to ongoing global warming (Figure 1.1; Huang et al., 2017). Scientists agree that human impacts since the industrial era have been the dominant cause of this changing climate (Hartmann et al., 2013a) and that an increase in atmospheric concentrations of greenhouse gases represents its main driver (Myhre et al., 2013). Carbon dioxide (CO₂) and methane (CH₄) are the two most important anthropogenic greenhouse gases (Smith et al., 2013). Thus, global carbon research is important to understand human induced impacts on global warming and to assess realistic climate change mitigation strategies (de Coninck et al., 2018). For this, not only anthropogenic greenhouse gas emissions are of interest but also the response of natural atmospheric CO₂ and CH₄ fluxes on a changing climate.



The objective of this study is to constrain carbon emissions from tropical wetland regions and to understand what drives these emissions. The study is structured into three major research topics. The first research topic focuses on tropical rivers that drain peatlands. It aims to explain moderate CO₂ fluxes observed from peat-draining rivers and to improve CO₂ emission estimates from these rivers. The second research topic aims to quantify the response of CO₂ emissions from tropical peat regions on the application of enhanced weathering. To achieve this, the CO₂ emission response from peat soils, peat-draining rivers and coastal areas on enhanced weathering induced *pH* changes are derived based on a case study for Sumatra. The third research topic aims to constrain CH₄ emissions from tropical wetland regions.

1. Objective and outline

For this, different emission datasets are evaluated by use of an atmospheric chemistry and transport model and satellite retrievals.

The thesis is structured into the following chapters:

Chapter 2 provides an introduction to the global carbon cycle with the focus on atmospheric CO₂ and CH₄ budgets, climate change mitigation strategies and the role of tropical wetlands in the carbon cycle.

Chapter 3 describes the methods used to obtain the data evaluated in this study. The measurement principles utilized during the field campaigns in Southeast Asia as well as the atmospheric transport model and satellite retrievals are described.

Chapter 4 illustrates the results of the first research topic. It analyses the carbon dynamics in tropical peat-draining rivers with the focus on the dependency of CO₂ emissions from those rivers on *pH*. Parts of this chapter have been published in Klemme et al. (in review, 2021).

Chapter 5 presents the results of the second research topic. It investigates the response of CO₂ emissions from tropical peat regions on enhanced weathering and provides an estimate for the impact of this response on the net CO₂ uptake by enhanced weathering.

Chapter 6 illustrates the results of the third research topic. It focuses on the evaluation of different wetland CH₄ emission datasets. For this, the datasets are used as input to an atmospheric chemistry and transport model and model results are compared to satellite data.

Chapter 7 summarizes the main findings from this study.

Chapter 8 provides an outlook on possible future work based on the results of this study.

2. Wetlands in the global carbon cycle

This chapter provides an introduction to the global carbon cycle and the role of tropical wetlands within it. Section 2.1 describes the global carbon cycle with the focus on atmospheric CO₂ and CH₄ budgets as well as on climate change mitigation strategies. Section 2.2 illustrates the role of wetlands in the global carbon cycle.

2.1. The global carbon cycle

The global carbon cycle (Figure 2.1) describes the exchange of carbon between different reservoirs. Depending on the time scale of the carbon exchange, one can distinguish between a slow and a fast component of the carbon cycle (Ciais et al., 2013). The fast component, with turnover times of years to decades, represents the carbon exchange between three major reservoirs: the atmosphere, the ocean and the land (Ciais et al., 2013). It includes carbon fluxes due to photosynthesis, respiration and fires as well as atmospheric gas exchange with surface waters and transport from the land to the ocean by rivers (Hannah, 2015). The slow component of the carbon cycle, with turnover times of 10,000 years and more, represents the carbon exchange with rocks and sediments (Ciais et al., 2013). It includes fluxes due to chemical weathering and volcanism as well as turnover and sedimentation in the ocean (Hannah, 2015).

Over the past centuries, anthropogenic activities such as deforestation and burning of fossil fuels have returned old carbon from stable carbon pools into the fast component of the carbon cycle (Ciais et al., 2013). Therefore, carbon concentrations in the reservoirs of the fast carbon cycle have increased. Approximately 50 % of the additional carbon is stored in the atmosphere, while the other half is absorbed by the land and the ocean (Hartmann et al., 2013a).

In the atmosphere, carbon exists mainly in the form of CO₂ and in smaller concentrations as CH₄, carbon monoxide (CO) and other trace gases. CO, with an atmospheric lifetime of approximately two months (Khalil and Rasmussen, 1990), is relatively quickly oxidized to CO₂ by reaction with atmospheric hydroxyl radicals (OH). CO₂ and CH₄, which are relatively stable in the atmosphere, are the two most important anthropogenic greenhouse gases (Smith et al., 2013). They absorb infrared radiation from the Earth's surface and re-emit it while letting most of the solar radiation pass through (Hansen et al., 2005). This process that causes an increase in the Earth's surface temperature is called the greenhouse effect. It becomes

2. Wetlands in the global carbon cycle

stronger with increasing atmospheric concentrations of greenhouse gases (Kweku et al., 2018). Subsection 2.1.1 and subsection 2.1.2 describe the atmospheric budgets of CO₂ and CH₄, respectively. Subsection 2.1.3 discusses possible climate change mitigation strategies with the focus on enhanced weathering.

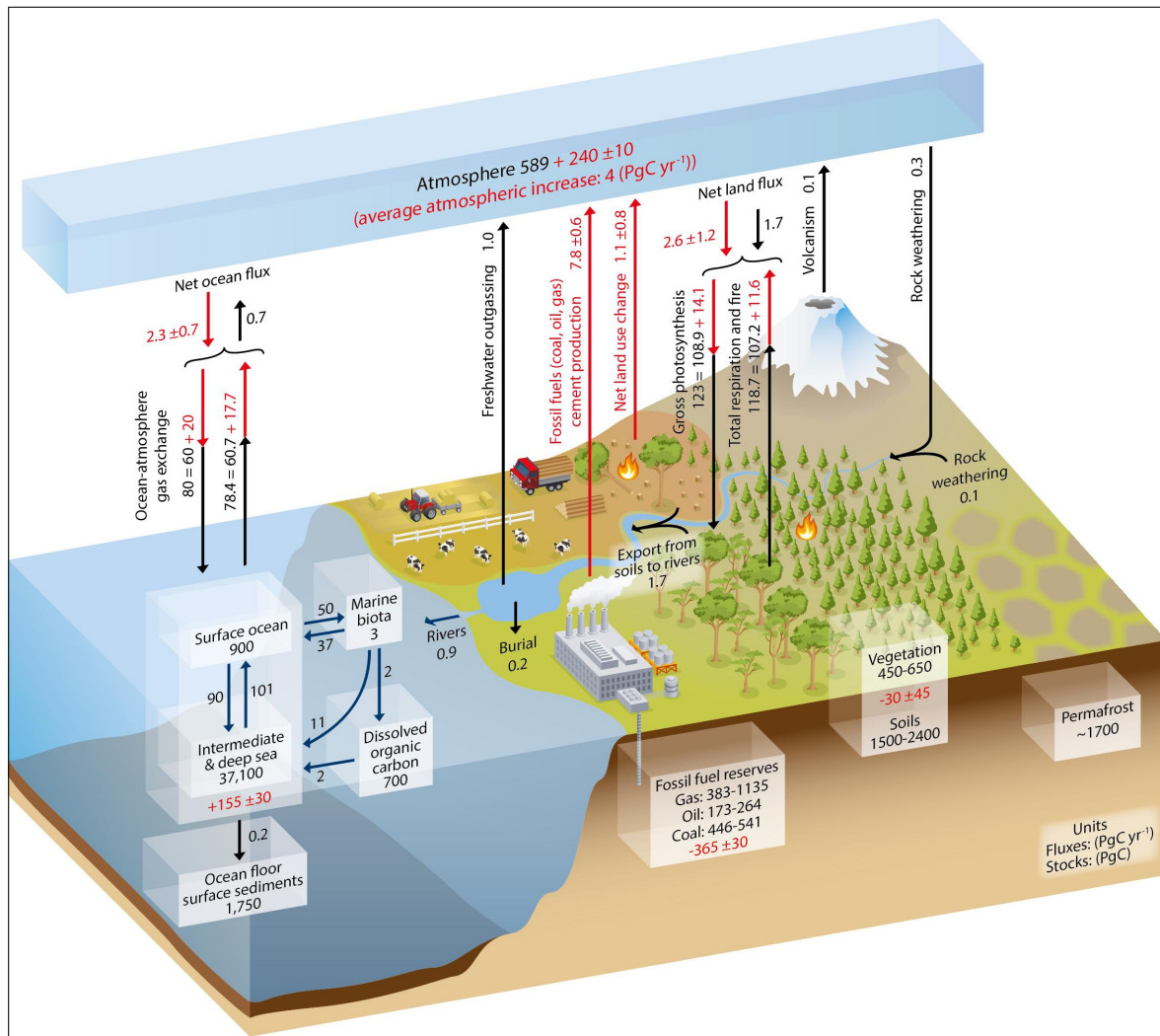


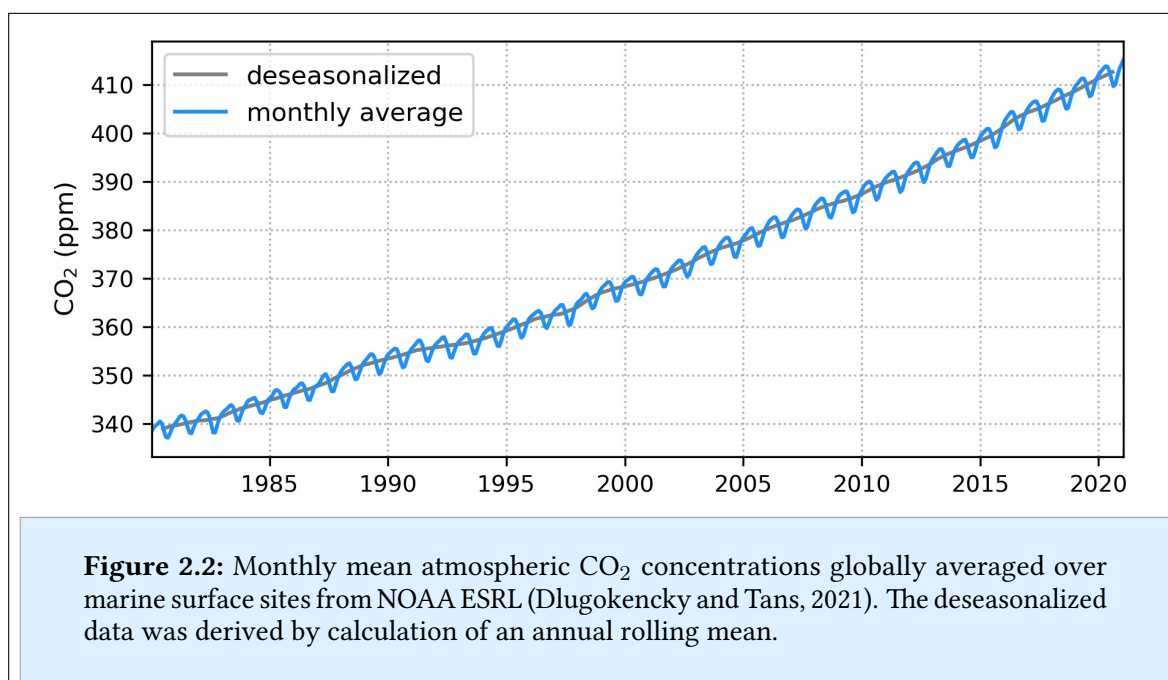
Figure 2.1: Illustration of the global carbon cycle (Ciais et al., 2013). Carbon stocks in the reservoirs are given in petagrams of carbon. Arrows represent exchange fluxes between reservoirs, which are given in petagrams of carbon per year. Black numbers represent the natural system based on data from 1750 as reference for the pre-industrial era. Red numbers indicate the change due to anthropogenic influences between 1750 and 2011.

2.1.1. Atmospheric carbon dioxide (CO₂)

CO₂ is the most important anthropogenic greenhouse gas (Smith et al., 2013). It makes up the majority of atmospheric carbon with concentrations of several hundred ppm and long

atmospheric lifetimes of centuries to more than 1,000 years (Archer et al., 2009). Atmospheric CO₂ concentrations increased from pre-industrial concentrations of 270 ppm (Joos and Spahni, 2008) to more than 410 ppm in 2021 (Figure 2.2).

This increase is caused by an imbalance between atmospheric CO₂ sources and sinks which is driven by the increase in anthropogenic CO₂ emissions since the industrial era (Friedlingstein et al., 2019). For a long time, the dominating force in these anthropogenic emissions was land use change (Friedlingstein et al., 2019). However, while land use change emissions stayed relatively constant, fossil fuel emissions increased since 1850 and approximately since 1950 they outweigh land use change emissions. Today, fossil fuel emissions are about five times higher than land use change emissions (Friedlingstein et al., 2019).



Based on estimates by Friedlingstein et al. (2019) within the decade of 2009 to 2018 fossil fuel emissions averaged to (9.5 ± 0.5) petagrams of carbon (PgC) per year and land use change emissions were (1.5 ± 0.7) PgC yr⁻¹. Those emissions caused an atmospheric CO₂ increase of about 4.9 PgC yr⁻¹, while (3.2 ± 0.6) PgC yr⁻¹ are taken up by the land and (2.5 ± 0.6) PgC yr⁻¹ by the ocean.

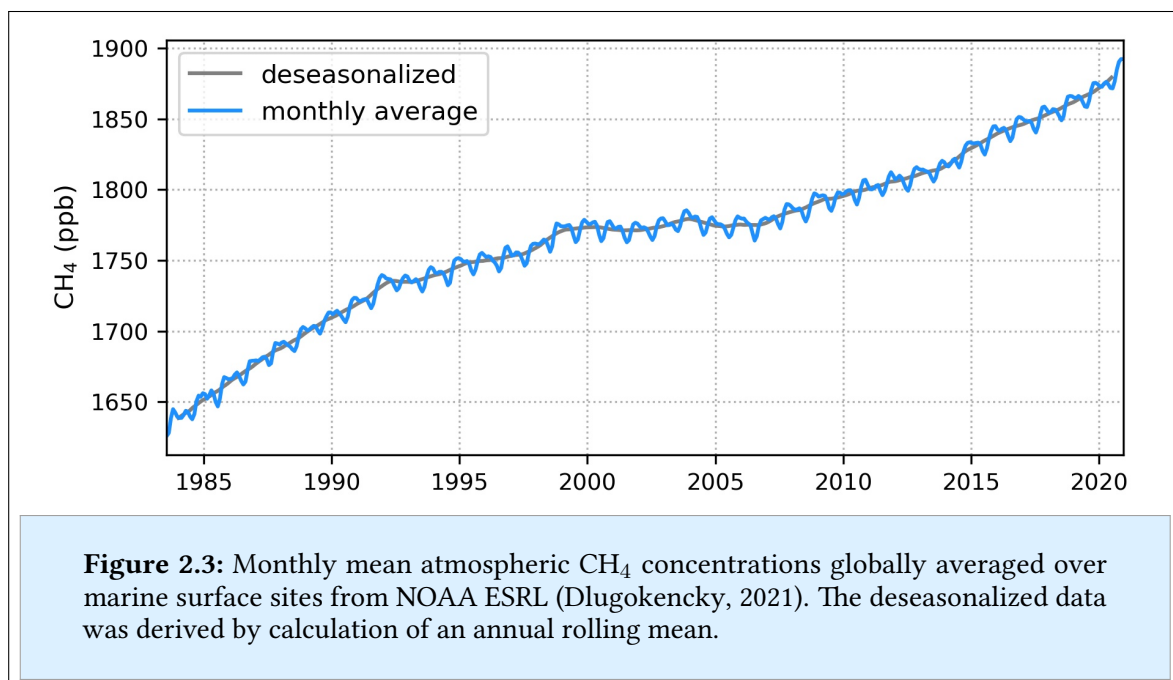
2.1.2. Atmospheric methane (CH₄)

CH₄ is the second most important anthropogenic greenhouse gas after CO₂ (Smith et al., 2013). Its instantaneous impact on the Earth's energy balance is much stronger than that of CO₂ (Myhre et al., 2013). Yet, its atmospheric lifetime of approximately one decade (Kaplan

2. Wetlands in the global carbon cycle

et al., 2006) lowers its global warming potential on a time horizon of 100 years to 28-34 (Myhre et al., 2013). Atmospheric CH₄ concentrations more than doubled from pre-industrial concentrations of 700 ppb (Loulergue et al., 2008) to about 1890 ppb in 2021 (Figure 2.3).

The atmospheric growth rate of CH₄ is determined by the balance between surface emissions and photochemical destruction by OH (Bousquet et al., 2006). Main anthropogenic CH₄ sources are agriculture and fossil fuel production and use (Saunois et al., 2020). Based on top-down estimates by Saunois et al. (2020) within the decade of 2008 to 2017 average fossil fuel emissions were 83 TgC yr⁻¹ and emissions from agriculture and waste were 163 TgC yr⁻¹, while biomass burning emissions (which are partially anthropogenic) were comparatively moderate with 23 TgC yr⁻¹. Additional CH₄ was emitted from wetlands (136 TgC yr⁻¹) and other natural sources (28 TgC yr⁻¹). Sinks from chemical reactions in the atmosphere compensated for the majority of these emissions (389 TgC yr⁻¹), while a smaller fraction (29 TgC yr⁻¹) is taken up by soils and approximately 10 TgC yr⁻¹ stay in the atmosphere (Saunois et al., 2020).



Other than the atmospheric CO₂ concentration, the concentration of CH₄ did not continuously increase over the past decades. For example, atmospheric CH₄ concentrations were fairly constant within the period of 1999 to 2006 (Figure 2.3). Possible explanations for the renewed atmospheric increase since 2007 are increased biogenic emissions as indicated by a decrease in the ratio of heavy CH₄ isotopes (Schaefer et al., 2016; Nisbet et al., 2016), increased

emissions from fossil fuels as indicated by concurrent ethane emissions (Hausmann et al., 2016) and decreased OH concentrations resulting in a reduced chemical sink of CH₄ (Turner et al., 2017; Rigby et al., 2017). However, it has not been possible to unambiguously link the observed CH₄ variations to specific sources (Turner et al., 2019).

2.1.3. Climate change mitigation

To mitigate climate change, a reduction in net greenhouse gas emissions is essential (Myhre et al., 2013). In 2016, the Paris Agreement was signed with the main objective to keep the global temperature increase at well below 2 °C above pre-industrial levels (Horowitz, 2016). For this, parties agreed to limit anthropogenic greenhouse gas emissions such that they will peak as soon as possible. The aim was to reach emission neutrality in the second half of the century (Horowitz, 2016). However, it has become clear that the reduction of greenhouse gas emissions to net zero is not sufficient to reach the Paris climate goal (Roy et al., 2018) and that further emission reduction is needed.

To achieve net negative atmospheric fluxes, atmospheric CO₂ removal strategies are discussed (de Coninck et al., 2018; Field and Mach, 2017). Such strategies include increased natural CO₂ uptake through reforestation, conservation agriculture and coastal restoration as well as CO₂ uptake through biomass based engineering like bio-energy with carbon capture and storage and CO₂ uptake through non-biological engineering approaches like direct air capture and enhanced weathering (Field and Mach, 2017).

Enhanced weathering is a CO₂ removal strategy that is based on large scale application of pulverized rocks over the land surface to accelerate weathering rates. Natural rock weathering consumes approximately 0.3 PgC yr⁻¹ of atmospheric CO₂, representing ≈ 3 % of the anthropogenic fossil fuel and land use change emissions (Figure 2.1). Studies on the cost efficiency of enhanced weathering have estimated promising carbon dioxide removal rates of up to 1,000 MgC km⁻² yr⁻¹ (Taylor et al., 2016; Strefler et al., 2018; Beerling et al., 2020) which could lower atmospheric CO₂ by 30 to 300 ppm until 2100 (Taylor et al., 2016).

2.2. Carbon dynamics in wetlands and other aquatic systems

Wetlands represent one of the world's largest carbon pools (Page et al., 2011). Differing definitions of wetlands are used. In this study they are referred to according to the definition in Wetlands (1995) as ecosystems that depend on constant or recurrent, shallow inundation or saturation at or near the surface of the substrate. Generally, wetlands can be divided

2. Wetlands in the global carbon cycle

into coastal wetlands and inland wetlands (Reddy and DeLaune, 2008a). Coastal wetlands exist in the forms of mangrove wetlands as well as tidal salt and freshwater marshes (Mitsch and Gosselink, 2015). Inland wetlands are comprised of freshwater marshes and peatlands as well as freshwater swamps and riparian wetlands (Mitsch and Gosselink, 2015). Short descriptions of these wetland types are given in Table 2.1.

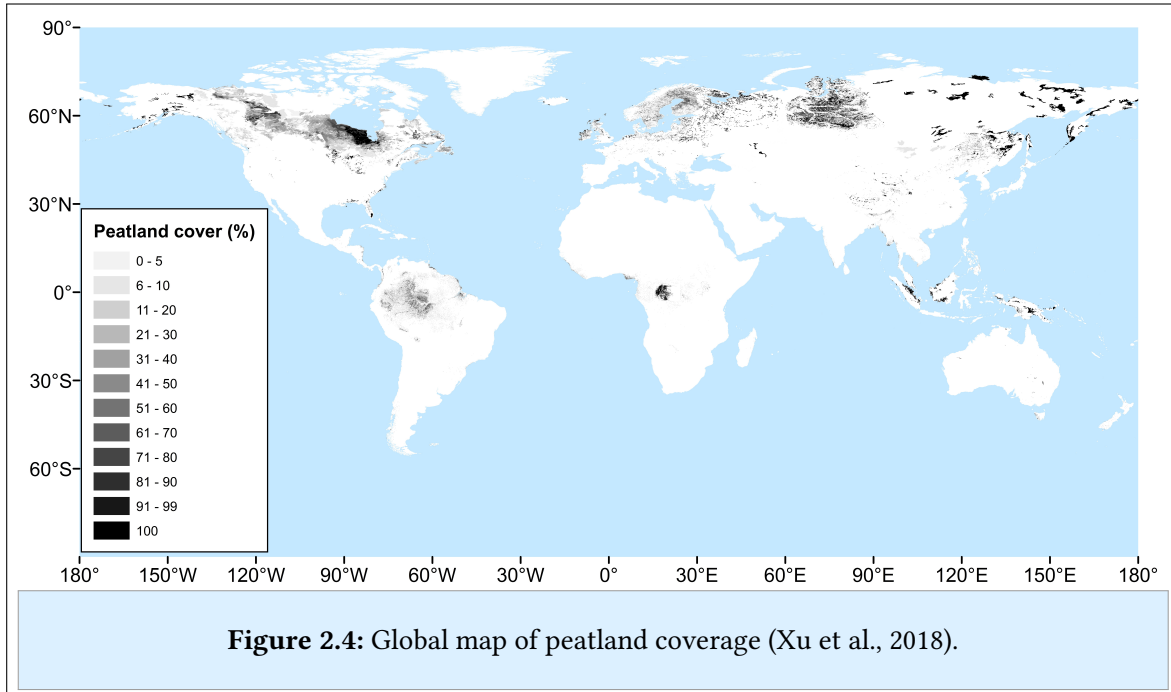
wetland type	description
mangrove swamp	wetland ecosystem in estuaries and marine shorelines where mangrove forests are present
tidal saltwater marsh	wetland ecosystem between land and open seawater that is covered by grasses, rushes or reeds and that is regularly flooded by the tides
tidal freshwater marsh	wetland ecosystem that is covered by herbaceous plants where influence of the tides causes flooding by freshwater rather than seawater
freshwater marsh	wetland ecosystem that is dominated by herbaceous plants like grasses, rushes and reeds
freshwater swamp	wetland ecosystem that is dominated by forests and does not accumulate large amounts of peat
peatlands	wetland ecosystem with thick waterlogged soil layers that consist of dead and decaying plant material
riparian wetlands	wetland ecosystem that is located along the margins of streams or rivers

Table 2.1: List and description of different wetland types (Finlayson, 2016a,b; Barendregt, 2016).

Other than mineral soils, which consist of approximately 50 % solids, one-quarter air and one-quarter water (Reddy and DeLaune, 2008b), wetland soils are water saturated and consist of 50 % solids and 50 % water. Due to those waterlogged soil conditions, the oxygen (O₂) availability in wetland soils is limited, causing slow decomposition of organic matter (Megonigal et al., 2003). These slow decomposition rates cause accumulation of organic matter in the soils (Page et al., 2011). Despite acting as a net carbon sink, wetlands are the largest natural source of atmospheric CH₄ and cause approximately one third of the global CH₄ emissions (Kirschke et al., 2013).

Wetlands cover (6 – 8) % of the global land surface and store about one-third of the terrestrial soil carbon (500 Pg; Keller, 2011). Approximately half of this carbon is stored in tropical wetlands, mainly in deep peat soils that occur under mangrove and swamp forests (Dalmagro et al., 2019). Peatlands are classified as wetlands with thick waterlogged soil layers that consist of dead and decaying plant material (Table 2.1; Wetlands International). Thus, the soil consists mainly of organic matter (65 %), has low pH and is poor in nutrients (Müller

et al., 2015). Though peatlands only cover $\approx 3\%$ of the global land area (Figure 2.4), they contain twice as much carbon as the world's forests (Wetlands International). Due to that immense amount of carbon, peatlands play an important role in the global carbon cycle.

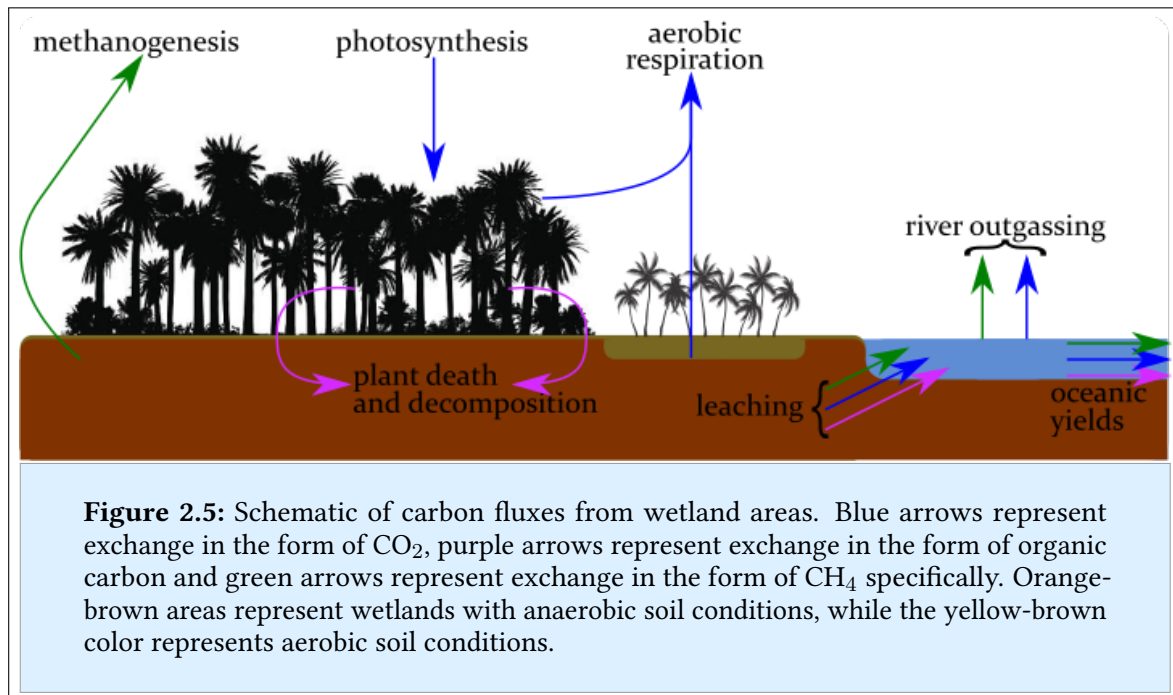


The carbon accumulation in wetlands is conditioned by the balance of carbon uptake through photosynthetic activity and carbon loss through aerobic respiration, anaerobic respiration (methanogenesis) and leaching into rivers (Figure 2.5). Part of the carbon that is leached into rivers is emitted to the atmosphere, while the remaining fraction is transported to the ocean. In natural wetlands, O_2 supply is generally restricted to a thin layer of surface soil and to the water column (Page et al., 2011). Thus, in the majority of the soil, slow anaerobic respiration in the form of methanogenesis is performed (Reddy and DeLaune, 2008e). Approximately 3% of the net primary production (NPP = photosynthesis - plant respiration) in natural wetland regions is emitted back into the atmosphere in the form of methane (Whiting and Chanton, 1993). However, the drainage of wetland soils, as for example performed on peat soils to create plantations, increases the O_2 availability and changes soil respiration to aerobic reactions which are performed at faster rates and cause increased emissions of CO_2 (Reddy and DeLaune, 2008e). Additionally, deforestation for creation of plantations lowers the photosynthetic CO_2 uptake by vegetation (Longobardi et al., 2016).

Subsection 2.2.1 and subsection 2.2.2 specify carbon dynamics in wetlands and aquatic systems for organic and inorganic carbon species, respectively. Subsection 2.2.3 and subsection 2.2.4

2. Wetlands in the global carbon cycle

describe aerobic and anaerobic decomposition processes, respectively, and subsection 2.2.5 illustrates the mechanics of gas exchange fluxes between surface waters and the atmosphere.



2.2.1. Organic carbon species in aquatic systems

The organic carbon in aquatic systems exists in a variety of forms that can be roughly grouped in humic substances, non-humic substances and phenolic substances (Reddy and DeLaune, 2008d). Humic substances are at the end of organic degradation and bear no morphological resemblance to the structures from which they were derived (Adey and Loveland, 2007). Non-humic substances, in contrast, are for example carbohydrates, proteins and fats (Reddy and DeLaune, 2008d). This portion of the organic carbon is considered labile. It includes simple sugars that can enter microbial cells and be rapidly degraded (Stevenson, 1994). Phenolic substances are often included in humic substances (Pind et al., 1994). Common phenolic substances are lignins and tannins. Lignins are present in cell walls of plants and make up the majority of peat soils (Wetzel, 1991). They are build by cross-linked phenolic polymers (Martone et al., 2009). Special enzymes are needed to break phenolic bounds and thereby degrade phenolic molecules (Freeman et al., 2001).

In the following, it will not be distinguished between the different forms of organic carbon other than by molecule size. The total organic carbon (TOC) is the sum of all organic carbon compounds. It can be separated into dissolved organic carbon (DOC) and particulate organic carbon (POC), whereat DOC is defined as the fraction of organic carbon that passes through

a filter of $0.45 \mu\text{m}$ pore size and POC is the remaining fraction with higher diameter. In wetland soils, DOC represents $\lesssim 1\%$ of the TOC (Reddy and DeLaune, 2008c). In wetland surface water and peat-draining rivers, however, the majority of TOC is in the form of DOC (Müller et al., 2015). POC and DOC can transition into each other by processes of decomposition ($\text{POC} \mapsto \text{DOC}$) and adsorption ($\text{DOC} \mapsto \text{POC}$).

2.2.2. Inorganic carbon species in aquatic systems

Like organic carbon, inorganic carbon can be separated into dissolved and particulate fractions. Particulate inorganic carbon (PIC) exists in the form of calcium carbonate (CaCO_3 ; Mitchell et al., 2017). While it is a major component in the global ocean carbon cycle, its concentrations in wetland soils and peat-draining rivers are generally low (Wit et al., 2018). In those systems, inorganic carbon mainly exists in dissolved forms of bicarbonate ions (HCO_3^-), carbonate ions (CO_3^{2-}) and the two electrically neutral forms of aqueous carbon dioxide ($\text{CO}_2(\text{aq})$) and true carbonic acid (H_2CO_3). The concentrations of H_2CO_3 are much smaller than the concentrations of $\text{CO}_2(\text{aq})$ and the two forms are commonly summarized as dissolved CO_2 (Zeebe and Wolf-Gladrow, 2001). Thus, the whole concentration of dissolved inorganic carbon (DIC) is given by the sum of the concentrations (indicated by squared brackets) of these species:

$$\text{DIC} = [\text{CO}_2] + [\text{HCO}_3^-] + [\text{CO}_3^{2-}]. \quad (2.1)$$

The three forms constantly change into each other by reacting with water (H_2O) and hydrogen ions (H^+ ; Zeebe and Wolf-Gladrow, 2001). The chemical equilibrium equation can be written as

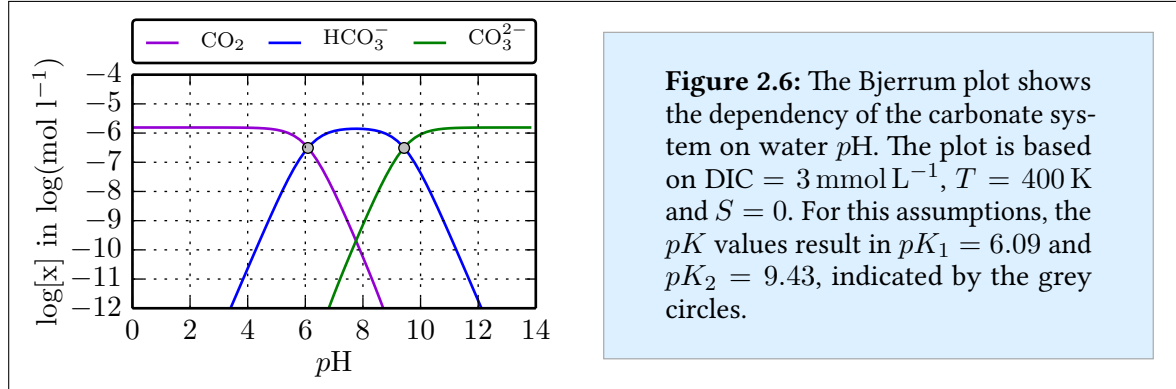


with the equilibrium constants K_1 and K_2 depending on salinity (S), pressure (p) and temperature (T). They can be approximated by

$$K_1(S, T, p) = \frac{[\text{HCO}_3^-][\text{H}^+]}{[\text{CO}_2]} \quad \text{and} \quad K_2(S, T, p) = \frac{[\text{CO}_3^{2-}][\text{H}^+]}{[\text{HCO}_3^-]}. \quad (2.3)$$

The ratio of the inorganic carbon species to each other depends on water $p\text{H}$ (Figure 2.6). For acidic conditions of $p\text{H} < 5$ the majority of DIC is in the form of CO_2 . This is of high importance for peat soils and peat-draining rivers, as the $p\text{H}$ in those is typically low (Pind et al., 1994; Wit et al., 2015).

2. Wetlands in the global carbon cycle



In order to generate a system of equations water alkalinity is introduced. It is defined as the number of H^+ molecules that equals the excess of proton acceptors over proton donors (Mattson, 2010). For the total alkalinity (TA), all water ions need to be considered. The carbonate alkalinity (CA) can be derived from the concentrations of HCO_3^- and CO_3^{2-} as

$$CA = [HCO_3^-] + 2 [CO_3^{2-}]. \quad (2.4)$$

An increase of CO_2 concentrations in water (e.g. due to invasion of anthropogenic CO_2) leads to an increase in DIC but no change in TA or CA, since it does not affect the charge balance (Zeebe and Wolf-Gladrow, 2001). Equation (2.4), in combination with equation (2.1) and the equations (2.3), constitutes a system of four equations with six unknowns ($[CO_2]$, $[HCO_3^-]$, $[CO_3^{2-}]$, $[H^+]$, DIC and CA). Therefore, it is sufficient to know two of the parameters in order to calculate the remaining four.

2.2.3. Aerobic decomposition

Aerobic decomposition uses O_2 as electron acceptor (Reddy and DeLaune, 2008e). During aerobic respiration, all carbon atoms within the organic substrate are oxidized to CO_2 (Reddy and DeLaune, 2008e). The breakdown of glucose under aerobic conditions can be written as



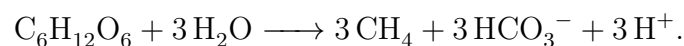
However, as mentioned before, specific enzymes are needed for the decomposition of phenolic compounds (Freeman et al., 2001), which make up the majority of carbon compounds in peat soils (Wetzel, 1991). One enzyme that is able to break phenolic bounds is phenol oxidase (Reddy and DeLaune, 2008e). It is the main decomposition impelling enzyme in peat areas (Pind et al., 1994). After the initial breakdown of phenolic substances into smaller molecules

by phenol oxidase, other enzymes help with subsequent decomposition processes (Reddy and DeLaune, 2008e). The activity of phenol oxidase depends on pH and O_2 availability (Freeman et al., 2001; Pind et al., 1994). Thus, in peat soils, which are acidic and O_2 -depleted, the enzyme activity is strongly limited, explaining the slow decomposition rate of organic matter in these regions.

The limiting effect of O_2 on phenol oxidase activity is represented by the Michaelis-Menten kinetics (Fang and Moncrieff, 1999; Pereira et al., 2017). This approach assumes that decomposition rates are linearly limited for low O_2 concentrations but that there is no limitation by O_2 once its concentration is sufficient to meet the decomposition demands (Keiluweit et al., 2016). Other than for the O_2 limitation, the form of pH limitation is still subject to discussion. Linear (Sinsabaugh, 2010) as well as exponential (Williams et al., 2000; Kang et al., 2018) correlations have been stated in literature.

2.2.4. Anaerobic decomposition

Anaerobic decomposition uses CO_2 as electron acceptor (Reddy and DeLaune, 2008e), which is energetically disadvantageous. As long as other electron acceptors are available, those will dominate the decomposition (Reddy and DeLaune, 2008e). In order of their energy yield other electron acceptors in wetlands are O_2 , nitrate, manganese dioxide, ferric oxide, and sulfate (Reddy and DeLaune, 2008e). Microorganisms that perform methanogenesis can, depending on their substrate utilization, be separated into three groups (Madigan and Martinko, 2006): 1.) CO_2 utilizers (eg. CO_2 : $CO_2 + 4H_2 \longrightarrow CH_4 + 2H_2O$), 2.) formate methyl utilizers (eg. methanol: $4CH_3OH \longrightarrow 3CH_4 + CO_2 + 2H_2O$) and 3.) acetate utilizers (eg. acetate: $CH_3COOH \longrightarrow CH_4 + CO_2$). The breakdown of glucose under anaerobic conditions can be written as



Methanogenesis is not only less effective in energy gain but decomposition rates are also much slower than for aerobic decomposition (Reddy and DeLaune, 2008e) and anaerobic microbial groups are largely incapable of utilizing substrates such as lignin and humic substances that require initial oxygenation by oxygenases (Reddy and DeLaune, 2008e). This is why anaerobic peat soils and also freshwater DOC to a large fraction consist of phenolic compounds (Wetzel, 1991). Many phenolic compounds are also known to inhibit the activity of enzymes (Reddy and DeLaune, 2008c).

2.2.5. Atmospheric gas exchange with surface waters

The gas exchange between water bodies and the atmosphere is regulated by processes of turbulence and molecular diffusion (Jähne et al., 1987). It can be described by the boundary layer theory (Bade, 2009). This theory states that the water system as well as the atmosphere are each well mixed due to turbulence. As turbulence declines towards the boundary between water and atmosphere, a boundary layer in which no turbulence exist is created between the two media. The upper surface of the water boundary layer, according to Henry's Law, is in equilibrium with the overlying air (Äschbach-Herting, 2014). This creates a concentration gradient between the water surface and the gas concentrations within the deeper water layer. According to the second law of thermodynamics, this concentration gradient induces a flux towards the system with lower gas concentration that according to Fick's law of diffusion is proportional to the concentration gradient. Since Henry's law states that the concentration of a gas in water is proportional to its partial pressure, the atmospheric flux (F_x) of a gas x can be derived from the difference in the partial pressure within the water (p_x) and the atmosphere (p_x^{air}) according to

$$F_x = k_x K_0^x (p_x - p_x^{\text{air}}) . \quad (2.5)$$

K_0^x is the gas specific and temperature-dependent Henry coefficient and k_x is the exchange coefficient of gas x. The exchange coefficient is a measure for the exchange velocity of gas between the water and the atmosphere. It mainly depends on water turbulence and wind speed (Andersson et al., 2016).

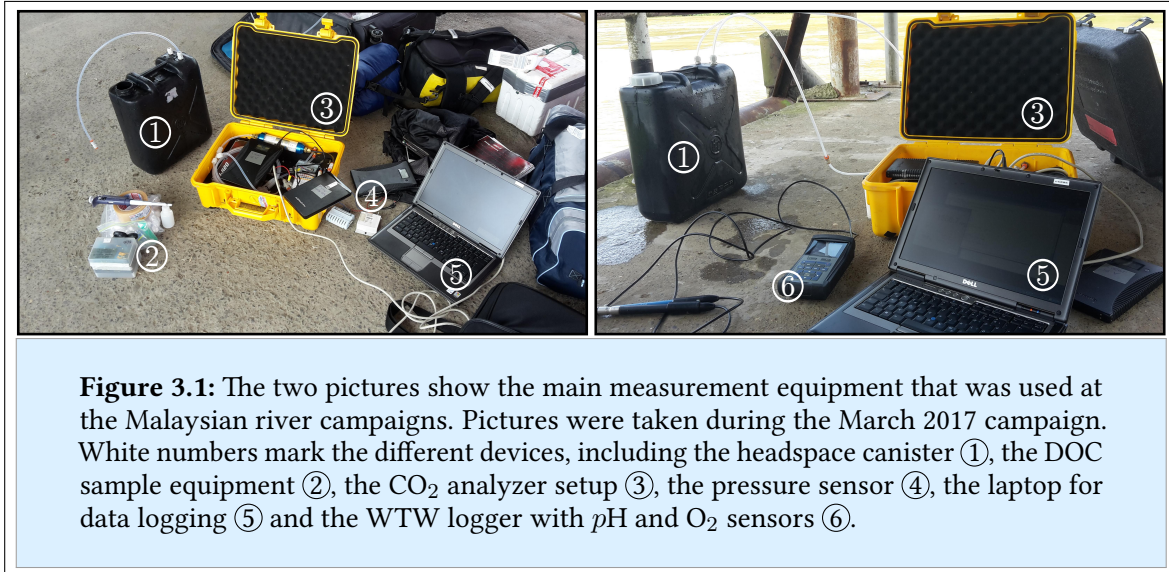
3. Methods

Data for the first two research topics of this study (chapter 4 & chapter 5) were measured in a number of research campaigns at Southeast Asian rivers. Those campaigns and the used measurement principles are illustrated in section 3.1, while section 3.2 describes how additional river parameters were determined. Section 3.3 focuses on the atmospheric chemistry and transport model and section 3.4 introduces the satellite data products that were used to determine modelled and measured CH₄ concentrations for the third research topic of this study (chapter 6).

3.1. River campaigns and measurements

River data for this study were derived from a total of 16 campaigns between 2004 and 2017 in Sumatra (Indonesia) and Sarawak (Malaysia). The individual campaigns and the included rivers are listed in the appendix in Table A.3. For the Indonesian rivers, ten measurement campaigns between 2004 and 2013 were conducted. Published data from Baum et al. (2007) were used for the Mandau, Tapung Kanan and Tapung Kiri rivers. Data from Wit et al. (2015) were used for the Siak, Indragiri, Batang Hari and Musi rivers and data from Rixen et al. (2016) were used for the Rokan and Kampar rivers.

For the Malaysian rivers, measurements were performed in six campaigns between 2014 and 2017. Data published by Müller-Dum et al. (2018) and by Müller et al. (2015) were used for the Rajang river and for the Maludam campaigns in 2014 and 2015, respectively. Additional campaigns for this study were conducted in March 2015 at the Simunjan and Sebuyau rivers as well as in January 2016, March 2017 and July 2017 at the Simunjan, Sebuyau and Maludam rivers. The measurements in March 2017 were performed as part of this study. Methods used in the individual campaigns are described in the respective publications. Measurement principles and equipment utilized to derive the non-published data for the additional campaigns are explained in the following parts of this section. Subsection 3.1.1 and subsection 3.1.2 focus on the measurement of dissolved CO₂ concentrations and atmospheric CO₂ fluxes, respectively. Subsection 3.1.3 describes the measurement of DOC concentrations, subsection 3.1.4 illustrates how concentrations of POC and PIC were measured and subsection 3.1.5 explains the measurements of O₂ concentrations and water pH.



3.1.1. Dissolved CO₂ measurements

The partial pressure of CO₂ ($p\text{CO}_2$) was measured by use of a LI-COR LI-820 CO₂ analyser (Figure 3.1, device ③), which is an absolute non-dispersive infra-red gas analyser (NDIR; LI-COR Inc, 2011). Its measurement principle is based on absorption of infrared radiation by the measured gas. The intensity of two different wavelengths is measured after passing a certain distance of an air filled path. One wavelength (3.95 μm) is CO₂ inactive and functions as a reference signal, while the other wavelength (4.26 μm) shows the CO₂ absorption (LI-COR Inc, 2011). From the two signals, the mole fraction of CO₂ in the air is determined. The range of the measured CO₂ can be defined manually up to 20,000 ppm. CO₂ concentrations were derived based on the measured $p\text{CO}_2$ as well as temperature-dependent Henry coefficients calculated according to Weiss (1974).

The LI-COR instrument measures gas concentrations in air. Accordingly, a device to create a thermodynamic equilibrium between water and air is needed to measure the dissolved CO₂ in water samples. For this, a headspace technique based on an air stream bubbling through water was used (Figure 3.2). A water sample was filled into a container, leaving a small air filled headspace. Through a closed circuit of tubes, air was pumped out of that headspace, through the gas analyser and back into the water canister, where it bubbled through the water back up into the headspace volume. In front of the analyser, particle and a moisture filters were installed to avoid contamination. For quicker equilibration time, a diffuser stone was attached to the gas outflow nozzle in the water. Thus, the air ascended in smaller bubbles that increase the gas-liquid interface area.

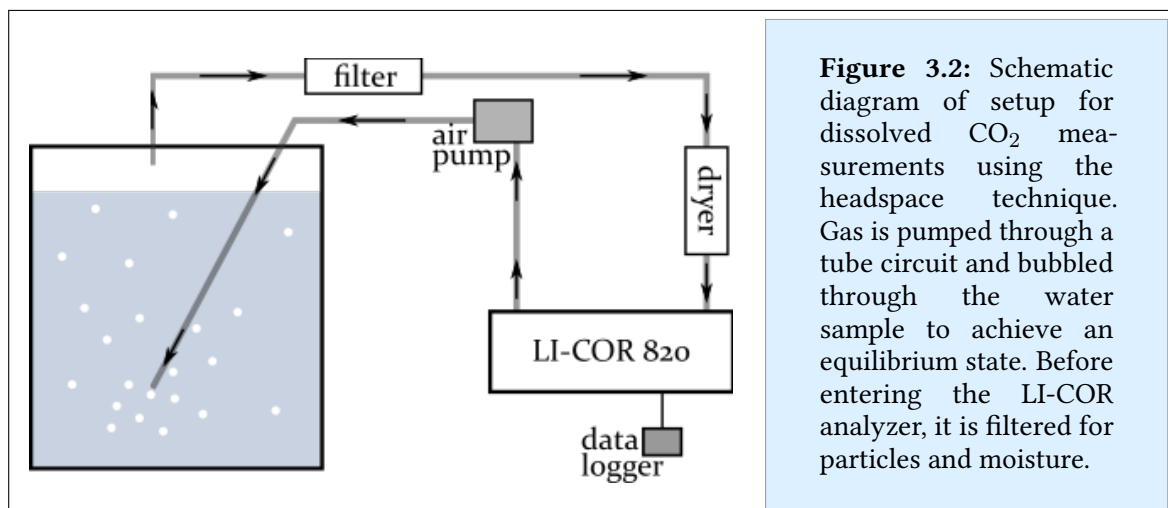


Figure 3.2: Schematic diagram of setup for dissolved CO₂ measurements using the headspace technique. Gas is pumped through a tube circuit and bubbled through the water sample to achieve an equilibrium state. Before entering the LI-COR analyzer, it is filtered for particles and moisture.

This measurement setup requires a discrete water sample that is manipulated during the measurement due to the removal of CO₂. This potentially shifts DIC towards higher carbonate concentrations and thereby induces a change in the sample *pH* (Figure 2.6). In order to minimize such manipulation, measurements were performed at a high water to air ratio. Fortunately, at the low *pH* in peat-draining rivers small changes in *pH* do not significantly impact the CO₂ fraction of DIC. The short equilibration time of the setup (≈ 5 min) additionally prevented significant temperature changes during measurements.

In 2015 and 2016, measurements were performed with a 10 L container and 0.5 L headspace volume. In 2016, due to the analyser setup, only CO₂ concentrations < 10,000 ppm could be measured. In the Simunjan river, the concentrations exceeded this limit. In March 2017, measurements were performed with a 15.6 L canister and 1 L headspace volume (Figure 3.1, device ①) and in July 2017, a 10 L glass flask with 0.5 L headspace volume was used.

3.1.2. Water-atmosphere flux measurements

A floating chamber technique was used to measure CO₂ exchange fluxes between rivers and the atmosphere. This technique is based on a closed system that is positioned on a water surface. To minimize the creation of artificial turbulence by the chamber it is allowed to drift freely. The chamber protects gas captured inside from interacting with the outside atmosphere. Therefore, the CO₂ change in the chamber is solely driven by gas exchange through the water surface. The flux between the water and the gas in the chamber is strong for high *p*CO₂ gradients between water and chamber air (equation (2.5)). The initial CO₂ increase in the chamber is nearly linear and then decreases with time until an equilibrium is reached. The initial linear increase can be used to calculate the atmospheric CO₂ flux

according to

$$F = \frac{\Delta[\text{CO}_2] V p}{\Delta t A R T} , \quad (3.1)$$

where $\Delta[\text{CO}_2]$ is the change of CO_2 concentration measured in the time Δt , V is the chamber volume, p is the pressure in the chamber, A is the exchange area, R is the universal gas constant and T is the chamber temperature (Beaulieu et al., 2012). Several measurements with a duration of ≈ 5 min each were conducted at each river. Chamber pressure and temperature during the initial linear CO_2 increase were approximated by atmospheric pressure and temperature.

Advantages of the floating chamber technique are the simple equipment and flux calculations. A disadvantage is that the chamber protects the water surface from disturbances like wind and rain, which may have a strong influence on the exchange. Therefore, this technique is well suited for measurements in rivers or small lakes, where river-air exchange is mainly caused by turbulence within the water.

Measurements in 2015 and in 2017 were performed using a floating chamber with a volume of 3 L and a surface area of 0.3 m². The measurements in 2014 were performed using a bigger chamber of 8.7 L with a surface area of 0.5 m². The CO_2 was measured with the LI-COR analyser described in subsection 3.1.1.

3.1.3. DOC measurements

For DOC measurements, 30 mL water samples were taken. In order to prevent conversion between DOC, POC and DIC, the samples were filtered through a 0.45 μm syringe filter and acidified using 21 % phosphoric acid to achieve a $\text{pH} < 2$. After acidification, the samples were frozen.

The general process of the DOC analysis can be split into three parts. 1) the removal of CO_2 and thus DIC from the sample, 2) the oxidation of DOC to CO_2 and 3) the detection of CO_2 . In this study, a Shimadzu TOC-VCSH analyser was used, combined with a Shimadzu ASI-V automatic sampler (Shimadzu Europa GmbH, 2015). These instruments were provided by the Centre for Tropical Marine Research (ZMT).

After preservation, the samples have a $\text{pH} < 2$. Therefore, the total DIC is in the form of CO_2 (Figure 2.6). The first part of the analytic procedure is the removal of this CO_2 , to have solely organic carbon in the sample. This is achieved by purging the sample with an inert gas (Cauwet, 1999). This procedure might also cause the removal of volatile organic carbon

from the sample, but since this is usually a very small fraction of the TOC, it is neglected. After removal of the inorganic carbon, the organic carbon is oxidized to CO₂. This is achieved through high temperature combustion (Cauwet, 1999; Shimadzu Europa GmbH, 2015). Small units of the DIC free sample are taken and combusted at a temperature of $\approx 720^\circ\text{C}$ in a stream of O₂. A platinum catalyst is used to assure oxidation of all DOC (Shimadzu Europa GmbH, 2015). After oxidation, the created CO₂ is measured using a NDIR gas analyser, which works similar to the LI-COR analyser described in subsection 3.1.1. Due to the analyser's high sensitivity, samples of 20 to 50 μL are sufficient for one measurement.

For each water sample, the oxidation and CO₂ measurements were repeated five times to reduce the random error. Additionally, samples of Hansell II standardized water samples were measured after each ten samples of river water, to check the analyser's calibration. Those samples are of 41 to 44 $\mu\text{mol L}^{-1}$ and were provided by the University of Miami.

3.1.4. Particulate carbon measurements

During the January 2016, March 2017 and July 2017 campaigns, concentrations of POC and PIC were measured. For this, water samples were filtered through pre-weighted and pre-combusted glass fiber filters (0.7 μm) to sample particulate material within the water volume. To determine the particulate carbon (organic and inorganic) within these samples, they were catalytically combusted at 1,050 $^\circ\text{C}$ and the combustion products were measured by thermal conductivity using an Euro EA3000 Elemental Analyser. For POC measurements, the same procedure was repeated after the addition of 1 molar hydrochloric acid that removes the inorganic carbon from the sample. Finally, PIC was determined from the difference between the total particulate carbon and the measured POC concentration.

3.1.5. pH and O₂ measurements

Dissolved O₂ concentrations and river pH were measured using digital IDS sensors and a Multi-3420 data logger (Figure 3.1, device ④). The IDS DO sensor measured the O₂ content in water that can be displayed as concentration in mg L^{-1} , saturation in % or partial pressure in mbar. It can measure concentrations up to 20 mg L^{-1} (GeoTech, 2015). The sensor includes an integrated temperature sensor that displays the temperature in $^\circ\text{C}$. After the sensor was used, it was rinsed with deionized water and stored in a protective casing.

The IDS pH electrode measures in the range from 0 to 14. Additionally, it can be switched to show the sensor voltage in mV and like the DO sensor it has an integrated temperature sensor. After use, it was rinsed with deionized water and stored in a protection case, filled

with a solution of 3 mol L^{-1} potassium chlorate. The sensor was calibrated before the measurements, using a Merck 1 buffer set (GeoTech, 2015).

3.2. Catchment properties and additional parameters

This section describes additional river catchment properties as well as carbon parameters that were compiled in order to further investigate carbon dynamics in peat-draining rivers. Subsection 3.2.1 describes how additional geographical and hydrological properties of the river catchments were derived, subsection 3.2.2 explains how exchange coefficients were calculated from measured CO_2 fluxes and subsection 3.2.3 shows how carbon yields from peat-draining rivers were calculated.

3.2.1. Determination of catchment properties

River catchment sizes were derived from Hydro-SHEDS (Lehner et al., 2006) at 15'' resolution. Sub-basins belonging to the catchments were identified using the HydroSHEDS 15 s flow directions data set and added to the main basins. Stream surface areas were determined using stream widths from the Global River Width from Landsat (GRWL) database (Allen and Pavelsky, 2018). For the Maludam, Sebuyau and Simunjan rivers, stream width was not available in GRWL, so it was calculated using the hydraulic equation by Raymond et al. (2012). River coverage was determined from the stream surface area divided by catchment size.

Peat maps were gathered from Global Forest Watch (2019) for Indonesia and Malaysia. The Indonesian peatland map was published by the Indonesia Ministry of Agriculture (2012), while the Malaysian peat map was made available by Wetlands International (2009) and is based on a national inventory by the Land and Survey Department of Sarawak (1968). Both maps include peatlands in different conditions, from undisturbed peat swamp forest to disturbed peat under plantations. Peat coverage was determined from the areal extent of peatlands in the catchments divided by catchment size.

Air temperature and precipitation for the individual river catchments were derived from the Asian Precipitation Highly-Resolved Observational Data Integration Towards Evaluation (APHRODITE) daily data product (Yatagai et al., 2020). 10 year means (2006 to 2015) were calculated for each catchment and uncertainties are given as standard deviation. River discharge was calculated from the difference between precipitation and evapotranspiration, multiplied by catchment area. The evapotranspiration was assumed to be 37.9% for moder-

ately to severely disturbed catchments and 67.7 % for undisturbed catchments (Moore et al., 2013). The value for undisturbed catchments was only used for the Maludam river. Discharge uncertainties were derived by Gaussian error propagation, considering uncertainties of catchment area, precipitation and evapotranspiration. An evapotranspiration uncertainty of 15 % is assumed, consistent with calculations by Rixen et al. (2016).

3.2.2. Atmospheric gas exchange coefficients

CO₂ exchange coefficients (k_{CO_2}) were determined from measured atmospheric CO₂ fluxes based on equation (2.5). Uncertainties were derived through Gaussian error propagation based on uncertainties in measured fluxes and CO₂ concentrations.

To compare coefficients derived for different gas species and at different water temperatures, exchange coefficients are usually converted to a standardized Schmidt number of 600. The Schmidt number is a constant that depends on water viscosity and gas diffusivity and it can be approximated for specific gas species based on water temperature and salinity. Schmidt numbers for CO₂ (Sc_{CO_2}) were calculated according to Wanninkhof (1992) and standardized exchange coefficients (k_{600}) were derived according to

$$k_{600} = \left(\frac{600}{Sc_{\text{CO}_2}(T)} \right)^{-n} \cdot k_{\text{CO}_2}. \quad (3.2)$$

An exponent of $n = 2/3$ (valid for smooth surfaces and low wind speeds; Zappa et al., 2007) was used for the small Malaysian rivers (Maludam, Sebuyau & Simunjan) and an exponent of $n = 1/2$ (valid for rough surfaces; Zappa et al., 2007) for the bigger rivers. Uncertainties of k_{600} are the relative uncertainties of k_{CO_2} .

3.2.3. River carbon yields

River carbon yields describe the carbon export by rivers per catchment area of the rivers. The oceanic DOC and DIC yields of the investigated rivers in this study were calculated based on measured or modeled DOC and DIC concentrations as well as calculated river discharges (Q) and catchment areas (A) according to

$$\text{DOC yield} = \frac{\text{DOC} \cdot Q}{A} \quad \& \quad \text{DIC yield} = \frac{\text{DIC} \cdot Q}{A}. \quad (3.3)$$

Uncertainties were derived through Gaussian error propagation, whereat the standard deviation in DOC or DIC concentration as well as uncertainties in discharge and catchment area

were considered. Total yields from Southeast Asian rivers were derived by weighing yields from individual rivers with river discharges.

Atmospheric CO₂ yields from the investigated rivers were derived from measured river $p\text{CO}_2$, water temperature (T), exchange coefficients (k_{CO_2}) and the catchment's river coverage ($p\%$) according to

$$\text{CO}_2 \text{ yield} = k_{\text{CO}_2}(T) \cdot K_{\text{CO}_2}(T) \cdot (p\text{CO}_2 - p\text{CO}_2^{\text{a}}) \cdot p\%. \quad (3.4)$$

For the atmospheric $p\text{CO}_2$ ($p\text{CO}_2^{\text{a}}$), monthly data from NOAA surface flask measurements at Bukit Kototabang were used (Dlugokencky and Tans, 2021). The temperature-dependent Henry coefficient ($K_{\text{CO}_2}(T)$) was calculated according to Weiss (1974). Uncertainties in the CO₂ yield were derived through Gaussian error propagation, whereat the standard deviation of the measured $p\text{CO}_2$ as well as uncertainties in the derived exchange coefficients and the catchment's river coverage were considered. Total CO₂ yields from Southeast Asian rivers were derived by weighing yields from individual rivers with river catchment areas.

3.3. Global atmospheric chemistry and transport model

The atmospheric chemistry and transport model used in this study is the TM5-MP. It is a global Eulerian model that simulates the transport and chemistry of atmospheric species in the troposphere (Williams et al., 2017). The model runs offline and can be used to calculate atmospheric gas concentrations from known gas emission data (forward modelling) or inversely to calculate gas emissions from known atmospheric gas concentrations (inverse modelling).

In this study the model was run forward to simulate atmospheric CH₄ concentrations based on different wetland CH₄ emission datasets. Subsection 3.3.1 explains the model principle and subsection 3.3.2 describes the CH₄ emission datasets used for the model runs presented in this study.

3.3.1. TM5-MP chemistry and transport model

The full chemistry version of the TM5-MP (massive parallel) model (Williams et al., 2017) was used to derive atmospheric CH₄ concentrations for this study. A model resolution of $3^\circ \times 2^\circ$ was used, whereby the model combines longitudinal grid cells in the polar regions ($> 80^\circ\text{N/S}$). The atmosphere was separated into 25 vertical layers with the upper boundary of the model set at 0.1 Pa (Huijnen et al., 2010). Meteorological fields for the model were taken from the ECMWF ERA-Interim reanalysis (Dee et al., 2011). The model meteorology is

updated every 3 h, with interpolation of fields for the intermediate time periods (Williams et al., 2017). Performed steps within the model are calculation of horizontal and vertical advection, vertical diffusion, atmospheric chemistry and gas sources and sinks (Huijnen et al., 2010).

The gas-phase chemistry in the model is performed based on the cb05 chemical mechanism as described by Huijnen et al. (2010). While for CH₄ the only atmospheric reaction is oxidation by OH according to $\text{OH} + \text{CH}_4 \longrightarrow \text{CH}_3 + \text{H}_2\text{O}$, the atmospheric chemistry of OH is more complex. The OH chemistry implemented in the cb05 mechanism has first been validated by Huijnen et al. (2010) and again by van Noije et al. (2014) and Myriokefalitakis et al. (2020). As the TM5-MP includes no explicit stratospheric chemistry, a stratospheric nudging term is applied to the top model layer in order to ensure realistic stratosphere–troposphere gas exchange (Williams et al., 2017). Additionally a surface nudging term is applied to balance missing CH₄ sources.

3.3.2. CH₄ emission datasets

The model includes CH₄ emissions from natural and anthropogenic sources. Natural sources include emissions from wetlands, wildfires, termites, oceans and wild animals. The main anthropogenic sources include emissions from energy and agriculture as well as waste treatment and disposal. All included emission data sources are listed in Table 3.1. CH₄ sinks are included in the form of soil consumption ($\approx 27 \text{ TgCH}_4 \text{ yr}^{-1}$; Spahni et al., 2011), the chemical sink through reaction with OH ($\approx 569 \text{ TgCH}_4 \text{ yr}^{-1}$) and stratospheric CH₄ loss ($\approx 55 \text{ TgCH}_4 \text{ yr}^{-1}$).

emission sector	global emissions	data source
wetlands (n)	149 TgCH ₄ yr ⁻¹	Saunio et al. (2020)
termites (n)	19 TgCH ₄ yr ⁻¹	Sanderson (1996)
ocean (n)	17 TgCH ₄ yr ⁻¹	Lambert and Schmidt (1993)
wild animals (n)	5 TgCH ₄ yr ⁻¹	Houweling et al. (1999)
biomass burning (n, a)	15 TgCH ₄ yr ⁻¹	CMIP6; Eyring et al. (2016)
energy (a)	151 TgCH ₄ yr ⁻¹	CMIP6; Eyring et al. (2016)
agriculture (a)	137 TgCH ₄ yr ⁻¹	CMIP6; Eyring et al. (2016)
waste (a)	65 TgCH ₄ yr ⁻¹	CMIP6; Eyring et al. (2016)
other (a)	14 TgCH ₄ yr ⁻¹	CMIP6; Eyring et al. (2016)

Table 3.1: List of CH₄ emission sectors and data sources. Natural and anthropogenic emissions are indicated by (n) and (a), respectively. Biomass burning includes emissions from natural and anthropogenic sources.

The main focus in the modelling part of this study is on CH₄ emissions from tropical wetlands. Model runs based on different wetland CH₄ emission datasets were performed. These datasets

3. Methods

were derived from thirteen biogeochemical soil and vegetation models (Table 3.2). They were collected to derive a bottom-up estimate of wetland CH₄ emissions for the global CH₄ budget published by the Global Carbon Project (GCP; Saunio et al., 2020) and were kindly provided for this study.

model	institution	prognostic	references
CLASS-CTEM	Environment and Climate Change Canada	yes	Melton and Arora (2016); Arora et al. (2018)
DLEM	Auburn University	no	Tian et al. (2010, 2015)
ELM	Lawrence Berkeley National Laboratory	yes	Riley et al. (2011)
JSBACH	MPI	no	Kleinen et al. (2020)
JULES	UKMO	yes	Hayman et al. (2014)
LPJ-GUESS	Lund University	no	McGuire et al. (2012)
LPJ-MPI	MPI	no	Kleinen et al. (2012)
LPJ-WSL	NASA GSFC	yes	Zhang et al. (2016)
LPX-Bern	University of Bern	yes	Spahni et al. (2011)
ORCHIDEE	LSCE	yes	Ringeval et al. (2011)
TEM-MDM	Purdue University	no	Zhuang et al. (2004)
TRIPLEX_GHG	UQAM	no	Zhu et al. (2014, 2015)
VISIT	NIES	yes	Ito and Inatomi (2012)

Table 3.2: List of models and institutions that provided the wetland emission datasets used in this study. Models that provided a prognostic dataset in addition to the diagnostic one are indicated under the prognostic column.

Each soil and vegetation model provided one emission dataset based on model runs with pre-set wetland area and dynamics datasets based on WAD2M (Wetland Area Dynamics for Methane Modelling; Zhang et al., 2021). Those datasets are from now on called diagnostic datasets. Nine of the thirteen models additionally provided prognostic datasets that were derived from model runs using individual calculations of wetland areas. The models that provided these prognostic datasets are indicated in Table 3.2. All 22 datasets (13 diagnostic & 9 prognostic) include monthly global 1° × 1° gridded wetland CH₄ emission data spanning the time from 2000 to 2017.

3.4. Satellite CH₄ data

The satellite CH₄ data product used in this study is the merged L2 product retrieved from the SCIAMACHY and GOSAT satellites using the Ensemble Median Algorithm (EMMA; Buchwitz et al., 2018; Reuter et al., 2013). EMMA combines individual soundings of seven different algorithms for SCIAMACHY and GOSAT retrievals into one data set (Reuter et al., 2013).

Short descriptions of the SCIAMACHY and GOSAT instruments are given in subsection 3.4.1 and subsection 3.4.2, respectively.

For both instruments, retrievals are based on nadir observations of reflected solar radiation in near-infrared O₂ and CH₄ absorption bands (Buchwitz et al., 2018). Radiative transfer and instrument models are then used to simulate the satellite's measurement of the atmosphere. An inversion method is used to find the atmospheric state that is in best agreement with the measurements and forward models (Reuter et al., 2013). The different retrieval algorithms included in the EMMA product are the BESD v01.00.01 and WFMD v2.2bcv7b for SCIAMACHY and the ACOS v2.9, NIES v02.xx, PPDF-DOAS, RemoteC v1.0 and UOL-FP v3.0 for GOSAT. Those algorithms are based on different absorption bands, use different inversion methods, and are based on different physical assumptions on the radiative transfer in scattering atmospheres (Reuter et al., 2013). The final dataset includes observations of the methane column-averaged dry-air mole fraction (XCH₄) for the time of 2013-2017.

3.4.1. SCIAMACHY satellite

The SCIAMACHY (Scanning Imaging Absorption Spectrometer for Atmospheric Cartography) instrument was located on the ESA Envisat satellite (Burrows et al., 1995; Bovensmann et al., 1999). It collected observations from August 2002 to April 2012. The main objective of its mission was to improve the knowledge of global atmospheric change and related issues of importance to the chemistry and physics of our atmosphere (Bovensmann et al., 1999).

SCIAMACHY performed measurements in nadir, limb, and solar/lunar occultation geometries (Gottwald et al., 2006c). The satellite was on a polar, sun-synchronous orbit with an equatorial crossing time of 10 a.m. and an orbital period of 100.6 minutes (Gottwald et al., 2006b). It performed roughly 14 orbit cycles per day with a repeat cycle of about 35 days. The average satellite altitude was 799.8 km (Gottwald et al., 2006b). In nadir mode, SCIAMACHY was scanning the atmosphere in flight direction with a swath width of up to 1,000 km and the retrieved data have a spatial resolution of roughly 60 × 30 km (Gottwald et al., 2006a).

3.4.2. GOSAT satellite

The GOSAT (Greenhouse gases Observing SATellite) is a satellite that hosts the TANSO-FTS (Thermal And Near infrared Sensor for carbon Observation - Fourier Transform Spectrometer) instrument (Yokota, 2004). This instrument has been collecting atmospheric CH₄ observations since April 2009. The GOSAT mission objective is to contribute to environmental administration by estimating greenhouse gas sources and sinks on a sub-continental scale

3. Methods

(Kasuya et al., 2009).

GOSAT performs nadir measurements from a sun-synchronous orbit with an equatorial crossing time of approximately 1 p.m. (Yokota, 2004). The satellite's altitude is approximately 666 km and it flies roughly 15 orbits a day with a repeat cycle of three days (Yoshida et al., 2008). GOSAT is scanning the atmosphere with a swath width of up to 790 km and the retrieved data represent circles of 10.5 km diameter.

4. Limitation of CO₂ production in peat-draining rivers

This chapter investigates the carbon dynamics in peat-draining rivers with the focus on dependencies of in-river decomposition on O₂ and pH. Parts of this chapter have been published in Klemme et al. (in review, 2021).

Section 4.1 gives an introduction to the investigated topic and study objective and section 4.2 describes the study area. Section 4.3 discusses the dependencies of river CO₂ and other measured parameters on peat coverage and DOC concentrations. Section 4.4 investigates parameters that limit the DOC decomposition in peat-draining rivers and section 4.5 illustrates a mechanism that prohibits this natural limitation in decomposition for specific campaigns on the Simunjan river. Finally, section 4.6 summarizes the results from this chapter.

4.1. Background and objective

Rivers and streams emit high amounts of CO₂ to the atmosphere (Cole et al., 2007), but estimates of these emissions vary strongly (0.6 – 1.8 PgC yr⁻¹, Aufdenkampe et al., 2011; Raymond et al., 2013). Studies agree that more than three-quarters of global river CO₂ emissions occur in the tropics (Raymond et al., 2013; Lauerwald et al., 2015). Despite scarcity in measurements from Southeast Asia, those regions are assumed to be emission hotspots due to the presence and degradation of carbon-rich peat soils (Wit et al., 2015).

Concentrations of DOC in peat-draining rivers are high and increase with increasing peat coverage of the river catchments (Wit et al., 2015). Riverine CO₂ is fed by the decomposition of this organic carbon (Rixen et al., 2016). However, despite DOC concentrations that can be more than four times higher than those in temperate regions (Butman and Raymond, 2011; Müller et al., 2015), measured CO₂ fluxes from tropical peat-draining rivers (25.2 gC m⁻² yr⁻¹) hardly exceed those from temperate rivers (18.5 gC m⁻² yr⁻¹, Wit et al., 2015; Butman and Raymond, 2011).

Possible reasons suggested for these moderate emissions are short residence times of peat derived DOC in rivers due to the location of peatlands near the coast (Müller et al., 2015) as well as the recalcitrant nature of DOC (Müller et al., 2016) and the lack of O₂ (Wit et al., 2015) which both lower the rate of DOC decomposition. Additionally, Borges et al. (2015) suggested a limitation of bacterial production and the resulting DOC decomposition in African peat-draining rivers as a consequence of low pH.

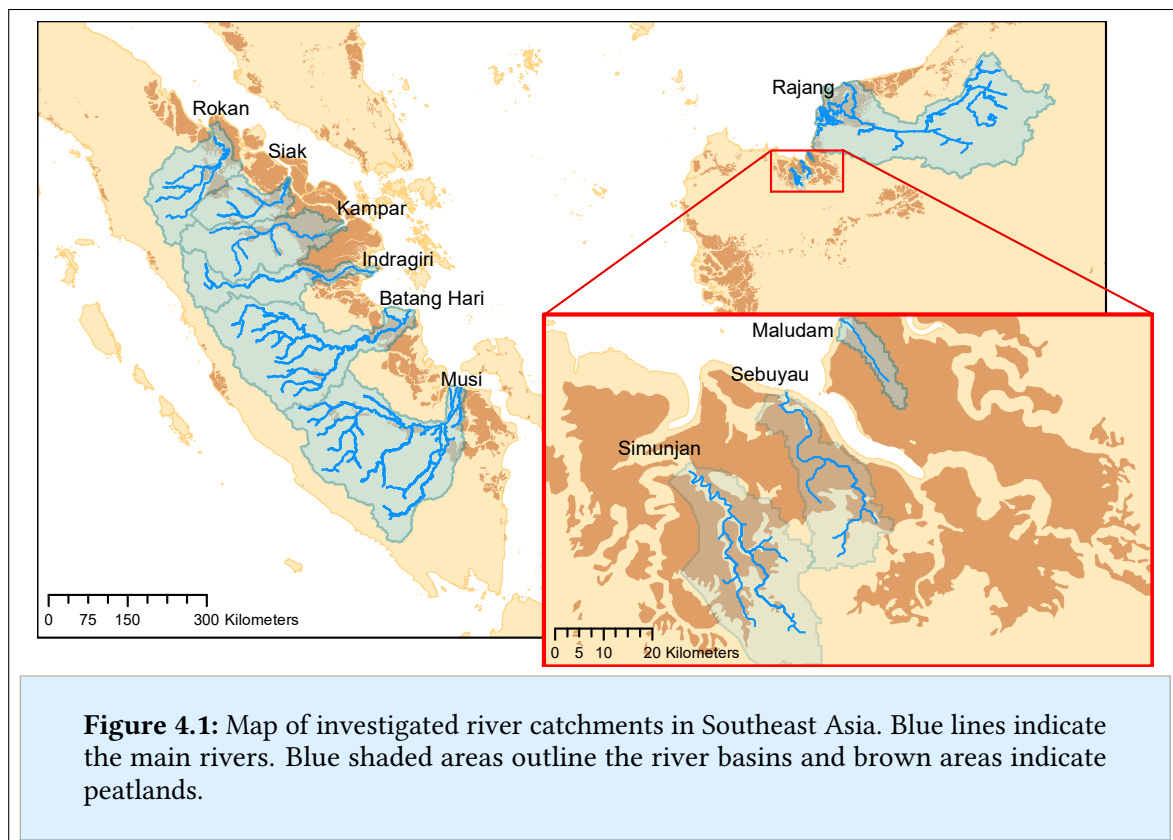
In the following, data from ten Southeast Asian rivers with varying peat coverage will be

4. Limitation of CO₂ production in peat-draining rivers

analysed in order to explain the observed moderate CO₂ emissions. The limiting impact of low pH and O₂ on decomposition rates within the rivers will be quantified and the impact of carbonates on those limitation processes will be discussed.

4.2. Study area

Southeast Asian peatlands store 42 Pg soil carbon across an area of 271,000 km² (Hooijer et al., 2010). More than 97 % of these peat soils are located in lowlands (Hooijer et al., 2006). The development of peatlands in Southeast Asia is favored by its tropical climate with high precipitation rates of about 2,700 mm yr⁻¹ (Yatagai et al., 2020). Southeast Asian rivers mostly originate in mountain regions and cut through coastal peatlands on their way to the ocean (Figure 4.1). The measured data included in this study were obtained in river parts that flow through peat soils to capture the influence of peatlands on the carbon dynamics in the rivers.



The collective data were derived from four rivers on Borneo (Sarawak, Malaysia) and six rivers on Sumatra (Indonesia). The investigated rivers on Borneo are the Rajang, Simunjan, Sebuyau and Maludam and the rivers surveyed on Sumatra are the Rokan, Kampar, Indragiri, Batang Hari, Musi and Siak (Figure 4.1). Additionally, data from the Siak's tributaries Tapung

Kiri, Tapung Kanan and Mandau were included.

Catchment properties of all rivers are listed in the appendix in Table A.1. Figure 4.2 shows exemplary pictures taken on the Maludam, Simunjan and Rajang rivers. It gives an idea on the different river sizes. The river discharge varies strongly between $3 \text{ m}^3 \text{ s}^{-1}$ for the Maludam and approximately $3,500 \text{ m}^3 \text{ s}^{-1}$ for the Rajang. It correlates with river catchment sizes that range from areas of 90 km^2 for the Maludam catchment to almost $60,000 \text{ km}^2$ for the Rajang and Musi catchments. Peat coverage ranges from 4 % in the Musi catchment to 91 % in the Maludam catchment, whereby the bigger rivers that originate in the uplands generally exhibit lower peat coverage than smaller coastal rivers. Fractions of river surface area within the catchments range between 0.39 % in the Maludam catchment and 0.94 % in the Sebuyau catchment and show no correlation with catchment sizes.

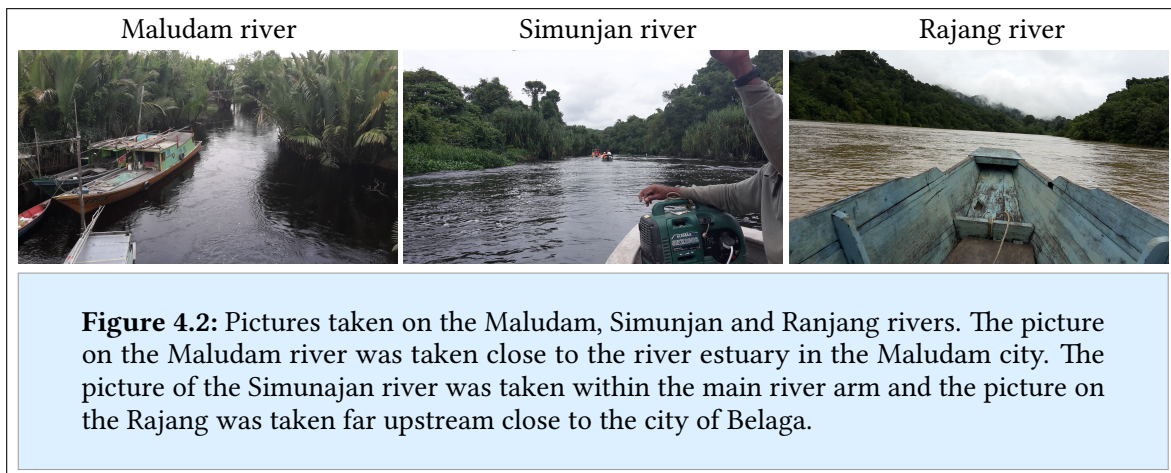


Figure 4.2: Pictures taken on the Maludam, Simunjan and Ranjang rivers. The picture on the Maludam river was taken close to the river estuary in the Maludam city. The picture of the Simunajan river was taken within the main river arm and the picture on the Rajang was taken far upstream close to the city of Belaga.

4.3. Interdependence of river carbon parameters

During the river campaigns, DOC, CO₂ and O₂ concentrations as well as the pH in the river water were measured. An overview and discussion of averaged data per campaign is provided in the appendix A.2.2. This section focuses on averaged river parameters. Subsection 4.3.1 studies the parameter's dependences on peat coverage and subsection 4.3.2 looks into the dependencies of CO₂ and O₂ on DOC and river pH. All averaged river parameters are listed in the appendix in Table A.1 and Table A.2.

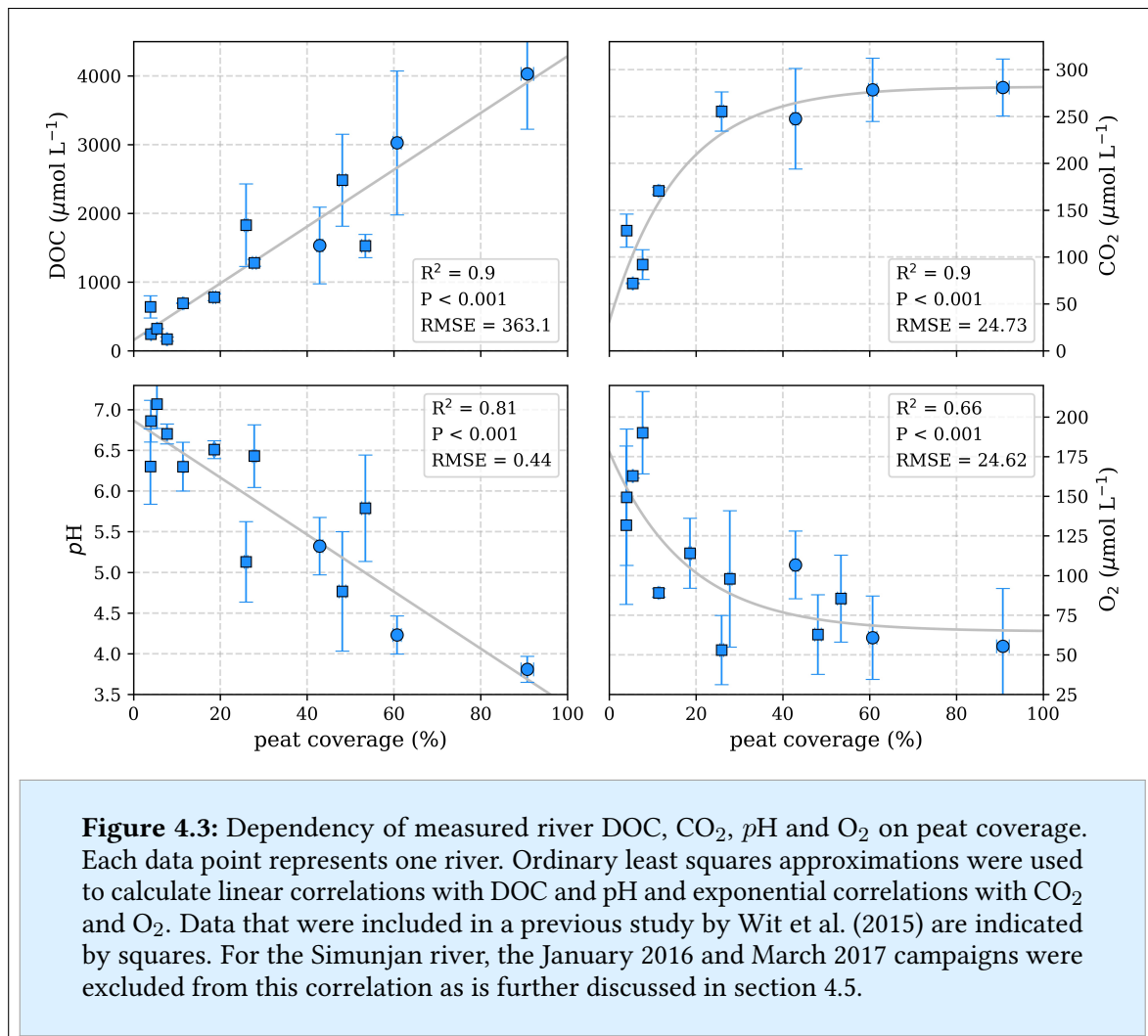
4.3.1. Correlation of river DOC, pH, CO₂ and O₂ with peat coverage

Data correlations with the peat coverage of river catchments yield a linear increase of the river DOC concentration with peat coverage as well as a negative linear correlation between river pH and peat coverage (Figure 4.3). This agrees with results by Wit et al. (2015) and

4. Limitation of CO₂ production in peat-draining rivers

confirms the importance of peat soils as a major DOC source to peat-draining rivers, whereas the decomposition of DOC and leaching of organic acids from peat areas lower the pH.

The river CO₂ concentration shows a strong increase with peat coverage for peat coverage < 30 % (Figure 4.3). This can be explained by increased DOC decomposition due to higher DOC concentrations and agrees with the results of Wit et al. (2015). Yet, despite further increase in DOC concentrations, CO₂ concentrations in rivers with peat coverage > 30 % level off, resulting in a fairly constant CO₂ for peat coverage > 50 % (Figure 4.3). The river O₂ concentration shows an opposite behaviour to the river CO₂. O₂ concentrations initially decrease with increasing peat coverage and show a decline in the regression rate for higher peat coverage, resulting in a minimum concentration of approximately 65 μmol L⁻¹ (Figure 4.3).



After an initial linear increase of river CO₂ with peat coverage, the CO₂ levels off to fairly constant concentrations for peat coverages > 50 %.

These correlations illustrate that despite the increase of DOC with peat coverage, CO₂ is levelling off. This behaviour causes the moderate CO₂ emissions measured at rivers of high peat coverage. From the measured CO₂ concentrations and exchange coefficients, CO₂ emissions from the investigated river can be derived. A comparison of those CO₂ emissions to the carbon export into the ocean as well as river CO₂ emission estimates for Malaysia, Indonesia and Southeast Asia are presented in the appendix A.2.3.

4.3.2. Correlation of river CO₂ and O₂ with DOC and pH

River DOC and pH are both linearly correlated with river peat coverage (Figure 4.3). This indicates that the general correlation between these parameters and CO₂ as well as O₂ is similar to the correlation of peat coverage with CO₂ and O₂. Accordingly, CO₂ and O₂ concentrations level off for high DOC concentrations and for low water pH (Figure 4.4).

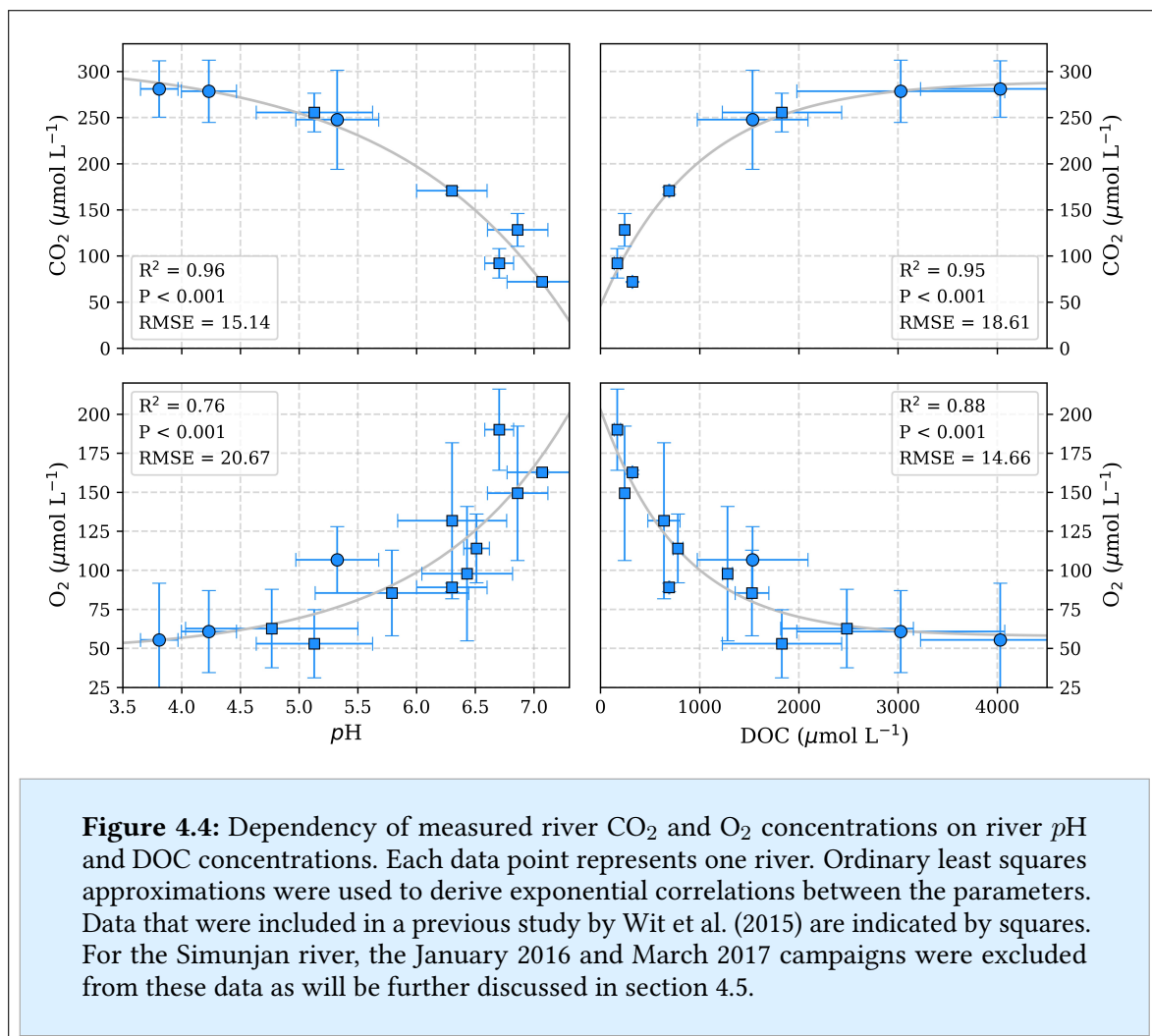
Decomposition of DOC is the biggest CO₂ source to rivers and likely the main cause for the observed correlation with CO₂. The river pH also impacts CO₂ concentrations through its impact the carbonate system. Yet, its impact on the CO₂ in rivers of pH < 5 is small, as almost all of the DIC is already in the form of CO₂ (Figure 2.6). Thus, the correlation between CO₂ and pH is likely caused implicitly through both their correlations with peat coverage (and DOC). A more in-depth discussion of the observed parameters for the individual campaigns is included in the appendix A.2.2.

Prior to this work, the correlation between river CO₂ and DOC concentrations as well as between O₂ and DOC concentrations has been assumed to be linear (Wit et al., 2015). This was confirmed for rivers with peat coverages of up to 25 % and DOC concentrations of up to 2,000 μmol L⁻¹. The assumption of these linear correlations was the main reasons why CO₂ emissions from Southeast Asian rivers were assumed to be high. The stagnation in CO₂ concentration for rivers of high DOC concentration observed in this study presents new information on such systems that have not been represented in past studies due to scarcity in data for rivers of high peat coverage.

While the CO₂ stagnation explains moderate CO₂ emissions measured at rivers of high peat coverage, the cause of this stagnation cannot be explained by the processes introduced so far. The main sources of river CO₂ are direct CO₂ leaching from soils (Abril and Borges,

4. Limitation of CO₂ production in peat-draining rivers

2019; Lauerwald et al., 2020) and the decomposition of leached DOC (Rixen et al., 2008). Both of these processes increase for rivers of high peat coverage. The main sink of river CO₂ is in-river photosynthesis. However, dark water colors in peat-draining rivers limit the light penetration into the river water column and thereby the in-stream photosynthetic reaction rates. This can be seen from the lack of diurnal CO₂ and O₂ variation in peat-draining rivers (Wit et al., 2015). Thus, the photosynthetic CO₂ consumption in peat-draining rivers is generally lower than in rivers of low peat coverage. All of these processes indicate that CO₂ concentrations in peat-draining rivers should be significantly higher than in rivers draining mineral soils.



Since CO₂ concentrations in peat-draining rivers are mainly driven by the process of DOC decomposition (Rixen et al., 2008), which also couples CO₂ production and O₂ consumption, a process that hampers decomposition rates in rivers of high peat coverage is a likely expla-

nation for the stagnation in CO₂ and O₂ (Figure 4.3). Section 4.4 investigates dependencies of DOC decomposition rates on O₂ and pH.

Prior to this work, CO₂ and O₂ were assumed to be linearly correlated with DOC. Stagnations of CO₂ and O₂ for high DOC indicate limitations in DOC decomposition.

4.4. Natural limitation in river CO₂ due to inhibition of decomposition

In subsection 2.2.3 the importance of the enzyme phenol oxidase for decomposition rates was mentioned as well as the limitation of its activity by O₂ availability and by pH. This section aims at the quantification of the impact that these parameters have on decomposition rates in and thereby on CO₂ emissions from the studied Southeast Asian rivers. Subsection 4.4.1 illustrates the theoretical concept and equations that this quantification is based upon. Then, subsection 4.4.2 presents and compares the results for two different approaches in the limitation by pH.

4.4.1. Quantification of the pH and O₂ impact on decomposition rates

The decomposition rate of DOC (R) is defined as molecules of CO₂ that are produced per available molecules of DOC during a specific time step and thus represents the proportionality factor between the CO₂ production rate and the DOC concentration:

$$R = \frac{\Delta[\text{CO}_2]}{\text{DOC} \cdot \Delta t} \Rightarrow \frac{\partial[\text{CO}_2]}{\partial t} = R \cdot \text{DOC}. \quad (4.1)$$

Since R can be limited by O₂ concentrations and by pH, it can be represented by a maximum decomposition rate (R_{max}) multiplied with limitation factors for the impact of O₂ (L_{O_2}) and pH (L_{pH}):

$$f_{\text{dec}} = \frac{\partial[\text{CO}_2]}{\partial t} = R_{\text{max}} \cdot L_{\text{O}_2} \cdot L_{\text{pH}} \cdot \text{DOC}. \quad (4.2)$$

Both L_{O_2} and L_{pH} can take values between 0 and 1. When O₂ concentrations and water pH are high enough not to limit the decomposition rate, both limitation factors are 1 and equation (4.2) simplifies to equation (4.1) with $R = R_{\text{max}}$.

In this study, an O₂ limitation factor based on the Michaelis-Menten equation is used as suggested by Pereira et al. (2017):

$$L_{\text{O}_2} = \frac{[\text{O}_2]}{K_m + [\text{O}_2]}. \quad (4.3)$$

4. Limitation of CO₂ production in peat-draining rivers

K_m is the Michaelis constant for O₂ inhibition that is also called the half saturation constant and gives the O₂ concentration at which the O₂ deficit limits decomposition rates by 50 % (Loucks and van Beek, 2017)

Publications state differing forms of pH limitation. In this study an exponential limitation factor (L_{pH}^{exp}) as suggested by Williams et al. (2000) is considered as well as a linear limitation factor (L_{pH}^{lin}) as suggested by Sinsabaugh (2010):

$$L_{pH}^{\text{exp}} = e^{\lambda \cdot (pH - pH_0)} \quad \& \quad L_{pH}^{\text{lin}} = \frac{pH}{pH_0} \quad (4.4)$$

λ is the exponential pH inhibition constant and pH_0 is a normalization constant that was set to 7.5 since this is reported to be the optimal pH for the activity of the decomposition impelling enzyme phenol oxidase (Pind et al., 1994; Kocabas et al., 2008). Since the pH limitation factors must be between 0 and 1, they are only valid for $pH \leq pH_0$. For higher pH , a different approach would be needed. However, for the acidic peat soils and peat-draining rivers investigated in this study the equations (4.4) are sufficient.

The DIC concentrations in peat-draining rivers, as a first approximation, result from an equilibrium between CO₂ emissions and CO₂ production by decomposition of DOC. Therefore, the parameters in equation (4.2) were optimized in such a way that the production of CO₂ in the water volume beneath a specific surface area equals the CO₂ flux to the atmosphere through this area. For this, the CO₂ production is calculated by multiplication of equation (4.2) with the product of river depth d and surface area A and the CO₂ emissions are calculated by multiplication of equation (2.5) with the surface area A . For the exponential limitation by pH this yields the equation

$$d \cdot A \cdot R_{\text{max}} \cdot \frac{[O_2]}{K_m + [O_2]} \cdot e^{\lambda \cdot (pH - pH_0)} \cdot \text{DOC} = A \cdot k_{\text{CO}_2}(T) \cdot ([CO_2] - K_{\text{CO}_2}(T) \cdot pCO_2^a). \quad (4.5)$$

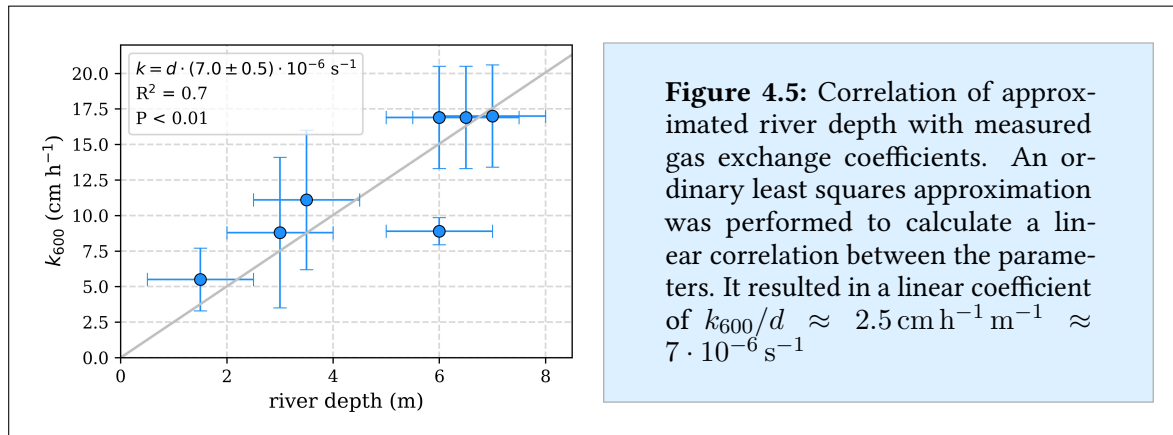
Analogously, O₂ concentrations in the rivers result from an equilibrium between the atmospheric O₂ flux and O₂ consumption due to decomposition. During decomposition, the O₂ consumption is proportional to the CO₂ production ($\Delta O_2 = -b \cdot \Delta CO_2$). The proportionality factor b is usually between 0 and 1 since a fraction of the O₂ used for decomposition is taken from the O₂ content in the dissolved organic matter (Rixen et al., 2008). Thus, the equilibrium between O₂ consumption within the water volume and O₂ flux through the water surface

area for exponential limitation by pH can be written as

$$-b \cdot d \cdot A \cdot R_{\max} \cdot \frac{[\text{O}_2]}{K_m + [\text{O}_2]} \cdot e^{\lambda \cdot (\text{pH} - \text{pH}_0)} \cdot \text{DOC} = A \cdot k_{\text{O}_2}(T) \cdot ([\text{O}_2] - K_{\text{O}_2}(T) \cdot p\text{O}_2^a). \quad (4.6)$$

In order to compare these dependences to measured data, equation (4.5) and equation (4.6) were solved for CO₂ concentrations and for O₂ concentrations, respectively. The resulting equations are quite complex and listed in the appendix in Table A.5. The analogously derived equations for CO₂ and O₂ concentrations that result from the linear pH approach are listed in the appendix in Table A.6. Based on these equations, least squares optimizations were performed for the decomposition parameters R_{\max} , b , K_m and λ such that CO₂(DOC, pH, O₂) and O₂(DOC, pH) were simultaneously optimized for the measured parameters of DOC, pH, T , CO₂ and O₂.

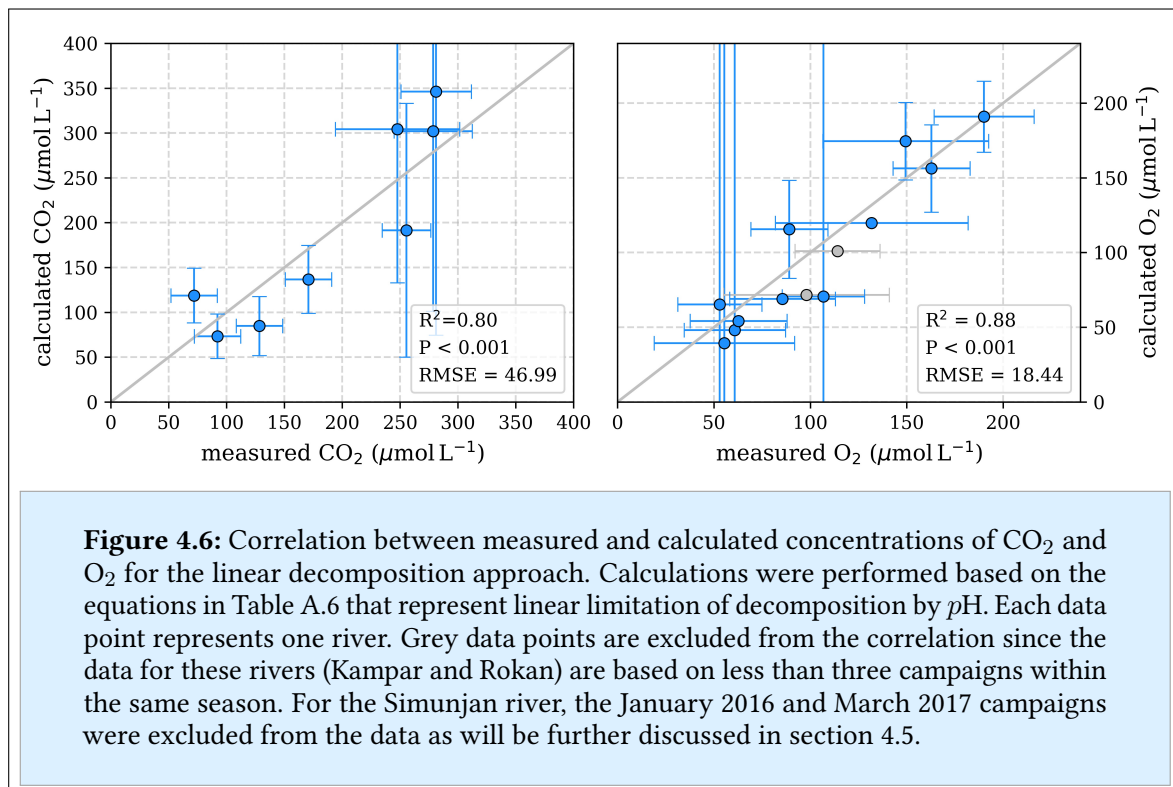
The equations in Table A.5 and Table A.6 depend on the river gas exchange coefficients for CO₂ (k_{CO_2}) and O₂ (k_{O_2}), which are both linked to k_{600} according to equation (3.2). Though exchange coefficients are poorly constrained and spatial as well as temporal extremely variable, a fairly good linear correlation between k_{600} and river depth (d) was found (Figure 4.5). Therefore a fixed ratio of $k_{600}/d = (7.0 \pm 0.5) \cdot 10^{-6} \text{ s}^{-1}$ was used for the least squares approximations of the equations in Table A.5 and Table A.6.



In the following, the CO₂ and O₂ concentrations calculated based on the resulting correlations for linear and for exponential pH limitation factors were compared to measured CO₂ and O₂ concentrations in order to gain a better understanding of the impact that pH and O₂ concentrations have on decomposition rates.

4.4.2. Evaluation of linear and exponential pH limitation of decomposition

Both the linear and the exponential approaches for the limitation of decomposition by pH reproduce the measured stagnation in CO₂ and O₂. The linear approach resulted in correlation coefficients between calculated and measured CO₂ and O₂ concentrations of $R^2 = 0.80$ and $R^2 = 0.88$, respectively (Figure 4.6). As indicated by these high correlation coefficients, the linear approach reproduces the observed stagnation in CO₂ and O₂ concentrations reasonably well. However, especially the values derived at high CO₂ and low O₂ concentrations, which are most strongly affected by the pH and O₂ limitation factors, contain high uncertainties.



The decomposition parameters resulting from this linear pH limitation of decomposition are listed in Table 4.1. Based on those values, the pH in the investigated rivers would limit decomposition rates by between 6 % in the Batang Hari and 49 % in the Maludam, while the low O₂ concentrations in the rivers would limit decomposition rates by between 71 % in the Batang Hari and 88 % in the Maludam and Siak rivers. Limitations factors derived for all rivers are listed in the appendix in Table A.4.

Like the linear approach, the exponential approach reproduces the stagnation in CO₂ and O₂ concentrations that was observed in the investigated rivers (Figure 4.7). The resulting correlation for CO₂ ($R^2 = 0.89$) is better than for the linear approach, while the O₂ correlation,

with $R^2 = 0.85$, is worse. Overall, the exponential limitation seems to be more realistic than the linear limitation as it is better in representing river CO₂ especially for high CO₂ concentrations which are most strongly effected by the pH limitation.

In the studied peat-draining rivers,
DOC decomposition is likely exponentially limited by pH.

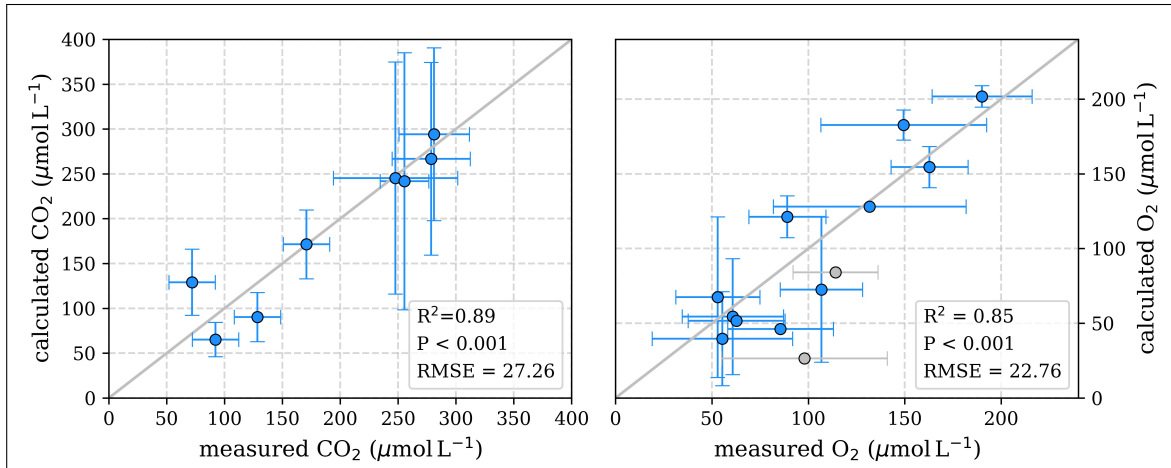


Figure 4.7: Correlation between measured and calculated concentrations of CO₂ and O₂. Calculations were performed based on the equations in Table A.5 which represent exponential limitation of decomposition by pH. Each data point represents one river. Grey data points are excluded from the correlation since the data for these rivers (Kampar and Rokan) are based on less than three campaigns within the same season. For the Simunjan river, the January 2016 and March 2017 campaigns are excluded from the data as will be further discussed in section 4.5.

The decomposition parameters that were derived for the exponential pH limitation are listed in Table 4.2. Based on these values the pH in the investigated rivers would limit decomposition rates by between 20 % in the Batang Hari and 85 % in the Maludam, while the O₂ concentration limits decomposition in the investigated rivers by ≤ 10 % (Table 4.3).

parameter	value	unit
R_{\max}	10 ± 11	$\mu\text{molCO}_2 \text{ molDOC}^{-1} \text{ s}^{-1}$
b	90 ± 25	%
K_m	390 ± 509	$\mu\text{mol L}^{-1}$

Table 4.1: Decomposition parameters derived for the linear pH approach. R_{\max} is the maximum decomposition rate, b is the proportionality factor for O₂ consumption and K_m is the Michaelis constant for O₂ limitation.

The proportionality factor for O₂ consumption by decomposition derived for both the linear approach with $b = (90 \pm 25)$ % and the exponential approach with $b = (81 \pm 10)$ % agree

4. Limitation of CO₂ production in peat-draining rivers

with the fraction of 0.8 that is stated in literature based on calculations from the O₂ to carbon ratio in peat soils (Rixen et al., 2008).

parameter	value	unit
R_{\max}	4.0 ± 0.8	$\mu\text{molCO}_2 \text{ molDOC}^{-1} \text{ s}^{-1}$
b	81 ± 10	%
K_m	6 ± 26	$\mu\text{mol L}^{-1}$
λ	0.52 ± 0.10	

Table 4.2: Decomposition parameters from the exponential pH approach. R_{\max} is the maximum decomposition rate, b is the proportionality factor for O₂ consumption, K_m is the Michaelis constant for O₂ limitation and λ is the exponential pH limitation constant.

Data of global soil phenol oxidase activity were published by Sinsabaugh et al. (2008). They state a global average soil phenol oxidase activity of $70.6 \mu\text{mol h}^{-1}$ per g organic matter. For a carbon content in peat organic matter of 38 mmol g^{-1} (Sinsabaugh, 2010) this represents approximately $0.5 \mu\text{mol mol}^{-1} \text{ s}^{-1}$. Sites of high phenol oxidase activity are listed with up to $3 \mu\text{mol mol}^{-1} \text{ s}^{-1}$ (Sinsabaugh et al., 2008). Thus, the derived maximum decomposition rates derived in this study, with $10 \mu\text{mol mol}^{-1} \text{ s}^{-1}$ for the linear pH approach and $4 \mu\text{mol mol}^{-1} \text{ s}^{-1}$ for the exponential pH approach are in a realistic order of magnitude. Yet, the linear estimate is by a factor of 3 larger than the highest rates stated in literature. This indicates that either decomposition in soils is generally limited by at least 60 % or that the linear pH decomposition approach overestimates the maximum decomposition rate.

The derived Michaelis constants for O₂ differ strongly with $K_m \approx 390 \mu\text{mol L}^{-1}$ for the linear pH approach and $K_m \approx 6 \mu\text{mol L}^{-1}$ for the exponential pH approach. The constant represents the O₂ concentration at which decomposition is limited by 50 %. Thus, a Michaelis constant that, as for the linear approach, is higher than the O₂ concentration in atmospheric equilibrium ($\approx 280 \mu\text{mol L}^{-1}$) would imply an O₂ deficit at atmospheric conditions that does not exist (Vaquer-Sunyer and Duarte, 2008). In the literature, Michaelis constants between 1 and $40 \mu\text{mol L}^{-1}$ are suggested for the O₂ impact on phenol oxidase, depending on the phenolic species (Fenoll et al., 2002). Thus, the linear pH decomposition approach seems to highly overestimate the limiting impact of O₂.

The Michaelis constant for the exponential approach is in good agreement with the literature data (Fenoll et al., 2002). Its large uncertainty ($> 400 \%$; Table 4.2) is caused by relatively high concentrations of O₂ in the rivers. Due to exchange with atmospheric O₂ the concentrations in all rivers exceed the median O₂ threshold to lethal hypoxic conditions of $50 \mu\text{mol L}^{-1}$ (Vaquer-Sunyer and Duarte, 2008). Thus, the O₂ limitation in peat-draining rivers is relatively

small (between 3 % and 10 %, Table 4.3) and consequentially a majority of the limitation is caused by the low *pH* in peat-draining rivers that limits the decomposition rates in rivers of high peat coverage (low *pH*) by up to 85 % (Table 4.3).

Low water *pH* in peat-draining rivers limits DOC decomposition by up to 85 %, while the impact of O₂ is much smaller (3 % to 10 %).

The calculated exponential *pH* coefficient of $\lambda = 0.5 \pm 0.1$ is similar to coefficients reported for high latitude peat soils ($\lambda = 0.65$ & $\lambda = 0.77$) that were determined via laboratory measurements of phenol oxidase activity (Williams et al., 2000). The fact that the exponential inhibition by *pH* can be found in those high latitude peat soils as well as in tropical peat-draining rivers suggests that the investigated correlations and processes are also relevant in other regions and that soil and water *pH* are important regulators of global carbon emissions.

River	<i>pH</i> lim. (%) = $(1 - L_{pH}^{exp})$	O ₂ lim. (%) = $(1 - L_{O_2})$	total lim. (%) = $(1 - L_{pH}^{exp} \cdot L_{O_2})$	River	<i>pH</i> lim. (%) = $(1 - L_{pH}^{exp})$	O ₂ lim. (%) = $(1 - L_{O_2})$	total lim. (%) = $(1 - L_{pH}^{exp} \cdot L_{O_2})$
Maludam	85 ± 5	10 ± 4	87 ± 6	Kampar	43 ± 6	6 ± 1	46 ± 7
Sebuyau	83 ± 6	9 ± 4	83 ± 6	Rokan	40 ± 6	5 ± 1	43 ± 6
Simunjan	68 ± 7	5 ± 1	70 ± 7	Siak	71 ± 7	10 ± 5	74 ± 8
Rajang	34 ± 5	3 ± 1	36 ± 5	Mandau	76 ± 7	9 ± 3	78 ± 7
Musi	28 ± 5	4 ± 1	31 ± 5	Tapung Kanan	59 ± 7	7 ± 2	62 ± 7
Batang Hari	20 ± 3	4 ± 1	23 ± 4	Tapung Kiri	46 ± 6	4 ± 1	49 ± 7
Indragiri	46 ± 6	6 ± 2	50 ± 7				

Table 4.3: List of fractions by which the decomposition in the individual rivers is lowered due to the impact of O₂ and *pH*. L_{O_2} and L_{pH}^{exp} are defined according to equation (4.3) and equation (4.4), respectively.

4.5. Suspension of maximum CO₂ concentration in the Simunjan river

In section 4.3 it was discussed that generally CO₂ concentrations stagnate for high peat coverage. An exception to this was observed during two campaigns in the Simunjan river (Figure 4.8). These campaigns were the only exception from otherwise low variation in the measured parameters along the rivers as well as between the different campaigns. In January 2016 and March 2017, DOC and CO₂ concentrations in the Simunjan river were significantly higher than in March 2015 and July 2017 (Table 4.4). O₂ concentrations during these campaigns ($\approx 50 \mu\text{mol L}^{-1}$) were lower than for the other Simunjan campaigns ($\approx 107 \mu\text{mol L}^{-1}$), while the water *pH* of 5.0 was slightly lower than during the other campaigns, where *pH* was 5.3 in average.

4. Limitation of CO₂ production in peat-draining rivers

The Simunjan campaigns with high DOC concentrations were accompanied by high concentrations of PIC in the form of CaCO₃ (Table 4.4), while CaCO₃ concentrations in July 2017 were much lower. Typically, concentrations of PIC in peat-draining rivers are low (Wit et al., 2018). Possible causes for high concentrations during these Simunjan campaigns could be increased erosion of mineral soils due to deforestation in mountain regions upstream or liming practices in plantations along the river. In either case, such high PIC concentrations at low river pH indicate high dissolution of carbonates.

	Campaign	pH	DOC (mmol L ⁻¹)	CO ₂ (μmol L ⁻¹)	O ₂ (μmol L ⁻¹)	CaCO ₃ (mg L ⁻¹)
Simunjan ₁	Mar 2015	5.2 ± 0.3	1.7 ± 0.7	268 ± 71	99 ± 10	n.d.
Simunjan ₂	Jan 2016	4.5 ± 0.3*	9.4 ± 1.2	> 330**	139 ± 9*	0.52 ± 0.34
Simunjan ₂	Mar 2017	5.0 ± 0.3	7.4 ± 0.6	475 ± 97	52 ± 19	0.63 ± 0.64
Simunjan ₁	Jul 2017	5.4 ± 0.3	1.4 ± 0.3	227 ± 16	115 ± 14	0.07 ± 0.05

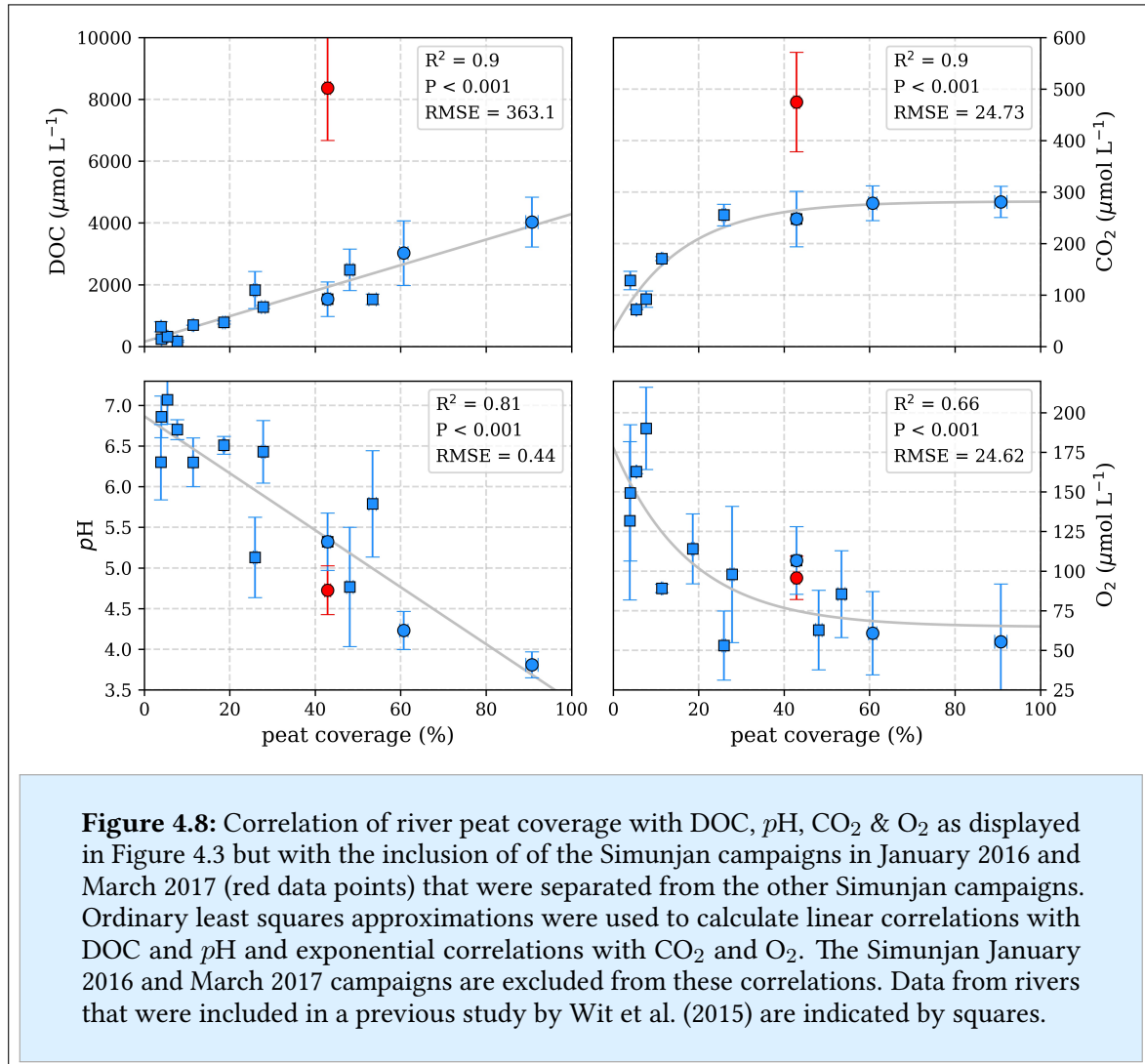
Table 4.4: Data measured for the four Simunjan campaigns. Values are means of measurements. Data variability is given by standard deviation of measurements. *Due to technical problems, the March 2017 pH, CO₂ and O₂ data need to be treated cautiously. **In March 2017 only a minimum CO₂ concentration could be derived due to technical problems.

High carbonate concentrations in turn could explain the observed high river CO₂ concentrations as they might have counteracted a decrease in pH due to decomposition of DOC. The observed high DOC concentrations in January 2016 and March 2017 indicate a high rate of CO₂ production by DOC decomposition according to equation (4.2). In the absence of carbonates, the resulting CO₂ increase would decrease the river pH (Figure 2.6) which in turn would limit the CO₂ production. However, high carbonate concentrations could suspend this natural limitation of CO₂ production, as they would counteract the pH decrease, and thereby enable higher decomposition rates.

High carbonate concentrations in the Simunjan river
suspend the pH limitation of DOC decomposition for rivers of high peat coverage.

This response to carbonate enrichment that was observed at the Simunjan river represents an important process that should also be considered for anthropogenic activities like liming and enhanced weathering. Liming is a practice to enhance soil fertility due to an increase in soil pH (Biasi et al., 2008) and enhanced weathering is a CO₂ removal technique based on the conversion of atmospheric CO₂ into carbonates (Field and Mach, 2017). Both of these practices result in enhancement of carbonates that could be leached into rivers and cause a

response similar to what was observed in the Simunjan river, where CO₂ emissions increased by almost 100 % compared to the campaigns with low carbonate concentrations.



4.6. Conclusion

In this chapter, measured data from ten Southeast Asian rivers were collected to investigate carbon dynamics in peat-draining rivers. Prior to this study, it was assumed, that CO₂ concentrations in rivers increase linearly with increasing river peat coverage of the river catchments due to enhanced leaching and decomposition of organic carbon. However, measured CO₂ emissions from Southeast Asian peat-draining rivers were hardly higher than emission from temperate rivers.

The data in this chapter show that CO₂ concentrations in Southeast Asian rivers stagnate for high peat coverages. Despite further increase in river DOC concentrations, CO₂ concen-

4. Limitation of CO₂ production in peat-draining rivers

trations are fairly constant for peat coverages > 50 %. It was found that this stagnation is caused by low water *pH* in rivers of high peat coverage that hampers decomposition rates due to limitation of phenol oxidase activity. This process provides an answer to the question why, in contrast to the high DOC export, CO₂ emissions from tropical peat-draining rivers are more moderate.

The most realistic cause for stagnating CO₂ concentrations is an exponential limitation of decomposition by *pH*. Calculations suggest that the low *pH* in rivers of high peat coverage reduces decomposition rates and thereby CO₂ production within the rivers by up to 85 %. Although this study is based on measurements in Southeast Asian peat-draining rivers, comparisons to laboratory studies of decomposition in temperate peat soils suggest that the investigated correlations and processes are also relevant in other regions and that soil and water *pH* are important regulators of global carbon emissions.

As observed in the Simunjan river, one cause for increased water *pH* in peat-draining rivers can be the input of carbonates. It was found that CO₂ concentrations during the Simunjan campaigns that were accompanied by enhanced concentrations of suspended carbonates were significantly higher than those during campaigns of low carbonate concentrations. Carbonate enhancement resulted in CO₂ emissions from the Simunjan river that were increased by almost 100 %. It is discussed that sources for enhanced carbonate concentrations can be rock weathering or soil erosion upstream of coastal peatland areas, or liming practices in plantations along the rivers, which are common practice to improve plant growth on acidic soils.

This carbonate impact should be considered when discussing the efficiency of enhanced weathering, which is a CO₂ removal strategy that extracts and binds anthropogenic CO₂ by transferring it to carbonate. The resultant *pH* increase, in regions of high peat coverage, could lead to enhanced decomposition and thereby emissions of CO₂ from rivers and soils. Chapter 5 will discuss the response of tropical peat areas, including peat-draining rivers, to enhanced weathering.

5. Response of tropical peat areas to enhanced weathering

This chapter investigates the response of tropical peat areas to the pH change induced by enhanced weathering. Parts of this chapter are currently being prepared for publication.

Section 5.1 provides an introduction to the topic and the study objective, section 5.2 gives a description of the study area and section 5.3 presents a summary of existing estimates for the CO_2 uptake by enhanced weathering. Section 5.4, section 5.5 and section 5.6 discuss the response of tropical peat soils, peat-draining rivers and coastal oceans to enhanced weathering, respectively. Section 5.7 concludes the overall impact of enhanced weathering on CO_2 emissions from tropical peat regions for a case study of Sumatra and finally, section 5.8 summarizes the results from this chapter.

5.1. Background and objective

The Paris climate agreement aims to limit the global average temperature rise to well below $2^\circ C$ with a target rise of less than $1.5^\circ C$ compared to pre-industrial times (de Coninck et al., 2018). While the reduction of anthropogenic CO_2 emissions is a key strategy to mitigate global warming, it has become clear that atmospheric CO_2 removal techniques have to be deployed to meet the target of the Paris agreement (de Coninck et al., 2018; Millar et al., 2017). One promising CO_2 removal technique is enhanced weathering (Field and Mach, 2017). It accelerates the natural process of CO_2 uptake by weathering via distribution of rock powder over the land surface (Hartmann et al., 2013b). During weathering, this atmospheric CO_2 is converted into HCO_3^- , which precipitates in soils or is washed out and transferred via rivers into the ocean. The input of HCO_3^- into the ocean counteracts ocean acidification and potentially favours the CO_2 uptake by the ocean (Hartmann et al., 2013b; Strefler et al., 2018; Köhler et al., 2010).

Since warm and humid climates accelerate weathering rates (Strefler et al., 2018), preferred target areas for enhanced weathering projects are tropical regions, including peatlands (Taylor et al., 2016; Beerling et al., 2020). First estimates of the cost efficiency of enhanced weathering considered application over all tropical land areas (Taylor et al., 2016). More recent studies pointed out that application on actively worked croplands would simplify transport and application procedures (Beerling et al., 2020) and thereby reduce overall application costs (Strefler et al., 2018). Combating climate change on one side and increasing the demand for agricultural products on the other side, represents a sustainability conflict that

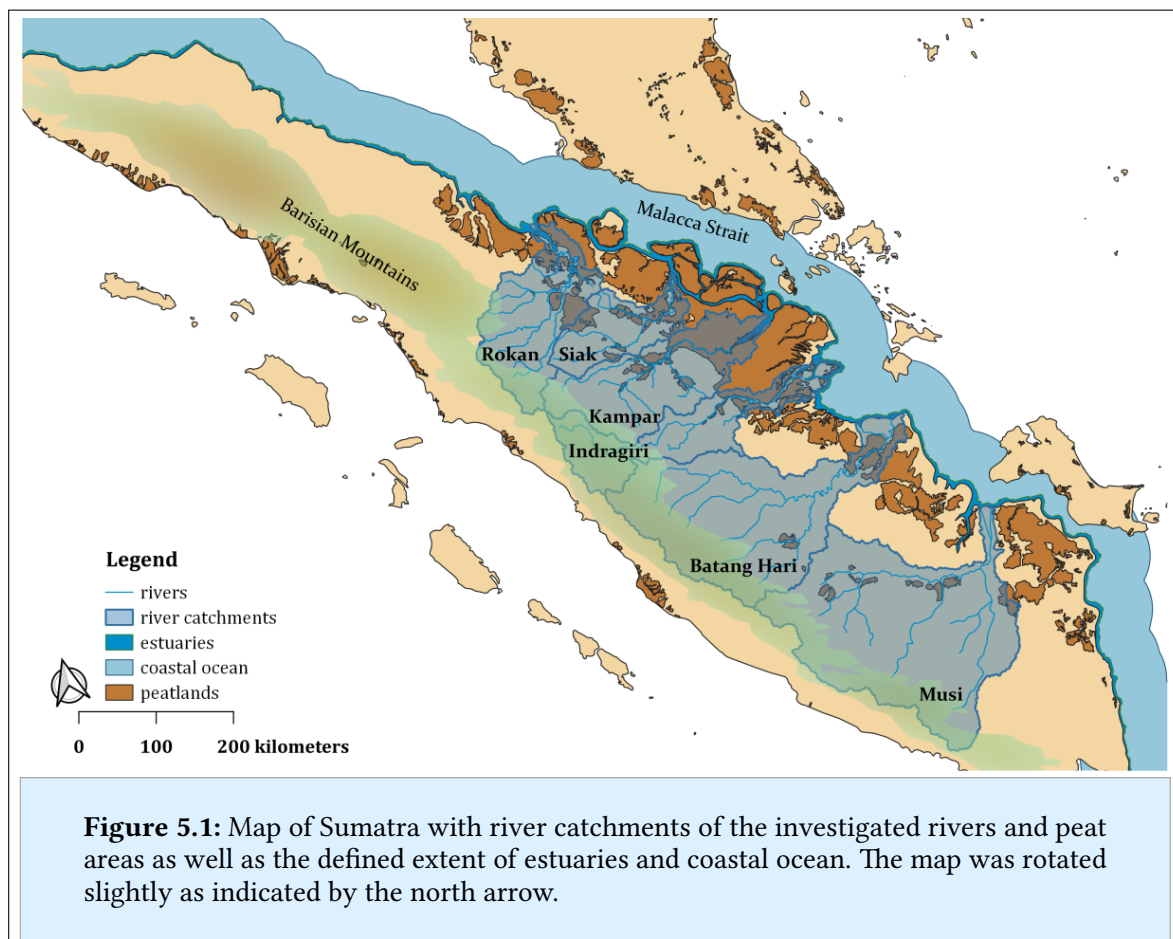
5. Response of tropical peat areas to enhanced weathering

now needs to be contextualized with enhanced weathering as a measure that is suggested to reduce atmospheric CO₂.

In the following, impacts of the enhanced weathering induced *pH* increase on carbon dynamics in tropical peat regions are investigated for a case study of Sumatra. Results are based on the *pH* dependence of decomposition that was derived in the previous chapter.

5.2. Study area

Sumatra hosts more than 70,000 km² of peatlands (Miettinen et al., 2016), representing 15.6 % of its surface area of 464,301 km² (Hooijer et al., 2006). This is more than 30 % of the whole Indonesian peat area and over 25 % of the Southeast Asian peat area (Hooijer et al., 2010). Most Sumatran rivers originate in the Barisan Mountains and cut through coastal peatlands before discharging into the Malacca Strait (Figure 5.1).



The aim of this study is to estimate the response of CO₂ emissions from Sumatra's soils, rivers and coastal regions to enhanced weathering application. For the coastal regions, it will

be differentiated between the river estuaries and the coastal ocean. The areal extent of these categories, analogous to the study by Wit et al. (2018), is defined by salinity with $S \leq 25$ for estuaries and $25 < S < 32.8$ for the coastal ocean. Based on the results by Wit et al. (2018), these salinity values correspond to distances of ≈ 3 km and ≈ 67 km from shore and represent areas of 10,818 km² and 127,674 km², respectively.

The calculations in this chapter are based on data from the investigated rivers at which CO₂ measurements were performed. Those rivers include the Siak, Indragiri, Musi and Batang Hari (Figure 5.1). Additionally, the Rajang, Simunjan, Sebuyau and Maludam rivers on Borneo (Sarawak, Malaysia; Figure 4.1) are included. The Rajang river originates in the Iran mountains, a mountain region located at the border between Malaysia and Indonesia, before cutting through coastal peatlands and discharging into the South China Sea. The smaller rivers on Borneo originate closer to the coast and exhibit high peat coverage. Since all rivers drain tropical peat soils and are exposed to similar climatic conditions, they are considered representative for Southeast Asian peat-draining rivers and are handled equivalent in this study's calculations.

5.3. Enhanced weathering estimates

Recent estimates of the CO₂ uptake by enhanced weathering were published by Taylor et al. (2016) and by Beerling et al. (Table 5.1, 2020).

appl. rate (kg m ⁻² yr ⁻¹)	appl. depth (cm)	CO ₂ uptake (gC m ⁻² yr ⁻¹)	HCO ₃ ⁻ formation (mol m ⁻² yr ⁻¹)	pH increase	reference
1	10	50	4.2	1.3*	Taylor et al. (2016)
1	30	70	5.8	2	Taylor et al. (2016)
4	15	30	2.5	< 0.5	Beerling et al. (2020)
5	10	250	20.8	2.5*	Taylor et al. (2016)
5	30	300	25.0	2.5	Taylor et al. (2016)

Table 5.1: List of previous enhanced weathering estimates for basalt application over tropical regions. Scenarios differ in rock application rate and depth.*Taylor et al. (2016) did not include pH estimates for a basalt application depth of 10 cm. The values listed here are estimated based in the change in pH they state for dunite rock application of different depths.

Taylor et al. (2016) estimated CO₂ uptake and soil pH changes based on optimized enhanced weathering scenarios for application of different rock types, rock application rates and depths. This chapter focuses on enhanced weathering with nutrient-rich basalt rocks. Those

rocks exist in huge amounts and have been found to co-benefit crop production and soil health (Beerling et al., 2020). In tropical regions, the estimated CO₂ uptake and pH increase for scenarios with basalt application range from 50 to 300 gC m⁻² yr⁻¹ and from 1.3 to 2.5, respectively (Table 5.1).

Simulations by Beerling et al. (2020) were performed for basalt application on cropland areas in different countries. For Indonesia, they resulted in formation of 2 to 3 mol HCO₃⁻ m⁻² yr⁻¹, which correlate to a CO₂ uptake between 24 and 36 gC m⁻² yr⁻¹. Those estimates are lower than the ones Taylor et al. (2016) stated for tropical weathering hotspot areas. They also result in a lower pH increase with less than 0.5 values for the region of Indonesia (Table 5.1). Further calculations in this chapter are based on the lower scale scenario by Taylor et al. (2016) for application rates of 1 kg m⁻² yr⁻¹ and an application depth of 10 cm over tropical weathering hotspot areas as well as on the scenario by Beerling et al. (2020) for application of 4 kg m⁻² yr⁻¹ over Indonesian cropland areas. Resulting CO₂ uptake and pH increase for those scenarios are (25 – 50) gC m⁻² yr⁻¹ and (0.2 – 1.3), respectively.

5.4. Response of soil carbon mobilisation to enhanced weathering

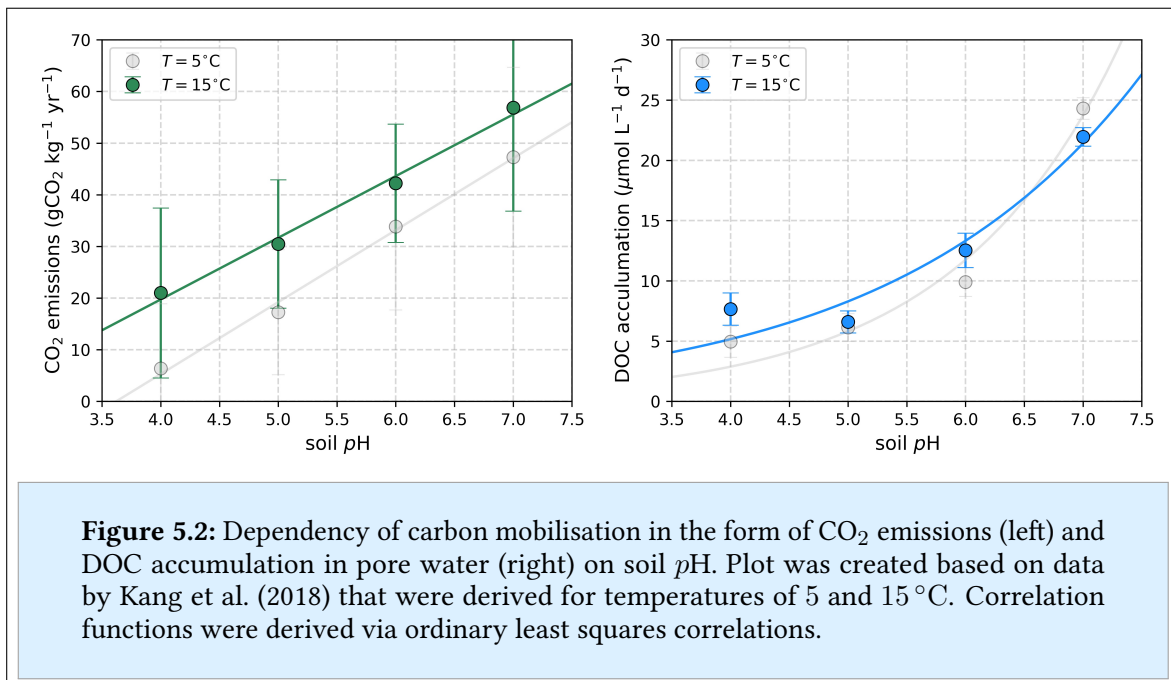
The application of enhanced weathering causes a pH increase in soils that impacts carbon mobilisation in from soil in the form of CO₂ emissions to the atmosphere and DOC leaching into rivers. Additionally the HCO₃⁻ created during weathering leaches into rivers. In the following parts of this sections, the impact of these processes on CO₂ emissions is quantified for application of enhanced weathering on peat soils as well as on all Sumatra's soils. Subsection 5.4.1 illustrates published dependencies of carbon mobilisation from peat soils on pH. Subsection 5.4.2, subsection 5.4.3 and subsection 5.4.4 illustrate the response of CO₂ emissions, DOC leaching and DIC leaching from soils to enhanced weathering, respectively.

5.4.1. Dependency of CO₂ and DOC mobilisation from peat soils on pH

The decomposition in peat soils and the associated mobilisation of peat carbon depend on the activity of the enzyme phenol oxidase (Freeman et al., 2004). Phenol oxidase, in turn, is strongly controlled by pH (Pind et al., 1994). Positive correlations between pH and decomposition rates in peat soils are reported in literature (Williams et al., 2000). Current estimates of the CO₂ uptake by enhanced weathering do not include this process (Taylor et al., 2016; Beerling et al., 2020). However, the pH increase associated with enhanced weathering scenarios (Table 5.1) would accelerate decomposition of peat carbon and thus exert a negative

feedback on the CO₂ uptake by enhanced weathering. To quantify this effect, published correlations between CO₂ emissions as well as pore water DOC and the pH in peat soils (Kang et al., 2018) are used.

Data by Kang et al. (2018) yield a linear correlation between peat soil pH and CO₂ emissions (Figure 5.2). Their study includes data for fixed temperatures of $T = 5\text{ }^{\circ}\text{C}$ and $T = 15\text{ }^{\circ}\text{C}$. The increase in CO₂ emissions per pH increase of 1 at 5 °C soils ($\approx 14\text{ gCO}_2\text{ kg}^{-1}\text{ yr}^{-1}$) is higher than at 15 °C ($\approx 12\text{ gCO}_2\text{ kg}^{-1}\text{ yr}^{-1}$, Figure 5.2). This could indicate that the response of CO₂ emissions to pH at tropical temperatures is even lower. However, there are no studies available that investigate this correlation for tropical peat. Thus, the correlation at 15 °C was used to calculate the response of soil CO₂ emissions to the enhanced weathering induced pH increase.



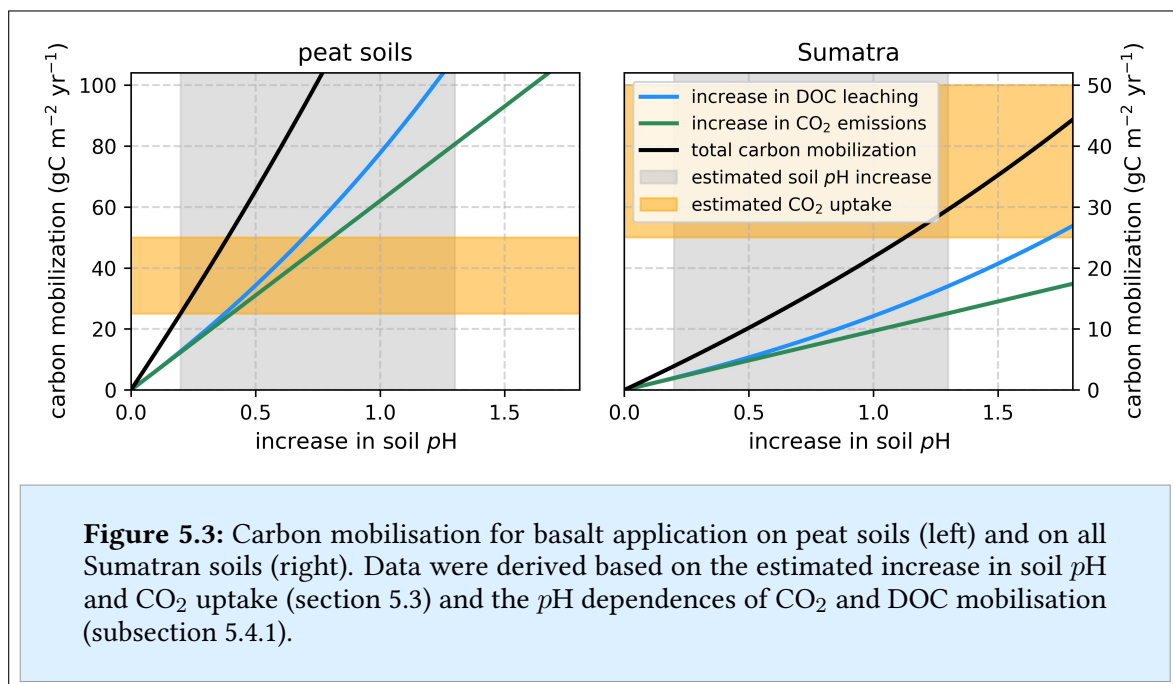
The correlation derived between accumulated pore water DOC and peat soil pH is non-linear. For $T = 5\text{ }^{\circ}\text{C}$, the dependency of DOC accumulation on pH is fairly good represented by a function $\sim 2^{pH}$. Thus, at this temperature, the DOC accumulation doubles for a pH increase of 1. For temperatures of 15 °C, the data yield a correlation function $\sim 1.6^{pH}$, which equals an increase of 60 % per pH increase of 1. Analogous to the CO₂–pH correlation, these data yield a decrease in the response of decomposition to pH changes for higher temperatures. This could indicate an even weaker response for peat soils at tropical temperatures. However,

5. Response of tropical peat areas to enhanced weathering

as for the CO_2 – $p\text{H}$ correlation, no data for tropical peat were available and the DOC – $p\text{H}$ correlation derived for $T = 15^\circ\text{C}$ has been used for further calculations in this study.

5.4.2. Response of CO_2 emissions from soils to enhanced weathering

In order to estimate the response of soil CO_2 emissions to enhanced weathering, the $p\text{H}$ increase of 0.2 to 1.3 (section 5.3) was combined with the linear CO_2 – $p\text{H}$ correlation (Figure 5.2). The CO_2 – $p\text{H}$ relation was applied to the upper 15 cm of peat soils, assuming a peat soil density of 0.127 g cm^{-3} (Warren et al., 2012).



The $p\text{H}$ increase caused by application of enhanced weathering on peat soils increases CO_2 emissions from the soils by $(12 - 81)\text{ gC m}^{-2}\text{ yr}^{-1}$ (Figure 5.3). For the lower bound of the enhanced weathering estimate ($p\text{H}$ increase of 0.2), this increase in CO_2 emissions ($12\text{ gC m}^{-2}\text{ yr}^{-1}$) already compensates half of the CO_2 uptake by enhanced weathering. For the upper bound ($p\text{H}$ increase of 1.3), peat soil CO_2 emissions alone are significantly higher than the estimated CO_2 uptake by enhanced weathering (Figure 5.3). These additional emissions represent $(8 - 26)\%$ of the CO_2 uptake by enhanced weathering.

Enhanced weathering application on peat soils could cause soil CO_2 emissions that are significantly higher than the CO_2 uptake by enhanced weathering.

While the increase in soil carbon mobilisation is specifically based on correlations derived for peat soils (Kang et al., 2018), estimates of the CO_2 uptake by enhanced weathering do

not differentiate between peat and mineral soils (Taylor et al., 2016; Beerling et al., 2020). Thus, it is not known whether the stated CO₂ capture rates for tropical areas are valid for tropical peat soils specifically. Therefore, the carbon mobilisation within Sumatra’s peat soils and its impact on the net CO₂ uptake for Sumatra were investigated (Figure 5.3) as representative for tropical peat regions. Atmospheric CO₂ emissions from Sumatra’s soils were derived by multiplication of the emissions from peat soils with Sumatra’s peat coverage of 15.6 % (Hooijer et al., 2006). The increase in CO₂ emissions from Sumatra’s soils results in (2 – 13) gC m⁻² yr⁻¹, representing up to almost one-quarter of the natural CO₂ emissions from Sumatra’s soils (Table 5.2; Prananto et al., 2020).

Enhanced weathering application on Sumatra’s soils causes soil CO₂ emissions that potentially re-emit 26 % of the CO₂ uptake by enhanced weathering.

5.4.3. Response of DOC leaching from soils to enhanced weathering

The response of DOC leaching from soils to enhanced weathering was derived from the enhanced weathering induced pH increase of 0.2 to 1.3 (section 5.3) and the derived DOC–pH correlation (Figure 5.2). Since this correlation was stated for pore water DOC concentrations and DOC leaching is directly linked to those concentrations (Worrall et al., 2002), the derived correlation can be used for DOC leaching rates. However, the DOC–pH correlation is not linear (Figure 5.2) which means that a reference value is needed to derive the response to a specific increase in pH. Therefore, natural DOC leaching from Sumatra’s peat soils (Table 5.2) was applied as reference value.

	atm. CO ₂ flux	DOC leaching	DIC leaching
natural	55 gC m ⁻² yr ⁻¹	20 gC m ⁻² yr ⁻¹	13 gC m ⁻² yr ⁻¹
enhanced weathering induced increase	(2 – 13) gC m ⁻² yr ⁻¹	(2 – 17) gC m ⁻² yr ⁻¹	(25 – 50) gC m ⁻² yr ⁻¹

Table 5.2: Natural soil carbon mobilisation and its feedback on enhanced weathering application on Sumatra. For the natural CO₂ flux, published fluxes from tropical peat soils (Prananto et al., 2020) were multiplied with Sumatra’s peat coverage. Natural DOC and DIC leaching rates were derived according to equation (5.1) that will be introduced in subsection 5.5.1.

The DOC mobilisation caused by enhanced weathering results in (13 – 109) gC m⁻² yr⁻¹ (Figure 5.3). The total carbon mobilisation from peat soils is given by the sum of increased CO₂ emissions and increased DOC leaching. For the lower bound of the enhanced weathering

5. Response of tropical peat areas to enhanced weathering

estimate (pH increase of 0.2) this total carbon mobilisation of approximately $25 \text{ gC m}^{-2} \text{ yr}^{-1}$ already compensates the CO_2 uptake by enhanced weathering. For the upper bound (pH increase of 1.3) the carbon mobilisation, with almost $200 \text{ gC m}^{-2} \text{ yr}^{-1}$, is much higher than the estimated CO_2 uptake of $50 \text{ gC m}^{-2} \text{ yr}^{-1}$ (Figure 5.3). This indicates that application of enhanced weathering on tropical peat soils could in fact create a net CO_2 source to the atmosphere.

The DOC mobilisation from Sumatra's soils is derived analogous to Sumatra's CO_2 mobilisation by multiplication of peat DOC mobilisation with Sumatra's peat coverage. It results in $(2 - 17) \text{ gC m}^{-2} \text{ yr}^{-1}$ (Figure 5.3) and is therewith in the range of natural leaching rates from Sumatra's soils (Table 5.2).

The total carbon mobilisation from Sumatra's soils (CO_2 mobilisation + DOC mobilisation) amounts to $(4 - 30) \text{ gC m}^{-2} \text{ yr}^{-1}$ (Figure 5.3). These values are solely based on the response of Sumatra's peat soils and therefore might underestimate the total carbon mobilisation as they omit the response of mineral soils. However, these results already imply that a significant amount of the CO_2 uptake by enhanced weathering is counteracted by carbon mobilisation within Sumatra's peat areas (Figure 5.3).

The enhanced weathering induced pH increase in Sumatra's soils causes soil carbon mobilisation of $(4 - 30) \text{ gC m}^{-2} \text{ yr}^{-1}$.

5.4.4. Response of DIC leaching from soils to enhanced weathering

The estimated response of DIC leaching to enhanced weathering in this study was derived based on the assumption that the carbon captured during atmospheric CO_2 uptake is transformed into HCO_3^- and over time leached into rivers. Thus, the maximum leaching rate is given by the rate of CO_2 uptake ($(25 - 50) \text{ gC m}^{-2} \text{ yr}^{-1}$). However, this assumption ignores the possibility of direct CO_2 re-emission due to the transformation of HCO_3^- to CO_2 under the acidic conditions in peat soils, as it was observed for liming experiments on plantations in peatlands (Biasi et al., 2008). In a worst-case scenario, these acidic conditions could cause direct re-emission of the total CO_2 uptake. In the other extreme, the total CO_2 uptake could be leached as HCO_3^- from soils.

Efficiency studies of enhanced weathering so far assumed that all of the captured carbon is transported to the ocean, which would represent the best-case scenario. In reality however, even if the majority of the CO_2 uptake is leached into rivers in the form of HCO_3^- , the acidic conditions in peat-draining rivers could cause this carbon to be transformed into CO_2 and

emitted to the atmosphere. At the same time, the enhanced HCO_3^- supply could increase the river $p\text{H}$ and thereby cause enhanced decomposition rates of the mobilized DOC which would further enhance river CO_2 concentrations and emissions. Section 5.5 investigates the fate of carbon leached into Sumatra's rivers.

5.5. Response of river carbon export to enhanced weathering

River carbon dynamics are impacted by enhanced weathering through the increase in DOC and DIC leaching from soils that was discussed in section 5.4. To quantify the impact of the increase in carbon leaching on river CO_2 emissions and the carbon export to the coast, a river box-model was constructed. Subsection 5.5.1 provides a description of this model. Subsection 5.5.2 and subsection 5.5.3 discuss the response of river CO_2 emissions and the oceanic carbon export to the enhanced leaching of DOC and DIC.

5.5.1. Description of river box-model

The river box model was constructed to simulate in-river carbon dynamics and derive their response to changed carbon supply. The model simulates temporal changes in concentrations of DOC, DIC, CA, CO_2 , O_2 and of water $p\text{H}$. It includes decomposition processes, atmospheric exchange fluxes and reactions in the carbonate system as well as river input fluxes through leaching and discharge fluxes into the ocean.

For each model run, leaching rates of DOC, DIC, CA and O_2 as well as the water temperature, the salinity, the ratio between discharge and water volume (Q/V) and the ratio between exchange coefficient and water depth (k_{600}/d) are fixed to calculate equilibrium concentrations of the river parameters.

Water temperatures of $T = 29^\circ\text{C}$ and salinities of $S = 0.001$ were used for all rivers. For (Q/V) an average ratio for all rivers of $(1.1 \pm 0.6) \cdot 10^{-6} \text{ s}^{-1}$ (correlation in the appendix in Figure A.1) was used and (k_{600}/d) was set to $(7.0 \pm 0.5) \cdot 10^{-6} \text{ s}^{-1}$, consistent with the calculations in subsection 4.4.1. Natural leaching rates were calculated by the sum of their sinks minus the sum of their sources:

$$\begin{aligned}
 \text{DOC}_{\text{leaching}} &= \text{DOC} \cdot Q + f_{\text{dec}}(\text{DOC}, \text{O}_2, p\text{H}) \\
 \text{DIC}_{\text{leaching}} &= \text{DOC} \cdot Q + F_{\text{CO}_2}(\text{CO}_2, k_{\text{CO}_2}, T) - f_{\text{dec}}(\text{DOC}, \text{O}_2, p\text{H}) \\
 \text{CA}_{\text{leaching}} &= \text{CA} \cdot Q \\
 \text{O}_{2,\text{leaching}} &= [\text{O}_2] \cdot Q + b \cdot f_{\text{dec}}(\text{DOC}, \text{O}_2, p\text{H}) + F_{\text{O}_2}(\text{O}_2, k_{\text{O}_2}, T) .
 \end{aligned} \tag{5.1}$$

5. Response of tropical peat areas to enhanced weathering

f_{dec} describes the CO_2 production by in-river decomposition according to equation (4.2) with exponential limitation by $p\text{H}$. b is the fraction of O_2 that is consumed in relation to the CO_2 production (81 %; Table 4.2). F_{CO_2} and F_{O_2} describe the atmospheric fluxes of CO_2 and O_2 , respectively. These fluxes were derived according to equation (2.5).

For model runs that simulate rivers impacted by enhanced weathering, the derived increase in leaching rates (Table 5.2) was added to the natural leaching rates. Enhanced DOC leaching was added to the $\text{DOC}_{\text{leaching}}$ and enhanced DIC leaching was added to the $\text{DIC}_{\text{leaching}}$ and the $\text{CA}_{\text{leaching}}$. For each model run, time steps of 10 min were used. The number of iterations were set to 52,560, amounting to 1 year of modelled concentrations. Generally, equilibrium concentrations were reached after approximately 1 month. An exemplary time series is shown in the appendix in Figure A.5.

During each iteration, $p\text{H}$ and CO_2 are calculated based on the current concentrations of DIC and CA according to the equation system explained in subsection 2.2.2. Then, the changes in DIC, DOC, CA and O_2 concentrations due to the processes of leaching, decomposition, atmospheric exchange and discharge are calculated according to:

$$\begin{aligned}\Delta\text{DIC} &= \frac{Q}{V} \cdot ([\text{DIC}_{\text{leaching}}] - [\text{DIC}_{\text{river}}]) + f_{\text{dec}} + d \cdot F_{\text{CO}_2} \\ \Delta\text{DOC} &= \frac{Q}{V} \cdot ([\text{DOC}_{\text{leaching}}] - [\text{DOC}_{\text{river}}]) - f_{\text{dec}} \\ \Delta\text{CA} &= \frac{Q}{V} \cdot ([\text{CA}_{\text{leaching}}] - [\text{CA}_{\text{river}}]) \\ \Delta[\text{O}_2] &= \frac{Q}{V} \cdot ([\text{O}_{2,\text{leaching}}] - [\text{O}_{2,\text{river}}]) - b \cdot f_{\text{dec}} + d \cdot F_{\text{O}_2}.\end{aligned}\tag{5.2}$$

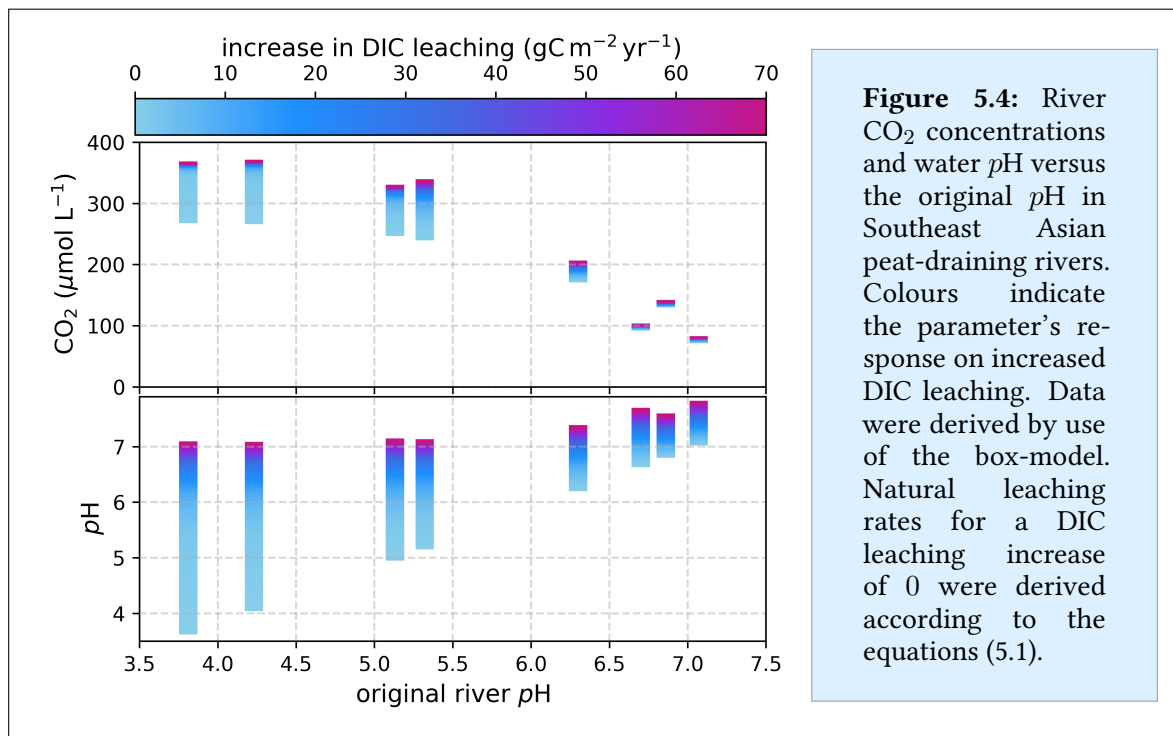
$[\text{X}_{\text{leaching}}]$ and $[\text{X}_{\text{river}}]$ are the concentrations of species X in the water input to the river and in the river water that discharges into the ocean, respectively. $[\text{X}_{\text{river}}]$ are the current concentrations in the modelled river that the changes according to the equations (5.2) are applied to for each iteration. Uncertainties of the derived concentrations were estimated from best/worst case runs of the box-model based on variation of the respiration parameters (R , K_m , λ & b ; Table 4.2) within their uncertainties.

5.5.2. Response of river CO_2 emissions to enhanced weathering

Natural runs of the river box-model (without impact of enhanced weathering) were performed for the individual rivers listed in section 5.2. CO_2 concentrations resulting from those runs range from approximately $70 \mu\text{mol L}^{-1}$ in the Batang Hari to about $270 \mu\text{mol L}^{-1}$ in the

Maludam and Sebuyau and show a good agreement with the measured concentrations in these rivers. Correlations between modelled and measured concentrations are shown in the appendix in Figure A.6.

An increase in DIC leaching (in the form of HCO_3^-) results in increased river $p\text{H}$, whereby rivers of high peat coverage (low original water $p\text{H}$) respond with a stronger $p\text{H}$ increase than rivers of low peat coverage (high original water $p\text{H}$; Figure 5.4). The $p\text{H}$ increase shifts the carbonate system in the rivers towards HCO_3^- and thereby lowers the CO_2 fraction of river DIC. However, this CO_2 decrease is overcompensated by enhanced supply of DIC due to increased HCO_3^- leaching and DOC decomposition. Rivers with a strong $p\text{H}$ increase also show a strong increase in CO_2 (Figure 5.4).



The $p\text{H}$ increase enhances decomposition rates in the rivers and thereby causes a reduction of DOC and O_2 concentrations (Figure 5.5). In the Maludam and Sebuyau rivers (original $p\text{H} < 4.5$), O_2 concentrations decrease below $20 \mu\text{mol L}^{-1}$ for a small increase in DIC leaching. Such low O_2 concentrations limit decomposition rates, which explains the small impact additional DIC leaching has on the CO_2 concentrations in these rivers (Figure 5.4). For the Siak river ($p\text{H} \approx 5.2$), low O_2 hampers decomposition for leaching enhancement of $\geq 20 \text{ gC m}^{-2} \text{ yr}^{-1}$. Rivers of low peat coverage ($p\text{H} > 6.5$) show almost no change in CO_2

5. Response of tropical peat areas to enhanced weathering

and O_2 concentrations. This can be explained by the low pH change in those rivers as well as by generally slow decomposition due to low DOC concentrations.

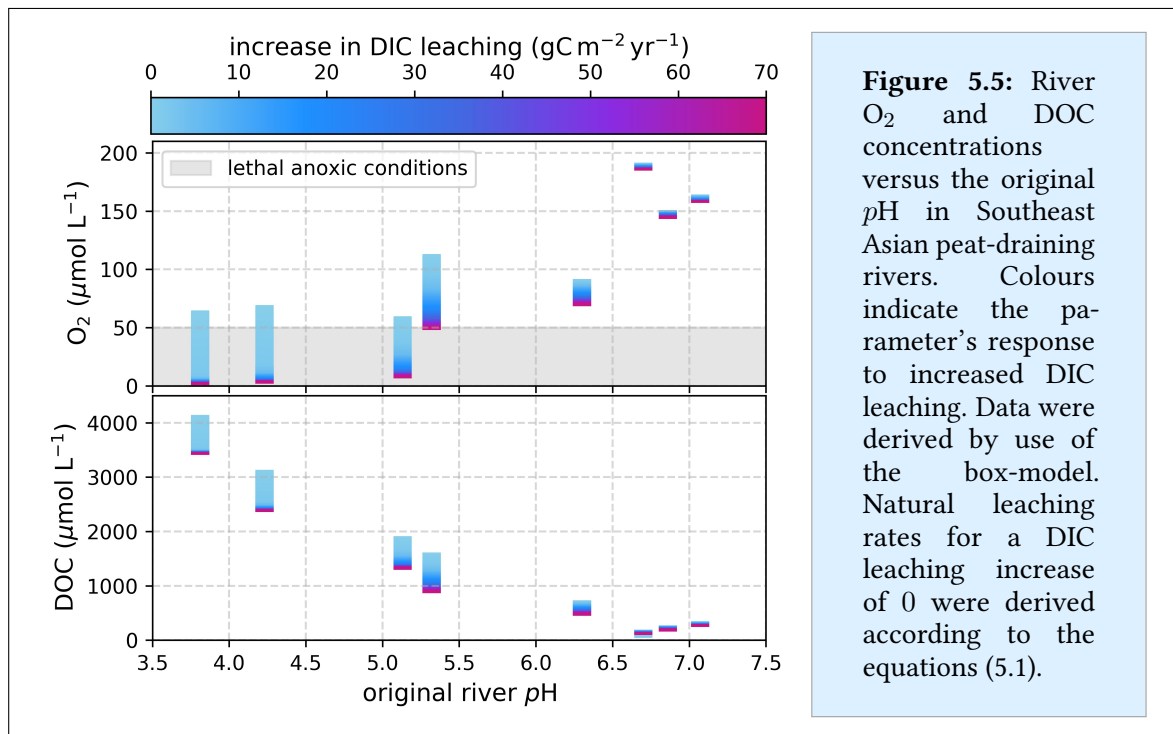


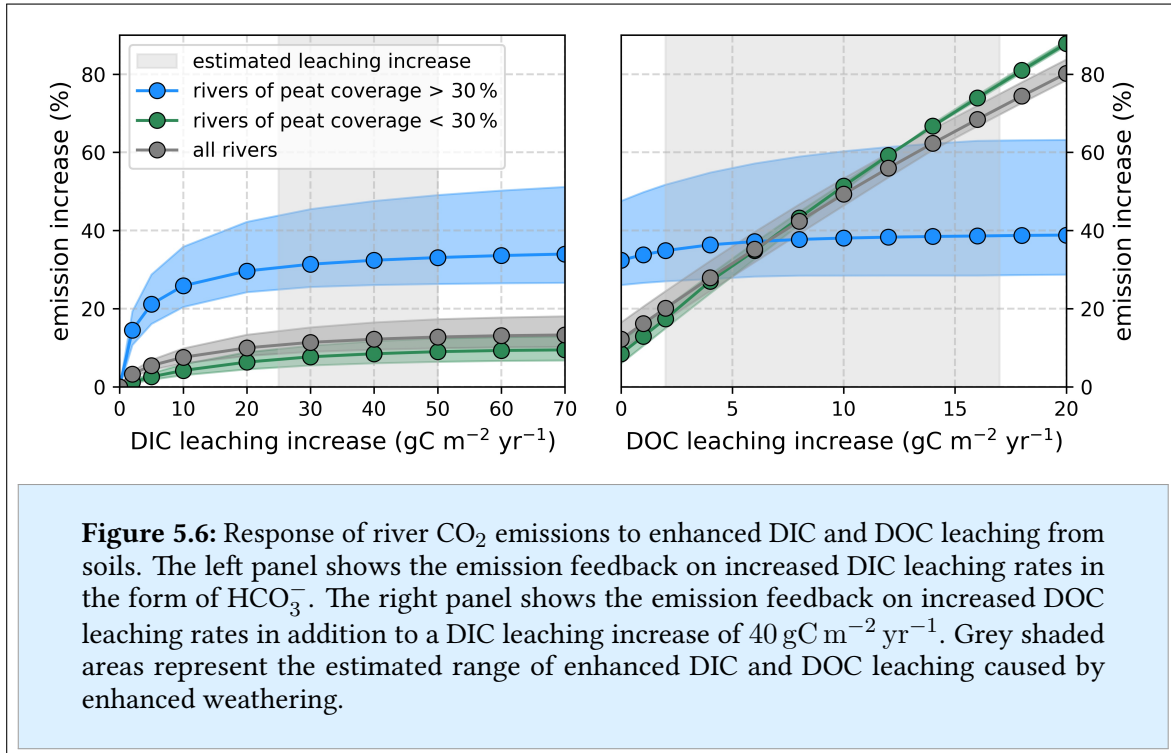
Figure 5.5: River O_2 and DOC concentrations versus the original pH in Southeast Asian peat-draining rivers. Colours indicate the parameter's response to increased DIC leaching. Data were derived by use of the box-model. Natural leaching rates for a DIC leaching increase of 0 were derived according to the equations (5.1).

Atmospheric river CO_2 fluxes were derived from modelled CO_2 concentrations in the rivers according to equation (2.5). For minimum and maximum flux estimates, exchange coefficients between $k_{600} = 7 \text{ cm h}^{-1}$ and $k_{600} = 20 \text{ cm h}^{-1}$ were considered. These exchange coefficients cover the range measured at the Southeast Asian rivers (appendix Table A.2). CO_2 fluxes based on the concentrations derived from box-model runs without increased leaching range between 2 and $18 \text{ gC m}^{-2} \text{ day}^{-1}$.

To compare the changes in river CO_2 emissions to the CO_2 uptake by enhanced weathering, CO_2 yields (emissions per catchment area) were derived according to equation (3.4). CO_2 yields from box-model runs without enhanced leaching range from $(4 - 12) \text{ gC m}^{-2} \text{ yr}^{-1}$ from the Batang Hari river to $(18 - 52) \text{ gC m}^{-2} \text{ yr}^{-1}$ from the the Maludam and Sebuyau rivers with average CO_2 yields from Sumatra of $(8 - 22) \text{ gC m}^{-2} \text{ yr}^{-1}$ (Table 5.3).

River CO_2 emissions increase with increasing DIC leaching rates and stagnate for high leaching rates (Figure 5.6), as the impact of HCO_3^- on pH becomes weaker (Figure 5.4) and O_2 depletion limits decomposition in rivers of high peat coverage (Figure 5.5). Due to this O_2 limitation, the stagnation is most prominent for rivers of high peat coverage (Figure 5.6). As explained in section 5.3, the upper bound of enhanced DIC leaching into rivers is repre-

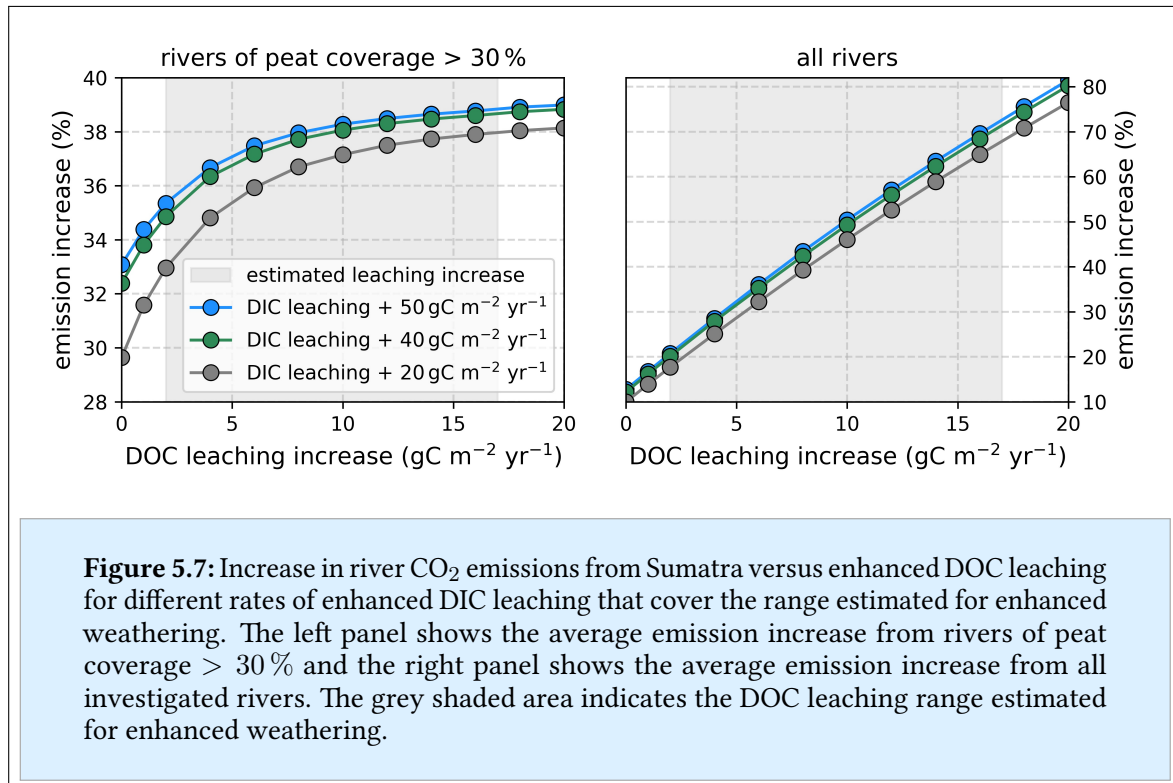
sented by the estimated enhanced weathering CO_2 uptake of $(25 - 50) \text{ gC m}^{-2} \text{ yr}^{-1}$. This leaching increase would correlate to an average increase in river CO_2 emissions of 11 to 13 %, whereby the rivers of high peat coverage (Maludam, Sebuyau, Simunjan & Siak) show the strongest emission increase of about 32 % (Figure 5.6). The increase in atmospheric CO_2 yields from Sumatra results to $(0.8 - 2.8) \text{ gC m}^{-2} \text{ yr}^{-1}$, which represents (3 – 6) % of the enhanced weathering CO_2 uptake.



An increase in DOC leaching in addition to the enhanced DIC leaching significantly increases CO_2 concentrations in and emissions from rivers of low peat coverage (Figure 5.6). Its impact on rivers of high peat coverage is much smaller due to depletion of O_2 (Figure 5.5) that hampers decomposition rates. Considering an increase in DIC leaching of $40 \text{ gC m}^{-2} \text{ yr}^{-1}$ and the estimated DOC leaching increase of $(2 - 17) \text{ gC m}^{-2} \text{ yr}^{-1}$, CO_2 emissions from Sumatra increase by (20 – 75) % compared to the natural box-model run (Figure 5.6).

Variation in DIC leaching results in comparatively small changes in the CO_2 emissions (Figure 5.7). Thus, the retrieved impact of enhanced DOC leaching at the DIC leaching rate of $40 \text{ gC m}^{-2} \text{ yr}^{-1}$ seems to be representative for the estimated range of enhanced DIC leaching. The combined enhanced weathering induced increase of DIC and DOC leaching into Sumatra's rivers (Table 5.2) results in CO_2 yields that increase by $(1.5 - 16.2) \text{ gC m}^{-2} \text{ yr}^{-1}$ (Table 5.3). This represents (6 – 32) % of the CO_2 uptake by enhanced weathering.

5. Response of tropical peat areas to enhanced weathering



The enhanced weathering induced carbon leaching into peat-draining rivers causes river CO₂ emissions that potentially re-emit (6 – 32) % of the CO₂ uptake.

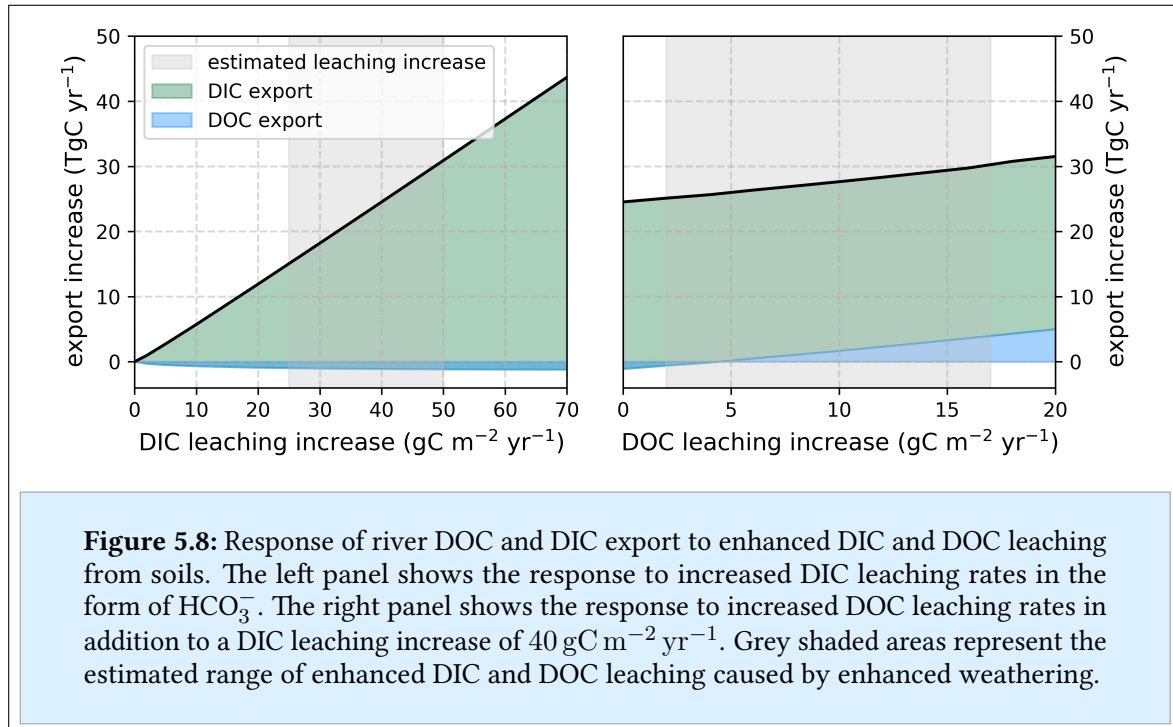
5.5.3. Response of river DOC and DIC discharge to enhanced weathering

The majority of riverine carbon that is not emitted to the atmosphere is discharged into the ocean. This carbon export in the form of DOC and DIC was derived via multiplication of modelled DOC and DIC concentrations in the individual rivers with their respective discharges. To derive the total carbon export from Sumatra's rivers into the ocean, the carbon export from individual rivers was weighted by river discharge and extrapolated to the surface area of Sumatra. The natural box-model run resulted in carbon export of 7.5 TgC yr⁻¹ in the form of DIC and 4.6 TgC yr⁻¹ in the form of DOC. These export rates are of the same order of magnitude as previous estimates for Sumatra stated by Wit et al. (2018).

To compare this carbon export to the CO₂ uptake by enhanced weathering, oceanic carbon yields (river carbon export per catchment area) of DOC and DIC were derived via equation (3.3). Natural carbon yields from the individual rivers range between 3 and 15 gC m⁻² yr⁻¹ for DIC and between 4 and 76 gC m⁻² yr⁻¹ for DOC. Average DIC and DOC yields from Sumatra result in 11.7 gC m⁻² yr⁻¹ and 6.9 gC m⁻² yr⁻¹, respectively (Table 5.3).

5. Response of tropical peat areas to enhanced weathering

Increased rates of DIC and DOC leaching from soils significantly increase the oceanic carbon export. For the DIC leaching increase estimated for enhanced weathering (Table 5.2), the oceanic DIC export from Sumatra's rivers increases by (16 – 32) TgC yr⁻¹ while the DOC export decreases by about 1 TgC yr⁻¹. For the combined increase in DIC and DOC leaching, the oceanic DIC export increases by (11 – 33) TgC yr⁻¹ and the oceanic DOC export changes by -1 to 4 TgC yr⁻¹ (Figure 5.8).



Enhanced weathering causes oceanic carbon yields to increase by (24 – 71) gC m⁻² yr⁻¹ in the form of DIC and by (-2 – 9) gC m⁻² yr⁻¹ in the form of DOC (Table 5.3). Accordingly, (22 – 80) gC m⁻² yr⁻¹ of the additionally leached carbon reach the ocean, while (2 – 16) gC m⁻² yr⁻¹ are emitted to the atmosphere. These enhanced yields from Sumatra's rivers do not add up with the increase in carbon leaching (Table 5.2). This is likely caused by the different ways of deriving average yields from Sumatra, as CO₂ yields were derived via weighing by catchment areas while DOC yields and DIC yields from Sumatra were derived via weighing by river discharge.

More than 70% of the carbon that is leached into rivers due to enhanced weathering reach the ocean in the form of DIC.

5. Response of tropical peat areas to enhanced weathering

	CO ₂ yield	DOC yield	DIC yield
natural	(8 – 22) gC m ⁻² yr ⁻¹	7 gC m ⁻² yr ⁻¹	12 gC m ⁻² yr ⁻¹
enhanced weathering induced increase	(2 – 16) gC m ⁻² yr ⁻¹	(-2 – 9) gC m ⁻² yr ⁻¹	(24 – 71) gC m ⁻² yr ⁻¹

Table 5.3: Natural river carbon yields from Sumatra and their response to the enhanced weathering induces increase in DIC and DOC leaching from soils (Table 5.2). Atmospheric CO₂ yields as well as oceanic DOC and DIC yields were calculated from CO₂, DOC and DIC concentrations derived via the river box-model according to equation (3.4) and the equations (3.3).

5.6. Response of coastal carbon emissions to enhanced weathering

Coastal carbon dynamics are impacted by enhanced weathering through the changed carbon export from rivers that was discussed in subsection 5.5.3. The impact of these changes on carbon emissions from the coast were derived via calculation of coastal water mixing. Subsection 5.6.1 explains the implemented mixing calculations and subsection 5.6.2 discusses the response of carbon emissions from Sumatra's estuaries and coastal oceans to enhanced weathering.

5.6.1. Description of coastal water mixing calculations

CO₂ concentrations in the river estuaries (≤ 3 km distance from shore) and in the coastal ocean (3 km – 67 km distance from shore, Figure 5.1) of Sumatra were estimated based on water mixing between river water and ocean water. Concentrations of carbon parameters in the river water were derived via the box-model and concentrations in the ocean water were assumed to be $\text{DIC}_{\text{ocean}} \approx 1,900 \mu\text{mol L}^{-1}$ and $\text{TA}_{\text{ocean}} \approx 2,200 \mu\text{mol L}^{-1}$ (Schlitzer, 2021). Additional assumptions for the calculations were that the total river alkalinity is given by the carbonate alkalinity ($\text{TA}_{\text{discharge}} = \text{CA}_{\text{river}}$) and that the whole DOC is oxidized to DIC when entering the estuaries ($\text{DIC}_{\text{discharge}} = \text{DIC}_{\text{river}} + \text{DOC}_{\text{river}}$).

The mixing ratios between river water and ocean water in estuaries and the coastal ocean were derived based on salinity. As salinity increases linearly with the amount of salt in a specific water volume, the river water fraction within estuaries and the coastal ocean can be estimated from average salinities in the respective regions. The estuarine area lies within the salinity range of approximately 0 to 25 (section 5.2). However, due to the uneven areal distribution of salinities in this estuarine region (Wit et al., 2018), average estuarine salinity is not equivalent to the mean value between the lower and upper salinity bounds.

The largest fraction of the estuarine area is located outside the river mouths with $S > 10$ and the increase in salinity per distance from shore weakens for greater distance from the river mouth (Wit et al., 2018). Therefore, an average estuarine salinity of $S_{\text{est}} \approx 20$ is used. For the coastal ocean, where the salinity increase with distance from shore is fairly constant (Wit et al., 2018), the mean salinity of $S_{\text{co}} \approx 28.9$ is used.

From known salinity of the ocean ($S_{\text{ocean}} \approx 32.8$, Schlitzer, 2021) and the rivers ($S_{\text{river}} \approx 0.001$, subsection 5.5.1) fractions of river water in estuaries (a_{est}) and in the coastal ocean (a_{co}) can be derived according to:

$$a_{\text{est}} = 1 - \frac{S_{\text{est}} - S_{\text{river}}}{S_{\text{ocean}} - S_{\text{river}}} \quad \text{and} \quad a_{\text{co}} = 1 - \frac{S_{\text{co}} - S_{\text{river}}}{S_{\text{ocean}} - S_{\text{river}}} \quad (5.3)$$

Based on those fractions, concentrations of DIC and TA in the estuaries and the coastal ocean were calculated to

$$\begin{aligned} \text{DIC}_{\text{est/co}} &= a_{\text{est/co}} \cdot \text{DIC}_{\text{river}} + (1 - a_{\text{est/co}}) \cdot \text{DIC}_{\text{ocean}} \\ \text{TA}_{\text{est/co}} &= a_{\text{est/co}} \cdot \text{TA}_{\text{river}} + (1 - a_{\text{est/co}}) \cdot \text{TA}_{\text{ocean}}. \end{aligned} \quad (5.4)$$

From these DIC and TA concentrations, estuarine and coastal CO_2 concentrations were derived. The CO2SYS program (Humphreys et al., 2020; Lewis and Wallace, 1998) was used for these coastal calculations of the carbonate system, as here the accurate calculations based on salinity are essential. For the earlier in-river box-model calculations (subsection 5.5.1), where high concentrations of organic acids impair the results of the CO2SYS program (Lyu et al., 2019), the equations explained in subsection 2.2.2 were used.

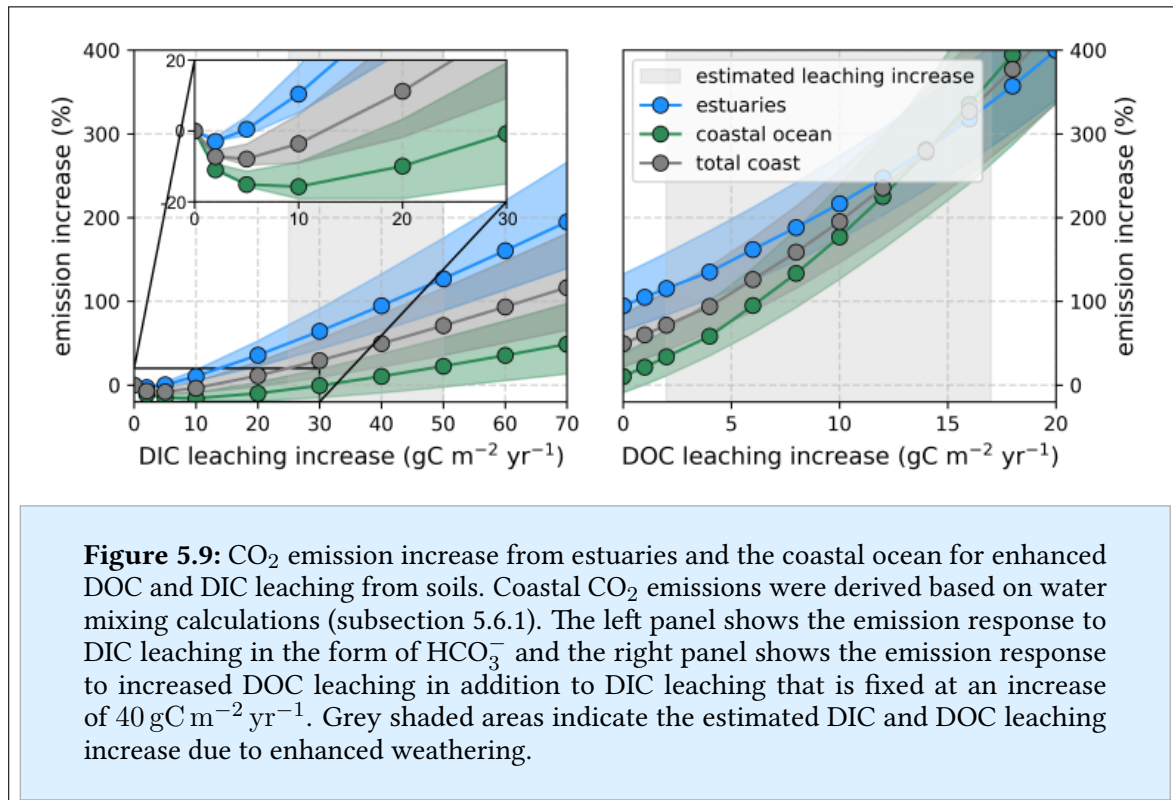
5.6.2. Response of coastal CO_2 emissions to enhanced weathering

Average natural CO_2 concentrations in Sumatra's estuaries and coastal ocean result in approximately $50 \mu\text{mol L}^{-1}$ and $15 \mu\text{mol L}^{-1}$, respectively. Atmospheric CO_2 emissions were derived via multiplication of the corresponding atmospheric CO_2 fluxes with the respective estuarine and coastal areas (Figure 5.1). Atmospheric fluxes were derived according to equation (2.5) with a coastal exchange coefficient of $k_{600} = 12 \text{ cm h}^{-1}$ (Wit et al., 2018). Emissions result in 11.6 TgC yr^{-1} , with 6.2 TgC yr^{-1} being emitted from the river estuaries and 5.4 TgC yr^{-1} from the coastal ocean.

CO_2 emissions from the coast initially decrease for enhanced soil DIC leaching (Figure 5.9). This is caused mainly by the accompanying increase in water pH that shifts the DIC towards carbonates and away from CO_2 (Figure 2.6) and thereby favors carbonate dissolution in

5. Response of tropical peat areas to enhanced weathering

the ocean. At higher rates of DIC leaching the increased carbon supply overcompensates the uptake by the ocean. River estuary emissions increase above natural emissions for a DIC leaching increase of $\geq 5 \text{ gC m}^{-2} \text{ yr}^{-1}$. Further from the shore, in the coastal ocean, emissions are below natural for a DIC leaching increase of up to $30 \text{ gC m}^{-2} \text{ yr}^{-1}$. Total coastal emissions exceed natural emissions for a leaching rate increase of $\geq 12 \text{ gC m}^{-2} \text{ yr}^{-1}$ (Figure 5.9).

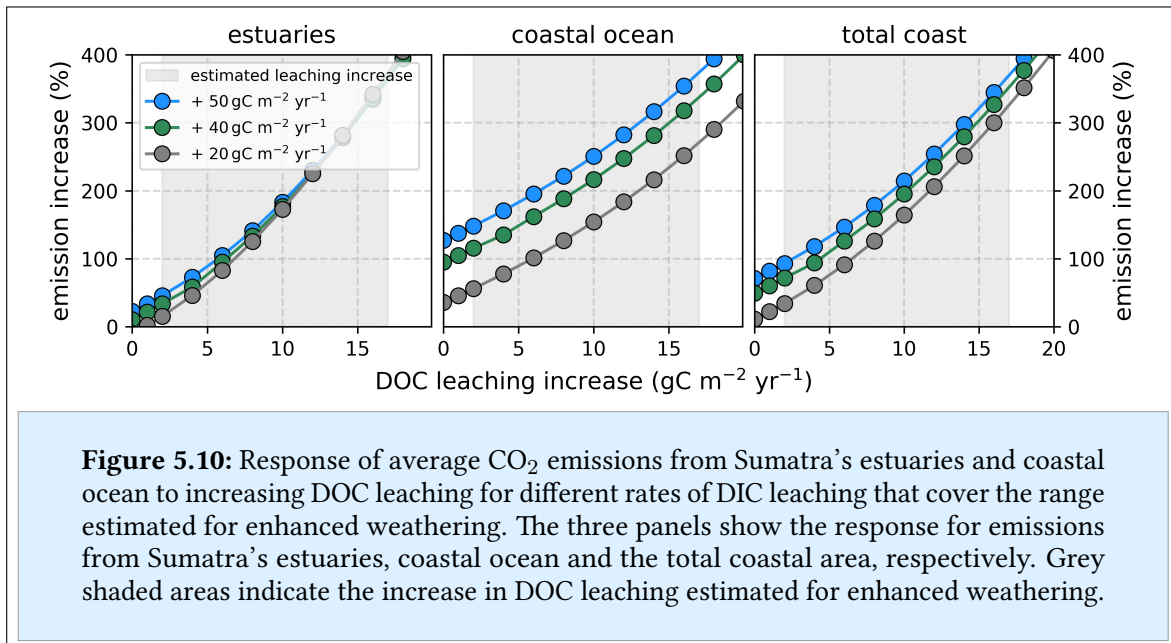


For the estimated enhanced weathering induced DIC leaching increase, total coastal emissions increase by (20 – 70) %, which corresponds to an absolute increase of (2.4 – 8.2) TgC yr⁻¹. (-0.3 – 1.4) TgC yr⁻¹ of these are emitted from the estuaries and (2.7 – 6.8) TgC yr⁻¹ are emitted from the coastal ocean. An increase in DOC leaching in addition to increased DIC leaching massively increases emissions from the estuaries and from the coastal ocean (Figure 5.9). Considering enhancement in DIC leaching of $40 \text{ gC m}^{-2} \text{ yr}^{-1}$ and the estimated increase in DOC leaching of (2 – 17) $\text{gC m}^{-2} \text{ yr}^{-1}$, total coastal CO₂ emissions increase by (70 – 380) % compared to natural emissions (Figure 5.9).

Variation of DIC leaching mainly effects coastal ocean emissions, while it shows no significant effect on estuary emissions (Figure 5.10). Considering the DIC and DOC leaching increase estimated for enhanced weathering (Table 5.2), the total coastal emissions in-

5. Response of tropical peat areas to enhanced weathering

crease by $(8 - 44) \text{ TgC yr}^{-1}$, of which $(2 - 25) \text{ TgC yr}^{-1}$ are emitted from the estuaries and $(6 - 19) \text{ TgC yr}^{-1}$ are emitted from the coastal ocean.



In order to compare the coastal emission increase to the CO₂ uptake by enhanced weathering, coastal CO₂ yields (emission increase per respective land area) were derived by division of absolute emissions with Sumatra's surface area (Table 5.4). The resulting fluxes indicate that at between 36 % and potentially more than 198 % of the CO₂ uptake by enhanced weathering could be re-emitted from coastal regions. However, it needs to be mentioned that the carbon loss through emissions from the estuaries was not considered when deriving emissions from the coastal ocean. While that impact might be negligible for the lower bound estimates, it likely causes overestimation in the upper bound of coastal ocean emissions.

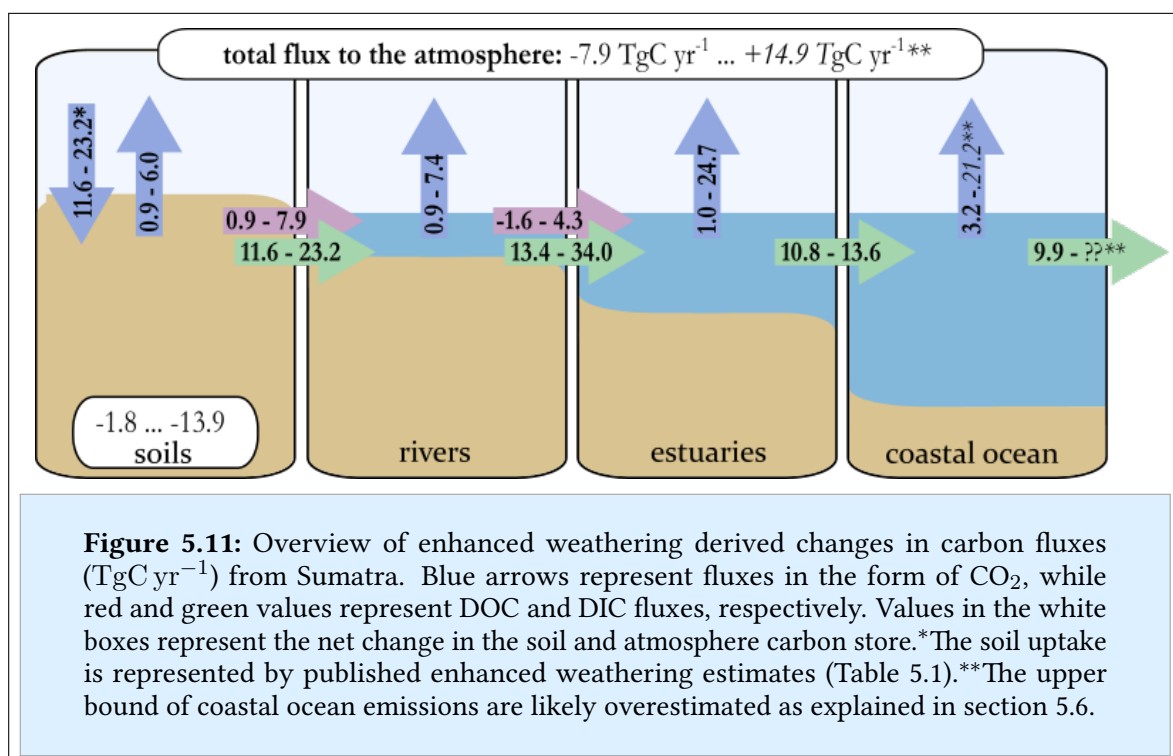
The feedback of coastal areas on enhanced weathering is extremely uncertain but could potentially cause re-emission of $(36 - 198) \%$ of the CO₂ uptake.

	estuary emissions	coastal ocean emissions	total coastal emissions
natural	6.2 TgC yr^{-1}	5.4 TgC yr^{-1}	11.6 TgC yr^{-1}
enhanced weathering induced increase	$(2 - 54) \text{ gC m}^{-2} \text{ yr}^{-1}$	$(11 - 45) \text{ gC m}^{-2} \text{ yr}^{-1}$	$(13 - 99) \text{ gC m}^{-2} \text{ yr}^{-1}$

Table 5.4: Natural carbon yields from Sumatra's coast and their response to increased DIC and DOC leaching from soils caused by enhanced weathering application (Table 5.2). CO₂ yields from estuaries and from the coastal ocean were calculated from CO₂ concentrations derived through water mixing described in subsection 5.6.1.

5.7. Sumatra's carbon emission response to enhanced weathering

This section summarizes the response of atmospheric carbon fluxes from Sumatra to enhanced weathering. Enhanced soil CO₂ emissions due to the enhanced weathering induced increase in soil pH amount to (0.9 – 6.0) TgC yr⁻¹ (Figure 5.11) which represents (8 – 26) % of the estimated enhanced weathering CO₂ uptake for Sumatra ((11.6 – 23.2) TgC yr⁻¹). Additionally, soil carbon is mobilized via enhanced DOC leaching from soils. This DOC leaching mobilizes (0.9 – 7.9) TgC yr⁻¹. Thus, the total carbon mobilisation from Sumatra's soils yields (1.8 – 13.9) TgC yr⁻¹ (Figure 5.11).



Captured CO₂ is assumed to be leached into rivers in the form of HCO₃⁻. This DIC leaching of (11.6 – 23.2) TgC yr⁻¹ in addition to the DOC leaching increase emissions from Sumatra's rivers, estuaries and coastal ocean by (0.9 – 7.4) TgC yr⁻¹, (1.0 – 24.7) TgC yr⁻¹ and (3.2 – 21.2) TgC yr⁻¹, respectively (Figure 5.11). With an enhanced weathering uptake of up to 23 TgC yr⁻¹, this implies that in a worst-case scenario the increase in carbon emissions due to feedback reactions on enhanced weathering application in peat regions could cause re-emission of (50 – 250) % of the CO₂ uptake by enhanced weathering. Since the CO₂ emission feedback strongly depends on the response of DOC leaching rates to enhanced weathering, more research into the response of those leaching rates to increased soil decomposition is

needed. Additionally, the estimates for coastal CO₂ emissions are based on simplified mixing calculations and need to be viewed with caution.

The response of CO₂ emissions from Sumatra to enhanced weathering could offset (50 – 250) % of the CO₂ uptake.

By exclusion of the highly uncertain emissions from estuaries and the coastal ocean, the response of CO₂ emissions from soils and rivers to enhanced weathering would reduce existing enhanced weathering CO₂ uptake estimates by (15 – 58) %. This would leave a net CO₂ uptake of roughly 21 gC m⁻² yr⁻¹. This indicates that enhanced weathering could potentially create a carbon sink over land areas that would decrease tracked CO₂ emissions from specific countries while creating a CO₂ source from coastal areas.

5.8. Conclusion

This chapter aimed to quantify the response of CO₂ emissions from tropical peat regions to application of enhanced weathering. Enhanced weathering is a CO₂ removal strategy that accelerates the CO₂ uptake by weathering via distribution of rock-powder over land. During weathering, the captured CO₂ is changed into HCO₃⁻. Enhanced HCO₃⁻ supply impacts the soil carbonate system and increases soil pH. It was estimated how enhanced weathering induced pH changes in tropical peat areas impact CO₂ emissions from peat soils, peat-draining rivers and the coast.

Results show that application of enhanced weathering on peat soils could cause enhanced soil decomposition such that soil CO₂ emissions increase by 12 to 81 gC m⁻² yr⁻¹. Those soil emissions alone could potentially be higher than the CO₂ uptake by enhanced weathering. However, the results are limited by data scarcity regarding the response of peat carbon mobilisation to changes in soil pH. Since no data was available for tropical peat, estimates in this chapter were derived based on published correlations by Kang et al. (2018) that are based on temperatures of 15 °C. Furthermore, it is possible that captured CO₂ is directly re-emitted from acidic peat soils. This process would lower the net CO₂ uptake by enhanced weathering as well as its impact on soil pH and the associated mechanisms discussed in this chapter.

A case study for enhanced weathering application on Sumatra was performed as representative for tropical peat regions. Soil emissions from Sumatra yielded an increase in CO₂ emissions of (2 – 13) gC m⁻² yr⁻¹, resulting in re-emission of (8 – 52) % of the CO₂ captured

5. Response of tropical peat areas to enhanced weathering

by enhanced weathering. The enhanced soil decomposition additionally increases leaching of DOC into peat-draining rivers.

In rivers, the enhanced carbonate supply is found to increase the *pH* and thereby shift the carbonate system away from CO₂. However, increased in-river decomposition overcompensates this CO₂ decrease. The overall feedback of river emissions on increased carbonate supply offsets 2 to 8 % of the CO₂ captured by enhanced weathering. The increased DOC supply additionally increases in-river decomposition, whereby rivers of high peat coverage show a weaker response due to O₂ depletion. The overall emission feedback of rivers on increased DIC and DOC leaching is found to offset (8–64) % of the CO₂ uptake by enhanced weathering.

Changes in the in-river carbon dynamics impact the oceanic carbon export and thereby influence CO₂ emissions from estuaries and the coastal ocean. The increased carbonate supply initially favours the CO₂ uptake by the ocean and causes decreased CO₂ emissions for enhanced DIC leaching of up to 20 gC m⁻² yr⁻¹. However, the additional increase in coastal emissions due to DOC leaching results to be more important. The results indicate that coastal emissions have the potential to completely compensate the CO₂ uptake by enhanced weathering. This strong dependence on DOC leaching shows the need for further studies on the impact of soil decomposition on leaching rates, which are highly uncertain.

Overall, CO₂ emissions from Sumatra's soils and rivers could reduce the net enhanced weathering CO₂ uptake by (15 – 58) %. The inclusion of CO₂ emissions from Sumatra's coast increases the estimated re-emission to at least 50 % with potentially more than 150 % of the estimated CO₂ uptake. These results show that the regional feedback in tropical peat areas has the potential to offset the CO₂ uptake by enhanced weathering. This suggests that tropical peat areas should be excluded from enhanced weathering application.

6. Towards validation of wetland CH₄ emissions

This chapter aims to evaluate CH₄ fluxes from wetland models by the use of atmospheric modelling and satellite comparisons. Initially, a full evaluation of the methane emission datasets listed in subsection 3.3.2 was planned. However, the discovery of unexpectedly high nudging fluxes shifted the study objective as will be further explained within this chapter.

Section 6.1 introduces the research topic and objective. Section 6.2 provides a description of the selected study regions. Section 6.3 illustrates results from a test study that was performed to check the study's feasibility. Section 6.4 visualizes and compares the different CH₄ emission datasets included in this study. Section 6.5 presents the results of model runs including nudging fluxes and the correlation of resulting CH₄ concentrations to satellite data. Section 6.6 illustrates results derived from model runs without nudging and provides a comparison between the model CH₄ budget and budgets published in literature. Finally, section 6.7 summarizes the findings within this chapter.

6.1. Background and objective

Wetlands are the largest natural source of atmospheric CH₄ (Saunois et al., 2020). They contribute about one-third of global CH₄ emissions (Kirschke et al., 2013) and dominate the inter-annual variability of global CH₄ concentrations (Bousquet et al., 2006). Yet, there are high uncertainties in estimates of wetland CH₄ emissions and their response to a changing climate (Kirschke et al., 2013).

In a recent study by the Global Carbon Project (GCP), a variety of CH₄ emission data products were compiled to understand and quantify the global CH₄ budget (Saunois et al., 2020). That study revealed strong discrepancies between process-based (bottom-up) emission estimates and those derived from atmospheric inversions (top-down, Table 6.1). Saunois et al. (2020) highlight that the most important source of uncertainty in their budget is attributable to natural emissions, especially those from wetlands and inland waters.

Bottom-up estimates of the wetland emissions stated by Saunois et al. (2020) were determined from data derived by the thirteen land surface models listed in Table 3.2. In the following, wetland CH₄ emission estimates from these thirteen land surface models will be analysed. The initial aim of this study was to evaluate these data for major tropical wetland regions by use of the TM5-MP atmospheric chemistry and transport model described in section 3.3 and the satellite retrievals described in section 3.4. Forward simulations of atmospheric CH₄ were derived based on the individual wetland emission datasets. From the resulting atmospheric

6. Towards validation of wetland CH₄ emissions

CH₄ concentrations, column-averaged dry-air mole fractions of CH₄ (XCH₄) were derived and compared to satellite retrievals.

(TgC yr ⁻¹)	agriculture & waste	fossil fuel & BMB	wetlands	other natural emissions	total sinks	atmospheric burden
bottom-up	206 (191 – 223)	158 (139 – 194)	149 (102 – 182)	222 (143 – 306)	625 (500 – 798)	112 (94 – 118)
top-down	217 (207 – 240)	141 (103 – 167)	181 (159 – 200)	37 (21 – 50)	556 (501 – 574)	13 (0 – 49)

Table 6.1: Global CH₄ budget as published by the GCP (Saunois et al., 2020). Emission estimates for the individual sectors are based on process-based studies (bottom-up) and atmospheric inversions (top-down)

However, the TM5-MP model adds additional CH₄ fluxes (nudging fluxes) to reproduce realistic atmospheric CH₄ concentrations. Those fluxes impact the modelled CH₄ concentrations and complicate the interpretation of inter-annual variations. Thus, the aim of this study shifted to an assessment of the impact that those nudging fluxes have on the retrieved concentrations and an evaluation of the internal model CH₄ budget to investigate why those nudging fluxes are needed.

6.2. Study Area

The five wetland regions that have been selected for this study are the Amazon, Pantanal, Congo, Ganges and Southeast Asian regions (Figure 6.1).

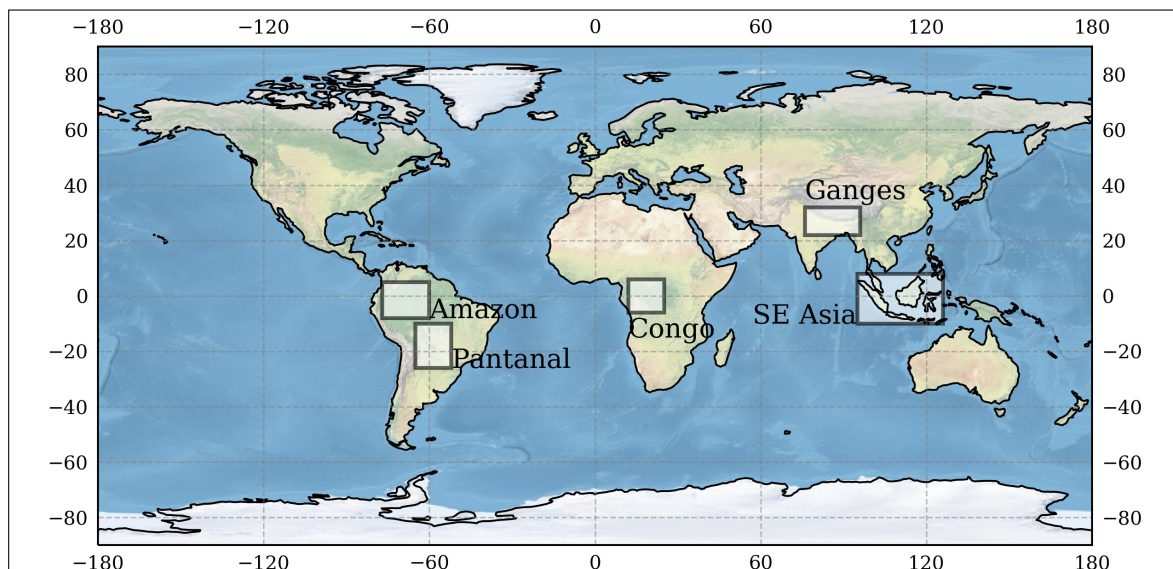


Figure 6.1: Map of the selected tropical wetland regions.

These regions represent tropical wetland CH₄ emission hotspots. They all contain significant wetland fractions and are at least partially located within the tropics (23°S to 23°N, Table 6.2).

Region	Description
Amazon 8°S - 5°N 77°W - 60°W	The Amazon region contains the western part of the Amazon Basin that includes the world's largest tropical forest. Wetlands cover more than 800,000 km ² of the Amazon catchment (Hess et al., 2015).
Congo 6°S - 6°N 12°E - 25°E	The Congo region contains the Congo Basin that includes the world's second largest tropical forest. Almost one-third (360,000 km ²) of the Congo catchment is covered by wetlands (Bwangoy et al., 2010).
SE Asia 10°S - 8°N 95°E - 126°E	The Southeast Asian region includes the Malaysian Peninsula, Borneo, Sumatra, Java and Sulawesi. Southeast Asia contains large areas of peat soils in the forms of undisturbed peat swamp forest as well as disturbed peat under plantations.
Ganges 22°N - 30°N 76°E - 96°E	The Ganges region includes the whole Ganges-Brahmaputra Basin. The majority of wetlands in this region are located close to the Ganges-Brahmaputra-Meghna Delta in Bangladesh that contains almost 80,000 km ² of wetlands (Islam, 2016).
Pantanal 21°S - 10°S 70°W - 52°W	The Pantanal region includes the most southern part of the Amazon Basin with the Mamore floodplain in addition to the Pantanal wetland. The Pantanal is the largest South American savannah floodplain, with a total area of 138,183 km ² (Bastviken et al., 2010)

Table 6.2: Description and location of selected wetland regions

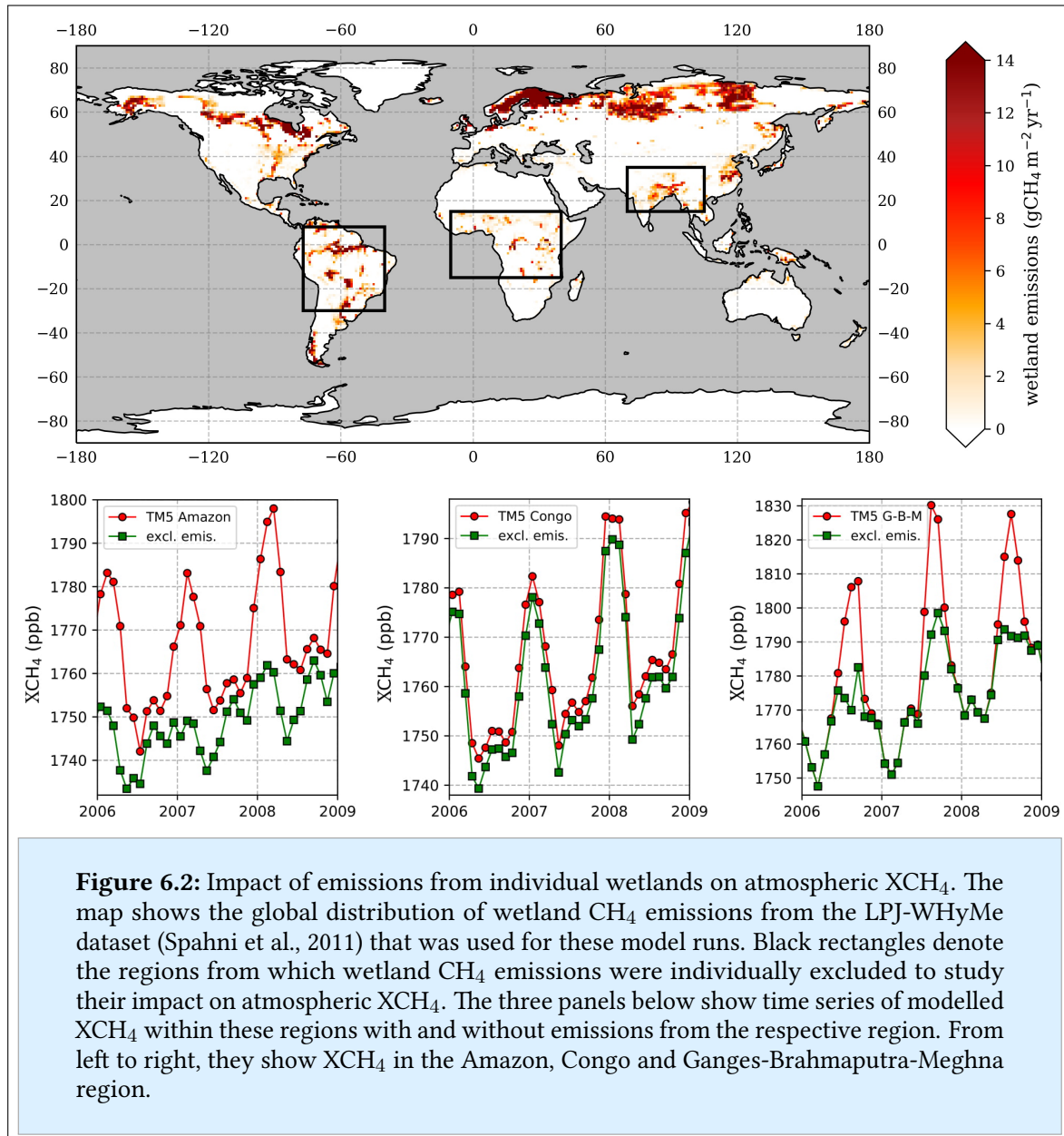
6.3. Impact of individual wetlands on regional atmospheric XCH₄

In order to determine whether the CH₄ emissions from individual wetlands result in regional variations of XCH₄ that can be detected by satellite, test model runs were performed. After a 7-year spin-up, the TM5-MP model was run for the years 2006 to 2009 with the model's internal wetland CH₄ emissions from the LPJ-WHyMe dataset (Spahni et al., 2011). Three additional runs were performed, where wetland emissions from specific regions were excluded. Comparatively large regions with huge wetland extent were chosen for this experiment: 1) South American wetlands including the Amazon and Pantanal region, 2) African wetlands including the Congo and Lake Victoria regions and 3) Asian wetlands in the region of the Ganges-Brahmaputra-Meghna Delta (Figure 6.2).

Average emissions from the three regions are approximately 42 TgCH₄ yr⁻¹ from the South American region, 40 TgCH₄ yr⁻¹ from the African region and 16 TgCH₄ yr⁻¹ from the Asian region. The strongest response to the removal of wetland emissions is visible in the Amazon region, where XCH₄ generally decreases and the seasonal XCH₄ amplitude is reduced by approximately 20 ppb (\approx 50 %, Figure 6.2). Removal of wetland emissions from the Congo region results in much weaker changes of atmospheric XCH₄ (\approx 5 ppb) with no impact on

6. Towards validation of wetland CH₄ emissions

the seasonality (Figure 6.2). In the Ganges region, the emission removal results in a decrease in the seasonal XCH₄ maxima of approximately 30 ppb ($\approx 50\%$), while it shows no impact on the XCH₄ minima (Figure 6.2).



The random error of single satellite retrievals in the EMMA product is ≈ 14 ppb with a regional bias to ground-based retrievals at sites of the Total Carbon Column Observing Network (TCCON) of ≈ 4 ppb (Reuter et al., 2020). Thus, the observed changes in seasonal XCH₄ for exclusion of regional wetlands of up to 30 ppb indicate that regional wetland emissions represent an observable fraction of the atmospheric XCH₄. However, the atmospheric XCH₄

response shown in Figure 6.2 is likely an underestimation due to the impact of nudging fluxes in the model. This will be further discussed in section 6.5.

CH₄ emissions from individual wetlands impact the regional XCH₄ concentrations and variations to a degree that is observable by satellite.

6.4. Differences between the wetland emissions datasets

In this section, the spatial distribution and absolute emissions stated in the different wetland CH₄ emission datasets (Table 3.2) are compared. Subsection 6.4.1 focuses on emissions from the diagnostic datasets that were derived based on uniform wetland extent and meteorology. Subsection 6.4.2 discusses emissions from the prognostic datasets derived from wetland extent and meteorology individually chosen by the different models.

6.4.1. Diagnostic wetland CH₄ emission datasets

As described in subsection 3.3.2, diagnostic datasets were derived using wetland extent and meteorology from WAD2M (Zhang et al., 2021). Global wetland CH₄ emissions in the thirteen diagnostic datasets range from 102 TgCH₄ yr⁻¹ in the TRIPLEX-GHG dataset to 180 TgCH₄ yr⁻¹ in the JULES dataset with an average of 148 TgCH₄ yr⁻¹ (Table 6.3). The global emission distribution shows high emissions from the wetland regions selected for this study (Figure 6.3). In general, emissions from tropical regions are high due to anaerobic decomposition in carbon rich tropical wetlands that is promoted by the warm tropical climate.

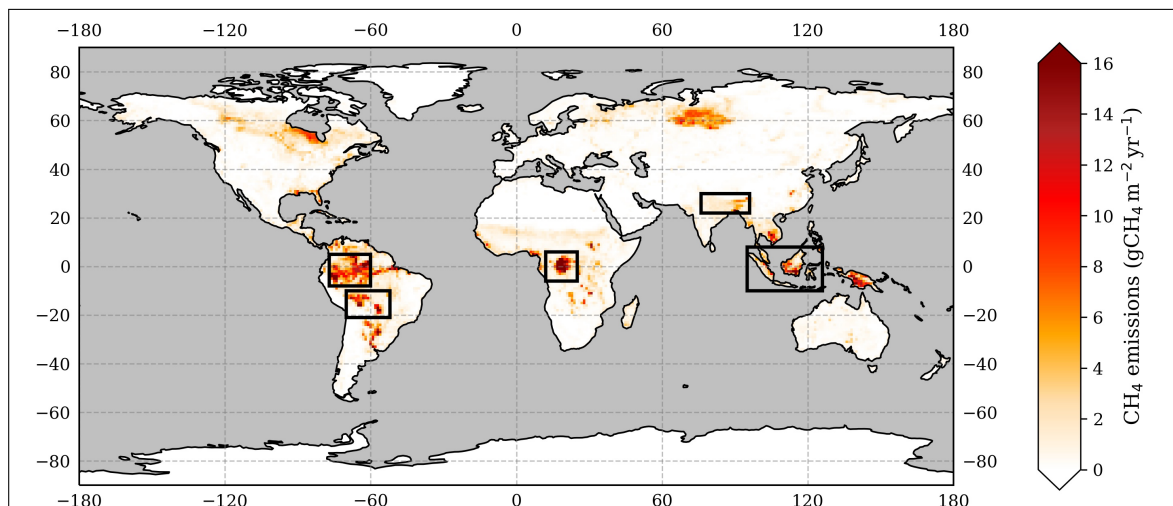
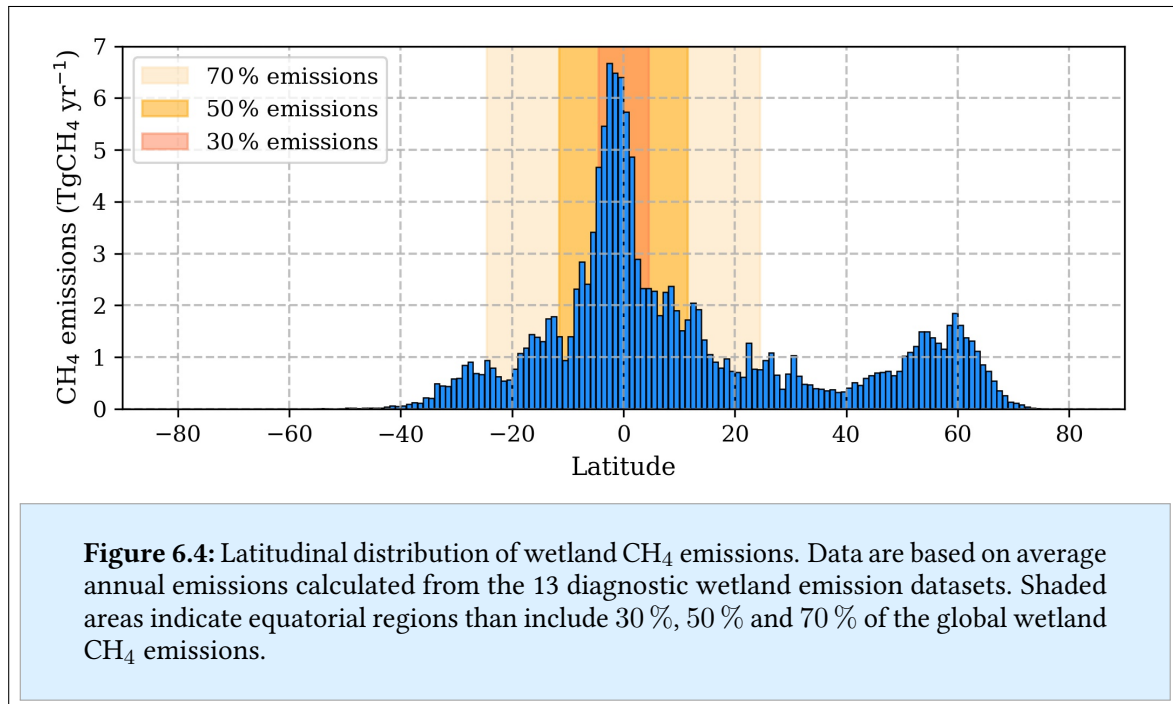


Figure 6.3: Global map of wetland CH₄ emissions. Data represent the average of the thirteen diagnostic wetland emission datasets. Black rectangles illustrate the wetland regions that were selected for this study. Emission maps for the individual datasets are shown in the appendix in Figure A.7.

6. Towards validation of wetland CH₄ emissions

The majority of wetland CH₄ emissions occur in tropical regions with 30 % being emitted between 5°S and 5°N and 50 % being emitted between 12°S and 12°N (Figure 6.4). Three-quarters of global wetland CH₄ emissions are emitted within the 30° latitude bands and northern high latitude peat soils between 50°N and 70°N emit more than half of the remaining emissions (Figure 6.4).



Flux estimates for the individual study regions vary strongly (Figure 6.5). The highest fluxes are estimated for the Amazon and Congo regions. For the Amazon region, CH₄ emission estimates range from 2.6 gCH₄ m⁻² yr⁻¹ to 12.2 gCH₄ m⁻² yr⁻¹. For the Congo region, fluxes range from 2.0 gCH₄ m⁻² yr⁻¹ to 13.9 gCH₄ m⁻² yr⁻¹ (Figure 6.5).

emissions (TgCH ₄ yr ⁻¹)	Amazon	Congo	SE Asia	Ganges	Pantanal	Global
mean	16.8	10.1	11.4	2.9	6.2	148.1
median	16.9	9.9	10.3	2.5	6.2	148.4
standard deviation	7.4	5.2	5.4	1.9	2.1	23.0

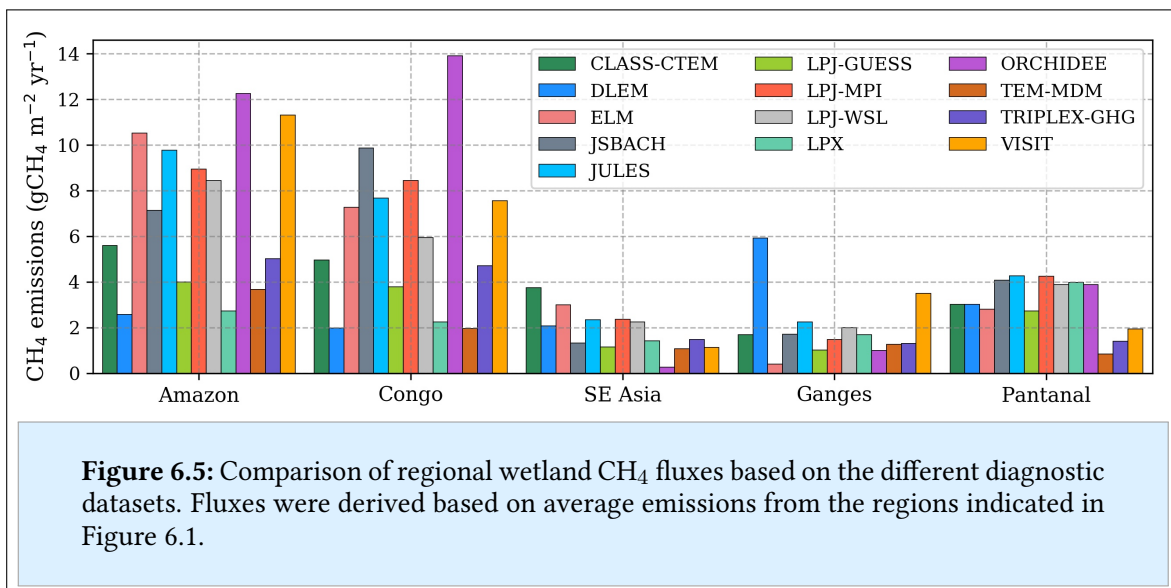
Table 6.3: Average regional emissions from selected wetland regions as well as global average emissions. Mean and median emissions as well as standard deviation based on annual emissions from the 13 diagnostic datasets. Emissions from the individual datasets are listed in the appendix in Table A.9

Though CH₄ emissions from Southeast Asia are also high, the modelled fluxes of (0.3 – 3.0) gCH₄ m⁻² yr⁻¹ are significantly lower than those for the other two equatorial wetland

regions (Figure 6.5). This is caused by the fact that a large fraction of the Southeast Asian grid box is covered by ocean. Fluxes derived from the Pantanal and Ganges regions are $(0.9 - 4.3) \text{ gCH}_4 \text{ m}^{-2} \text{ yr}^{-1}$ and $(0.4 - 3.5) \text{ gCH}_4 \text{ m}^{-2} \text{ yr}^{-1}$, respectively.

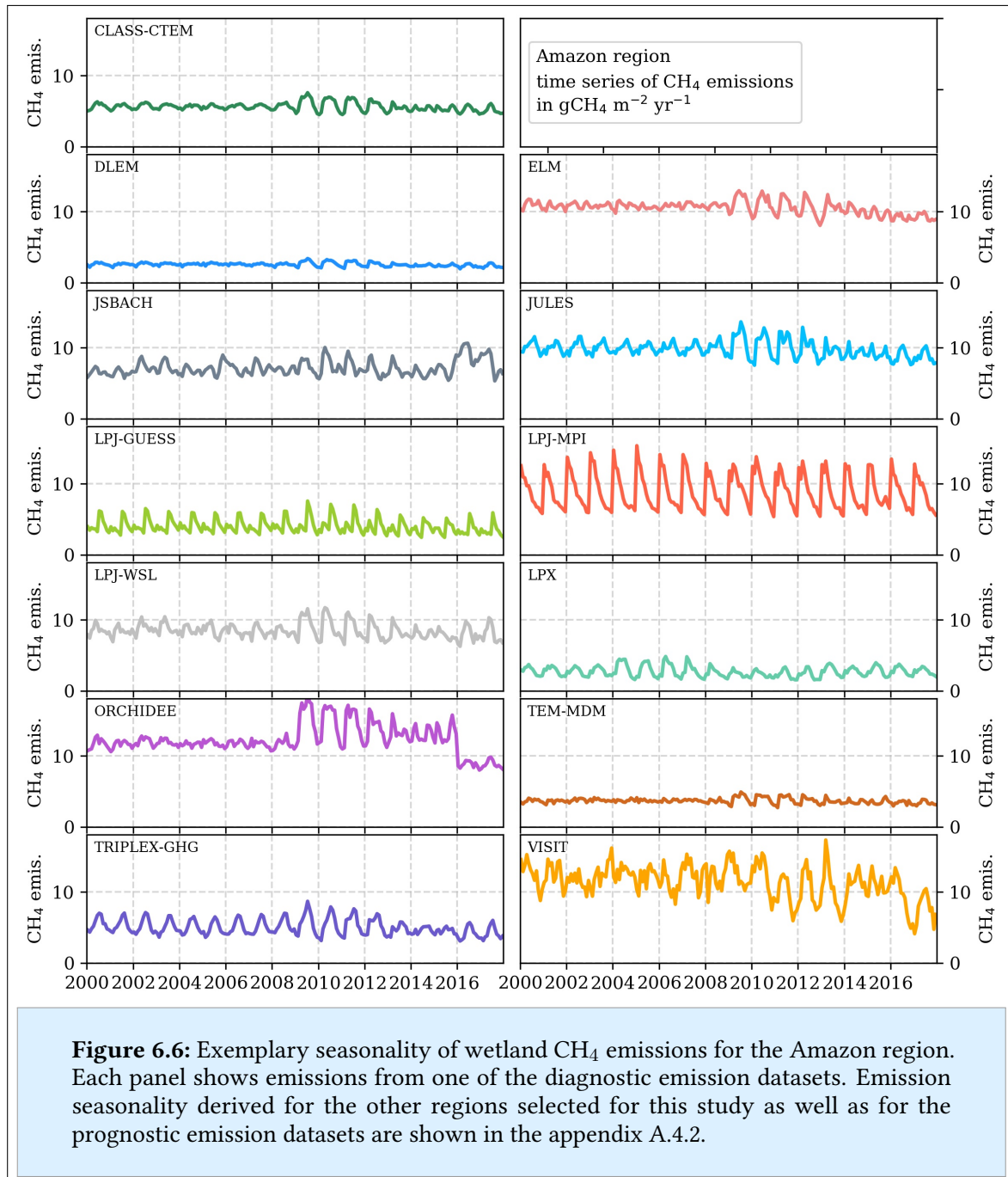
Regional wetland CH₄ fluxes from the diagnostic datasets differ by a factor of up to 15.

The datasets additionally show strong differences in the seasonality of regional CH₄ fluxes. For example in the Amazon region, the LPJ-MPI dataset shows a strong emission seasonality with an amplitude of approximately $5 \text{ TgCH}_4 \text{ m}^{-2} \text{ yr}^{-1}$. The DLEM and TEM-MDM datasets, in contrast, barely show any seasonality at all (Figure 6.6). Some, but not all, of the datasets show an increase in the seasonal emission amplitude for the years 2009 and 2013. Regional emission seasonality for the other selected wetland regions are shown in the appendix A.4.2.



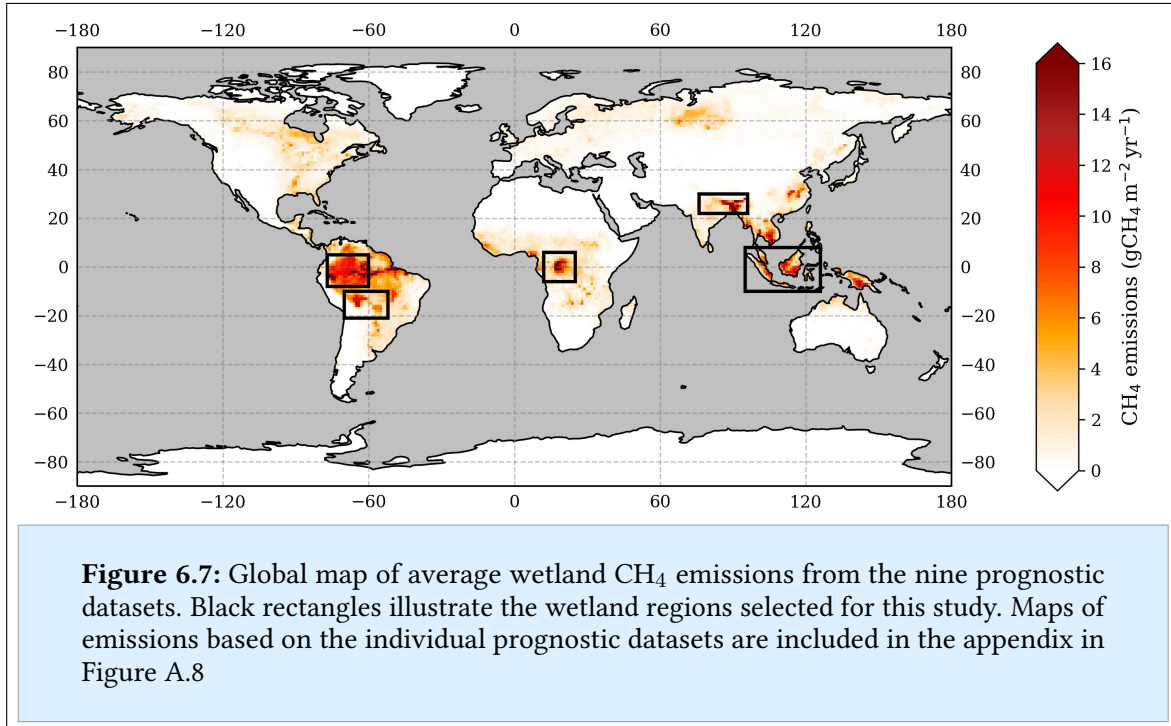
Total wetland CH₄ emissions for the selected wetland regions were derived from the fluxes in Figure 6.5 and the respective extent of the region's gridbox (Figure 6.1). The highest emissions come from the Amazon region, followed by the Congo and Southeast Asian regions (Table 6.3). The Pantanal and Ganges regions show significantly lower emissions than the equatorial regions (Table 6.3). Obviously, the average fluxes as well as total emissions from the selected regions strongly depend on the grid box extent that was chosen to represent these wetlands.

6. Towards validation of wetland CH₄ emissions

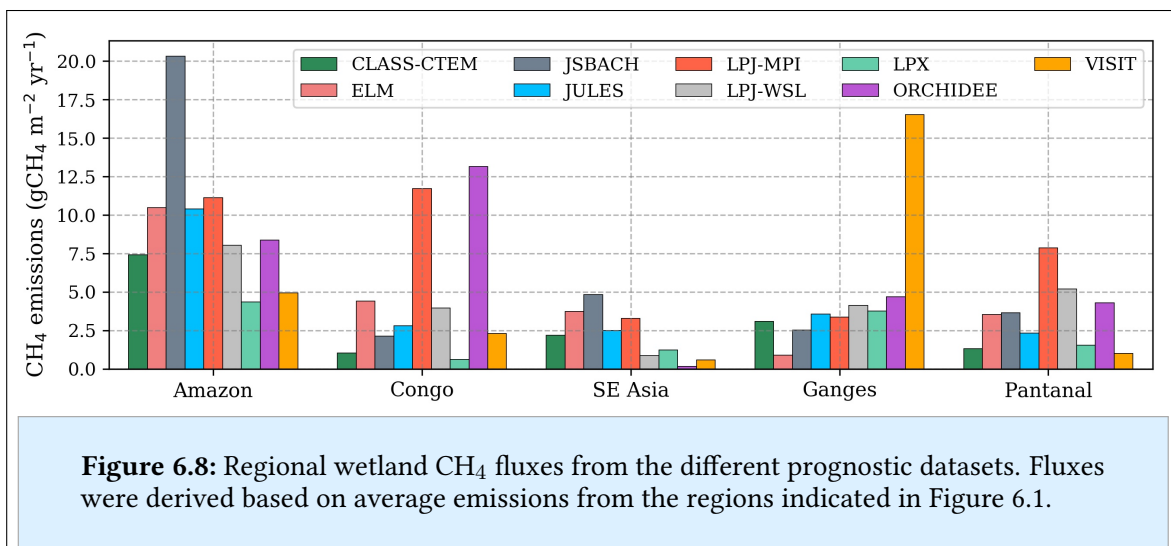


6.4.2. Prognostic wetland CH₄ emission datasets

Prognostic emission data were provided by nine of the thirteen wetland models. They were derived based on wetland extent and meteorology data individually chosen for the different models. The overall global emission patterns from these prognostic datasets (Figure 6.7) are similar to those derived from the diagnostic datasets (Figure 6.3). Yet, differences between the individual prognostic datasets are more pronounced than those between the diagnostic datasets.



Emission maps for the individual datasets are shown in the appendix in Figure A.8. Total emissions from the prognostic datasets range between 124 TgCH₄ yr⁻¹ in the LPJ-WSL dataset and 316 TgCH₄ yr⁻¹ in the LPJ-MPI dataset with average emissions of 185 TgCH₄ yr⁻¹. These are higher than those derived from the diagnostic datasets. Regional prognostic emission estimates differ more than the diagnostic datasets (Figure 6.8).



The strongest difference in estimated regional fluxes was found for the Congo region, where the highest emission estimate, stated by the ORCHIDEE dataset (13.2 gCH₄ m⁻² yr⁻¹), is more than 20 times higher than the lowest emission estimate, stated by the LPX dataset

(0.6 gCH₄ m⁻² yr⁻¹). Total regional emissions from the prognostic datasets for the studied regions can be found in the appendix in Table A.10.

Emission estimates without preset wetland extent state higher CH₄ emissions and show higher variability between the regional fluxes.

6.5. Modelled CH₄ concentrations and nudging fluxes

In this section, CH₄ concentrations modelled based on the individual diagnostic wetland CH₄ emission datasets discussed in subsection 6.4.1 are compared to satellite XCH₄ retrievals. The initial objective of this model study was to evaluate the emission datasets through this comparison. However, evaluation of the modelled data revealed an unexpectedly high impact of internal model nudging calculations.

Subsection 6.5.1 explains the nudging calculations and shows the resulting nudging fluxes for the performed model runs. The impact of those nudging fluxes on the modelled XCH₄ variations and correlations to satellite data will be further examined in a follow-up study. However, subsection 6.5.2 and subsection 6.5.3 show preliminary results for the correlations of modelled XCH₄ concentrations and of de-trended annual XCH₄ variations to satellite data, respectively. As an example, these correlations will be shown for the Amazon region, while data for the other regions can be found in the appendix A.4.3.

6.5.1. Modelled nudging emissions

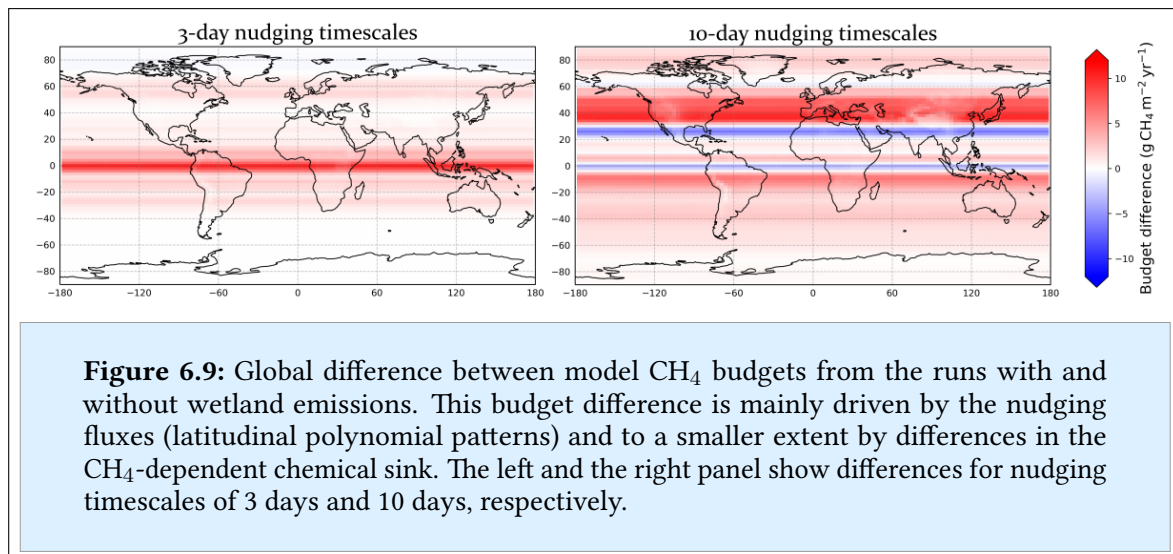
The surface nudging term in the TM5-MP model introduces additional fluxes that nudge the modelled CH₄ concentrations towards a reference field of surface CH₄ observations. It was included to the TM5-MP model as described by Williams et al. (2013) in order to account for uncertainties in CH₄ sources and sinks and to better constrain surface CH₄ concentrations and variations (Bândă et al., 2016). This nudging term creates seasonally dependent emissions based on the gradient between modelled CH₄ concentrations and reference concentrations stated in the Coupled Model Intercomparison Project Phase 6 database (CMIP6; Eyring et al., 2016). The emissions are calculated as a latitudinal polynomial but are not allowed to vary along the longitudes (Figure 6.9).

For the model runs presented in this study, nudging calculations were performed based on a 10-day time scale. This time scale was chosen based on results from Bândă et al. (2016) that indicate this time scale to be appropriate to derive monthly variations representative of regional monthly emission signals. Bândă et al. (2016) state that compared to 3-day nudging

time scales, similar global nudging fluxes were found while local nudging was 2 to 3 times smaller. Thus, the impact of nudging fluxes on regional XCH₄ is weaker for 10-day nudging time scales than for 3-day nudging time scales.

Nudging calculations introduce additional CH₄ fluxes to the model that depend on the modelled concentrations and differ between model runs.

Comparison runs on a 3-day nudging time scale were performed to compare the impact of nudging calculations for the two time scales. Resulting nudging fluxes for the 3-day time scale are predominantly located at the equator, while nudging fluxes calculated on the 10-day time scale are more spread out and dominate in higher latitudes (Figure 6.9). This supports the results by Bândă et al. (2016) that the local seasonal impact of nudging fluxes is less dominant for the calculations on 10-day time scales. Yet, the overall nudging emissions for both time scales are in the same order of magnitude.



6.5.2. Correlation of modelled XCH₄ with satellite data

In order to evaluate the individual wetland emission datasets, modelled XCH₄ for specific wetland regions was compared to data derived via satellite measurements. For each wetland CH₄ emission dataset (Table 3.2), a model run for the years 2000-2018 was performed. Atmospheric composition in 2000 was set to results from test runs using the LPJ-WHyMe wetland emissions. To allow for a solid comparison between the model results and satellite data, the models were sampled at the same time and location as the satellite observations and the measurement-specific averaging kernels were applied.

6. Towards validation of wetland CH₄ emissions

This section focuses on data derived for the Amazon region. Modelled data for other regions can be found in the appendix A.4.3. In the Amazon region, modelled concentrations based on all emission datasets were able to reproduce the atmospheric XCH₄ fairly well (Figure 6.10).

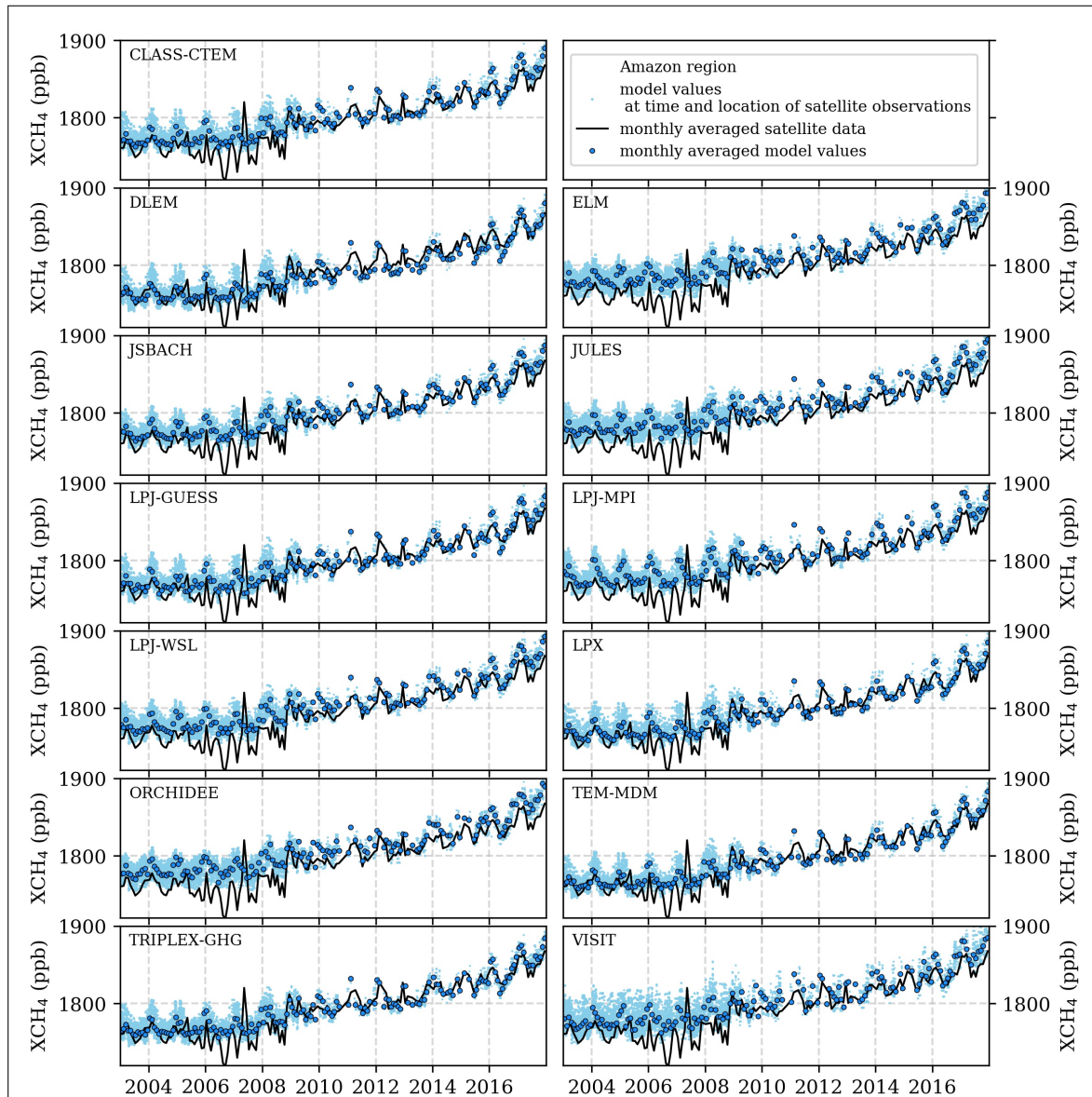


Figure 6.10: Time series of modelled and measured XCH₄ in the Amazon region. Black data represent the median of monthly satellite XCH₄ observations. Each panel shows correlation to one of the derived model runs, whereby each run is based on one of the diagnostic wetland CH₄ emission datasets. Model values at specific time and location of the satellite observation as well as the median monthly concentrations from the runs are shown. Correlation coefficients derived for the individual datasets are listed in Table A.11.

Correlation coefficients between modelled and measured monthly median XCH₄ range between 0.82 and 0.85 and root mean square errors are between 14 ppb and 23 ppb (Table 6.4). The best correlation of monthly median values in the Amazon region is resulting from the model run based on the JSBACH dataset (Table 6.4).

	CLASS-CTEM	DLEM	ELM	JS-BACH	JULES	LPJ-GUESS	LPJ-MPI	LPJ-WSL	LPX	ORCH-IDEE	TEM-MDM	TRIP-LEX	VISIT
R²	0.842	0.837	0.844	0.853	0.835	0.824	0.825	0.850	0.842	0.844	0.846	0.846	0.843
RMSE	16.6	13.8	22.6	17.2	23.3	16.0	20.9	19.6	14.9	22.3	13.9	14.2	19.4

Table 6.4: Correlation coefficients R^2 and root mean square errors (RMSE in ppb) derived for the correlation of satellite XCH₄ observations with modelled concentrations based on the diagnostic wetland emission datasets.

However, this good correlation with satellite observations is likely caused by the nudging fluxes that regulate modelled CH₄ concentrations based on reference data. Thus, it is more meaningful to investigate the interannual variation of XCH₄, which is mainly driven by wetland emissions (Bousquet et al., 2006) and for a 10-day nudging time scale is assumed to yield data representative for the individual emission datasets (Bândă et al., 2016).

6.5.3. Correlation of de-trended annual XCH₄ variations to satellite data

To derive correlations between the inter-annual variation in modelled XCH₄ and satellite observation of XCH₄, the data shown in Figure 6.10 were de-trended via subtraction of a rolling annual mean. The resulting XCH₄ seasonality for all wetland emission datasets shows an unexpectedly good agreement with satellite observations (Figure 6.11). It is surprising that despite large differences in the seasonality of wetland CH₄ emissions between the different datasets (Figure 6.6), modelled seasonal XCH₄ variations differ by only a few ppb (Figure 6.11). This is especially striking due to the fact that the test model run with exclusion of wetlands in the Amazon region indicated that approximately 50 % of the observed XCH₄ variation is caused by wetland emissions (section 6.3). The lack of difference between the seasonal variations in XCH₄ modelled based on differing wetland emissions indicates significant corrections in the seasonality via nudging fluxes.

For correlations between the modelled and the measured XCH₄ seasonality, data derived between November 2005 and April 2009 were excluded. This exclusion was performed due to proceeding detector degradation in the spectral range used for the methane column retrieval in the SCIAMACHY instrument (Schneising et al., 2011). This detector degradation lowered the number of available detector pixels and caused larger scatter in retrieved data. Since data

6. Towards validation of wetland CH₄ emissions

in tropical regions tend to be scarce due to cloud cover over the inter tropical convergence zone (Buchwitz et al., 2005), this enlarged scatter does impact the derived median data for the investigated regions. Thus, it was decided to exclude the impacted data from the correlation. Time series from April 2009 onwards, when the GOSAT satellite retrievals provided additional data, are again included to the correlation.

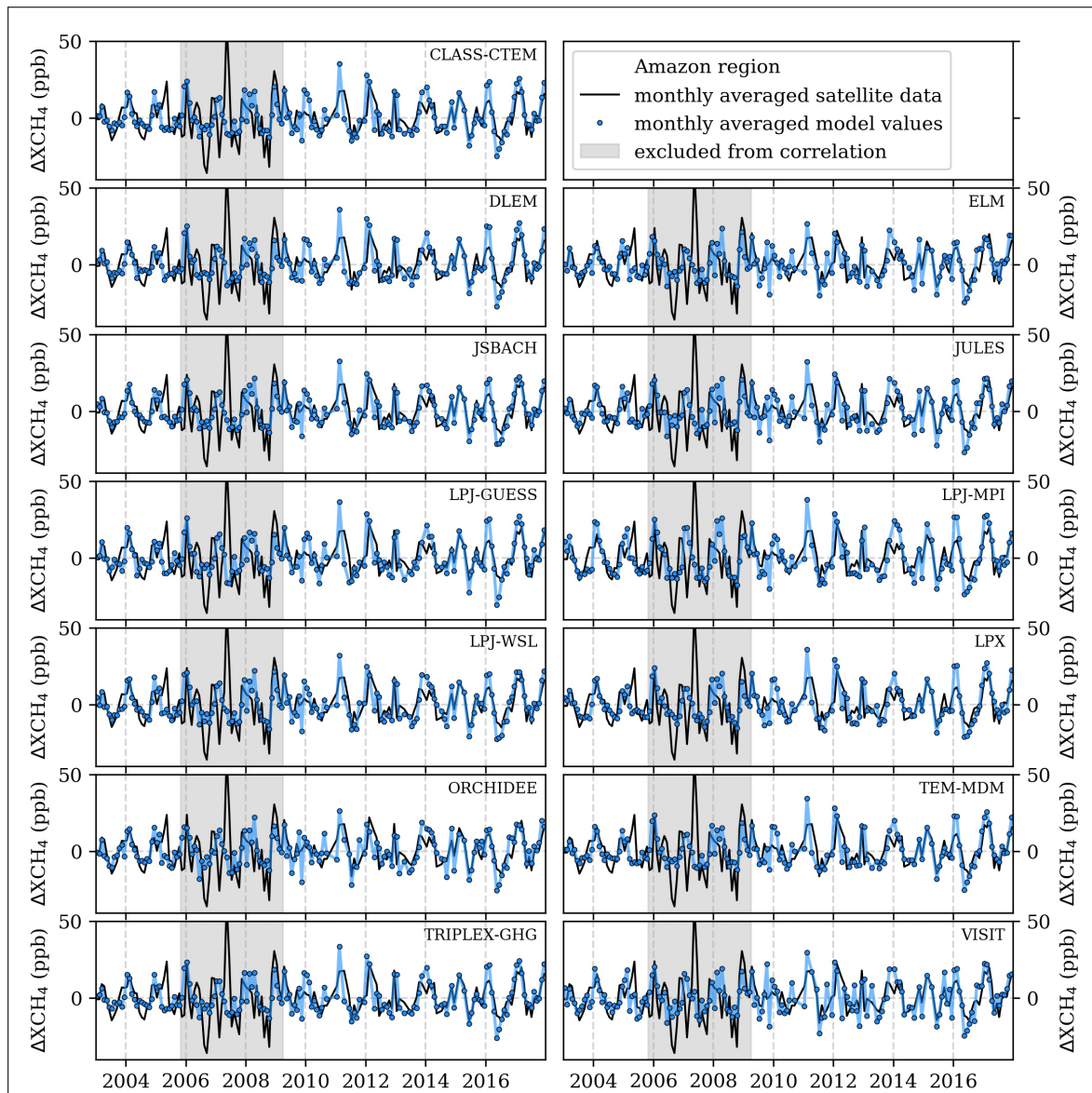


Figure 6.11: Time series of de-trended XCH₄ seasonality in the Amazon region. Black data represent monthly median XCH₄ variation derived via satellite and blue data represent the modelled XCH₄ variation. Panels show the resulting data from model runs including the different diagnostic wetland emission datasets. The grey shaded area indicates months excluded from performed data correlations.

The best correlation in the de-trended data, like for the absolute XCH₄ correlation (subsection 6.5.2), was achieved by the model run using the JSBACH wetland emission dataset. For these emission data, the correlation of de-trended XCH₄ yielded a correlation coefficient of $R^2 = 0.53$ and a root mean square error of 7.4 ppb. Correlation of the de-trended data generally result in weaker correlation coefficients than correlation of the absolute XCH₄ since the considered concentration range is much smaller and outliers create large errors.

XCH₄ seasonalities modelled from differing wetland emission datasets show little differences despite strong discrepancies between emission seasonalities.

It needs to be mentioned again that the significance of the results shown in this section needs further evaluation, as nudging calculations impact the seasonality as well as absolute concentrations.

	CLASS-CTEM	DLEM	ELM	JS-BACH	JULES	LPJ-GUESS	LPJ-MPI	LPJ-WSL	LPX	ORCH-IDEE	TEM-MDM	TRIP-LEX	VISIT
R^2	0.444	0.432	0.442	0.522	0.434	0.394	0.504	0.508	0.467	0.463	0.440	0.414	0.411
RMSE	8.4	8.5	8.0	7.4	8.5	9.1	9.1	7.8	8.4	7.7	8.2	8.3	8.9

Table 6.5: Correlation coefficients R^2 and root mean square errors (RMSE in ppb) derived for the correlation of satellite de-trended annual XCH₄ variation with modelled data based on the diagnostic wetland emission datasets. Data derived between November 2005 and April 2009 were excluded from these correlations due to detector degradation in the SCIAMACHY instrument.

6.5.4. Impact of wetlands on modelled XCH₄ for model runs including nudging

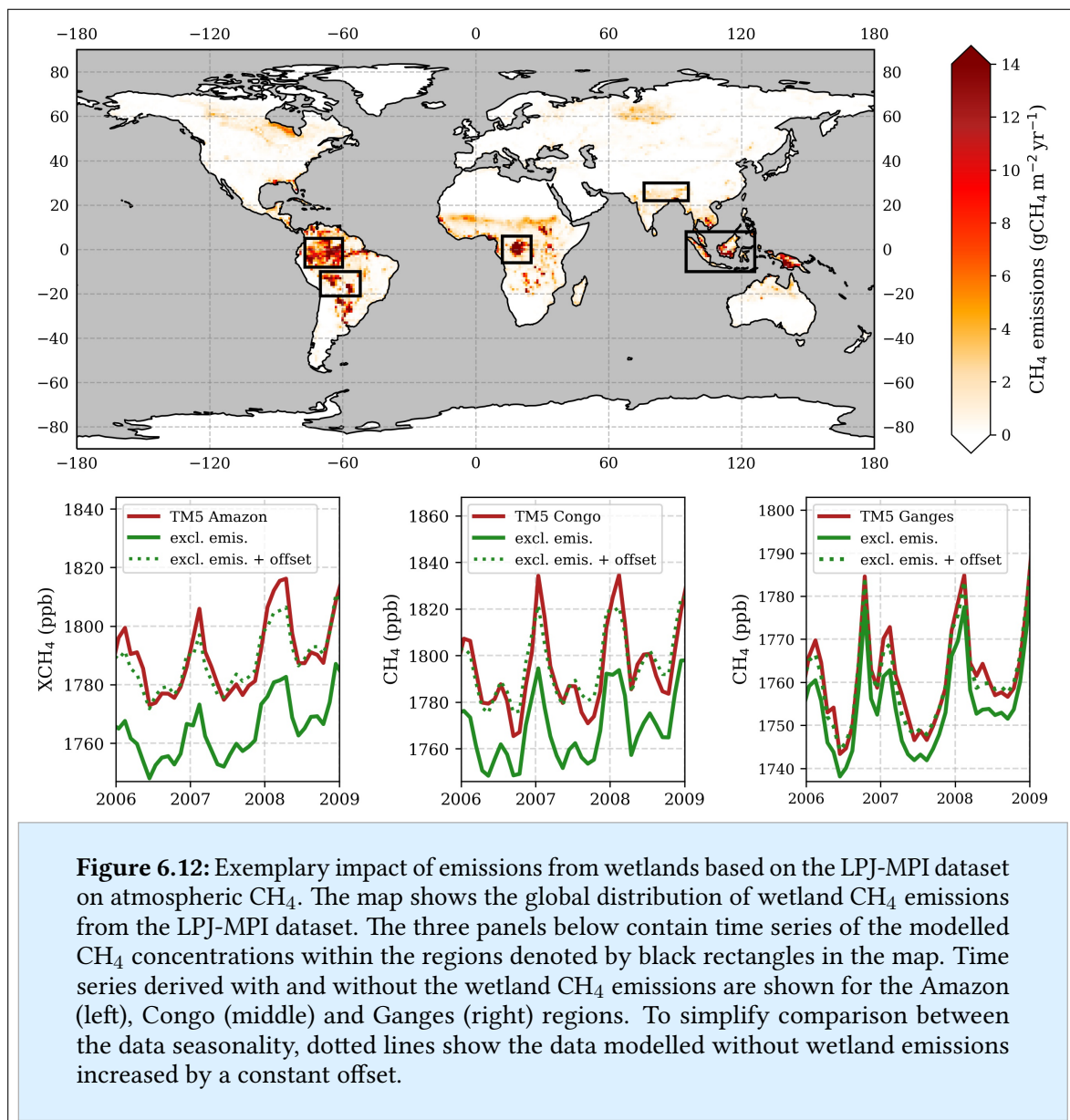
In order to assess the significance of the correlations derived in subsection 6.5.2 and subsection 6.5.3 for the validation of the wetland emission datasets, the impact of local wetland emissions on atmospheric XCH₄ and its variation need to be known. For this, model runs excluding individual wetlands analogue to the test study in section 6.3 were planned. To get a first estimate, one run that excluded all wetland emissions was performed and resulting concentrations were compared to those derived with inclusion of the diagnostic wetland emission datasets.

Exclusion of global wetland emissions mainly creates an offset in the resulting XCH₄ (Figure 6.12). Even for the LPJ-MPI dataset whose emission data show the strongest seasonal variation (Figure 6.6), the response in the seasonality ((10 – 25) % for the Amazon region) is weaker than it was observed for the test model runs described in section 6.3 (50 % for the

6. Towards validation of wetland CH₄ emissions

Amazon region). This lower impact on the seasonality is likely caused by the fact that for the test run emissions from individual wetlands were excluded, while global wetland emissions were excluded for the model results shown in Figure 6.12.

The exclusion of global wetland CH₄ emissions is an extreme measure and creates a strong atmospheric CH₄ deficit resulting in high nudging fluxes. Those nudging fluxes strongly impact atmospheric CH₄ concentrations and potentially seasonal CH₄ variations. The impact of nudging fluxes on the modelled seasonal XCH₄ variation likely increases for higher flux values. Thus, it is important to know the order of magnitude of the included nudging fluxes.



Model runs without wetland emissions result in a XCH₄ offset compared to other runs. Changes in the XCH₄ seasonality are less pronounced than expected (< 25 %).

Because of the uncertainties associated with the model nudging fluxes, model runs without nudging calculations were considered for the evaluation of wetland emission datasets. However, since the chemical CH₄ sink depends on absolute atmospheric CH₄ concentrations, it must be ensured that the overall model CH₄ budget yields realistic CH₄ concentrations. Those model runs without nudging emissions and the model CH₄ budgets are investigated in section 6.6.

6.6. Deficit in the modelled XCH₄

In this section, results from model runs without nudging calculations are evaluated to quantify the impact of nudging emissions on modelled XCH₄ concentrations. Subsection 6.6.1 shows modelled XCH₄ without nudging and discusses the resulting emission deficit. Subsection 6.6.2 investigates possible causes for this deficit via comparison of the model's internal emission budgets to CH₄ budgets stated by the GCP (Saunois et al., 2020).

6.6.1. Deficit in the model CH₄ budget

Without the nudging fluxes, modelled XCH₄ concentrations are significantly lower than XCH₄ derived from satellite observations (Figure 6.13). The lowest concentrations are observed in the run with the TRIPLEX-GHG dataset and are roughly 300 ppb lower than satellite observations. Modelled concentrations using the ELM dataset are the closest to measured concentrations whilst still being ≈ 160 ppb lower than satellite retrievals (Figure 6.13).

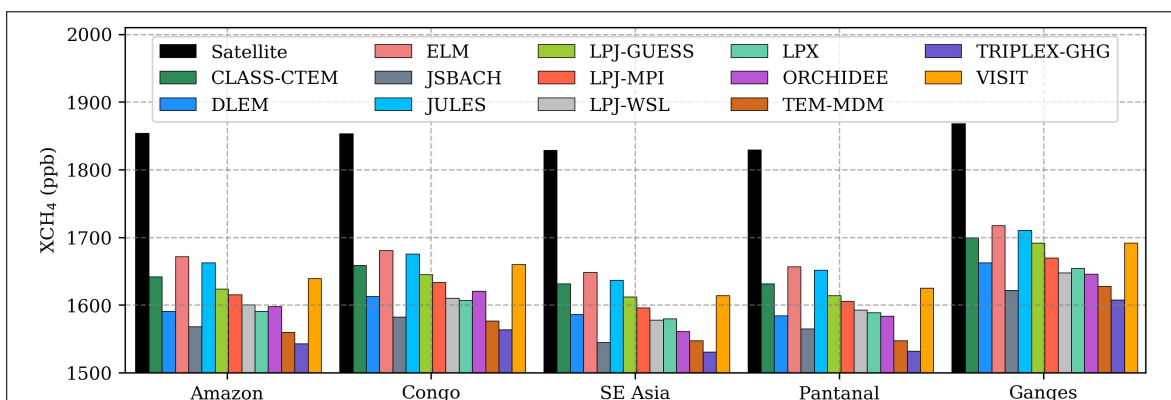


Figure 6.13: Regional atmospheric XCH₄ from satellite retrievals and from model runs without nudging fluxes. Regions are defined as shown in Figure 6.1. Data are given as average concentrations for the year 2007.

6. Towards validation of wetland CH₄ emissions

Nudging fluxes that were generated in the model runs with nudging to realize observed atmospheric XCH₄ range between 84 TgCH₄ yr⁻¹ and 148 TgCH₄ yr⁻¹ (Table 6.6). Model runs including more moderate wetland emissions, like the TRIPLEX-GHG dataset, naturally generate higher nudging emissions than model runs with higher wetland emissions like the JULES dataset. On average, the emission deficit in the model amounts to 120 TgCH₄ yr⁻¹.

Model runs without nudging fluxes result in atmospheric XCH₄ that is by 150 to 300 ppb smaller than satellite observations.

This deficit in atmospheric CH₄ indicates that either the emissions included in the model (≈ 570 TgCH₄ yr⁻¹ Table 3.1) are too low by about 20 % or that the CH₄ sinks in the model are overestimated. Subsection 6.6.2 compares the model CH₄ sources and sinks to budgets stated in literature to find the cause for the observed atmospheric CH₄ deficit.

	CLASS-CTEM	DLEM	ELM	JSBACH	JULES	LPJ-GUESS	LPJ-MPI
wetland emissions (TgCH ₄ yr ⁻¹)	178	149	167	129	180	167	161
Nudging flux (TgCH ₄ yr ⁻¹)	97	120	84	148	89	104	113
	LPJ-WSL	LPX	ORCHIDEE	TEM-MDM	TRIPLEX	VISIT	Average
wetland emissions (TgCH ₄ yr ⁻¹)	143	140	139	107	102	163	148
Nudging flux (TgCH ₄ yr ⁻¹)	130	126	135	148	161	103	120

Table 6.6: Global wetland emissions and generated nudging fluxes. Data are based on comparison between model simulation with and without nudging emissions for the years 2003-2008. All results are given for the diagnostic datasets.

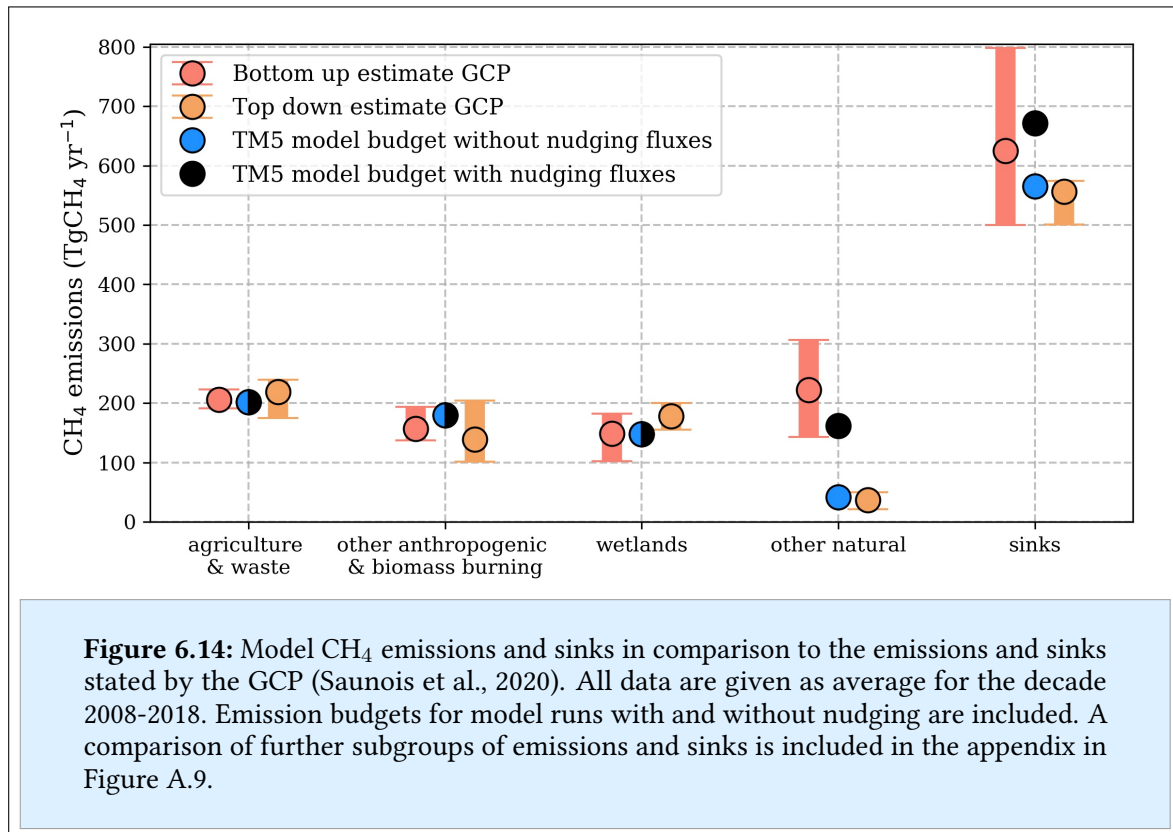
6.6.2. Evaluation of CH₄ sources and sinks

CH₄ sources included in the TM5-MP model can be generally grouped into natural and anthropogenic emission sectors (Table 3.1). Emissions from the natural sector are dominated by wetland emissions and emissions from the anthropogenic sector are dominated by agriculture and waste emissions. Model emissions from these sectors as well as other natural emissions, other anthropogenic emissions and CH₄ sinks were compared to estimates from the global CH₄ budget by the GCP (Saunois et al., 2020, Figure 6.14).

Saunois et al. (2020) provided separate CH₄ budgets based on their top-down and bottom-up estimates. For most categories, the CH₄ emission estimates agree well (Figure 6.14). The only category where estimates differ strongly are non-wetland natural emissions with a top-down estimate of 37 TgCH₄ yr⁻¹ and a bottom-up estimate of 222 TgCH₄ yr⁻¹ (Figure 6.14). One explanation Saunois et al. (2020) suggest for this discrepancy is double-counting of CH₄

emissions from wetlands in the bottom-up estimate of inland water emissions.

The emissions used for model calculations in this study (without nudging emissions) are within the uncertainties of the top-down emission estimates stated by Saunio et al. (2020, Figure 6.14). As discussed before, the atmospheric CH₄ concentrations resulting from this emission budget are significantly lower than satellite observations (Figure 6.13). Derived nudging fluxes indicate a missing CH₄ source of $\approx 120 \text{ TgCH}_4 \text{ yr}^{-1}$ (Table 6.6). Inclusion of these nudging fluxes to the model budget supports the bottom-up estimate of CH₄ emissions by Saunio et al. (2020) (Figure 6.14). This indicates that the missing CH₄ emissions in the model could be attributed to inland water emissions, which were not included in the TM5-MP model budget (Table 3.1).



The total CH₄ budget (CH₄ sources - CH₄ sinks) derived for the model runs with nudging emissions is in the same order of magnitude as the top-down estimate by the GCP, while the bottom-up estimate by the GCP yields a CH₄ budget that is much higher (Table 6.7). However, while all model emissions and sinks for the run with nudging emissions result in values within the uncertainties stated by the GCP bottom-up estimate, natural emissions in the model are on the lower end of that estimate and CH₄ sinks are on the upper side (Figure 6.14). As a consequence, the overall CH₄ budget for the TM5-MP model runs with

nudging emissions is in the same order of magnitude as top-down emissions and the observed atmospheric growth rates (Table 6.7). These results indicate that estimates from the top-down approach by the GCP could underestimate natural inland water emissions as well as CH₄ sinks, whereas the two CH₄ fluxes compensate each other in terms of the absolute atmospheric CH₄ budget.

The TM5-MP model CH₄ budget suggests higher inland water emissions and CH₄ sinks than estimates stated by the GCP top-down budget.

	budget (TgCH ₄ yr ⁻¹)
model budget with nudging:	+ 19
model budget without nudging:	+ 5
bottom-up estimate GCP:	+ 112
top-down estimate GCP:	+ 13
observed atmospheric growth rate:	+ 18

Table 6.7: Atmospheric CH₄ budgets (difference between global CH₄ sources and sinks) from the model runs in this study and from the study by the GCP (Saunois et al., 2020). For comparison, the atmospheric growth rate observed via satellite is included as well.

6.7. Conclusion

This chapter aimed at the evaluation of wetland CH₄ emission datasets derived from various soil and vegetation models. The different emission datasets show strong differences in atmospheric CH₄ fluxes. For datasets with uniform assumptions of wetland extent, global emissions range between 102 and 180 TgCH₄ yr⁻¹, while datasets derived with individually set wetland extent vary stronger and show higher CH₄ emissions.

Test runs of the TM5-MP atmospheric chemistry and transport model show that fluxes from individual wetlands generate observable changes in the seasonality of local XCH₄ concentrations in tropical wetland regions.

Correlation of satellite data with modelled XCH₄ for all emission datasets agree fairly well. Yet, this agreement is mainly caused by modelled nudging fluxes that are generated based on differences between modelled CH₄ and reference data. Nudging calculations on 10-day time scales have been used since those were reported to yield results that represent local CH₄ emission in the XCH₄ seasonality. Yet, comparison of de-trended annual XCH₄ variation yielded little difference between the model runs performed for the different wetland emission datasets. Since the seasonality of wetland emissions between the datasets varies strongly, this lack of variability in modelled XCH₄ seasonality indicates that the modelled seasonality, like the absolute concentrations, is impacted by modelled nudging fluxes.

Quantification of these nudging fluxes amounts to $\approx 120 \text{ TgCH}_4 \text{ yr}^{-1}$. Thus, CH₄ emissions in the model are 20 % lower than they needed to be to generate atmospheric XCH₄ observed from satellite. This deficit in CH₄ emissions results in modelled XCH₄ that is by (150 – 300) ppb lower than satellite observations.

A comparison of the internal model CH₄ budget to the atmospheric CH₄ budgets stated in the literature indicates that missing inland water emissions might be the reason for this emission deficit. However, inland water emissions at such high scales disagree with the recently published top-down estimate of CH₄ budgets by the GCP. Further investigation of the modelled CH₄ budgets indicates that this top-down estimate by the GCP might be underestimating inland water emissions as well as atmospheric CH₄ sinks.

7. Overall Conclusions

In this study, carbon fluxes from tropical wetlands were investigated. The study consists of three major research topics: 1) The investigation of carbon dynamics in Southeast Asian peat-draining rivers with the focus on the dependences of CO₂ emissions from those rivers, 2) the response of CO₂ emissions from tropical peat regions to the application of enhanced weathering and 3) the evaluation of CH₄ emissions from large tropical wetlands by use of atmospheric modelling and satellite observations.

Research topic 1: Carbon dynamics in peat-draining rivers

For the research of carbon dynamics in peat-draining rivers, measured data from ten South-east Asian rivers were analysed. Prior to this study, it was assumed, that CO₂ concentrations in rivers increase linearly with increasing catchment peat coverage due to enhanced leaching and decomposition of organic carbon from peat soils into rivers.

The data collected for this study show that CO₂ concentrations in Southeast Asian peat-draining rivers stagnate for high peat coverage. Despite further increase in river DOC concentration, CO₂ concentrations are fairly constant for peat coverages > 50 %.

Data evaluation based on different approaches for the limitation of DOC decomposition revealed an exponential limitation of DOC decomposition by water *pH*. It was found that the low *pH* in rivers of high peat coverage limits DOC decomposition by up to 85 %. This limitation process provides an answer to the question why, in contrast to the high DOC export, CO₂ emissions from tropical peat-draining rivers are not significantly higher than emissions from temperate rivers.

Carbonate enhancement during two campaigns at one of the rivers resulted in CO₂ concentrations that were increased by almost 100 %. This is explained by the *pH*-increasing impact of carbonates that weakens the limitation in decomposition.

Research topic 2: Feedback of tropical peat areas on enhanced weathering

Enhanced weathering is a CO₂ removal strategy that extracts CO₂ from the atmosphere while converting it into carbonates. To determine the feedback of CO₂ emissions from tropical peat regions on this carbonate enhancement and the accompanying *pH* increase, correlations between peat soil *pH* and soil carbon mobilisation as well as the *pH*-dependent decomposition rate determined in the first part of this study were used.

It is found that the application of enhanced weathering on peat soils could cause enhanced CO₂ emissions of (12 – 81) gC m⁻² yr⁻¹ and thereby potentially counteract the total CO₂

uptake by enhanced weathering. Furthermore, it is possible that captured CO₂ is directly re-emitted from acidic peat soils.

A case study for enhanced weathering application on Sumatra resulted in soil carbon mobilization of (1.8 – 13.9) TgC yr⁻¹ of which (0.9 – 6.0) TgC yr⁻¹ are emitted as CO₂. The rest is leached as DOC into rivers and together with enhanced carbonate leaching causes CO₂ emissions from peat-draining rivers, estuaries and the coastal ocean to increase by (0.9 – 7.4) TgC yr⁻¹, (1.0 – 24.7) TgC yr⁻¹ and (3.2 – 21.2) TgC yr⁻¹, respectively.

Overall, carbon emissions from Sumatra's soils and rivers could reduce the net enhanced weathering CO₂ uptake by (15 – 58) %. The inclusion of CO₂ emissions from Sumatra's coast increases the estimated re-emission to at least 50 % and potentially more than 150 % of the enhanced weathering CO₂ uptake. These results indicate that the regional feedback in tropical peat regions has the potential to offset the CO₂ uptake by enhanced weathering. This suggests that tropical peat areas should be excluded from enhanced weathering application.

Research topic 3: Evaluation of modelled wetland CH₄ emissions

To study the CH₄ emissions from major wetlands, the evaluation of datasets derived from 13 soil and vegetation models via atmospheric modelling and correlation to satellite data was planned. Comparison of emission datasets from the different soil and vegetation models revealed strong differences in regional atmospheric CH₄ fluxes and flux seasonality. For datasets with uniform assumptions of wetland extent, global emissions ranged between 102 and 180 TgCH₄ yr⁻¹, while datasets derived with individually set wetland extents varied stronger and showed higher CH₄ emissions.

Comparison of modelled XCH₄ to satellite observations resulted in a good correlation for all emission datasets. The best correlation was found for the JSBACH dataset. However, these good correlations were impacted by nudging fluxes in the model. Model runs excluding nudging revealed a discrepancy of (150 – 300) ppb by which modelled data were lower than satellite observations. Examination of the model CH₄ budget revealed missing CH₄ sources of ≈ 120 TgCH₄ yr⁻¹. Thus, the CH₄ emissions used by the model were by 20 % too low.

The model emissions used in this study agree with top-down CH₄ budgets stated in literature. Comparison to literature bottom-up CH₄ budgets indicated that missing inland water emissions might be the cause of the observed CH₄ deficit. Further evaluation of the model CH₄ budgets suggest higher inland water emissions and atmospheric CH₄ sinks than stated by top-down estimates in the literature.

8. Outlook

The research of carbon dynamics in peat-draining rivers in this study revealed an exponential limitation of the CO₂ production by decomposition in peat-draining rivers in Southeast Asia. The fact that a similar stagnation in CO₂ concentrations was observed for studies in African rivers indicates that similar processes control CO₂ emissions from tropical regions in general. Additional studies in tropical peat areas outside of Southeast Asia could validate this assumption. Additional studies in Southeast Asian rivers could improve the performed correlations and result in more robust results, considering especially the impact of seasonal variations in river carbon dynamics.

Further research on the response of tropical peat regions to enhanced weathering is needed to validate the results stated in this study. Here it is essential to quantify the response of carbon mobilisation from tropical peat soils to pH. To investigate this, leaching experiments as well as field measurements with soil chambers would be useful. Soil chamber experiments could also yield information on the response of direct re-emissions from acidic peat soils. Furthermore, the water mixing calculations that were performed in this study to yield a first approximation of coastal emission responses on enhanced weathering should be improved by use of more complex coastal modelling.

For the evaluation of wetland CH₄ emission datasets, model runs including inland water emissions in the scale of missing emissions as derived from the nudging fluxes will be performed. From those model runs, correlation of modelled XCH₄ seasonality to satellite data is planned. Those correlations should provide information on the quality of different wetland emission datasets for individual tropical wetland regions. Comparison runs for all of the emission datasets excluding specific wetland regions could yield further information on the impact of regional wetlands on atmospheric XCH₄. Finally, model runs with tracked CH₄ from individual sources are planned to understand the impact of wetland sources in even more detail. In order to reduce calculation times, model runs are planned to be performed using the a priori run of the newly developed adjoined TM5-4DVAR-MP model. This run would resemble a CH₄ tracer run including reaction with prescribed atmospheric OH fields rather than full chemistry model calculations.

A. Appendix

Section A.1 lists the abbreviations used within this study. Section A.2, section A.3 and section A.4 are individual appendices for chapter 4, chapter 5 and chapter 6, respectively.

A.1. Abbreviations

Subsection A.1.1 and subsection A.1.2 provide alphabetical lists of the acronyms and chemical formulas used in this study.

A.1.1. Acronyms

CA:	Carbonate Alkalinity
DIC:	Dissolved Inorganic Carbon
DOC:	Dissolved Organic Carbon
EMMA:	Ensemble Median Algorithm
GCP:	Global Carbon Project
GOSAT:	Greenhouse gases Observing SATellite
NPP:	Net Primary Production
NDIR:	Non-Dispersive Infra Red
PIC:	Particulate Inorganic Carbon
POC:	Particulate Organic Carbon
SCIAMACHY:	Scanning Imaging Absorption Spectrometer for Atmospheric Chartography
SE Asia:	Southeast Asia
TA:	Total Alkalinity
TCCON:	Total Carbon Column Observing Network
TOC:	Total Organic Carbon
VOC:	Volatile Organic Carbon
WAD2M:	Wetland Area Dynamics for Methane Modelling

A.1.2. Chemical formulas

C₆H₁₂O₆:	glucose
CaCO₃:	calcium carbonate
CH₄:	methane
CH₃COOH:	acetate
CH₃OH:	methanol

CO:	carbon monoxide
CO ₂ :	carbon dioxide
CO ₃ ²⁻ :	carbonate ion
H ₂ :	hydrogen
H ⁺ :	hydrogen ion
H ₂ CO ₃ :	true carbonic acid
H ₂ O:	water
O ₂ :	oxygen
OH:	hydroxyl radical
pCO ₂ :	partial pressure of carbon dioxide
XCH ₄ :	methane column-averaged dry-air mole fraction

A.2. Appendix to chapter 4

This section presents the appendix to chapter 4 - *Limitation of CO₂ production in peat-draining rivers*. Subsection A.2.1 contains additional figures and tables to the study presented in chapter 4. Subsection A.2.2 shows data correlations for individual river campaigns and subsection A.2.3 presents estimates for regional river CO₂ emissions from Southeast Asia.

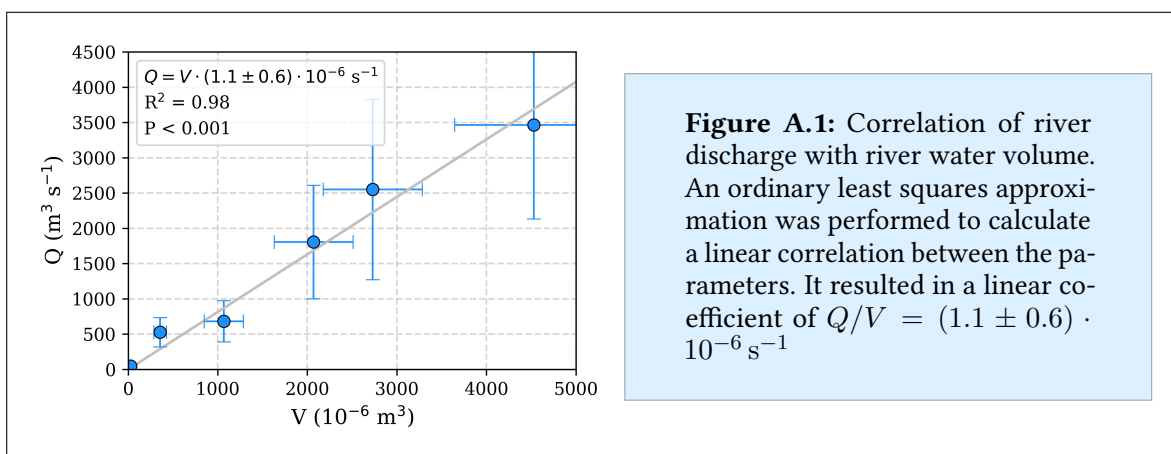
A.2.1. Additional figures and tables

River	peat coverage (%)	catchment area (km ²)	river coverage (%)	air temperature (°C)	precipitation (mm yr ⁻¹)	discharge (m ³ s ⁻¹)
Maludam	90.7 ± 1.5	91.1 ± 0.8	0.39 ± 0.10	26.98 ± 0.16	3 142 ± 415	2.9 ± 1.1
Sebuyau	60.7 ± 1.0	451 ± 4	0.94 ± 0.11	26.95 ± 0.17	3 262 ± 448	29 ± 11
Simunjan	42.9 ± 0.7	758 ± 6	1.00 ± 0.18	26.75 ± 0.16	3 256 ± 462	48 ± 18
Rajang	7.7 ± 0.1	51 699 ± 414	1.46 ± 0.03	25.94 ± 0.14	3 407 ± 461	3 466 ± 1 334
Musi	4.0 ± 0.1	57 602 ± 461	0.73 ± 0.03	26.40 ± 0.13	2 251 ± 566	2 551 ± 1 278
Batang Hari	5.4 ± 0.1	43 778 ± 350	0.79 ± 0.03	25.89 ± 0.15	2 098 ± 410	1 808 ± 804
Indragiri	11.4 ± 0.2	17 713 ± 142	1.00 ± 0.03	26.66 ± 0.12	1 958 ± 349	683 ± 292
Kampar	27.8 ± 0.5	23 610 ± 189	1.90 ± 0.04	26.39 ± 0.12	2 050 ± 366	953 ± 408
Rokan	18.6 ± 0.3	19 953 ± 160	0.71 ± 0.03	26.40 ± 0.16	2 301 ± 270	904 ± 332
Siak	25.9 ± 0.4	11 719 ± 94	0.43 ± 0.02	26.87 ± 0.16	2 288 ± 331	528 ± 208
Mandau*	48.1 ± 0.8	3 004 ± 24	n.d.	27.38 ± 0.17	2 254 ± 340	133 ± 53
Tapung Kanan*	53.4 ± 0.9	2 335 ± 19	n.d.	27.06 ± 0.16	2 368 ± 395	109 ± 45
Tapung Kiri*	3.9 ± 0.1	2 469 ± 20	n.d.	27.04 ± 0.15	2 337 ± 432	114 ± 49

Table A.1: Catchment properties and hydrological data of the investigated rivers. All data is derived as mean values over the whole river catchment as described in section 3.2. *For the Siak tributaries, peat coverage and catchment area are taken from Baum et al. (2007).

River	pH	T_{water} (°C)	DOC ($\mu\text{mol L}^{-1}$)	O_2 ($\mu\text{mol L}^{-1}$)	$p\text{CO}_2$ (μatm)	k_{600} (cm h^{-1})	publication
Maludam	3.8 ± 0.2	26.0 ± 0.5	4031 ± 805	55 ± 36	8500 ± 908	5 ± 2	this study, Müller et al. (2015)
Sebuyau	4.2 ± 0.2	27.8 ± 0.6	3026 ± 1047	61 ± 26	8834 ± 1050	9 ± 5	this study
Simunjan***	5.3 ± 0.4	28.2 ± 0.6	1533 ± 559	107 ± 21	7949 ± 1775	11 ± 5	this study
Rajang	6.7 ± 0.1	28.8 ± 1.2	169 ± 32	190 ± 26	2994 ± 494	9 ± 1	Müller-Dum et al. (2018)
Musi*	6.9 ± 0.3	30.6 ± 0.3	244 ± 5	149 ± 43	4316 ± 593	17 ± 4	Rixen et al. (2016), Wit et al. (2015)
Batang Hari*	7.1 ± 0.3	30.0 ± 0.1	321 ± 4	163 ± 1	2400 ± 18	17 ± 4	Rixen et al. (2016), Wit et al. (2015)
Indragiri*	6.3 ± 0.3	31.5 ± 0.1	692 ± 5	89 ± 3	5777 ± 103	17 ± 4	Rixen et al. (2016), Wit et al. (2015)
Kampar	6.4 ± 0.4	29.4 ± 0.7	1280 ± 44	98 ± 43	n.d.	n.d.	Rixen et al. (2016)
Rokan	6.5 ± 0.1	28.9 ± 1.1	781 ± 53	114 ± 22	n.d.	n.d.	Rixen et al. (2016)
Siak**	5.1 ± 0.5	30.0 ± 0.2	1829 ± 601	53 ± 22	8555 ± 747	17 ± 4	Rixen et al. (2016), Wit et al. (2015)
Mandau	4.8 ± 0.7	30.3 ± 2.3	2484 ± 669	63 ± 25	n.d.	n.d.	Baum et al. (2007)
Tapung Kanan	5.8 ± 0.7	30.3 ± 1.0	1526 ± 169	86 ± 27	n.d.	n.d.	Baum et al. (2007)
Tapung Kiri	6.3 ± 0.5	30.8 ± 2.2	640 ± 162	132 ± 50	n.d.	n.d.	Baum et al. (2007)

Table A.2: Measured data from the investigated rivers and the data sources. *pH values from Wit et al. (2015), measured between 2009 and 2013 are on free scale. **At the Siak, pH measurements on NBS scale (prior 2009) and free scale (2009 to 2013) are combined. ***For the Simunjan river, data from the January 2016 and March 2017 campaigns (Table 4.4) are excluded.



A. Appendix

River	03.04	09.04	08.05	03.06	04.06	11.06	03.08	10.09	10.12	04.13	03.14	03.15	01.16	08.16	03.17	07.17
Maludam	-	-	-	-	-	-	-	-	-	-	✓	✓	✓	-	✓	✓
Sebuyau	-	-	-	-	-	-	-	-	-	-	-	✓	✓	-	✓	✓
Simunjan	-	-	-	-	-	-	-	-	-	-	-	✓	✓	-	✓	✓
Rajang	-	-	-	-	-	-	-	-	-	-	-	-	✓	✓	✓	-
Musi	-	-	-	-	-	-	-	✓	✓	✓	-	-	-	-	-	-
Batang Hari	-	-	-	-	-	-	-	✓	✓	✓	-	-	-	-	-	-
Indragiri	-	-	-	-	-	-	-	✓	-	✓	-	-	-	-	-	-
Kampar	-	-	-	-	✓	-	✓	-	-	-	-	-	-	-	-	-
Rokan	-	-	-	-	✓	-	✓	-	-	-	-	-	-	-	-	-
Siak	✓	✓	✓	✓	-	✓	-	✓	-	✓	-	-	-	-	-	-
Mandau	✓	✓	✓	✓	-	-	-	-	-	-	-	-	-	-	-	-
Tapung Kanan	✓	✓	✓	✓	-	-	-	-	-	-	-	-	-	-	-	-
Tapung Kiri	✓	✓	✓	✓	-	-	-	-	-	-	-	-	-	-	-	-

Table A.3: List of river campaigns, indicated by month and year. Check marks specify the rivers that were included in the specific campaigns.

River	pH lim. (%) = $(1 - L_{pH}^{\text{lin}})$	O ₂ lim. (%) = $(1 - L_{O_2})$	total lim. (%) = $(1 - L_{pH}^{\text{lin}} \cdot L_{O_2})$	River	pH lim. (%) = $(1 - L_{pH}^{\text{lin}})$	O ₂ lim. (%) = $(1 - L_{O_2})$	total lim. (%) = $(1 - L_{pH}^{\text{lin}} \cdot L_{O_2})$
Maludam	49 ± 2	87 ± 23	93 ± 2	Kampar	14 ± 5	80 ± 32	83 ± 13
Sebuyau	44 ± 3	87 ± 22	92 ± 3	Rokan	13 ± 2	77 ± 28	83 ± 9
Simunjan	29 ± 2	79 ± 27	85 ± 8	Siak	32 ± 7	88 ± 19	92 ± 4
Rajang	11 ± 2	67 ± 34	71 ± 20	Mandau	36 ± 10	86 ± 22	91 ± 5
Musi	9 ± 3	72 ± 36	75 ± 23	Tapung Kanan	23 ± 9	82 ± 26	91 ± 10
Batang Hari	6 ± 4	71 ± 32	72 ± 32	Tapung Kiri	16 ± 6	75 ± 37	79 ± 19
Indragiri	16 ± 4	81 ± 25	84 ± 9				

Table A.4: List of fractions by which the decomposition in the individual rivers is lowered due to the impact of pH and O₂ for the linear approach. L_{O_2} and L_{pH}^{lin} are defined according to equation (4.3) and equation (4.4), respectively.

$$\text{CO}_2(\text{DOC}, pH, \text{O}_2) = K_{\text{CO}_2}(T) \cdot p\text{CO}_2^a + \frac{d \cdot R_{\text{max}} \cdot \text{DOC} \cdot \frac{\text{O}_2}{K_m + \text{O}_2} \cdot \exp(\lambda \cdot (p\text{H} - pH_0))}{k_{\text{CO}_2}(T)}$$

$$\text{O}_2(\text{DOC}, pH) = \sqrt{\left(\frac{b \cdot d \cdot R_{\text{max}} \cdot \text{DOC} \cdot \exp(\lambda \cdot (p\text{H} - pH_0)) + k_{\text{O}_2}(T) \cdot (K_m - K_{\text{O}_2}(T) \cdot p\text{O}_2^b)}{2 \cdot k_{\text{O}_2}(T)} \right)^2 + K_{\text{O}_2}(T) \cdot p\text{O}_2^a \cdot K_m} - \frac{b \cdot d \cdot R_{\text{max}} \cdot \text{DOC} \cdot \exp(\lambda \cdot (p\text{H} - pH_0)) + k_{\text{O}_2}(T) \cdot (K_m - K_{\text{O}_2}(T) \cdot p\text{O}_2^b)}{2 \cdot k_{\text{O}_2}(T)}$$

Table A.5: Equations to derive CO_2 and O_2 for the exponential $p\text{H}$ limitation approach of DOC decomposition. The parameters R_{max} , K_m , λ and b (Table 4.2) were derived by least squares optimization of this equation based on measured DOC , $p\text{H}$, T , O_2 and CO_2 data in the investigated rivers.

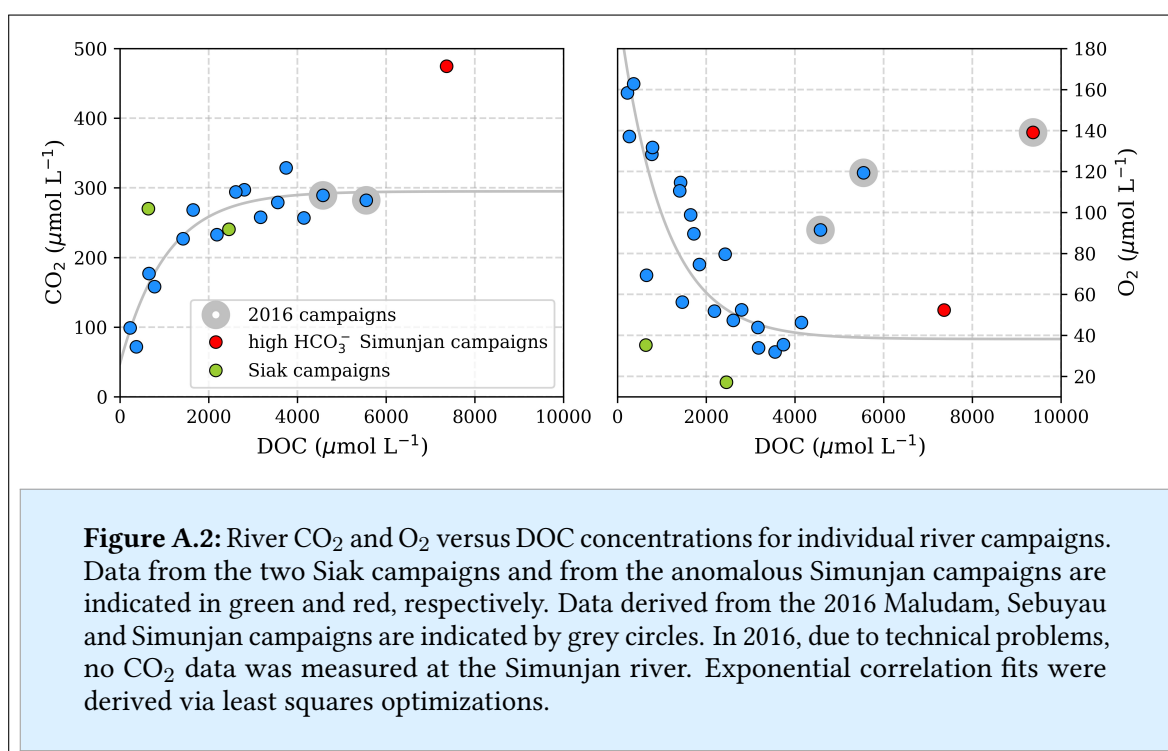
$$\text{CO}_2(\text{DOC}, pH, \text{O}_2) = K_{\text{CO}_2}(T) \cdot p\text{CO}_2^a + \frac{d \cdot R_{\text{max}} \cdot \text{DOC} \cdot \frac{\text{O}_2}{K_m + \text{O}_2} \cdot \frac{p\text{H}}{p\text{H}_0}}{k_{\text{CO}_2}(T)}$$

$$\text{O}_2(\text{DOC}, pH) = \sqrt{\left(\frac{b \cdot d \cdot R_{\text{max}} \cdot \text{DOC} \cdot \frac{p\text{H}}{p\text{H}_0} + k_{\text{O}_2}(T) \cdot (K_m - K_{\text{O}_2}(T) \cdot p\text{O}_2^b)}{2 \cdot k_{\text{O}_2}(T)} \right)^2 + K_{\text{O}_2}(T) \cdot p\text{O}_2^a \cdot K_m} - \frac{b \cdot d \cdot R_{\text{max}} \cdot \text{DOC} \cdot \frac{p\text{H}}{p\text{H}_0} + k_{\text{O}_2}(T) \cdot (K_m - K_{\text{O}_2}(T) \cdot p\text{O}_2^b)}{2 \cdot k_{\text{O}_2}(T)}$$

Table A.6: Equations to derive CO_2 and O_2 for the linear $p\text{H}$ limitation approach of DOC decomposition. The parameters R_{max} , K_m and b (Table 4.1) were derived by least squares optimization of this equation based on measured DOC , $p\text{H}$, T , O_2 and CO_2 data in the investigated rivers.

A.2.2. Discussion of individual river campaigns

The general dependencies of river CO_2 and O_2 on DOC concentration that were observed for averaged river data (Figure 4.4) are also visible in the data derived for individual campaigns (Figure A.2). However, next to the campaigns with high HCO_3^- concentrations in the Simunjan river, some more outliers are visible (Figure A.2). Campaigns at the Siak river yield lower O_2 concentrations than other rivers with similar DOC. This can be explained by the depth of the Siak river. The Siak with river depth of up to 30 m is one of the deepest rivers in Indonesia. Thus, the assumption of a uniform ratio between exchange coefficients and river depths (Figure 4.5) might not be true for the Siak river. Thus, the O_2 consumption by decomposition might be higher compared to the O_2 invasion from the atmosphere.

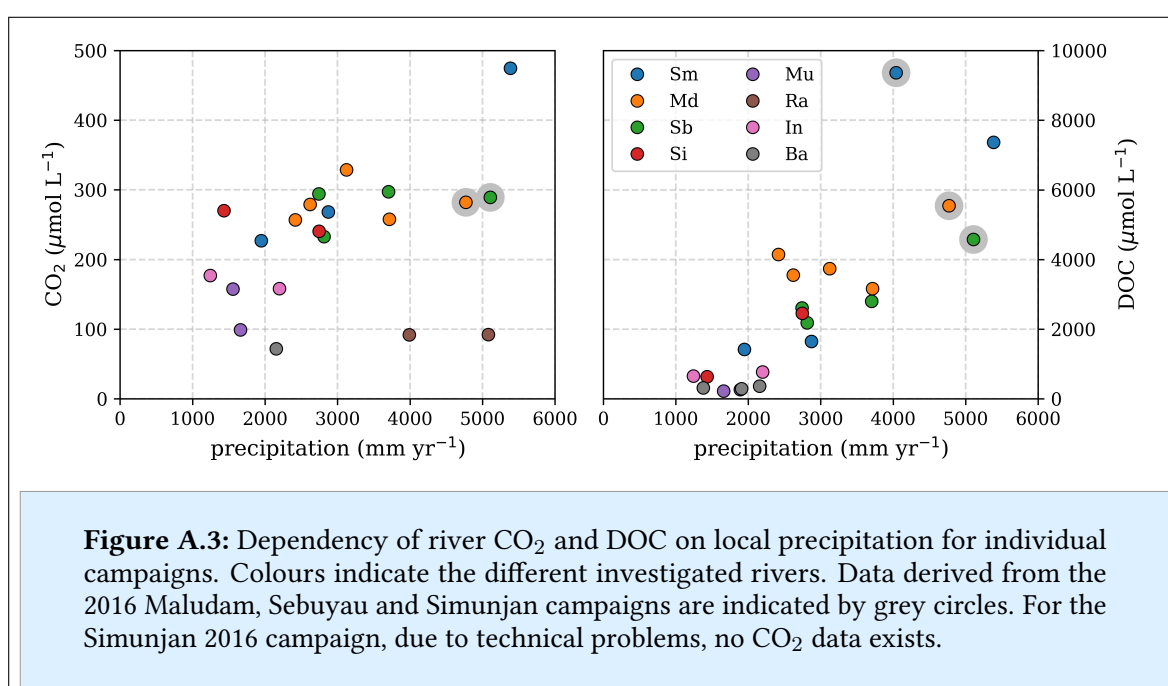


In 2016, not only data at the Simunjan river yielded high DOC concentrations. At the Maludam and Sebuyau rivers DOC concentrations were also higher than during the other campaigns at those rivers (Figure A.2). Additionally, O_2 concentrations during these campaigns are high. The CO_2 concentrations in the Maludam and Sebuyau rivers, however, other than for the Simunjan river, are not higher than during the other campaigns (Figure A.2).

An explanation for this could be high precipitation during these campaigns that enhanced DOC leaching and atmospheric O_2 fluxes into the rivers. For the Maludam and Sebuyau rivers, where pH is low, the CO_2 production by decomposition would not have been significantly

increased by the enhanced DOC due to the exponential pH limitation (section 4.4). In the Simunjan river, however, where carbonate enrichment hinders the pH limitation, CO_2 concentrations would have been increased by high DOC decomposition (section 4.5).

The January 2016 campaigns were the only campaigns at the Malaysian rivers that were performed during the rain season. Accordingly, the precipitation during these campaigns were high (Figure A.3). Correlation of measured CO_2 and DOC with precipitation indicate a positive correlation between DOC and precipitation, while no correlation of CO_2 with precipitation was observed (Figure A.3). This supports the assumption that enhanced DOC concentrations for these campaigns were caused by high precipitation.

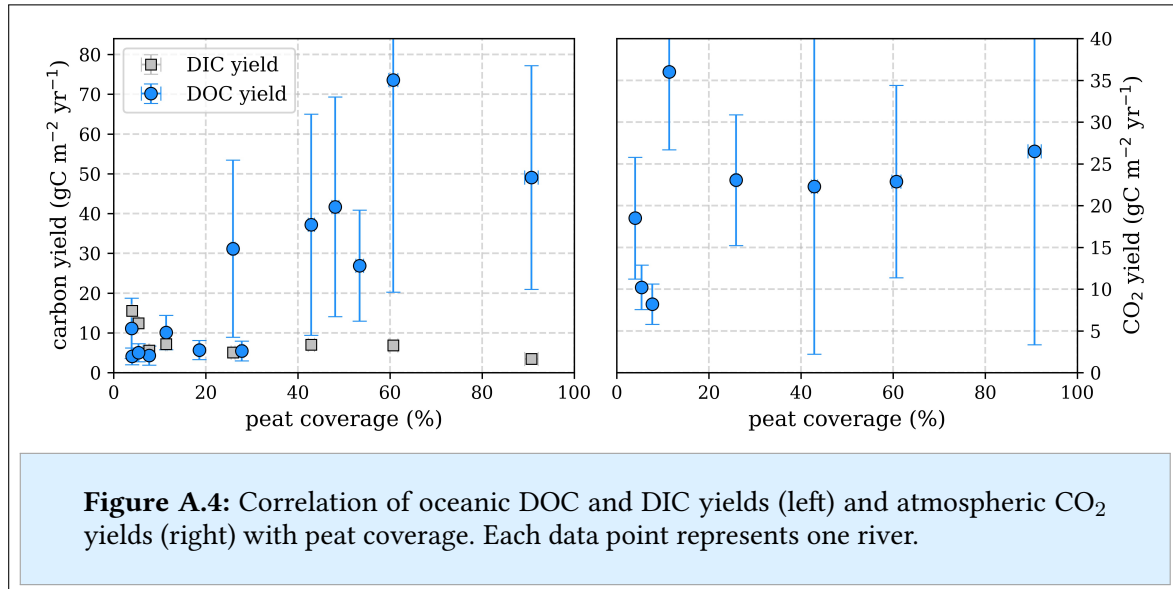


A.2.3. CO_2 emission estimates for Southeast Asian peat-draining rivers

The carbon export per land surface area is called carbon yield. DOC/DIC yields denote the DOC/DIC discharge into the ocean per m^2 of river catchment and were derived according to the equations (3.3). CO_2 yields indicate river CO_2 emissions per m^2 of river catchment. They were derived according to equation (3.4). DOC yields from the investigated Southeast Asian rivers show stronger variation than DOC concentrations. Yet, they generally increase with increasing peat coverage of the river catchments (Figure A.4).

DIC yields decrease with increasing peat coverage. In rivers of high peat coverage DIC yields are negligible compared to DOC and CO_2 yields (Figure A.4). In rivers of low peat coverage, however, they are in the same order of magnitude. CO_2 yields from the investigated rivers

show no distinct correlation to peat coverages (Figure A.4). This is mainly caused by the variation in measured gas exchange coefficients that are lower for the smaller Malaysian rivers which exhibit the highest peat coverage. Exchange coefficients are spatially as well as temporally extremely variable and thus contain high uncertainties.



The river outgassing fraction denotes the fraction of mobilized soil carbon that is emitted from rivers to the atmosphere. It is derived from the quotient between atmospheric CO₂ yields and the total river carbon yields (DOC yield + DIC yield + CO₂ yield). In general, rivers of peat coverage > 25 % show a lower outgassing fraction than rivers of higher peat coverage (Table A.7). The average outgassing fraction of rivers with low peat coverage of ≤ 25 % is 50 %, while the average outgassing fraction from rivers of peat coverage > 25 % is 32 %. This is caused by the fact that the oceanic DOC yield increases with peat coverage, while the changes in DIC and CO₂ yields are smaller (Figure A.4).

To be able to compare these CO₂ emissions to previous estimates, they were extrapolated based on the derived correlation between CO₂ and peat coverage (Figure 4.3) and on averaged river exchange coefficients to represent emissions from Malaysia, Indonesia and total South-east Asia. Those fluxes as well as derived exchange coefficients and previous estimates from Raymond et al. (2013), Lauerwald et al. (2015) and Wit et al. (2015) are listed in Table A.8.

These results range between those of Lauerwald et al. (2015) and Wit et al. (2015). In addition to the large regions in Table A.8, emissions from Sarawak and from Sumatra were calculated. Emissions from Sarawak result in (2.8 ± 1.6) TgC yr⁻¹ and emissions from Sumatra are (16.7 ± 7.5) TgC yr⁻¹. Thus, the emissions from Sarawak represent approximately half the

Malaysian emissions, consistent with it hosting about half the Malaysian peat area (Miettinen et al., 2016) and emissions from Sumatra represent approximately one-third of the Southeast Asian emissions, while hosting about 25.5 % of the Southeast Asian peatlands.

	peat coverage (%)	DOC yield (gC m ⁻² yr ⁻¹)	DIC yield (gC m ⁻² yr ⁻¹)	CO ₂ yield (gC m ⁻² yr ⁻¹)	Outgassing (%)
Maludam	90.7 ± 1.5	49 ± 28	3 ± 2	27 ± 23	24 ± 52
Sebuyau	60.7 ± 1.0	74 ± 53	7 ± 3	23 ± 12	22 ± 25
Simunjan	42.9 ± 0.7	37 ± 28	7 ± 3	22 ± 20	34 ± 56
Siak	25.9 ± 0.4	31 ± 22	5 ± 2	23 ± 8	39 ± 34
Indragiri	11.4 ± 0.2	10 ± 4	7 ± 3	36 ± 9	68 ± 39
Rajang	7.7 ± 0.1	4 ± 2	6 ± 2	8 ± 2	45 ± 31
Batang Hari	5.4 ± 0.1	5 ± 2	12 ± 6	10 ± 3	37 ± 24
Musi	4.0 ± 0.1	4 ± 2	16 ± 8	19 ± 7	49 ± 41

Table A.7: Calculated DOC, DIC and CO₂ yields as well as the outgassing fractions of the total mobilized carbon for the studied rivers.

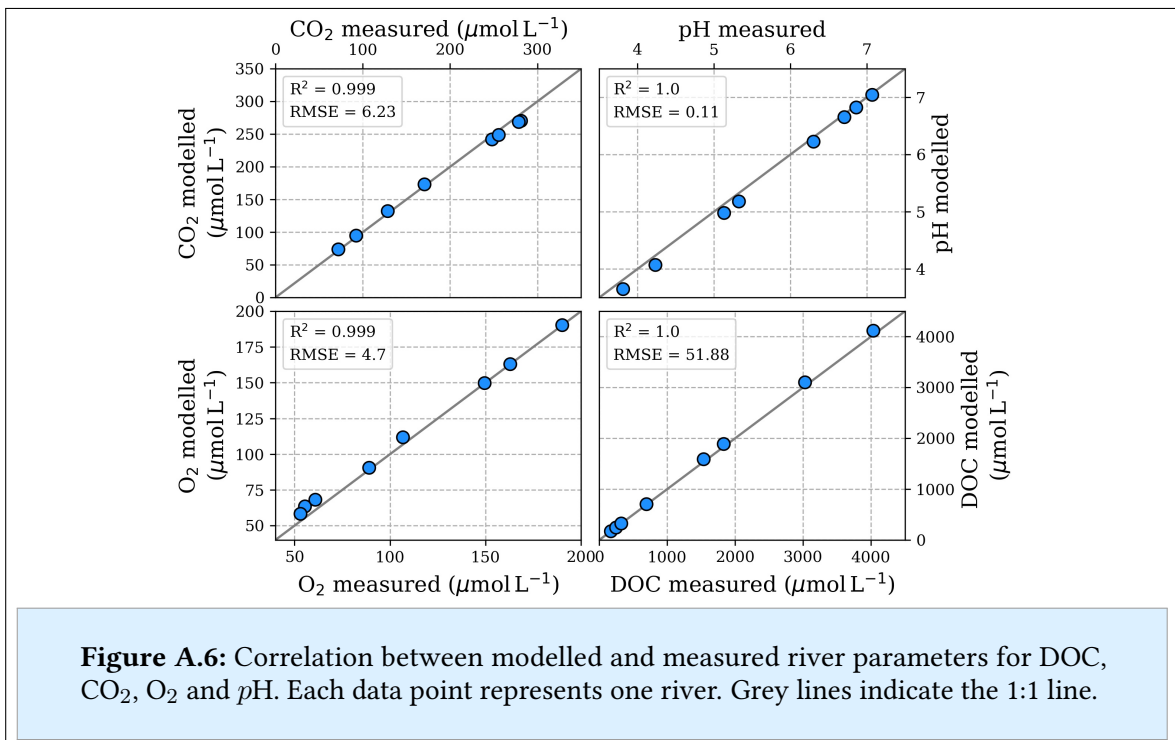
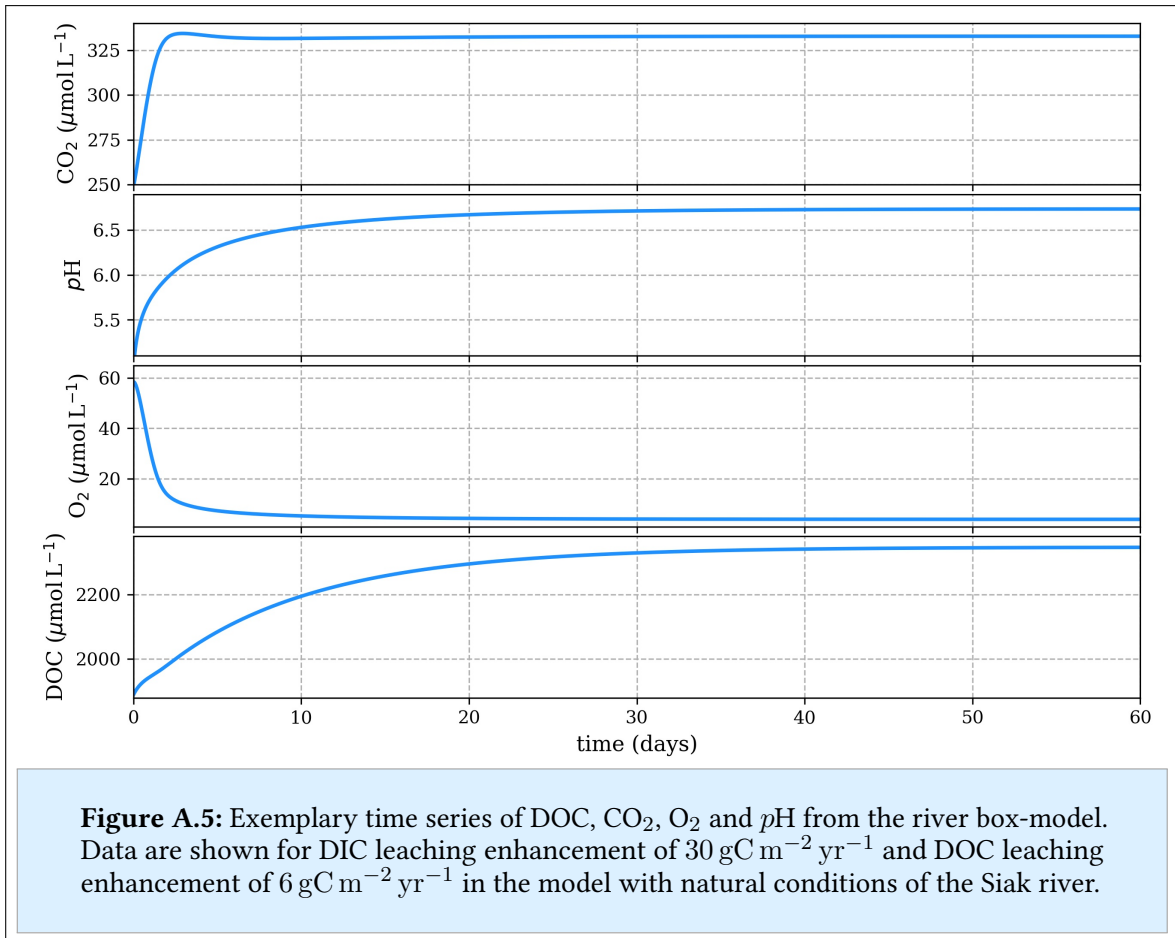
Study	Malaysia		Indonesia		Southeast Asia	
	<i>k</i> _{CO₂}	flux (TgC yr ⁻¹)	<i>k</i> _{CO₂}	flux (TgC yr ⁻¹)	<i>k</i> _{CO₂}	flux (TgC yr ⁻¹)
Raymond et al. (2013)*	47.4 ± 11.4	48.8 ± 5.9	59.9 ± 11.3	144.7 ± 54.5	63.4 ± 19.6	181.5 ± 64.8
Lauerwald et al. (2015)*	24.6 ± 2.9	4.9 ± 1.6	24.6 ± 2.9	33.1 ± 10.7	24.6 ± 2.9	44.6 ± 14.4
Wit et al. (2015)	21.8 ± 11.5	6.2 ± 11.6	21.9 ± 4.7	53.8 ± 12.4	21.8 ± 7.0	66.8 ± 15.7
This study	10.2 ± 3.6	5.8 ± 3.4	22.0 ± 4.7	59.9 ± 27.0	13.4 ± 1.8	53.6 ± 6.2

Table A.8: Estimates on regional CO₂ emissions from Malaysia, Indonesia and Southeast Asia. Exchange coefficients are stated for a CO₂ Schmidt number of 360 (30 °C) consistent with the stated literature values. *Values from Raymond et al. (2013) and Lauerwald et al. (2015) for the specific regions were derived by Wit et al. (2015).

A.3. Appendix to chapter 5

Subsection A.3.1 includes additional figures to chapter 5 - *Response of tropical peat areas to enhanced weathering*.

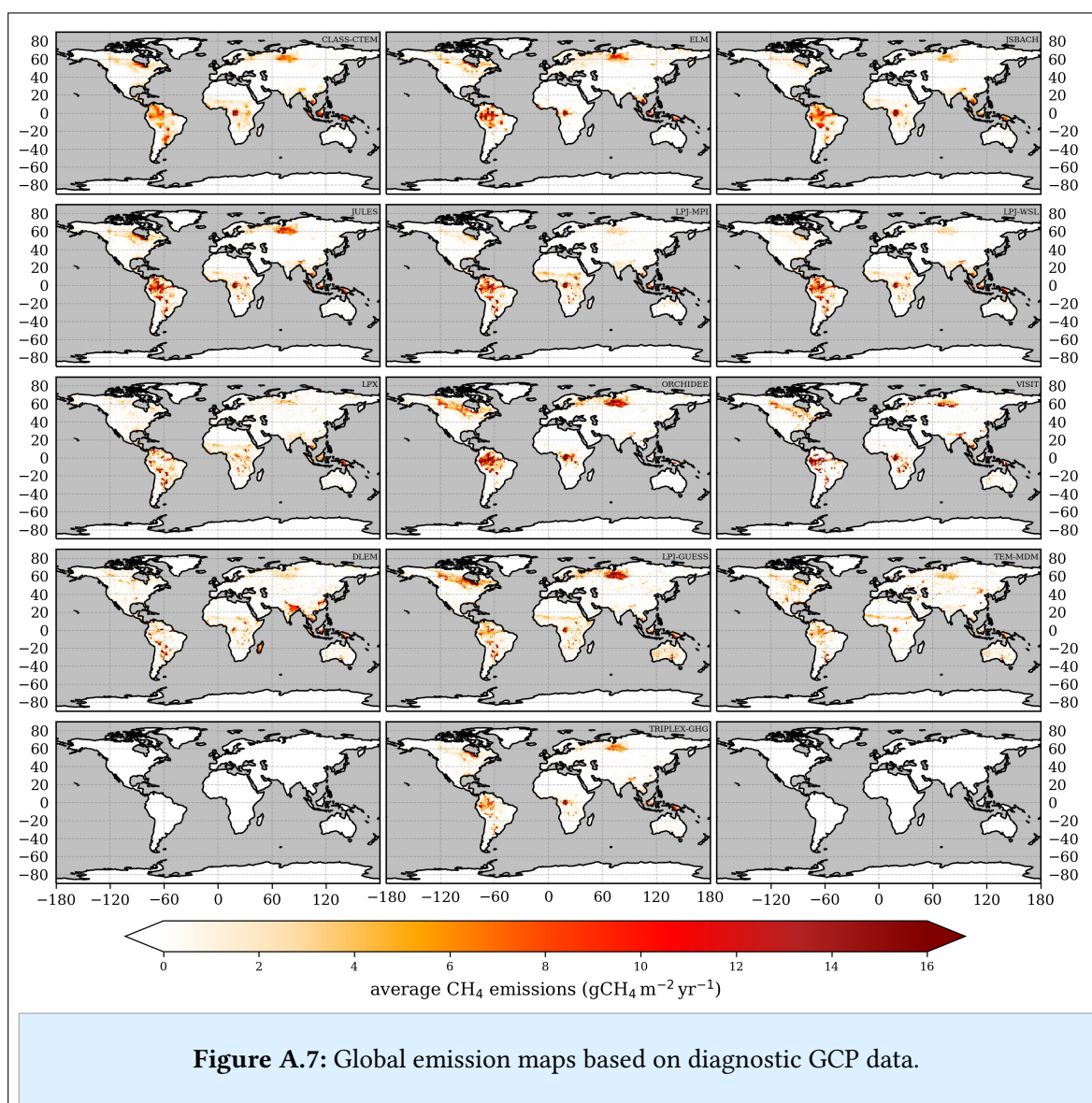
A.3.1. Additional figures and tables

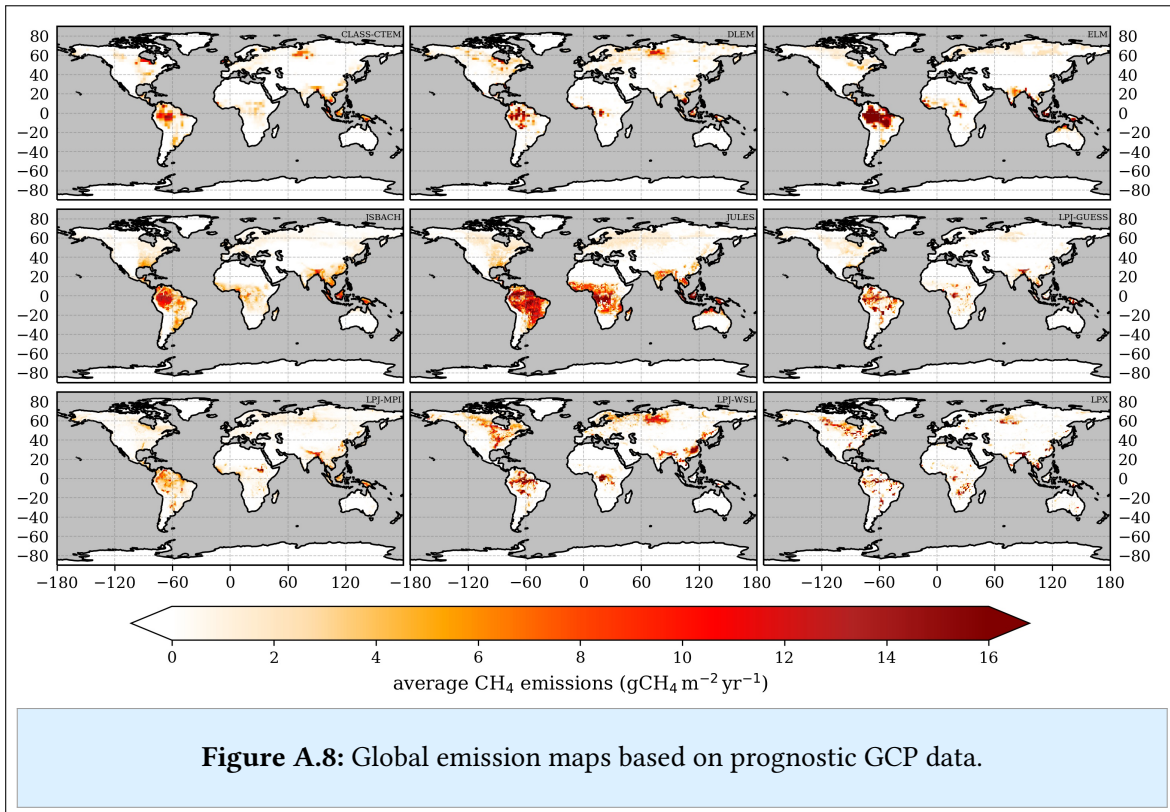


A.4. Appendix to chapter 6

This section presents the appendix to chapter 6 - *Towards validation of wetland CH₄ emissions*. Subsection A.4.1 contains additional figures and tables to the study presented in chapter 6. Subsection A.4.2 displays the regional seasonality of wetland CH₄ for additional regions. Subsection A.4.3 provides the time series and correlations between modelled and measured XCH₄ data.

A.4.1. Additional figures and tables





emissions (TgCH ₄ yr ⁻¹)	Amazon	Congo	SE Asia	Ganges	Pantanal	Global
CLASS-CTEM	13.3	8.1	23.6	2.5	6.1	178.4
DLEM	6.1	3.2	13.0	8.8	6.1	148.7
ELM	25.0	11.9	18.9	0.6	5.7	167.0
JSBACH	16.9	16.1	8.3	2.5	8.2	128.5
JULES	23.2	12.5	14.7	3.3	8.6	180.4
LPJ-GUESS	9.5	6.2	7.2	1.5	5.5	166.8
LPJ-MPI	21.2	13.8	14.8	2.2	8.6	161.2
LPJ-WSL	20.0	9.7	14.1	3.0	7.8	143.4
LPX	6.4	3.7	9.0	2.5	8.1	140.2
ORCHIDEE	29.1	22.7	1.6	1.5	7.8	139.0
TEM-MDM	8.7	3.2	6.8	1.9	1.7	106.6
TRIPLEX-GHG	11.9	7.7	9.2	1.9	2.8	102.4
VISIT	26.9	12.3	7.0	5.2	3.9	162.8
mean	16.8	10.1	11.4	2.9	6.2	148.1
median	16.9	9.9	10.3	2.5	6.2	148.4
standard deviation	7.4	5.2	5.4	1.9	2.1	23.0

Table A.9: Emissions from selected wetland regions as well as global emissions from the diagnostic datasets.

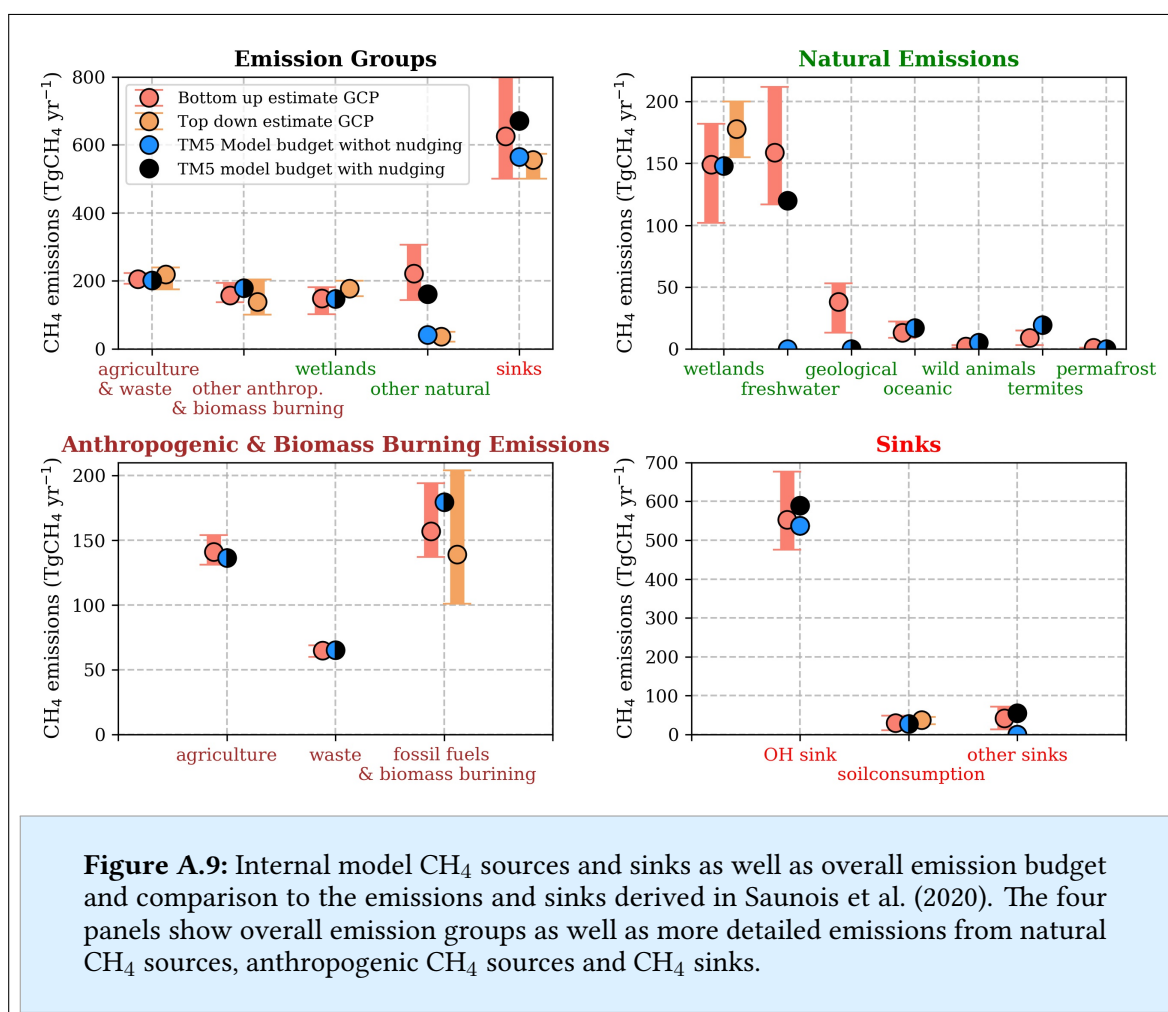
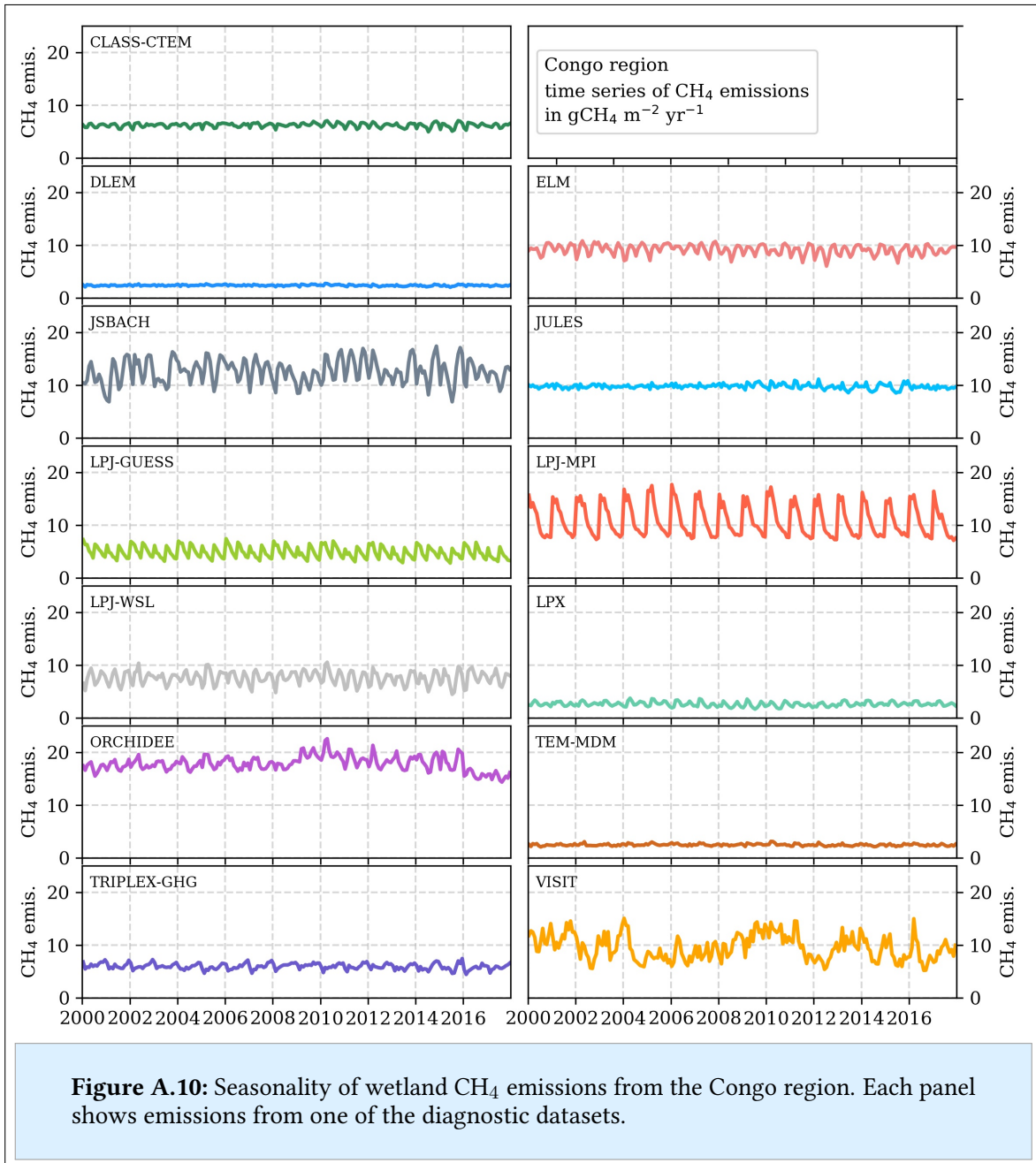


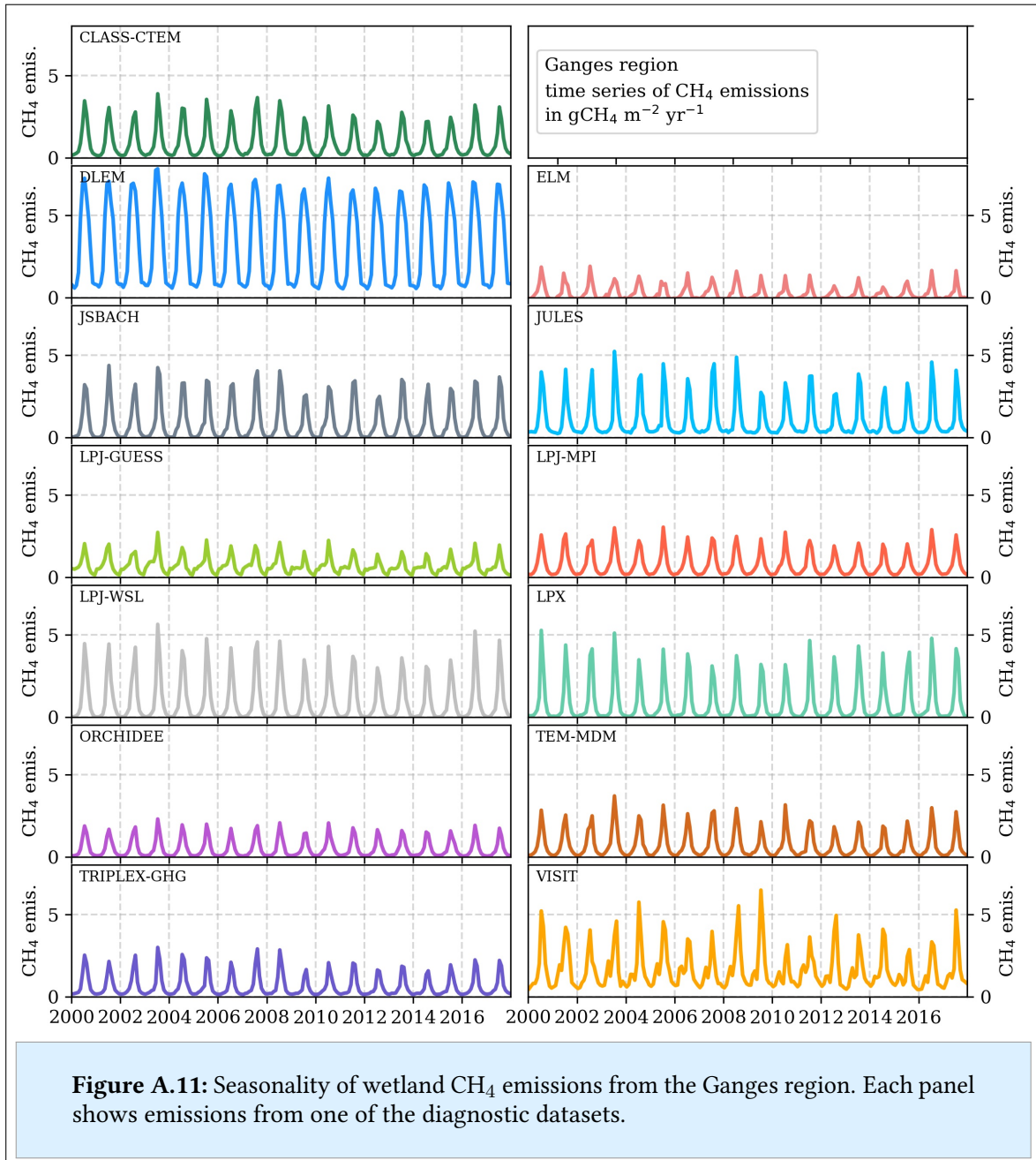
Figure A.9: Internal model CH₄ sources and sinks as well as overall emission budget and comparison to the emissions and sinks derived in Saunois et al. (2020). The four panels show overall emission groups as well as more detailed emissions from natural CH₄ sources, anthropogenic CH₄ sources and CH₄ sinks.

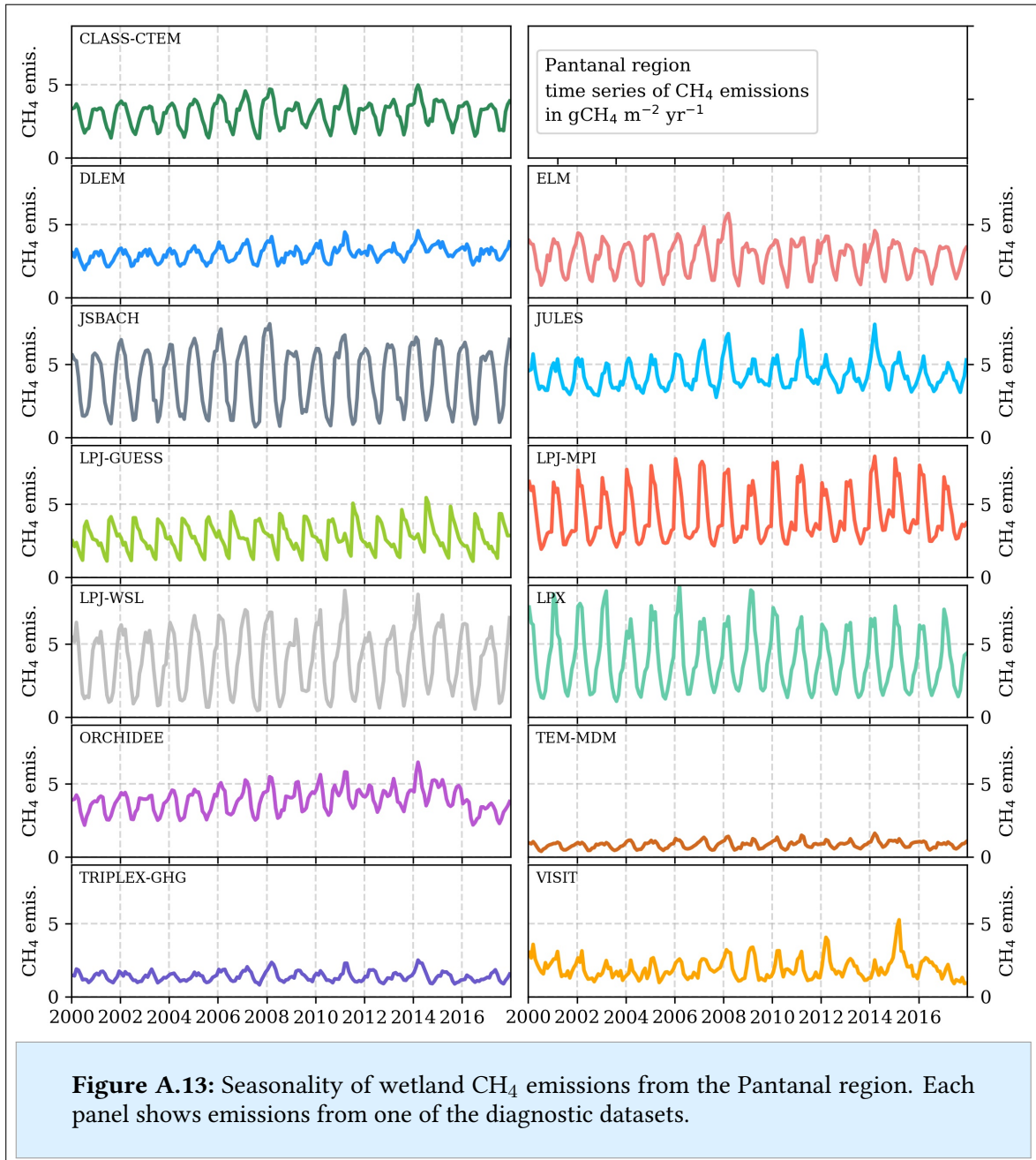
emissions (TgCH ₄ yr ⁻¹)	Amazon	Congo	SE Asia	Ganges	Pantanal	Global
CLASS-CTEM	17.6	1.7	13.7	4.6	2.7	134.4
ELM	24.9	7.2	23.5	1.3	7.2	218.3
JSBACH	48.2	3.5	30.3	3.8	7.4	230.9
JULES	24.7	4.6	15.7	5.3	4.7	180.4
LPJ-MPI	26.4	19.1	20.6	5.0	15.9	316.3
LPJ-WSL	19.0	6.5	5.3	6.1	10.5	123.5
LPX	10.3	1.0	7.7	5.6	3.1	127.8
ORCHIDEE	19.9	21.5	1.0	7.0	6.9	184.7
VISIT	11.7	3.7	3.6	24.6	2.1	162.5
mean	22.5	7.6	13.5	7.0	6.9	184.7
median	21.2	5.5	13.6	5.4	7.0	174.7
standard deviation	10.0	6.7	8.9	6.1	4.0	55.6

Table A.10: Emissions from selected wetland regions as well as global emissions from the prognostic datasets.

A.4.2. Seasonality of wetland CH₄ emissions







A. Appendix

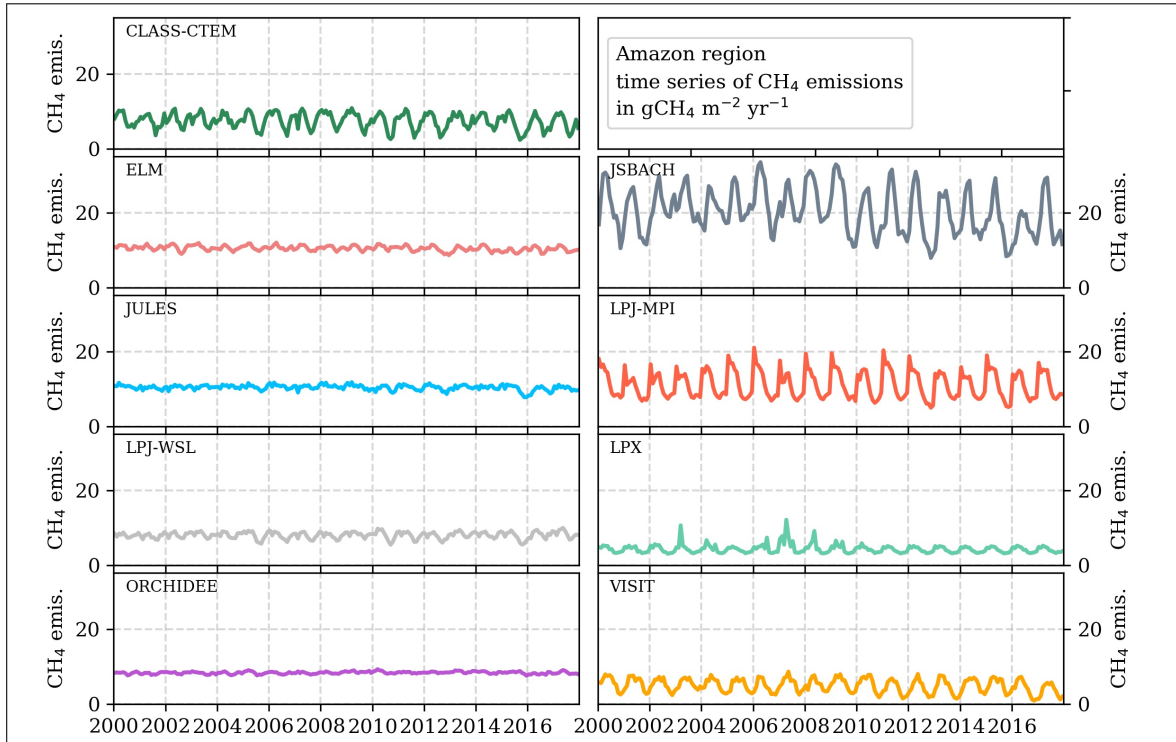


Figure A.14: Seasonality of wetland CH₄ emissions from the Amazon region. Each panel shows emissions from one of the prognostic datasets.

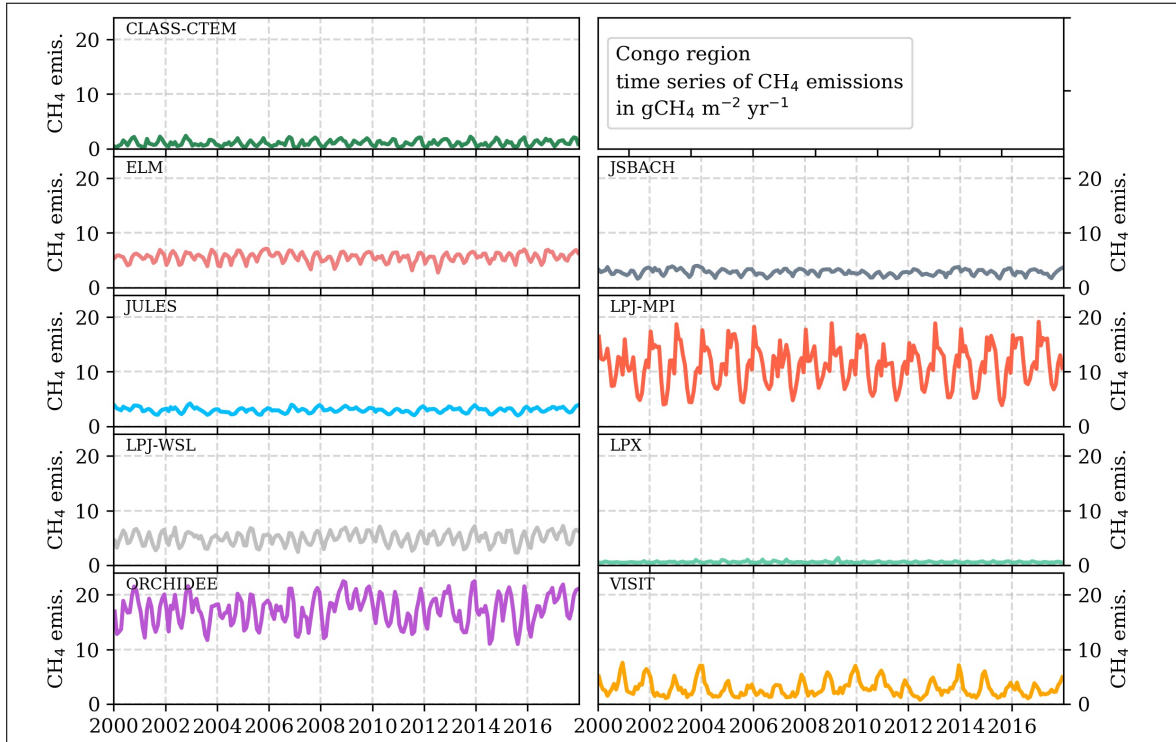


Figure A.15: Seasonality of wetland CH₄ emissions from the Congo region. Each panel shows emissions from one of the prognostic datasets.

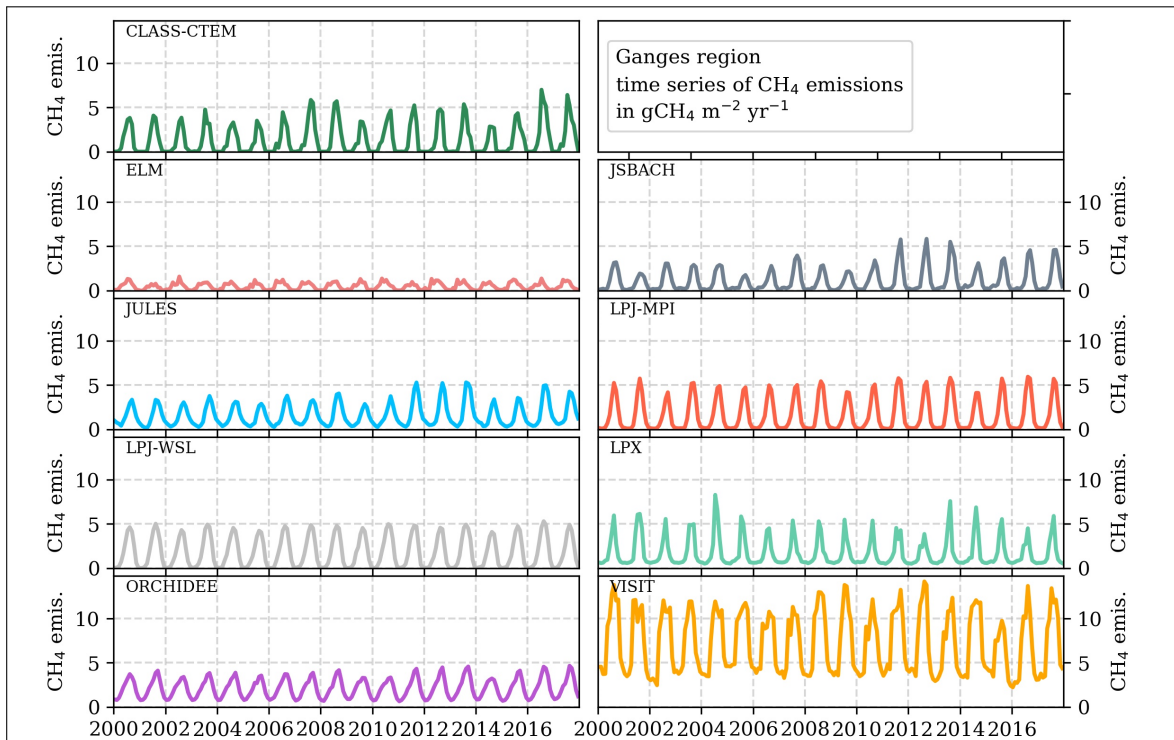


Figure A.16: Seasonality of wetland CH₄ emissions from the Ganges region. Each panel shows emissions from one of the prognostic datasets.

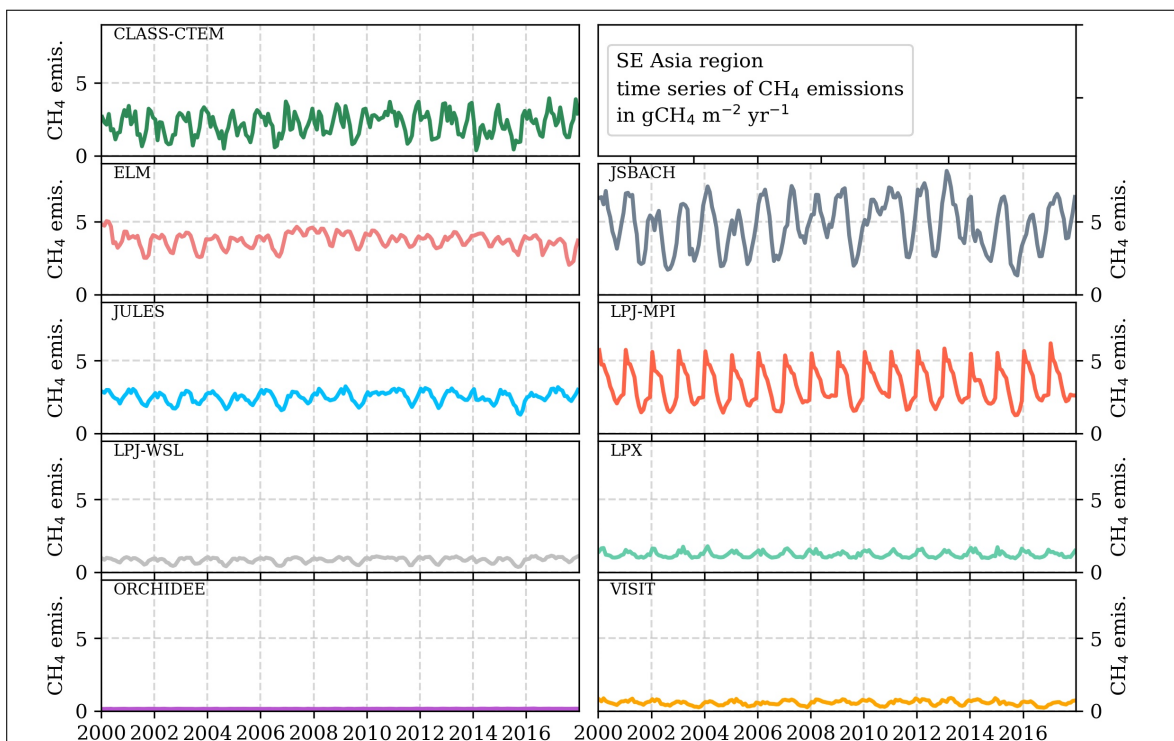
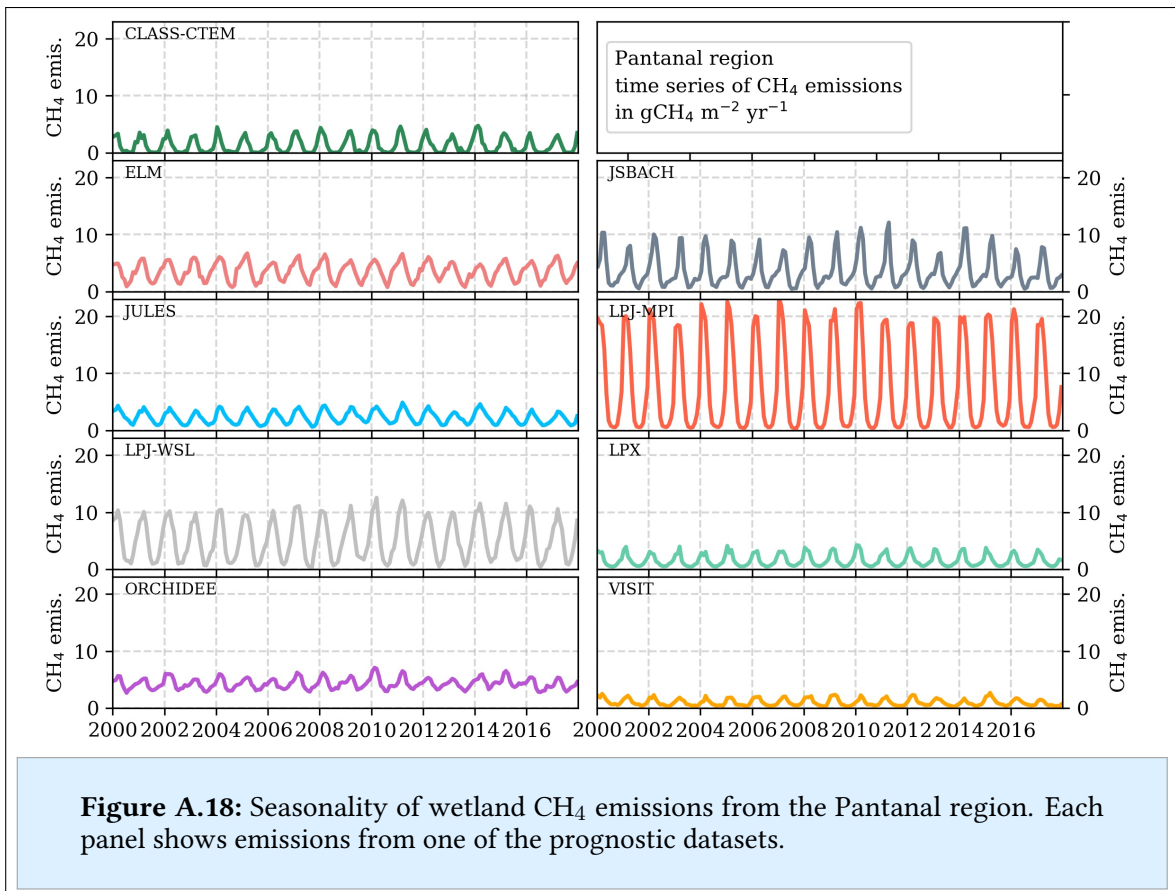


Figure A.17: Seasonality of wetland CH₄ emissions from the Southeast Asian region. Each panel shows emissions from one of the prognostic datasets.



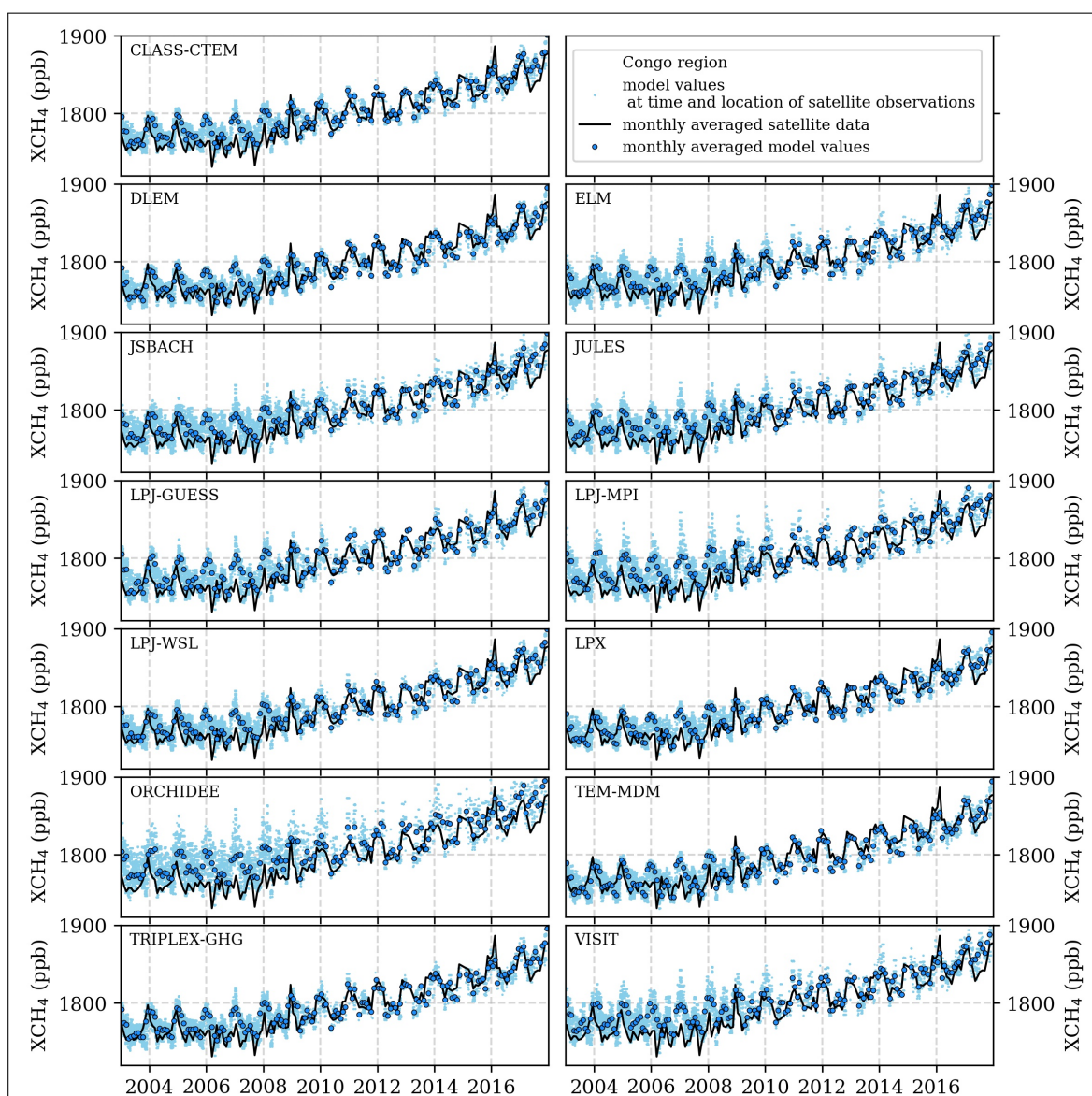
A.4.3. Correlation of modelled XCH₄ to satellite data for additional regions

Figure A.19: Time series of modelled and measured XCH₄ in the Congo region. Black data represent the median of monthly satellite XCH₄ observations. Panels show correlation to derived model runs based on the individual diagnostic wetland CH₄ emission datasets. Model values at specific time and location of the satellite observation as well as the median monthly concentrations from the runs are shown.

	CLASS-CTEM	DLEM	ELM	JS-BACH	JULES	LPJ-GUESS	LPJ-MPI	LPJ-WSL	LPX	ORCHIDEE	TEM-MDM	TRIPLEX	VISIT
R^2	0.866	0.855	0.848	0.848	0.848	0.821	0.800	0.858	0.863	0.822	0.852	0.861	0.844
RMSE	15.4	13.7	15.4	16.4	17.8	17.3	20.9	15.0	13.6	22.1	13.5	13.7	18.2

Table A.11: Correlation coefficients R^2 and root mean square errors (RMSE in ppb) derived for the correlation of satellite XCH₄ observations with modelled concentrations over the Congo region based on the diagnostic wetland emission datasets.

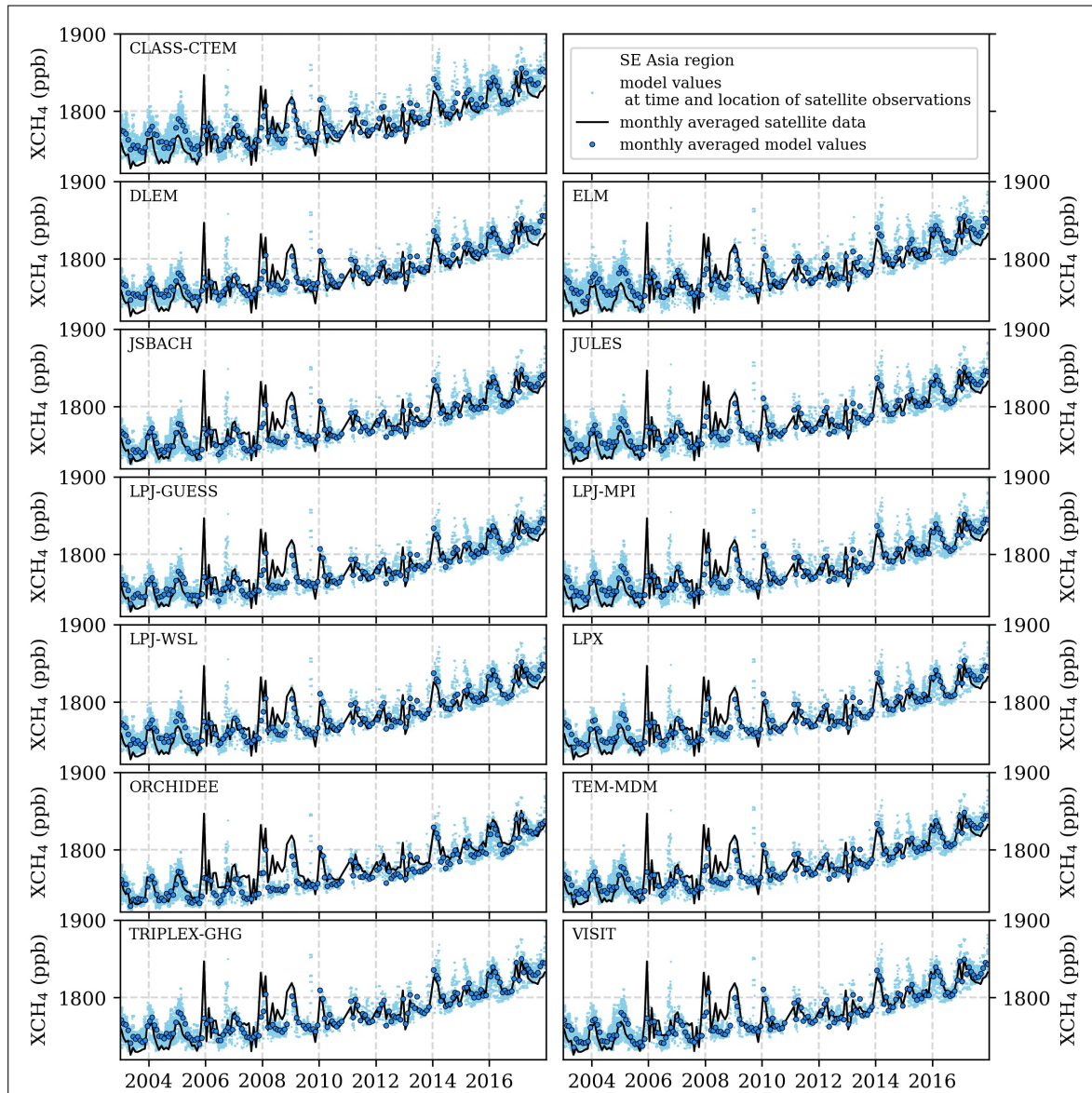


Figure A.20: Time series of modelled and measured XCH₄ in the Southeast Asia region. Black data represent the median of monthly satellite XCH₄ observations. Panels shows correlation to derived model runs based on the individual diagnostic wetland CH₄ emission datasets. Model values at specific time and location of the satellite observation as well as the median monthly concentrations from the runs are shown.

	CLASS-CTEM	DLEM	ELM	JS-BACH	JULES	LPJ-GUESS	LPJ-MPI	LPJ-WSL	LPX	ORCHIDEE	TEM-MDM	TRIPLEX	VISIT
R²	0.806	0.800	0.802	0.810	0.808	0.801	0.803	0.808	0.804	0.802	0.807	0.808	0.812
RMSE	15.4	14.4	14.9	13.3	13.3	13.4	13.5	13.5	13.4	15.8	13.2	13.2	13.1

Table A.12: Correlation coefficients R^2 and root mean square errors (RMSE in ppb) derived for the correlation of satellite XCH₄ observations with modelled concentrations over the Southeast Asian region based on the diagnostic wetland emission datasets.

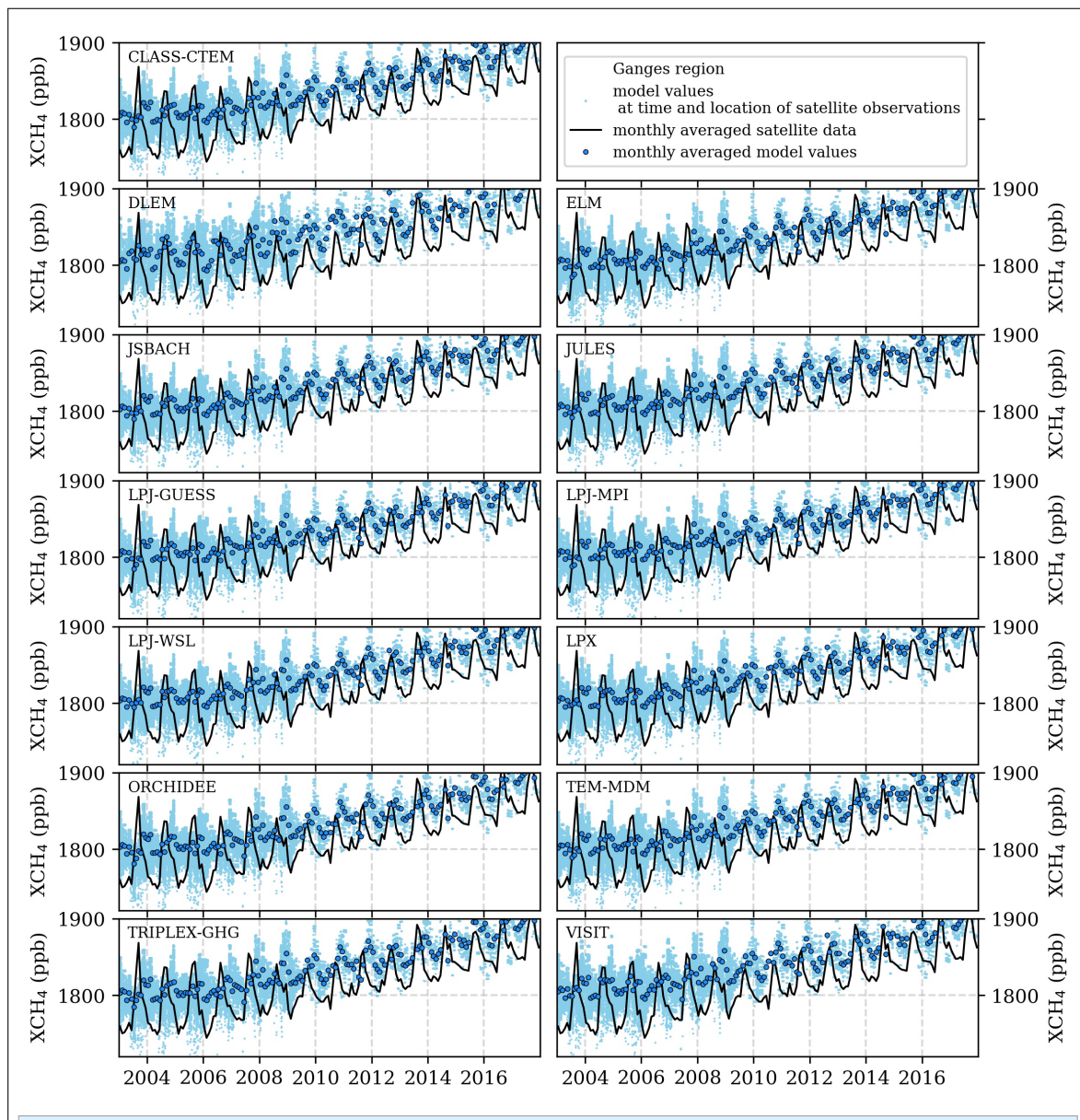


Figure A.21: Time series of modelled and measured XCH_4 in the Ganges region. Black data represent the median of monthly satellite XCH_4 observations. Panels show correlation to derived model runs based on the individual diagnostic wetland CH_4 emission datasets. Model values at specific time and location of the satellite observation as well as the median monthly concentrations from the runs are shown.

	CLASS-CTEM	DLEM	ELM	JS-BACH	JULES	LPJ-GUESS	LPJ-MPI	LPJ-WSL	LPX	ORCHIDEE	TEM-MDM	TRIPLEX	VISIT
R^2	0.873	0.729	0.859	0.864	0.867	0.849	0.881	0.869	0.879	0.860	0.865	0.865	0.870
RMSE	36.4	40.0	36.8	34.9	36.3	36.1	36.6	35.6	35.4	35.0	35.3	34.6	36.7

Table A.13: Correlation coefficients R^2 and root mean square errors (RMSE in ppb) derived for the correlation of satellite XCH_4 observations with modelled concentrations over the Ganges region based on the diagnostic wetland emission datasets.

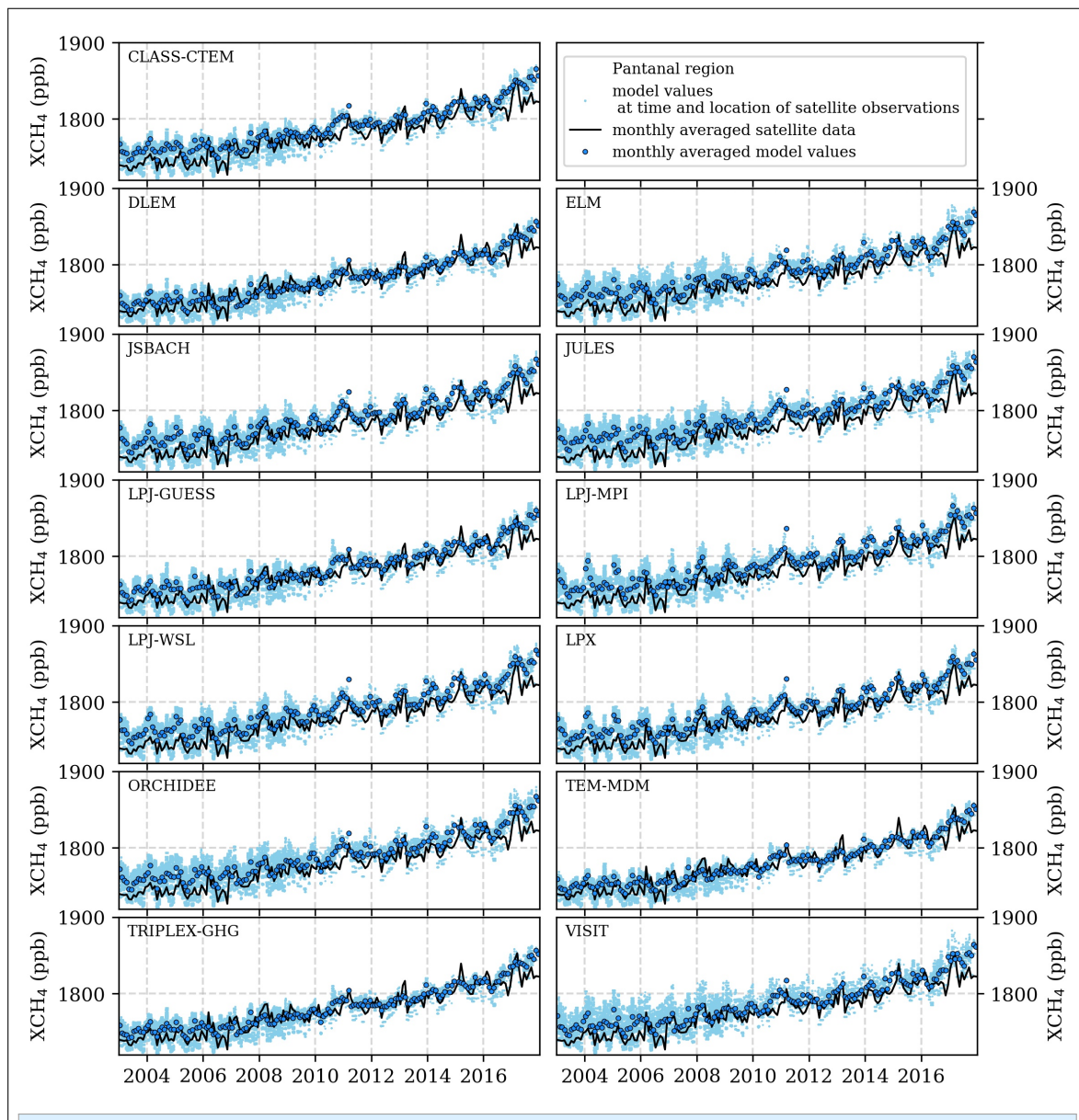


Figure A.22: Time series of modelled and measured XCH₄ in the Pantanal region. Black data represent the median of monthly satellite XCH₄ observations. Panels shows correlation to derived model runs based on the individual diagnostic wetland CH₄ emission datasets. Model values at specific time and location of the satellite observation as well as the median monthly concentrations from the runs are shown.

	CLASS-CTEM	DLEM	ELM	JS-BACH	JULES	LPJ-GUESS	LPJ-MPI	LPJ-WSL	LPX	ORCH-IDEE	TEM-MDM	TRIP-LEX	VISIT
R^2	0.621	0.865	0.558	0.641	0.635	0.575	0.570	0.642	0.651	0.568	0.608	0.610	0.682
RMSE	15.9	11.1	17.8	16.7	19.4	13.9	18.1	17.6	16.2	16.7	11.2	11.5	15.1

Table A.14: Correlation coefficients R^2 and root mean square errors (RMSE in ppb) derived for the correlation of satellite XCH₄ observations with modelled concentrations over the Pantanal region based on the diagnostic wetland emission datasets.

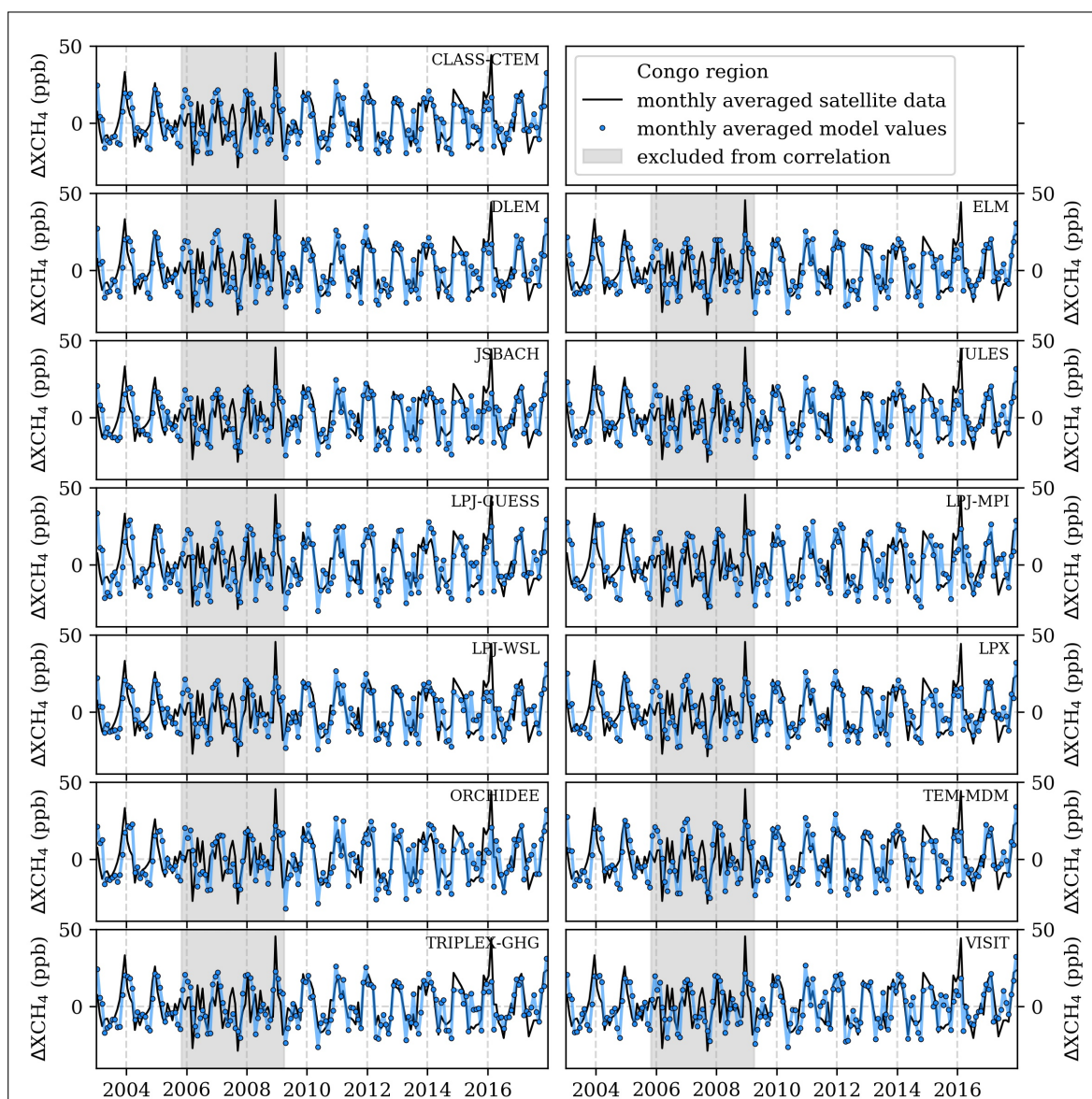


Figure A.23: Time series of de-trended XCH₄ seasonality in the Congo region. Black data represent monthly median XCH₄ variation derived via satellite. Panels include resulting data from model runs based on the individual diagnostic wetland emission datasets. The grey shaded area indicates months excluded from performed data correlations.

	CLASS-CTEM	DLEM	ELM	JS-BACH	JULES	LPJ-GUESS	LPJ-MPI	LPJ-WSL	LPX	ORCH-IDEE	TEM-MDM	TRIP-LEX	VISIT
R^2	0.562	0.557	0.548	0.468	0.480	0.482	0.409	0.525	0.548	0.437	0.561	0.550	0.460
RMSE	9.1	9.5	9.5	10.2	10.2	11.3	12.4	9.6	9.3	11.3	9.6	9.3	10.4

Table A.15: Correlation coefficients R^2 and root mean square errors (RMSE in ppb) derived for the correlation of satellite de-trended annual XCH₄ variation over the Congo region with modelled data based on the diagnostic wetland emission datasets. Data derived between November 2005 and April 2009 were excluded from the correlations due to detector degradation in the SCIAMACHY instrument.

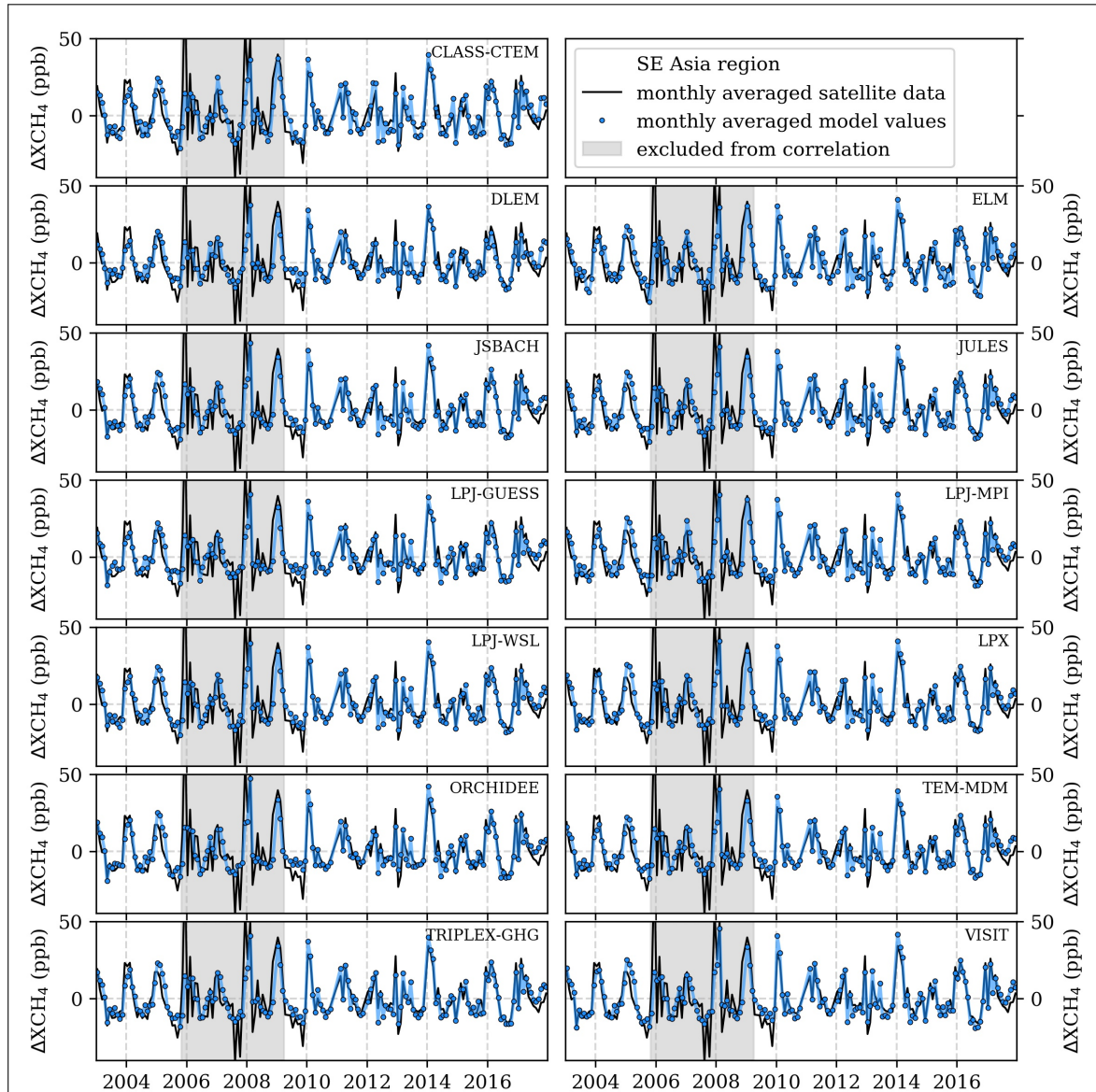


Figure A.24: Time series of de-trended XCH₄ seasonality in the Southeast Asian region. Black data represent monthly median XCH₄ variation derived via satellite. Panels include resulting data from model runs based on the individual diagnostic wetland emission datasets. The grey shaded area indicates months excluded from performed data correlations.

	CLASS-CTEM	DLEM	ELM	JS-BACH	JULES	LPJ-GUESS	LPJ-MPI	LPJ-WSL	LPX	ORCH-IDEE	TEM-MDM	TRIP-LEX	VISIT
R²	0.784	0.786	0.789	0.821	0.818	0.788	0.800	0.826	0.829	0.803	0.815	0.821	0.825
RMSE	6.3	6.0	6.3	5.7	5.7	6.0	5.9	5.5	5.5	5.9	5.6	5.6	5.7

Table A.16: Correlation coefficients R^2 and root mean square errors (RMSE in ppb) derived for the correlation of satellite de-trended annual XCH₄ variation over the Southeast Asian region with modelled data based on the diagnostic wetland emission datasets. Data derived between November 2005 and April 2009 were excluded from the correlations due to detector degradation in the SCIAMACHY instrument.

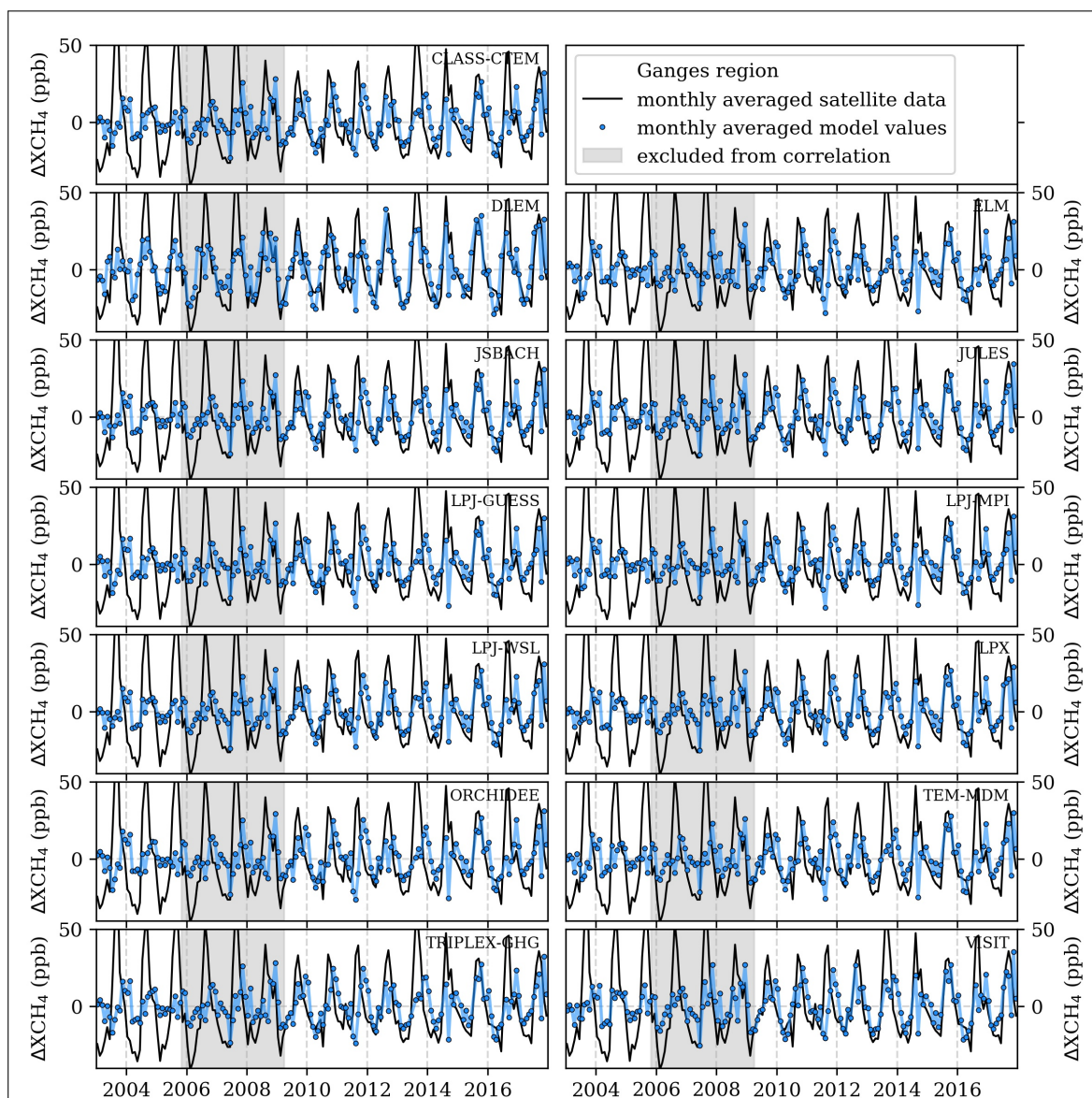


Figure A.25: Time series of de-trended XCH_4 seasonality in the Ganges region. Black data represent monthly median XCH_4 variation derived via satellite. Panels include resulting data from model runs based on the individual diagnostic wetland emission datasets. The grey shaded area indicates months excluded from performed data correlations.

	CLASS-CTEM	DLEM	ELM	JS-BACH	JULES	LPJ-GUESS	LPJ-MPI	LPJ-WSL	LPX	ORCHIDEE	TEM-MDM	TRIPLEX	VISIT
R^2	0.011	0.354	0.025	0.151	0.136	0.039	0.031	0.147	0.162	0.034	0.083	0.092	0.240
RMSE	23.1	19.6	25.1	22.5	22.8	24.7	24.8	22.5	22.3	24.9	23.6	23.5	21.2

Table A.17: Correlation coefficients R^2 and root mean square errors (RMSE in ppb) derived for the correlation of satellite de-trended annual XCH_4 variation over the Ganges region with modelled data based on the diagnostic wetland emission datasets. Data derived between November 2005 and April 2009 were excluded from the correlations due to detector degradation in the SCIAMACHY instrument.

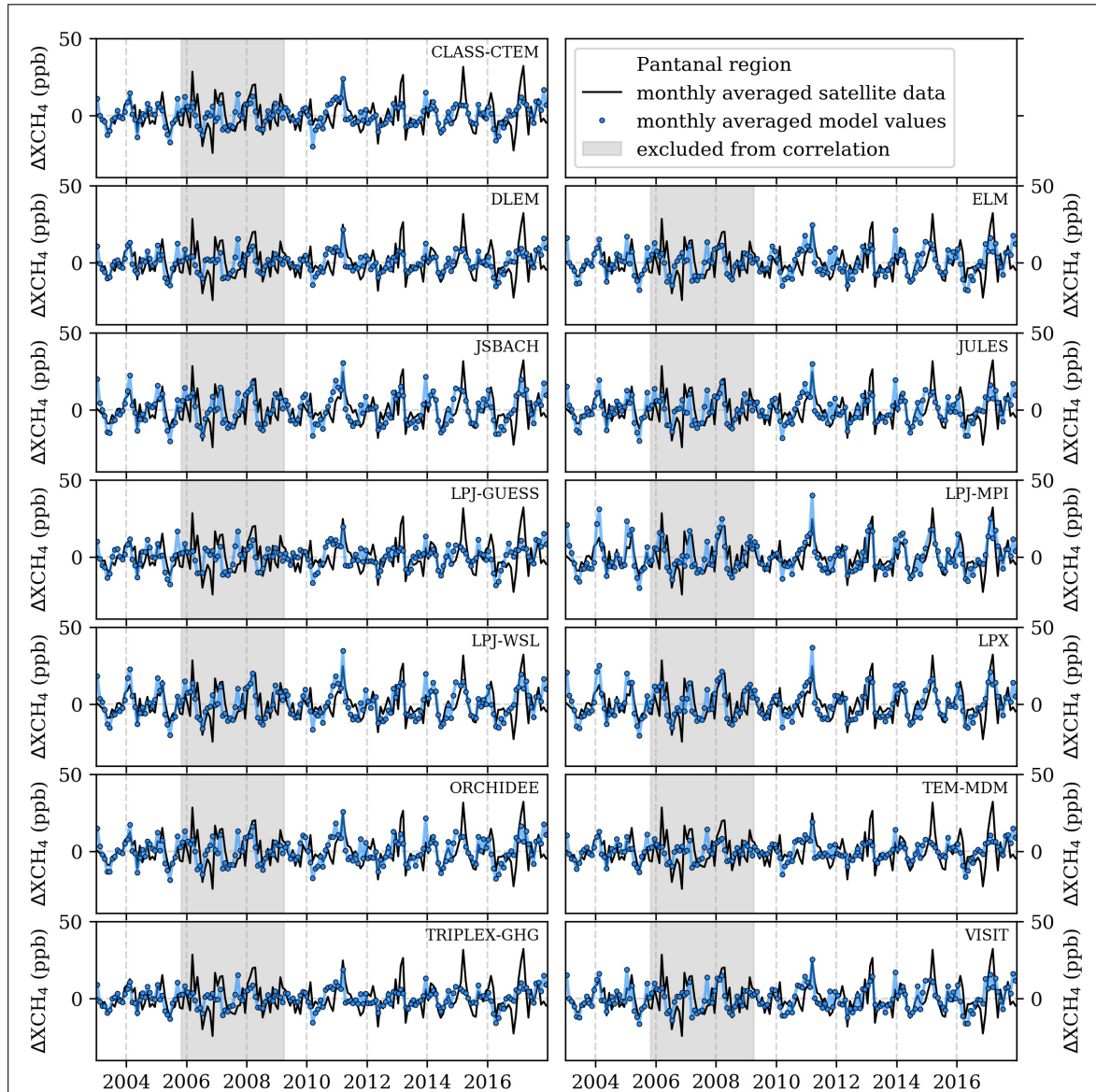


Figure A.26: Time series of de-trended XCH₄ seasonality in the Pantanal region. Black data represent monthly median XCH₄ variation derived via satellite. Panels include resulting data from model runs based on the individual diagnostic wetland emission datasets. The grey shaded area indicates months excluded from performed data correlations.

	CLASS-CTEM	DLEM	ELM	JS-BACH	JULES	LPJ-GUESS	LPJ-MPI	LPJ-WSL	LPX	ORCHIDEE	TEM-MDM	TRIPLEX	VISIT
R^2	0.295	0.225	0.276	0.346	0.313	0.164	0.478	0.371	0.449	0.273	0.236	0.226	0.321
RMSE	7.9	8.2	8.5	8.5	8.2	9.0	7.7	8.3	7.7	8.5	8.1	8.1	8.0

Table A.18: Correlation coefficients R^2 and root mean square errors (RMSE in ppb) derived for the correlation of satellite de-trended annual XCH₄ variation over the Pantanal region with modelled data based on the diagnostic wetland emission datasets. Data derived between November 2005 and April 2009 were excluded from the correlations due to detector degradation in the SCIAMACHY instrument.

References

- G. Abril and A. V. Borges. Ideas and perspectives: Carbon leaks from flooded land: do we need to replumb the inland water active pipe? *Biogeosciences*, 16(3):769–784, 2019. DOI: 10.5194/bg-16-769-2019.
- W. H. Adey and K. Loveland. The Input of Organic Energy: Particulates and Feeding. In *Dynamic Aquaria (Third Edition)*, pages 93–100. Academic Press, London, 2007. DOI: 10.1016/B978-0-12-370641-6.50015-7.
- G. H. Allen and T. M. Pavelsky. Global extent of rivers and streams. *Science*, 361:585–588, 2018. DOI: 10.1126/science.aat0636.
- A. Andersson, A. Rutgersson, and E. Sahlee. Using eddy covariance to estimate air-sea gas transfer velocity for oxygen. *Journal of Marine Systems*, 159:67–75, 2016. DOI: 10.1016/j.jmarsys.2016.02.008.
- D. Archer, M. Eby, V. Brovkin, A. Ridgwell, L. Cao, U. Mikolajewicz, K. Caldeira, K. Matsumoto, G. Munhoven, A. Montenegro, and K. Tokos. Atmospheric lifetime of fossil fuel carbon dioxide. *Annual Review of Earth and Planetary Sciences*, 37(1):117–134, 2009. DOI: 10.1146/annurev.earth.031208.100206.
- V. K. Arora, J. R. Melton, and D. Plummer. An assessment of natural methane fluxes simulated by the class-ctem model. *Biogeosciences*, 15(15):4683–4709, 2018. DOI: 10.5194/bg-15-4683-2018.
- W. Äschbach-Herting. Gasaustausch - Lösungsgleichgewicht zwischen Gas- und Wasserphase. *Script Uni Heidelberg*, pages 95–101, 2014.
- A. K. Aufdenkampe, E. Mayorga, P. A. Raymond, J. M. Melack, S. C. Doney, S. R. Alin, R. E. Aalto, and K. Yoo. Riverine coupling of biogeochemical cycles between land, oceans and atmosphere. *Front Ecol Environ*, 2011. DOI: 10.1890/100014.
- D. Bade. Gas exchange at the air–water interface. In G. E. Likens, editor, *Encyclopedia of Inland Waters*, pages 70–78. Academic Press, Oxford, 2009. DOI: 10.1016/B978-012370626-3.00213-1.
- N. Bândă, M. Krol, M. van Weele, T. van Noije, P. Le Sager, and T. Röckmann. Can we explain the observed methane variability after the Mount Pinatubo eruption? *Atmospheric Chemistry and Physics*, 16(1):195–214, 2016. DOI: 10.5194/acp-16-195-2016.
- A. Barendregt. *Tidal Freshwater Wetlands, the Fresh Dimension of the Estuary*, pages 1–14. Springer Netherlands, Dordrecht, 2016. DOI: 10.1007/978-94-007-6173-5_103-2.
- D. Bastviken, A. L. Santoro, H. Marotta, L. Q. Pinho, D. F. Calheiros, P. Crill, and A. Enrich-Prast. Methane Emissions from Pantanal, South America, during the Low Water Season: Toward More Comprehensive Sampling. *Environmental Science & Technology*, 44(14): 5450–5455, 2010. DOI: 10.1021/es1005048.
- A. Baum, T. Rixen, and J. Samiaji. Relevance of peat draining rivers in central Sumatra for the riverine input of dissolved organic carbon into the ocean. *Estuarine, Coastal and Shelf Science*, 73:563–570, 2007. DOI: 10.1016/j.ecss.2007.02.012.

References

- J. J. Beaulieu, W. D. Shuster, and J. A. Rebbholz. Controls on gas transfer velocities in a large river. *Journal of Geophysical Research*, 2012. DOI: 10.1029/2011JG001794.
- D. J. Beerling, E. P. Kantzas, M. R. Lomas, P. Wade, R. M. Eufrazio, P. Renforth, B. Sarkar, M. G. Andrews, R. H. James, R. H. James, C. R. Pearce, J.-F. Mercure, H. Pollitt, P. B. Holden, N. R. Edwards, M. Khanna, L. Koh, S. Quegan, N. F. Pidgeon, I. A. Janssens, J. Hansen, and S. A. Banwart. Potential for large-scale CO₂ removal via enhanced rock weathering with croplands. *Nature*, 583, 2020. DOI: 10.1038/s41586-020-2448-9.
- C. Biasi, S. E. Lind, N. M. Pekkarinen, J. T. Huttunen, N. J. Shurpali, N. P. Hyvönen, M. E. Repo, and P. J. Martikainen. Direct experimental evidence for the contribution of lime to CO₂ release from managed peat soil. *Soil Biology and Biochemistry*, 40(10):2660–2669, 2008. DOI: 10.1016/j.soilbio.2008.07.011.
- A. V. Borges, F. Darchambeau, C. R. Teodoru, T. R. Marwick, F. Tamooh, N. Geeraert, F. O. Omengo, F. Guérin, T. Lambert, C. Morana, E. Okuku, and S. Bouillon. Globally significant greenhouse-gas emissions from African inland waters. *Nature Geoscience*, 2015. DOI: 10.1038/ngeo2486.
- P. Bousquet, P. Ciais, J. B. Miller, E. J. Dlugokencky, D. A. Hauglustaine, C. Prigent, G. R. Van der Werf, P. Peylin, E.-G. Brunke, C. Carouge, R. L. Langenfelds, J. Lathière, F. Papa, M. Ramonet, M. Schmidt, L. P. Steele, S. C. Tyler, and J. White. Contribution of anthropogenic and natural sources to atmospheric methane variability. *Nature*, 443, 2006. DOI: 10.1038/nature05132.
- H. Bovensmann, J. P. Burrows, M. Buchwitz, J. Frerick, S. Noël, V. V. Rozanov, K. V. Chance, and A. P. H. Goede. SCIAMACHY: Mission Objectives and Measurement Modes. *Journal of the Atmospheric Sciences*, 56(2):127–150, 1999. DOI: 10.1175/1520-0469(1999)056<0127:SMOAMM>2.0.CO;2.
- M. Buchwitz, R. de Beek, J. P. Burrows, H. Bovensmann, T. Warneke, J. Notholt, J. F. Meirink, A. P. H. Goede, P. Bergamaschi, S. Körner, M. Heimann, and A. Schulz. Atmospheric methane and carbon dioxide from sciamachy satellite data: initial comparison with chemistry and transport models. *Atmospheric Chemistry and Physics*, 5(4):941–962, 2005. DOI: 10.5194/acp-5-941-2005.
- M. Buchwitz, M. Reuter, O. Schneising, H. Bovensmann, J. P. Burrows, H. Boesch, J. Anand, R. Parker, R. G. Detmers, I. Aben, O. P. Hasekamp, C. Crevoisier, R. Armante, C. Zehner, and D. Schepers. Copernicus Climate Change Service (C3S) Global Satellite Observations of Atmospheric Carbon Dioxide and Methane. *Advances in Astronautics Science and Technology*, 1, 2018. DOI: 10.1007/s42423-018-0004-6.
- J. Burrows, E. Hölzle, A. Goede, H. Visser, and W. Fricke. SCIAMACHY—scanning imaging absorption spectrometer for atmospheric cartography. *Acta Astronautica*, 35(7):445–451, 1995. DOI: 10.1016/0094-5765(94)00278-T.
- D. Butman and P. A. Raymond. Significant efflux of carbon dioxide from streams and rivers in the United States. *Nature Geoscience*, 4, 2011. DOI: 10.1038/ngeo1294.

- J.-R. B. Bwangoy, M. C. Hansen, D. P. Roy, G. D. Grandi, and C. O. Justice. Wetland mapping in the Congo Basin using optical and radar remotely sensed data and derived topographical indices. *Remote Sensing of Environment*, 114(1):73–86, 2010. DOI: 10.1016/j.rse.2009.08.004.
- G. Cauwet. *Determination of dissolved organic carbon and nitrogen by high temperature combustion*, chapter 15, pages 407–420. John Wiley & Sons, Ltd, 1999. DOI: 10.1002/9783527613984.ch15.
- P. Ciais, C. Sabine, G. Bala, L. Bopp, V. Brovkin, J. Canadell, A. Chhabra, R. DeFries, J. Galloyay, M. Heimann, C. Jones, C. Le Quéré, R. Myneni, S. Piao, and P. Thornton. *Carbon and Other Biogeochemical Cycles*, page 465–570. Cambridge University Press, 2013. DOI: 10.1017/CBO9781107415324.015.
- J. J. Cole, Y. T. Prairie, N. F. Caraco, W. H. McDowell, L. J. Tranvik, R. G. Striegl, C. M. Duarte, P. Kortelainen, J. A. Downing, J. J. Middelburg, and J. Melack. Plumbing the global carbon cycle. *Ecosystems*, 2007. DOI: 10.1007/s10021-006-9013-8.
- H. J. Dalmagro, P. H. Zanella de Arruda, G. L. Vourlitis, M. J. Lathuillière, J. de S. Nogueira, E. G. Couto, and M. S. Johnson. Radiative forcing of methane fluxes offsets net carbon dioxide uptake for a tropical flooded forest. *Global Change Biology*, 25(6):1967–1981, 2019. DOI: 10.1111/gcb.14615.
- H. de Coninck, A. Revi, M. Babiker, P. Bertoldi, M. Buckeridge, A. Cartwright, W. Dong, J. Ford, S. Fuss, J.-C. Hourcade, D. Ley, R. Mechler, P. Newman, A. Revokatova, S. Schultz, L. Steg, and T. Sugiyama. Strengthening and Implementing the Global Response. In: *Global Warming of 1.5°C. An IPCC Special Report on the impacts of global warming of 1.5°C above pre-industrial levels and related global greenhouse gas emission pathways, in the context of strengthening the global response to the threat of climate change, sustainable development, and efforts to eradicate poverty*, 2018. URL <https://www.ipcc.ch/sr15/>.
- D. P. Dee, S. M. Uppala, A. J. Simmons, P. Berrisford, P. Poli, S. Kobayashi, U. Andrae, M. A. Balmaseda, G. Balsamo, P. Bauer, P. Bechtold, A. C. M. Beljaars, L. van de Berg, J. Bidlot, N. Bormann, C. Delsol, R. Dragani, M. Fuentes, A. J. Geer, L. Haimberger, S. B. Healy, H. Hersbach, E. V. Hólm, L. Isaksen, P. Kållberg, M. Köhler, M. Matricardi, A. P. McNally, B. M. Monge-Sanz, J.-J. Morcrette, B.-K. Park, C. Peubey, P. de Rosnay, C. Tavolato, J.-N. Thépaut, and F. Vitart. The ERA-Interim reanalysis: configuration and performance of the data assimilation system. *Quarterly Journal of the Royal Meteorological Society*, 137(656): 553–597, 2011. DOI: 10.1002/qj.828.
- E. Dlugokencky. Trends in atmospheric methane, national oceanic & atmospheric administration, earth system research laboratory (noaa/esrl), 2021. URL www.esrl.noaa.gov/gmd/ccgg/trends_ch4/.
- E. Dlugokencky and P. Tans. Trends in atmospheric carbon dioxide, national oceanic & atmospheric administration, earth system research laboratory (noaa/esrl), 2021. URL www.esrl.noaa.gov/gmd/ccgg/trends/global.html.
- V. Eyring, S. Bony, G. A. Meehl, C. A. Senior, B. Stevens, R. J. Stouffer, and K. E. Taylor. Overview of the Coupled Model Intercomparison Project Phase 6 (CMIP6) experimental

References

- design and organization. *Geoscientific Model Development*, 9(5):1937–1958, 2016. DOI: 10.5194/gmd-9-1937-2016.
- C. Fang and J. Moncrieff. A model for soil CO₂ production and transport 1:: Model development. *Agricultural and Forest Meteorology*, 95(4):225 – 236, 1999. DOI 10.1016/S0168-1923(99)00036-2.
- L. G. Fenoll, J. N. Rodríguez-López, F. García-Molina, F. García-Cánovas, and J. Tudela. Michaelis constants of mushroom tyrosinase with respect to oxygen in the presence of monophenols and diphenols. *The International Journal of Biochemistry & Cell Biology*, 34(4):332–336, 2002. DOI: 10.1016/S1357-2725(01)00133-9.
- C. B. Field and K. J. Mach. Rightsizing carbon dioxide removal. *Science*, 356(6339):706–707, 2017. DOI: 10.1126/science.aam9726.
- C. M. Finlayson. *Freshwater Marshes and Swamps*, pages 1–14. Springer Netherlands, Dordrecht, 2016a. DOI: 10.1007/978-94-007-6173-5_200-1.
- C. M. Finlayson. *Mangroves*, pages 1–16. Springer Netherlands, Dordrecht, 2016b. DOI: 10.1007/978-94-007-6173-5_258-1.
- C. Freeman, N. Ostle, and H. Kang. An enzymic ‘latch’ on a global carbon store. *Nature*, 409: 149, 2001. DOI: 10.1038/35051650.
- C. Freeman, N. Ostle, N. Fenner, and H. Kang. A regulatory role for phenol oxidase during decomposition in peatlands. *Soil Biology and Biochemistry*, 36(10):1663 – 1667, 2004. DOI: 10.1016/j.soilbio.2004.07.012.
- P. Friedlingstein, M. W. Jones, M. O’Sullivan, R. M. Andrew, J. Hauck, G. P. Peters, W. Peters, J. Pongratz, S. Sitch, C. Le Quéré, D. C. E. Bakker, J. G. Canadell, P. Ciais, R. B. Jackson, P. Anthoni, L. Barbero, A. Bastos, V. Bastrikov, M. Becker, L. Bopp, E. Buitenhuis, N. Chandra, F. Chevallier, L. P. Chini, K. I. Currie, R. A. Feely, M. Gehlen, D. Gilfillan, T. Gkritzalis, D. S. Goll, N. Gruber, S. Gutekunst, I. Harris, V. Haverd, R. A. Houghton, G. Hurtt, T. Ilyina, A. K. Jain, E. Joetzjer, J. O. Kaplan, E. Kato, K. Klein Goldewijk, J. I. Korsbakken, P. Landschützer, S. K. Lauvset, N. Lefèvre, A. Lenton, S. Lienert, D. Lombardozzi, G. Marland, P. C. McGuire, J. R. Melton, N. Metzl, D. R. Munro, J. E. M. S. Nabel, S.-I. Nakaoka, C. Neill, A. M. Omar, T. Ono, A. Peregon, D. Pierrot, B. Poulter, G. Rehder, L. Resplandy, E. Robertson, C. Rödenbeck, R. Séférian, J. Schwinger, N. Smith, P. P. Tans, H. Tian, B. Tilbrook, F. N. Tubiello, G. R. van der Werf, A. J. Wiltshire, and S. Zaehle. Global carbon budget 2019. *Earth System Science Data*, 11(4):1783–1838, 2019. DOI: 10.5194/essd-11-1783-2019.
- GeoTech. Multi 3420 digital meter for digital ids sensors. Operating Manual, 2015. URL www.wtw.com.
- Global Forest Watch. Global peatlands, 2019. URL <https://www.arcgis.com/home/item.html?id=f7cf86a081ff48c794edeb5a2d9dbfa7>.
- M. Gottwald, H. Bovensmann, G. Lichtenberg, S. Noel, A. von Bargaen, S. Slijkhuis, A. Piters, R. Hoogeveen, C. von Savigny, M. Buchwitz, A. Kokhanovsky, A. Richter, A. Rozanov, T. Holzer-Popp, K. Bramstedt, J.-C. Lambert, J. Skupin, F. Wittrock, H. Schrijver, and

- J. Burrows. *SCIAMACHY's View of the Earth's Atmosphere*, chapter 10, pages 119–145. Published by DLR, 2006a. url: https://atmos.eoc.dlr.de/projects/scops/sciamachy_book/sciamachy_book.html.
- M. Gottwald, H. Bovensmann, G. Lichtenberg, S. Noel, A. von Bargaen, S. Slijkhuis, A. Pipers, R. Hoogeveen, C. von Savigny, M. Buchwitz, A. Kokhanovsky, A. Richter, A. Rozanov, T. Holzer-Popp, K. Bramstedt, J.-C. Lambert, J. Skupin, F. Wittrock, H. Schrijver, and J. Burrows. *ENVISAT - SCIAMACHY' Host*, chapter 2, pages 23–30. Published by DLR, 2006b. URL: https://atmos.eoc.dlr.de/projects/scops/sciamachy_book/sciamachy_book.html.
- M. Gottwald, H. Bovensmann, G. Lichtenberg, S. Noel, A. von Bargaen, S. Slijkhuis, A. Pipers, R. Hoogeveen, C. von Savigny, M. Buchwitz, A. Kokhanovsky, A. Richter, A. Rozanov, T. Holzer-Popp, K. Bramstedt, J.-C. Lambert, J. Skupin, F. Wittrock, H. Schrijver, and J. Burrows. *Instrument Operations*, chapter 4, pages 23–30. Published by DLR, 2006c. url: https://atmos.eoc.dlr.de/projects/scops/sciamachy_book/sciamachy_book.html.
- L. Hannah. Chapter 19 - carbon sinks and sources. In L. Hannah, editor, *Climate Change Biology (Second Edition)*, pages 403–422. Academic Press, Boston, 2015. DOI: 10.1016/B978-0-12-420218-4.00019-6.
- J. Hansen, L. Nazarenko, R. Ruedy, M. Sato, J. Willis, A. Del Genio, D. Koch, A. Lacis, K. Lo, S. Menon, T. Novakov, J. Perlwitz, G. Russell, G. A. Schmidt, and N. Tausnev. Earth's energy imbalance: Confirmation and implications. *Science*, 308(5727):1431–1435, 2005. DOI: 10.1126/science.1110252.
- D. Hartmann, A. Klein Tank, M. Rusticucci, L. Alexander, S. Brönnimann, Y. Charabi, F. Dentener, E. Dlugokencky, D. Easterling, A. Kaplan, B. Soden, P. Thorne, M. Wild, and P. Zhai. *Observations: Atmosphere and Surface*, book section 2, page 159–254. Cambridge University Press, 2013a. DOI: 10.1017/CBO9781107415324.008.
- J. Hartmann, A. J. West, P. Renforth, P. Köhler, C. L. De La Rocha, D. A. Wolf-Gladrow, H. H. Dürr, and J. Scheffran. Enhanced chemical weathering as a geoengineering strategy to reduce atmospheric carbon dioxide, supply nutrients, and mitigate ocean acidification. *Reviews of Geophysics*, 51(2):113–149, 2013b. DOI: 10.1002/rog.20004.
- P. Hausmann, R. Sussmann, and D. Smale. Contribution of oil and natural gas production to renewed increase in atmospheric methane (2007–2014): top–down estimate from ethane and methane column observations. *Atmospheric Chemistry and Physics*, 16(5):3227–3244, 2016. DOI: 10.5194/acp-16-3227-2016.
- G. D. Hayman, F. M. O'Connor, M. Dalvi, D. B. Clark, N. Gedney, C. Huntingford, C. Prigent, M. Buchwitz, O. Schneising, J. P. Burrows, C. Wilson, N. Richards, and M. Chipperfield. Comparison of the hadgem2 climate-chemistry model against in situ and sciamachy atmospheric methane data. *Atmospheric Chemistry and Physics*, 14(23):13257–13280, 2014. DOI: 10.5194/acp-14-13257-2014.
- L. L. Hess, J. M. Melack, A. G. Affonso, C. Barbosa, M. Gastil-Buhl, and E. M. L. M. Novo. Wetlands of the Lowland Amazon Basin: Extent, Vegetative Cover, and Dual-season Inundated Area as Mapped with JERS-1 Synthetic Aperture Radar. *Wetlands*, 35(4), 2015. DOI: 10.1007/s13157-015-0666-y.

- A. Hooijer, M. Silvius, and S. P. H. Wösten, and. PEAT-CO₂, Assessment of CO₂ emissions from drained peatlands in SE Asia. *Delft Hydraulics report Q3943*, 2006. URL https://www.researchgate.net/publication/285726396_PEAR-CO2_assessment_of_CO2_emissions_from_drained_peatlands_in_SE_Asia.
- A. Hooijer, S. Page, J. G. Canadell, M. Silvius, J. Kwadijk, H. Wösten, and J. Jauhiainen. Current and future CO₂ emissions from drained peatlands in Southeast Asia. *Biogeosciences*, 7(5): 1505–1514, 2010. DOI: 10.5194/bg-7-1505-2010.
- C. A. Horowitz. Paris Agreement. *International Legal Materials*, 55(4):740–755, 2016. DOI: 10.1017/S0020782900004253.
- S. Houweling, T. Kaminski, F. Dentener, J. Lelieveld, and M. Heimann. Inverse modeling of methane sources and sinks using the adjoint of a global transport model. *Journal of Geophysical Research: Atmospheres*, 104(D21):26137–26160, 1999. DOI: 10.1029/1999JD900428.
- B. Huang, P. W. Thorne, V. F. Banzon, T. Boyer, G. Chepurin, J. H. Lawrimore, M. J. Menne, T. M. Smith, R. S. Vose, , and H.-M. Zhang. Noaa extended reconstructed sea surface temperature (ersst), version 5: Noaa national centers for environmental information., 2017. DOI: 10.7289/V5T72FNM.
- V. Huijnen, J. Williams, M. van Weele, T. van Noije, M. Krol, F. Dentener, A. Segers, S. Houweling, W. Peters, J. de Laat, F. Boersma, P. Bergamaschi, P. van Velthoven, P. Le Sager, H. Eskes, F. Alkemade, R. Scheele, P. Nédélec, and H.-W. Pätz. The global chemistry transport model tm5: description and evaluation of the tropospheric chemistry version 3.0. *Geoscientific Model Development*, 3(2):445–473, 2010. DOI: 10.5194/gmd-3-445-2010.
- M. P. Humphreys, L. Gregor, D. Pierrot, S. M. A. C. van Heuven, E. R. Lewis, and D. W. R. Wallace. PyCO₂SYs: marine carbonate system calculations in Python., 2020. DOI: 10.5281/zenodo.4757055.
- Indonesia Ministry of Agriculture. Indonesia peat lands., 2012. URL <http://www.cifor.org/pid/6419>.
- S. N. Islam. Deltaic floodplains development and wetland ecosystems management in the Ganges–Brahmaputra–Meghna Rivers Delta in Bangladesh. *Sustainable Water Resources Management*, 2, 2016. DOI: 10.1007/s40899-016-0047-6.
- A. Ito and M. Inatomi. Use of a process-based model for assessing the methane budgets of global terrestrial ecosystems and evaluation of uncertainty. *Biogeosciences*, 9(2):759–773, 2012. DOI: 10.5194/bg-9-759-20120.
- B. Jähne, K. O. Münnich, R. Bösinger, A. Dutzi, W. Huber, and P. Libner. On the parameters influencing air-water gas exchange. *Journal of Geophysical Research: Oceans*, 92(C2): 1937–1949, 1987. DOI: 10.1029/JC092iC02p01937.
- F. Joos and R. Spahni. Rates of change in natural and anthropogenic radiative forcing over the past 20,000 years. *Proceedings of the National Academy of Sciences*, 105(5):1425–1430, 2008. DOI: 10.1073/pnas.0707386105.

- H. Kang, M. J. Kwon, S. Kim, J. Lee, Seunghoon Rogelj, T. G. Jones, A. C. Johncock, A. Haraguchi, and C. Freeman. Biologically driven DOC release from peatlands during recovery from acidification. *Nature Communications*, 9, 2018. DOI: 10.1038/s41467-018-06259-1.
- J. O. Kaplan, G. Folberth, and D. A. Hauglustaine. Role of methane and biogenic volatile organic compound sources in late glacial and holocene fluctuations of atmospheric methane concentrations. *Global Biogeochemical Cycles*, 20(2), 2006. DOI: 10.1029/2005GB002590.
- M. Kasuya, M. Nakajima, and T. Hamazaki. Greenhouse gases observing satellite (gosat) program overview and its development status. *Transactions of the Japan society for aeronautic and space science, space technology Japan*, 7(ists26), 2009. DOI: 10.2322/tstj.7.To_4_5.
- M. Keiluweit, P. S. Nico, M. Kleber, and S. Fendorf. Are oxygen limitations under recognized regulators of organic carbon turnover in upland soils? *Biogeochemistry*, 2016. DOI: 10.1007/s10533-015-0180-6.
- J. Keller. Wetlands and the global carbon cycle: what might the simulated past tell us about the future? *New Phytologist*, 192(4):789–792, 2011. DOI: 10.1111/j.1469-8137.2011.03954.x.
- M. Khalil and R. Rasmussen. The global cycle of carbon monoxide: Trends and mass balance. *Chemosphere*, 20(1):227–242, 1990. DOI: 10.1016/0045-6535(90)90098-E.
- S. Kirschke, P. Bousquet, P. Ciais, M. Saunois, J. G. Canadell, E. J. Dlugokencky, P. Bergamaschi, D. Bergmann, D. R. Blake, L. Bruhwiler, P. Cameron-Smith, S. Castaldi, F. Chevallier, L. Feng, A. Fraser, M. Heimann, E. L. Hodson, S. Houweling, B. Josse, P. J. Fraser, P. B. Krummel, J.-F. Lamarque, R. L. Langenfelds, C. Le Quéré, V. Naik, S. O’Doherty, P. I. Palmer, I. Pison, D. Plummer, B. Poulter, R. G. Prinn, M. Rigby, B. Ringeval, M. Santini, M. Schmidt, D. T. Shindell, I. J. Simpson, R. Spahni, L. P. Steele, S. A. Strode, K. Sudo, S. Szopa, G. R. van der Werf, A. Voulgarakis, M. van Weele, R. F. Weiss, J. E. Williams, and G. Zeng. Three decades of global methane sources and sinks. *Nature Geosci.*, 6:813–823, 2013. DOI: 10.1038/ngeo1955.
- T. Kleinen, V. Brovkin, and R. J. Schuldt. A dynamic model of wetland extent and peat accumulation: results for the holocene. *Biogeosciences*, 9(1):235–248, 2012. DOI: 10.5194/bg-9-235-2012.
- T. Kleinen, U. Mikolajewicz, and V. Brovkin. Terrestrial methane emissions from the last glacial maximum to the preindustrial period. *Climate of the Past*, 16(2):575–595, 2020. DOI: 10.5194/cp-16-575-2020.
- A. Klemme, T. Rixen, D. Müller-Dum, M. Müller, J. Notholt, and T. Warneke. CO₂ emissions from peat-draining rivers regulated by water pH. *Biogeosciences Discussions [preprint]*, 2021:1–20, in review, 2021. DOI: 10.5194/bg-2021-13.
- D. S. Kocabas, U. Bakir, S. E. V. Phillips, M. J. McPherson, and Z. B. Ogel. Purification, characterization, and identification of a novel bifunctional catalase-phenol oxidase from *Scytalidium thermophilum*. *Appl Microbiol Biotechnol*, 79:407–415, 2008. DOI: 10.1007/s00253-008-1437-y.

- P. Köhler, J. Hartmann, and D. A. Wolf-Gladrow. Geoengineering potential of artificially enhanced silicate weathering of olivine. *Proceedings of the National Academy of Sciences*, 107(47):20228–20233, 2010. DOI: 10.1073/pnas.1000545107.
- D. Kweku, O. Bismark, A. Maxwell, K. Desmond, K. Danso, E. Oti-Mensah, A. Quachie, and B. Adormaa. Greenhouse Effect: Greenhouse Gases and Their Impact on Global Warming. *Journal of Scientific Research and Reports*, 17(6):1–9, 2018. DOI: 10.9734/JSRR/2017/39630.
- G. Lambert and S. Schmidt. Reevaluation of the oceanic flux of methane: Uncertainties and long term variations. *Chemosphere*, 26(1):579–589, 1993. DOI: 10.1016/0045-6535(93)90443-9.
- R. Lauerwald, G. G. Laruelle, J. Hartmann, P. Ciais, and P. A. G. Regnier. Spatial patterns in CO₂ evasion from global river network. *Global Biogeochemical Cycles*, 29:534–554, 2015. DOI: 10.1002/2014GB004941.
- R. Lauerwald, P. Regnier, B. Guenet, P. Friedlingstein, and P. Ciais. How Simulations of the Land Carbon Sink Are Biased by Ignoring Fluvial Carbon Transfers: A Case Study for the Amazon Basin. *One Earth*, 3(2):226–236, 2020. DOI: 10.1016/j.oneear.2020.07.009.
- B. Lehner, K. Verdin, and A. Jarvis. HydroSHEDS, Technical Documentation. Version 1.0, Pages 1-27. Technical report, HydroSHEDS, 2006. URL <https://core.ac.uk/reader/5210660>.
- E. Lewis and D. W. R. Wallace. Program Developed for CO₂ System Calculations. *ORNL/CDIAC-105, Carbon Dioxide Information Analysis Center*, 1998. DOI: 10.15485/1464255.
- LI-COR Inc. Li-840a instruction manual. Lincoln Nebraska 68504, 2011. URL <https://www.licor.com/env/support/LI-840A/manuals.html>.
- P. Longobardi, A. Montenegro, H. Beltrami, and M. Eby. Deforestation induced climate change: Effects of spatial scale. *PLOS ONE*, 11(4):1–34, 04 2016. DOI: 10.1371/journal.pone.0153357.
- D. P. Loucks and E. van Beek. *Water Quality Modeling and Prediction*, pages 417–467. Springer International Publishing, Cham, 2017. DOI: 10.1007/978-3-319-44234-1_10.
- L. Louergue, A. Schilt, R. Spahni, V. Masson-Delmotte, T. Blunier, B. Lemieux, J.-M. Barnola, D. Raynaud, T. F. Stocker, and J. Chappellaz. Orbital and millennial-scale features of atmospheric CH₄ over the past 800,000 years. *Nature*, 453, 2008. DOI: 10.1038/nature06950.
- L.-N. Lyu, D. Lu, C. Sun, H. Ding, L.-M. Yu, and G.-P. Yang. A new software of calculating the pH values of coastal seawater: Considering the effects of low molecular weight organic acids. *Marine Chemistry*, 211:108–116, 2019. DOI: 10.1016/j.marchem.2019.03.011.
- M. Madigan and J. Martinko. *Brock Biology of Microorganisms*. Pearson Prentice Hall, Upper Saddle River, NJ., 11 edition, 2006. URL <https://www.academia.edu/43055809>.
- P. T. Martone, J. M. Estevez, F. Lu, K. Ruel, M. W. Denny, C. Somerville, and J. Ralph. Discovery of Lignin in Seaweed Reveals Convergent Evolution of Cell-Wall Architecture. *Current Biology*, 19(2):169 – 175, 2009. DOI: 10.1016/j.cub.2008.12.031.

- M. D. Mattson. *Biogeochemistry of inland waters*, chapter Alkalinity, pages 348–353. Elsevier, 2010. ISBN:9780128102244.
- A. D. McGuire, T. R. Christensen, D. Hayes, A. Heroult, E. Euskirchen, J. S. Kimball, C. Koven, P. Lafleur, P. A. Miller, W. Oechel, P. Peylin, M. Williams, and Y. Yi. An assessment of the carbon balance of arctic tundra: comparisons among observations, process models, and atmospheric inversions. *Biogeosciences*, 9(8):3185–3204, 2012. DOI: 10.5194/bg-9-3185-2012.
- P. Megonigal, M. Hines, and P. Visscher. Anaerobic Metabolism: Linkages to Trace Gases and Aerobic Processes. *Treatise on Geochemistry*, 8:317–424, 11 2003. DOI: 10.1016/B0-08-043751-6/08132-9.
- J. R. Melton and V. K. Arora. Competition between plant functional types in the canadian terrestrial ecosystem model (ctem) v. 2.0. *Geoscientific Model Development*, 9(1):323–361, 2016. DOI: 10.5194/gmd-9-323-2016.
- J. Miettinen, C. Shi, and S. C. Liew. Land cover distribution in the peatlands of Peninsular Malaysia, Sumatra and Borneo in 2015 with changes since 1990. *Global Ecology and Conservation*, 6:67–78, 2016. DOI: 10.1016/j.gecco.2016.02.004.
- R. J. Millar, J. S. Fuglestvedt, P. Friedlingstein, J. Rogelj, M. J. Grubb, H. D. Matthews, R. B. Skeie, P. M. Forster, D. J. Frame, and M. R. Allen. Emission budgets and pathways consistent with limiting warming to 1.5 °C. *Nature Geosci*, 10:741–747, 2017. DOI: 10.1038/ngeo3031.
- C. Mitchell, C. Hu, B. Bowler, D. Drapeau, and W. M. Balch. Estimating particulate inorganic carbon concentrations of the global ocean from ocean color measurements using a reflectance difference approach. *Journal of Geophysical Research: Oceans*, 122(11):8707–8720, 2017. DOI: 10.1002/2017JC013146.
- W. Mitsch and J. Gosselink. *Wetlands*. Wiley, 2015. ISBN 9781119019787.
- S. Moore, C. D. Evans, S. E. Tage, M. H. Garnett, T. G. Jones, C. Freeman, A. Hooijer, A. J. Wiltshire, S.H.Limin, and V. Gauci. Deep instability of deforsted tropical peatlands revealed by fluival organic carbon fluxes. *Nature*, 493:660–663, 2013. DOI: 10.1038/nature11818.
- D. Müller, T. Warneke, T. Rixen, M. Müller, S. Jamahari, N. Denis, A. Mujahid, and J. Notholt. Lateral carbon fluxes and CO₂ outgassing from a tropical peat-draining river. *Biogeosciences*, 12:5967–5979, 2015. DOI: 10.5194/bg-12-5967-2015.
- D. Müller, T. Warneke, T. Rixen, M. Müller, A. Mujahid, H. Bange, and J. Notholt. Fate of peat-derived carbon and associated CO₂ and CO emissions from two Southeast Asian estuaries. *Biogeosciences*, 2016. DOI: 10.5194/bg-12-8299-2015.
- D. Müller-Dum, T. Warneke, T. Rixen, M. Müller, A. Christodoulou, A. Baum, J. Oakes, B. D. Eyre, and J. Notholt. Impact of peatlands on carbon dioxide (CO₂) emissions from the Rajang River and Estuary, Malaysia. *Biogeosciences*, 16:17–32, 2018. DOI: 10.5194/bg-2018-391.
- G. Myhre, D. Shindell, F.-M. Bréon, W. Collins, J. Fuglestvedt, J. Huang, D. Koch, J.-F. Lamarque, D. Lee, B. Mendoza, T. Nakajima, A. Robock, G. Stephens, T. Takemura, and

References

- H. Zhang. *Anthropogenic and Natural Radiative Forcing*, book section 8, pages 659–740. Cambridge University Press, 2013. DOI: 10.1017/CBO9781107415324.008.
- S. Myriokefalitakis, N. Daskalakis, A. Gkouvousis, A. Hilboll, T. van Noije, J. E. Williams, P. Le Sager, V. Huijnen, S. Houweling, T. Bergman, J. R. Nüß, M. Vrekoussis, M. Kanakidou, and M. C. Krol. Description and evaluation of a detailed gas-phase chemistry scheme in the TM5-MP global chemistry transport model (r112). *Geoscientific Model Development*, 13 (11):5507–5548, 2020. DOI: 10.5194/gmd-13-5507-2020.
- E. G. Nisbet, E. J. Dlugokencky, M. R. Manning, D. Lowry, R. E. Fisher, J. L. France, S. E. Michel, J. B. Miller, J. W. C. White, B. Vaughn, P. Bousquet, J. A. Pyle, N. J. Warwick, M. Cain, R. Brownlow, G. Zazzeri, M. Lanoisellé, A. C. Manning, E. Gloor, D. E. J. Worthy, E.-G. Brunke, C. Labuschagne, E. W. Wolff, and A. L. Ganesan. Rising atmospheric methane: 2007–2014 growth and isotopic shift. *Global Biogeochemical Cycles*, 30(9):1356–1370, 2016. DOI: 10.1002/2016GB005406.
- S. E. Page, J. O. Rieley, and C. J. Banks. Global and regional importance of the tropical peatland carbon pool. *Global Change Biology*, 17:798–818, 2011. DOI: 10.1111/j.1365-2486.2010.02279.x.
- M. Pereira, A. Amaro, M. Pintado, and M. Poças. Modeling the effect of oxygen pressure and temperature on respiration rate of ready-to-eat rocket leaves. A probabilistic study of the Michaelis-Menten model. *Postharvest Biology and Technology*, 131:1 – 9, 2017. DOI: 10.1016/j.postharvbio.2017.04.006.
- A. Pind, C. Freeman, and M. A. Lock. Enzymic degradation phenolic materials in peatlands. *Plant and Soil*, 159:227–231, 1994. DOI: 10.1007/BF00009285.
- J. A. Prananto, B. Minasny, L.-P. Comeau, R. Rudiyanto, and P. Grace. Drainage increases CO₂ and N₂O emissions from tropical peat soils. *Global Change Biology*, 26(8):4583–4600, 2020. DOI: 10.1111/gcb.15147.
- P. A. Raymond, C. J. Zappa, D. Butman, T. L. Bott, J. Potter, P. Mulholland, A. E. Laursen, W. H. McDowell, and D. Newbold. Scaling the gas transfer velocity and hydraulic geometry in streams and small rivers. *Limnology and Oceanography: Fluids and Environments*, 2:41–53, 2012. DOI: 10.1215/21573689-1597669.
- P. A. Raymond, J. Hartmann, S. Sobek, M. Hoover, C. McDonald, D. Butman, R. Striegel, E. Mayorga, C. Humborg, P. Kortelainen, H. Dürr, M. Meybeck, P. Ciais, and P. Guth. Global carbon dioxide emissions from inland waters. *Nature*, 503:355–359, 2013. DOI: 10.1038/nature12760.
- K. R. Reddy and R. D. DeLaune. *Types of wetlands*, chapter 3.2, pages 31–34. CRC Press, 2008a. ISBN 978-1-56670-678-0.
- K. R. Reddy and R. D. DeLaune. *Wetland Soils*, chapter 3.4, pages 35–41. CRC Press, 2008b. ISBN 978-1-56670-678-0.
- K. R. Reddy and R. D. DeLaune. *Major Components of Carbon Cycle in Wetlands*, chapter 5.2, pages 114–119. CRC Press, 2008c. ISBN 978-1-56670-678-0.

- K. R. Reddy and R. D. DeLaune. *Characteristics of Detritus and soil organic matter*, chapter 5.4, pages 121–129. CRC Press, 2008d. ISBN 978-1-56670-678-0.
- K. R. Reddy and R. D. DeLaune. *Decomposition*, chapter 5.5, pages 129–151. CRC Press, 2008e. ISBN 978-1-56670-678-0.
- M. Reuter, H. Bösch, H. Bovensmann, A. Bril, M. Buchwitz, A. Butz, J. P. Burrows, C. W. O'Dell, S. Guerlet, O. Hasekamp, J. Heymann, N. Kikuchi, S. Oshchepkov, R. Parker, S. Pfeifer, O. Schneising, T. Yokota, and Y. Yoshida. A joint effort to deliver satellite retrieved atmospheric CO_2 concentrations for surface flux inversions: the ensemble median algorithm emma. *Atmospheric Chemistry and Physics*, 13(4):1771–1780, 2013. DOI: 10.5194/acp-13-1771-2013.
- M. Reuter, M. Buchwitz, O. Schneising, S. Noël, H. Bovensmann, J. P. Burrows, H. Boesch, A. Di Noia, J. Anand, R. J. Parker, P. Somkuti, L. Wu, O. P. Hasekamp, I. Aben, A. Kuze, H. Suto, K. Shiomi, Y. Yoshida, I. Morino, D. Crisp, C. W. O'Dell, J. Notholt, C. Petri, T. Warneke, V. A. Velasco, N. M. Deutscher, D. W. T. Griffith, R. Kivi, D. F. Pollard, F. Hase, R. Sussmann, Y. V. Té, K. Strong, S. Roche, M. K. Sha, M. De Mazière, D. G. Feist, L. T. Iraci, C. M. Roehl, C. Retscher, and D. Schepers. Ensemble-based satellite-derived carbon dioxide and methane column-averaged dry-air mole fraction data sets (2003–2018) for carbon and climate applications. *Atmospheric Measurement Techniques*, 13(2):789–819, 2020. DOI: 10.5194/amt-13-789-2020.
- M. Rigby, S. A. Montzka, R. G. Prinn, J. W. C. White, D. Young, S. O'Doherty, M. F. Lunt, A. L. Ganesan, A. J. Manning, P. G. Simmonds, P. K. Salameh, C. M. Harth, J. Mühle, R. F. Weiss, P. J. Fraser, L. P. Steele, P. B. Krummel, A. McCulloch, and S. Park. Role of atmospheric oxidation in recent methane growth. *Proceedings of the National Academy of Sciences*, 114(21):5373–5377, 2017. DOI: 10.1073/pnas.1616426114.
- W. J. Riley, Z. M. Subin, D. M. Lawrence, S. C. Swenson, M. S. Torn, L. Meng, N. M. Mahowald, and P. Hess. Barriers to predicting changes in global terrestrial methane fluxes: analyses using clm4me, a methane biogeochemistry model integrated in cesm. *Biogeosciences*, 8(7):1925–1953, 2011. DOI: 10.5194/bg-8-1925-2011.
- B. Ringeval, P. Friedlingstein, C. Koven, P. Ciais, N. de Noblet-Ducoudré, B. Decharme, and P. Cadule. Climate- CH_4 feedback from wetlands and its interaction with the climate- CO_2 feedback. *Biogeosciences*, 8(8):2137–2157, 2011. DOI: 10.5194/bg-8-2137-2011.
- T. Rixen, A. Baum, T. Pohlmann, W. Blazer, J. Samiaji, and C. Jose. The Siak, a tropical black water river in central Sumatra on the verge of anoxia. *Biogeochemistry*, 90:129–140, 2008. DOI: 10.1007/s10533-008-9239-y.
- T. Rixen, A. Baum, F. Wit, and J. Samiaji. Carbon leaching from tropical peat soils and consequences for carbon balances. *Frontiers in Earth Science*, 4:74, 2016. DOI: 10.3389/feart.2016.00074.
- J. Roy, P. Tschakert, H. Waisman, S. Halim, P. Antwi-Agyei, P. Dasgupta, B. Hayward, M. Kanninen, D. Liverman, C. Okereke, P. Pinho, K. Riahi, A. Rodriguez, F. A. . Durand, M. Babiker, M. Bangalore, P. Bertoldi, B. Choudhary, A. Cartwright, R. Djalante, K. Ebi,

- N. Ellis, F. Engelbrecht, M. Figueroa, M. Gupta, A. Haileselassie, K. Henrique, D. Huppmann, S. Huq, D. Jacob, R. James, D. Ley, P. Marcotullio, O. Massera, R. Mechler, S. Mehrotra, P. Newman, S. Parkinson, A. Revi, W. Rickels, D. Salili, L. Schipper, J. Schmidt, S. Schultz, P. Smith, W. Solecki, S. Some, N. T. Ruat, A. Thomas, P. Urquhart, and M. W. Singh. Chapter 5: Sustainable development, poverty eradication and reducing inequalities. In *Global Warming of 1.5 °C an IPCC special report on the impacts of global warming of 1.5 °C above pre-industrial levels and related global greenhouse gas emission pathways, in the context of strengthening the global response to the threat of climate change*. Intergovernmental Panel on Climate Change, 2018. URL <http://pure.iiasa.ac.at/id/eprint/15517/>.
- M. G. Sanderson. Biomass of termites and their emissions of methane and carbon dioxide: A global database. *Global Biogeochemical Cycles*, 10(4):543–557, 1996. DOI: 10.1029/96GB01893.
- M. Saunois, A. R. Stavert, B. Poulter, P. Bousquet, J. G. Canadell, R. B. Jackson, P. A. Raymond, E. J. Dlugokencky, S. Houweling, P. K. Patra, P. Ciais, V. K. Arora, D. Bastviken, P. Bergamaschi, D. R. Blake, G. Brailsford, L. Bruhwiler, K. M. Carlson, M. Carrol, S. Castaldi, N. Chandra, C. Crevoisier, P. M. Crill, K. Covey, C. L. Curry, G. Etiope, C. Frankenberg, N. Gedney, M. I. Hegglin, L. Höglund-Isaksson, G. Hugelius, M. Ishizawa, A. Ito, G. Janssens-Maenhout, K. M. Jensen, F. Joos, T. Kleinen, P. B. Krummel, R. L. Langenfelds, G. G. Laruelle, L. Liu, T. Machida, S. Maksyutov, K. C. McDonald, J. McNorton, P. A. Miller, J. R. Melton, I. Morino, J. Müller, F. Murguía-Flores, V. Naik, Y. Niwa, S. Noce, S. O’Doherty, R. J. Parker, C. Peng, S. Peng, G. P. Peters, C. Prigent, R. Prinn, M. Ramonet, P. Regnier, W. J. Riley, J. A. Rosentreter, A. Segers, I. J. Simpson, H. Shi, S. J. Smith, L. P. Steele, B. F. Thornton, H. Tian, Y. Tohjima, F. N. Tubiello, A. Tsuruta, N. Viovy, A. Voulgarakis, T. S. Weber, M. van Weele, G. R. van der Werf, R. F. Weiss, D. Worthy, D. Wunch, Y. Yin, Y. Yoshida, W. Zhang, Z. Zhang, Y. Zhao, B. Zheng, Q. Zhu, Q. Zhu, and Q. Zhuang. The global methane budget 2000–2017. *Earth System Science Data*, 12(3):1561–1623, 2020. DOI: 10.5194/essd-12-1561-2020.
- H. Schaefer, S. E. M. Fletcher, C. Veidt, K. R. Lassey, G. W. Brailsford, T. M. Bromley, E. J. Dlugokencky, S. E. Michel, J. B. Miller, I. Levin, D. C. Lowe, R. J. Martin, B. H. Vaughn, and J. W. C. White. A 21st-century shift from fossil-fuel to biogenic methane emissions indicated by 13ch4. *Science*, 352(6281):80–84, 2016. ISSN 0036-8075. DOI: 10.1126/science.aad2705.
- R. Schlitzer. Ocean data view. ODV 5.4.0, 2021. URL <https://odv.awi.de>.
- O. Schneising, M. Buchwitz, M. Reuter, J. Heymann, H. Bovensmann, and J. P. Burrows. Long-term analysis of carbon dioxide and methane column-averaged mole fractions retrieved from sciamachy. *Atmospheric Chemistry and Physics*, 11(6):2863–2880, 2011. DOI: 10.5194/acp-11-2863-2011.
- Shimadzu Europa GmbH. Toc-determination in seawater. Application news, 2015. www.shimadzu.eu (21.05.2021).
- R. Sinsabaugh. Phenol oxidase, peroxidase and organic matter dynamics of soil. *Soil Biology and Biochemistry*, 42:391–404, 2010. DOI: 10.1016/j.soilbio.2009.10.014.

- R. L. Sinsabaugh, C. L. Lauber, M. N. Weintraub, B. Ahmed, S. D. Allison, C. Crenshaw, A. R. Contosta, D. Cusack, S. Frey, M. E. Gallo, T. B. Gartner, S. E. Hobbie, K. Holland, B. L. Keeler, J. S. Powers, M. Stursova, C. Takacs-Vesbach, M. P. Waldrop, M. D. Wallenstein, D. R. Zak, and L. H. Zeglin. Stoichiometry of soil enzyme activity at global scale. *Ecology Letters*, 11(11):1252–1264, 2008. DOI: 10.1111/j.1461-0248.2008.01245.x.
- K. R. Smith, M. A. Desai, J. V. Rogers, and R. A. Houghton. Joint co₂ and ch₄ accountability for global warming. *Proceedings of the National Academy of Sciences*, 110(31):E2865–E2874, 2013. DOI: 10.1073/pnas.1308004110.
- R. Spahni, R. Wania, L. Neef, M. van Weele, I. Pison, P. Bousquet, C. Frankenberg, P. N. Foster, F. Joos, I. C. Prentice, and P. van Velthoven. Constraining global methane emissions and uptake by ecosystems. *Biogeosciences*, 8(6):1643–1665, 2011. DOI: 10.5194/bg-8-1643-2011.
- F. Stevenson. *Organic Matter in Soils: Pools, Distribution, Transformations, and Function*, book section 1, pages 1–23. Wiley, 1994. ISBN 978-0-471-59474-1.
- J. Strefler, T. Amann, N. Bauer, E. Kriegler, and J. Hartmann. Potential and costs of carbon dioxide removal by enhanced weathering of rocks. *Environmental Research Letters*, 13(3):034010, mar 2018. DOI: 10.1088/1748-9326/aaa9c4.
- L. L. Taylor, J. Quirk, R. M. S. Thorley, P. A. Kharecha, J. Hansen, A. Ridgwell, M. R. Lomas, S. A. Banwart, and D. J. Beerling. Enhanced weathering strategies for stabilizing climate and averting ocean acidification. *Nature Climate Change*, 6:1758–1798, 2016. DOI: 10.1038/nclimate2882.
- H. Tian, X. Xu, M. Liu, W. Ren, C. Zhang, G. Chen, and C. Lu. Spatial and temporal patterns of ch₄ and n₂o fluxes in terrestrial ecosystems of north america during 1979–2008: application of a global biogeochemistry model. *Biogeosciences*, 7(9):2673–2694, 2010. DOI: 10.5194/bg-7-2673-2010.
- H. Tian, G. Chen, C. Lu, X. Xu, W. Ren, B. Zhang, K. Banger, B. Tao, S. Pan, M. Liu, C. Zhang, L. Bruhwiler, and S. Wofsy. Global methane and nitrous oxide emissions from terrestrial ecosystems due to multiple environmental changes. *Ecosystem Health and Sustainability*, 1(1):1–20, 2015. DOI: 10.1890/EHS14-0015.1.
- A. J. Turner, C. Frankenberg, P. O. Wennberg, and D. J. Jacob. Ambiguity in the causes for decadal trends in atmospheric methane and hydroxyl. *Proceedings of the National Academy of Sciences*, 114(21):5367–5372, 2017. DOI: 10.1073/pnas.1616020114.
- A. J. Turner, C. Frankenberg, and E. A. Kort. Interpreting contemporary trends in atmospheric methane. *Proceedings of the National Academy of Sciences*, 116(8):2805–2813, 2019. DOI: 10.1073/pnas.1814297116.
- T. P. C. van Noije, P. Le Sager, A. J. Segers, P. F. J. van Velthoven, M. C. Krol, W. Hazeleger, A. G. Williams, and S. D. Chambers. Simulation of tropospheric chemistry and aerosols with the climate model EC-Earth. *Geoscientific Model Development*, 7(5):2435–2475, 2014. DOI: 10.5194/gmd-7-2435-2014.

References

- R. Vaquer-Sunyer and C. M. Duarte. Thresholds of hypoxia for marine biodiversity. *PNAS*, 2008. DOI: 10.1073/pnas.0803833105.
- R. Wanninkhof. Relationship between wind speed and gas exchange over the ocean. *Journal of Geophysical Research: Oceans*, 97:7373–7382, 1992. DOI: 10.1029/92JC00188.
- M. W. Warren, J. B. Kauffman, D. Murdiyarso, G. Anshari, K. Hergoualc’h, S. Kurnianto, J. Purbopuspito, E. Gusmayanti, M. Afifudin, J. Rahajoe, L. Alhamd, S. Limin, and A. Iswandi. A cost-efficient method to assess carbon stocks in tropical peat soil. *Biogeosciences*, 9(11): 4477–4485, 2012. DOI: 10.5194/bg-9-4477-2012.
- R. F. Weiss. Carbon dioxide in water and seawater: The solubility of a non-ideal gas. *Marine Chemistry*, 2:203–215, 1974. DOI: 10.1016/0304-4203(74)90015-2.
- Wetlands. *Wetlands: Characteristics and Boundaries*. National Academies Press, 1995. ISBN 9780309587228.
- Wetlands International. A quick scan of peatlands in malaysia. *Wetlands International - Malaysia: Petaling Jaya*. URL <http://luk.staff.ugm.ac.id/rawa/Wetlands/PeatlandsInMalaysia.pdf>.
- Wetlands International. Indonesia and malaysia peat lands., 2009. URL <http://data.globalforestwatch.org>.
- R. Wetzel. *Microbial Enzymes in Aquatic Environments.*, chapter Extracellular Enzymatic Interactions: Storage, Redistribution, and Interspecific Communication. Brock/Springer Series in Contemporary Bioscience. Springer, New York, 1991. DOI: 10.1007/978-1-4612-3090-8_2.
- G. J. Whiting and J. P. Chanton. Primary production control of methane emission from wetlands. *Nature*, 364, 1993. DOI: 10.1038/364794a0.
- C. J. Williams, E. A. Shingara, and J. B. Yavitt. Phenol oxidase activity in peatlands in new york state: Response to summer drought and peat type. *Wetlands*, 20:416–421, 2000. DOI: 10.1672/0277-5212(2000)020[0416:POAIP]2.0.CO;2.
- J. E. Williams, P. F. J. van Velthoven, and C. A. M. Brenninkmeijer. Quantifying the uncertainty in simulating global tropospheric composition due to the variability in global emission estimates of Biogenic Volatile Organic Compounds. *Atmospheric Chemistry and Physics*, 13(5):2857–2891, 2013. DOI: 10.5194/acp-13-2857-2013.
- J. E. Williams, K. F. Boersma, P. Le Sager, and W. W. Verstraeten. The high-resolution version of tm5-mp for optimized satellite retrievals: description and validation. *Geoscientific Model Development*, 10(2):721–750, 2017. DOI: 10.5194/gmd-10-721-2017.
- F. Wit, D. Müller, A. Baum, T. Warneke, W. S. Pranowo, and M. Müller. The impact of disturbed peatlands on river outgassing in Southeast Asia. *Nature Communications*, 6, 2015. DOI: 10.1038/ncomms10155.

- F. Wit, T. Rixen, A. Baum, W. S. Pranowo, and A. A. Hutahaean. The Invisible Carbon Footprint as a hidden impact of peatland degradation inducing marine carbonate dissolution in Sumatra, Indonesia. *Scientific Reports*, 8:2045–2322, 2018. DOI: 10.1038/s41598-018-35769-7.
- F. Worrall, T. P. Burt, R. Y. Jaeban, J. Warburton, and R. Shedden. Release of dissolved organic carbon from upland peat. *Hydrological Processes*, 16(17):3487–3504, 2002. DOI: 10.1002/hyp.1111.
- J. Xu, P. J. Morris, J. Liu, and J. Holden. PEATMAP: Refining estimates of global peatland distribution based on a meta-analysis. *CATENA*, 160:134–140, 2018. DOI: 10.1016/j.catena.2017.09.010.
- A. Yatagai, M. Maeda, S. Khadgarai, M. Masuda, and P. Xie. End of the Day (EOD) Judgment for Daily Rain-Gauge Data. *Atmosphere*, 2020. DOI: 10.3390/atmos11080772.
- T. Yokota. A nadir looking swir fts to monitor co₂ column density for japanese gosat project. *Proc. 24th ISTS (Selected Papers), JSASS & Organizing Comm. of the 24th ISTS*, 2004. url: <https://ci.nii.ac.jp/naid/10024344084/en/>.
- J. Yoshida, T. Kawashima, J. Ishida, K. Hamada, J. Tanii, Y. Katsuyama, H. Suto, A. Kuze, M. Nakajima, and T. Hamazaki. Prelaunch performance test results of TANSO-FTS and CAI on GOSAT. In M. Strojnik, editor, *Infrared Spaceborne Remote Sensing and Instrumentation XVI*, volume 7082, pages 308 – 316. International Society for Optics and Photonics, SPIE, 2008. DOI: 10.1117/12.800701.
- C. J. Zappa, W. R. McGillis, P. A. Raymond, J. B. Edson, E. J. Hintsä, H. J. Zemmeling, J. W. H. Dacey, and D. T. Ho. Environmental turbulent mixing controls on air-water gas exchange in marine aquatic systems. *Geophysical Research Letters*, 2007. DOI: 10.1029/2006GL028790.
- R. E. Zeebe and D. Wolf-Gladrow. *CO₂ in seawater: Equilibrium, Kinetics, Isotopes*, chapter 1, pages 1–84. Elsevier Oceanography Series 65. Elsevier, Amsterdam, 1st edition, 2001. URL <https://epic.awi.de/id/eprint/4276/>.
- Z. Zhang, N. E. Zimmermann, J. O. Kaplan, and B. Poulter. Modeling spatiotemporal dynamics of global wetlands: comprehensive evaluation of a new sub-grid topmodel parameterization and uncertainties. *Biogeosciences*, 13(5):1387–1408, 2016. DOI: 10.5194/bg-13-1387-2016.
- Z. Zhang, E. Fluet-Chouinard, K. Jensen, K. McDonald, G. Hugelius, T. Gumbrecht, M. Carroll, C. Prigent, A. Bartsch, and B. Poulter. Development of the global dataset of wetland area and dynamics for methane modeling (wad2m). *Earth System Science Data*, 13(5):2001–2023, 2021. DOI: 10.5194/essd-13-2001-2021.
- Q. Zhu, J. Liu, C. Peng, H. Chen, X. Fang, H. Jiang, G. Yang, D. Zhu, W. Wang, and X. Zhou. Modelling methane emissions from natural wetlands by development and application of the triplex-ghg model. *Geoscientific Model Development*, 7(3):981–999, 2014. DOI: 10.5194/gmd-7-981-2014.
- Q. Zhu, C. Peng, H. Chen, X. Fang, J. Liu, H. Jiang, Y. Yang, and G. Yang. Estimating global natural wetland methane emissions using process modelling: spatio-temporal patterns

References

- and contributions to atmospheric methane fluctuations. *Global Ecology and Biogeography*, 24(8):959–972, 2015. DOI: 10.1111/geb.12307.
- Q. Zhuang, J. M. Melillo, D. W. Kicklighter, R. G. Prinn, A. D. McGuire, P. A. Steudler, B. S. Felzer, and S. Hu. Methane fluxes between terrestrial ecosystems and the atmosphere at northern high latitudes during the past century: A retrospective analysis with a process-based biogeochemistry model. *Global Biogeochemical Cycles*, 18(3), 2004. DOI: 10.1029/2004GB002239.

Acknowledgements

First of all, I would like to thank my supervisor PD Dr. Thorsten Warneke for his guidance and support throughout all stages of my study. His inventiveness and motivation strongly improved my work experience and research results. My honest gratitudes also go to Dr. Tim Rixen from ZMT and to Dr. Nikolaos Daskalakis from the IUP LAMOS group, who provided their assistance and knowledge in the fields of research that lie outside the expertise of our working group. Tim consistently helped advance my research on tropical peat regions with his enthusiasm and knowledge and Nikos introduced me to atmospheric transport modelling and was a huge help with all kinds of questions regarding the modelling part of my study.

After that, I want to thank Prof. Dr. Justus Notholt for his support and my accommodation in his working group. In this context I also thank my colleagues from the working group who warmly welcomed me in their midst and provide their help throughout the years. On campus and in home office they were available for chats and I am grateful for the nice work environment. Special thanks go to Dr. Matthias Buschmann who was always available to answer various questions arising throughout my PhD journey and to Lukas Heizmann for his proofread of my thesis.

Moreover, I am grateful for the nice cooperation with our colleagues in Malaysia. Most notably, I want to thank Prof. Dr. Moritz Müller for his organisation of the measurement campaigns and for the collaboration on my research papers. Also, I want to thank the Sarawak Forestry Department and Sarawak Biodiversity Centre for permission to conduct collaborative research in Sarawak.

I would like to thank the Global Carbon Project for providing wetland emission datasets for my study. Special thanks in this regard go to Dr. Benjamin Poulter from NASA and Dr. Marielle Sainois from LSCE for their cooperation and our insightful discussions.

Another thanks goes to Prof. Dr. Mihalis Vrekoussis for dedicating his time to be the second reviewer of my thesis and to the other members of my PhD committee Prof. Dr. Annette Ladstätter-Weißenmayer and Prof. Dr. Stefan Bornholdt.

Finally, I want to thank my family for their love and support throughout my PhD journey and my life in general. Specifically I want to thank my parents Gabriele and Hans-Dieter Klemme for enabling me to study and their encouragement throughout the way. I want to thank my sister Victoria Klemme who helped me to unwind and remember life outside education. And ultimately, I want to thank my partner Linus Pleines for his love and understanding and for the emotional support during stressful episodes of my PhD journey.

Thank you all.